A Novel Procedure Based on 2D Finite Element Modeling and Orthogonal Cutting Tests to Predict Machinability and Tool Wear Evolution Considering the Microstructure Effect of Lamellar Ferrite-Pearlite Steels

Mikel Sáez de Buruaga Echeandia

Mondragon Unibertsitatea
Mechanical and Manufacturing Department

March, 2018

Mondragon Unibertsitatea
Faculty of Engineering

Submitted for the degree of Doctor
in Mondragon Unibertsitatea

A Novel Procedure Based on 2D Finite Element Modeling and Orthogonal Cutting Tests to Predict Machinability and Tool Wear Evolution Considering the Microstructure Effect of Lamellar Ferrite-Pearlite Steels

Mikel Sáez de Buruaga Echeandia

Supervised by:

Dr. Pedro José Arrazola Arriola
High Performance Machining
Mondragon Unibertsitatea

Dr. Jon Ander Esnaola Ramos
Structural Mechanics and Design
Mondragon Unibertsitatea

March, 2018

Declaration

I hereby declare that this thesis is the result of my own work and that, to the best of my knowledge and belief, no part of this dissertation has previously been submitted for any similar qualification or degree.

Abstract

The main contribution of this Ph.D. is the development of a finite element based procedure to predict machinability considering the effect of lamellar ferrite-pearlite microstructures. The findings of this study give support to the understanding of the machinability of ferrite-pearlite steels. To cover a wide range of ferrite-pearlite microstructures, the analysis was focused on four steels with different carbon content: 16MnCr5, 27MnCr5, C45 and C60.

Based on an Arbitrary Eulerian Lagrangian formulation, an orthogonal cutting Finite Element model in conjunction with a tool wear simulation strategy was provided for the prediction of scientific (cutting forces, tool temperatures, chip formation, etc.) and industrial relevant outcomes (machinability/tool wear). The required inputs that describe the flow stress of the workpiece material, the friction behavior in the tool-workpiece interface, and the tool wear rate were defined as functions dependent on microstructure and composition properties. Based on rheological characterization tests, a new material constitutive model was proposed to represent the behavior of ferrite-pearlite steels (MSB model). The main contribution of this model is that the strain hardening behavior of the ferrite-pearlite steels was modeled as a function of the chemical composition, and the microstructure parameters of pearlite fraction, interlamellar spacing and ferritic mean grain size. Frictional behavior was also identified as dependent on the ferrite content and the relative sliding velocity at the interface. In addition, a unique wear rate equation was identified to predict the wear on the rake and flank faces of the tool, based on specially designed orthogonal tests. This was set out as uncoupled mechanical and thermally activated wear phenomena, in which the mechanical wear was identified as an equation dependent on the carbon content of the steels and the sliding distance. The thermal wear was modeled by an Arrhenius type equation, in which the activation energy required for thermal wear to occur was found to be the same for all the tested ferrite-pearlite steels.

The trends observed in the simulations were in good agreement with the orthogonal cutting tests as regards both scientific and industrial relevant outputs. The values of crater depth (K_{T}) and flank wear land (V_{B}), and the scientific variables of cutting forces (F_{c}), chip thickness (t_2) and tool temperature were predicted with an error in the range of 5-20%. The major limitation of the developed model was found in the prediction of contact length (l_{c}) or crater length (K_{B}) and feed forces (F_{f}), which were underestimated by 25-60%.

In addition to the numerical approaches, two original empirical strategies were developed in the course of this research. One concerned the establishment of a direct relationship between the radiation of the tool surface and the real surface temperature without the need of characterizing the emissivity of the tool. The other was focused on the orthogonal cutting procedure in which fundamental variables were linked to tool wear. The combination of these two setups permitted the accurate characterization of the wear behavior of the steels, and demonstrated that the wear evolution on both the rake and flank faces could be modeled with the same wear rate equation.

Resumen

La principal contribución de la tesis es el desarrollo de un procedimiento basado en elementos finitos enfocado a la predicción de maquinabilidad y evolución del desgaste, considerando el efecto de la microestructura de los aceros formados por ferrita y perlita laminar. Adicionalmente, los resultados experimentales obtenidos contribuyen al estudio de la maquinabilidad de dichos aceros. Con el objetivo de desarrollo y validación del modelo numérico en un amplio rango de microestructuras ferrita-perlita, cuatro aceros con diferente contenido en carbono fueron seleccionados: 16MnCr5, 27MnCr5, C45 y C60.

Basado en la formulación Arbitraria Euleriana Lagrangiana, se ha desarrollado un modelo de elementos finitos en conjunto con una estrategia de simulación del desgaste para la predicción de variables científicas (fuerzas de corte, temperaturas, formación de viruta, etc.) y variables de relevancia industrial (maquinabilidad y desgaste de herramientas). Los parámetros de entrada necesarios que describen la tensión a fluencia del material, la fricción en la intercara pieza-herramienta, y el modelo de desgaste han sido definidos en función de la composición del material y propiedades microestructurales. En base a ensayos experimentales de reología, se ha propuesto un novedoso modelo constitutivo de material para representar el comportamiento de los aceros ferrita-perlita (modelo MSB). La principal contribución es la modelización del endurecimiento por deformación del material en base a la composición, el porcentaje de perlita, el espaciado interlaminar de la perlita y el tamaño de grano medio de la ferrita. El modelo de fricción ha sido definido en función del porcentaje de ferrita del material y la velocidad de deslizamiento entre la pieza y herramienta. Por último, se ha propuesto una única ley de degaste capaz de representar tanto el desgaste de flanco como el desgaste de cráter en la herramienta. Dicha ley describe el desgaste como fenómenos mecánicos y de activación térmica desacoplados, en la cual la parte mecánica es modelizada en base al contenido en carbono del acero y la longitud de deslizamiento. La parte correspondiente al fenómeno térmico se modeliza con una ecuación tipo Arrhenius, en la cual se ha identificado como la energía de activación es la misma para todo el rango de aceros estudiados.

Los resultados tanto empíricos como provenientes de las simulaciones obtienen tendencias muy similares en cuanto a variables científicas e industriales se refiere. La predicción de profundidad de cráter (K_{T}), longitud de desgaste de flanco (V_{B}), fuerza de corte (F_{c}) y espesor de viruta (t_2) obtuvieron un error del 5-20% en comparación con los resultados experimentales de corte ortogonal. La mayor limitación reside en la predicción de la longitud de contacto (l_{c}) y la fuerza de avance (F_{f}), las cuales son estimadas un 25-60% inferiores.

Además del procedimiento numérico, se han desarrollado dos novedosas estrategias empíricas en el transcurso de la investigación. La primera consiste en el desarrollo de un setup para la obtención de una relación directa entre la radiación emitida por la superficie de la herramienta y la temperatura real de dicha superficie, sin necesidad de caracterizar la emisividad. El segundo procedimiento se enfoca en obtener de forma sincronizada la evolución de las variables fundamentales y el desgaste en la herramienta en el proceso de corte ortogonal. Mediante las dos estrategias empíricas se han podido caracterizar los mecanismos de desgaste para los diferentes aceros ferrita-perlita, y con ello establecer una única ley capaz de representar el desgaste de flanco y cráter.

Laburpena

Tesiaren ekarpen nagusia mekanizagarritasuna eta higaduraren eboluzioa aurreikustera bideratuta dagoen elementu finituetan oinarritzen den prozedura garatzea da, ferrita eta perlitazko lamelez osatutako altzairuen mikroestrukturaren eragina kontuan hartuta. Gainera, lortutako emaitza esperimentalak laguntzen du altzairu horien makinagarritasuna ulertzeko. Ferrita-perlitazko mikroestruktura mota zabalean garatutako modeloa balioztatzeko, karbono-eduki desberdina duten lau altzairu hautatu dira: 16MnCr5, 27MnCr5, C45 eta C60.

Lagrangiar Euleriar Arbitrario formulazioan oinarrituta, elementu finituen modelo bat garatu da, higadura simulazio estrategiakin batera aldagai zientifikoen (ebaketa indarrak, tenperaturak, txirbilaren formazioa) eta garrantzizko aldagai industrialak (makinagarritasuna eta herraminten higadura) aurreikusteko. Beharrezkoak diren sarrera parametroak, hau da, materialaren tentsio-deformazio deskribatzen duen modeloa, erreminta eta piezan harteko marrus- kadura eta higadura modeloa, propietate mikroestrukturalen eta konposizioaren arabera definitu dira. Reologia esperimentuetan oinarriturik, altzairu ferritiko-perlitikoen portaera errepresentatzen duen material modelo berria proposatu da (MSB modeloa). Konposizioan, perlita ehunekoan, perlitaren distantzia interlaminarean eta ferritaren batez besteko ale-tamainaren arabera materialaren deformazioren aurkako gogortasuna deskribatzea da modeloaren kontribuzio nagusia. Marrus- kadura legea, ferrita ehunekoaren arabera eta pieza eta erremintaren arteko abiadura erlatiboaren arabera definitu da. Azkenik, higadura lege bakar bat planteatu da erremintaren flanko eta krater higadura errepresentatzeko gai dena. Lege honek, higadura fenomeno desakoplatu mekaniko eta aktibazio termikoen bitartez deskribatzen du, non atal mekanikoa altzairuaren karbonoaren edukian eta irristatze luzeeran oinarritzen den. Fenomeno termikoari dagokion higadura Arrhenius motako ekuazio batekin modelatzen da, zeinean aktibazio energetikoa berdina dela aurkitu da aztertutako altzairu guztientzat.

Emaitza enpirikoek zein simulaziokoek, joera berdinak lortzen dituzte aldagai zientifiko eta industrialak astertzerakoan. Krater sakoneraren (K_{T}) aurreikuspena, flankoaren higadura luzera (V_{B}), ebaketa indarra (F_{c}) eta txirbil lodiera (t_2) %5-20ko akatsa lortu dute ebaketa ortogonalaren emaitza esperimentalekin alderatuta. Kontaktu luzera (l_{c}) eta aitzinamendu indarra (F_{f}) aurreikustean da modeloaren muga handiena, emaitzak %25-60 txikiagoak izanik.

Elementu finituen modeluaz gain, bi ikerketa-estrategia enpiriko garatu dira ikerketan zehar. Lehenengoak, erremintaren gainazalak duen tenperatura erreala eta igortzen duen erradiazioaren arteko lotura zehazten du, erremintaren emisibitatea karakterizatu beharrik gabe. Bigarren prozeduran, modu sinkronizatuan funtsezko aldagaien eboluzioa eta erremintaren higadura lortzen dira ebaketa ortogonaleko prozesuan. Bi estrategia enpiriko hauen bitartez, ferrita-perlita altzairuen higadura mekanismoak karakterizatu egin dira eta horren bidez, kraterraren eta flankoaren higadura errepresentatzeko gai den lege bakarra ezarri da.

Agradecimientos

Mi primer agradecimiento está dedicado a los directores de tesis, Pedro Arrazola y Jon Ander Esnaola, por depositar la confianza en mí para llevar a cabo esta investigación, y por la dedicación continua durante el desarrollo de la misma. También agradecer a todo el grupo de Mecanizado de Alto Rendimiento por toda la colaboración prestada, por su actitud formativa, y sobre todo por su gran compañerismo.

Mis más sinceros agradecimientos a Patxi Aristimuño y Exabier Hormaetxe, por la gran ayuda prestada en la puesta a punto de los ensayos experimentales. A Dani Soler, por los grandes avances realizados en termografía, y a Ainhara Garay y Erika Dominguez, por su ayuda en los análisis de microestructura. También agradecer a Ibon Poveda su colaboración en el desarrollo del modelo de desgaste. Y en definitiva, al resto de personas que también han aportado su granito de arena en el desarrollo.

También me gustaría mencionar a los participantes del proyecto IMMAC. En especial a Jöel Rech y Cedric Courbon, por facilitarme los datos de fricción, y a Amandine Roth y Sebastien Allain, por su ayuda prestada en el desarrollo del modelo constitutivo de material. Por supuesto, también nombrar a los representantes de Ascometal y Sidenor, Enrico D'Eramo y Diego Herrero, por facilitarnos la gran cantidad de aceros necesarios para el desarrollo de la tesis.

De todos los agradecimientos, el más especial se lo debo a mis compañeros doctorandos. No solo por su ayuda y sus enseñanzas, sino también por los grandes momentos y entretenimientos que hemos pasado. La tesis no habría sido lo mismo sin el café de las 10, ni las partidas de pin-pon después de comer. Podría poner los nombres de todos, pero un "mila esker gotxus" es suficiente para que entiendan lo mucho que han significado estos años.

Por último, como no, agradecer a mi familia, a Zelai, y amigos fuera de la universidad que me han apoyado y motivado durante el largo recorrido que ha sido la tesis. Mila esker familia.

Contents

List of Figures

List of Tables

Glossary

Symbols in roman characters:

a_{p}	Depth of cut (mm)
A	Yield stress value (MPa)
A_{f}	Yield stress value of ferrite (MPa)
A_{p}	Yield stress value of pearlite (MPa)
A_{sh2}	Effective contact are in the secondary shear zone (mm^2)
A_{w}	Frequency factor in Arrhenius type equations (-)
B	Strength coefficient (MPa)
B_{f}	Strength coefficient of ferrite (MPa)
B_{p}	Strength coefficient of pearlite (MPa)
B^*	Thermal sensitivity coefficient in MSB model (-)
C	Strain rate sensitivity coefficient (-)
C_{f}	Strain rate sensitivity coefficient of ferrite (-)
C_{p}	Strain rate sensitivity coefficient of pearlite (-)
C_{p}	Specific heat ($\mathrm{J{\cdot}kg^{-1}{\cdot}m^{-3}}$)
d	Overhang distance (mm)
d_α	Grain size of ferrite (µm)
d_μ	Exponent of friction model (-)
d_0	Diameter of compression specimens (mm)
D^*	Temperature related empirical constant in strain rate equation (D^*=0.0064)
E	Young modulus (MPa)
E_{a}	Activation energy (kJ)
f	Feed (mm)
f_α	Volumetric fraction of ferrite (%)
f_{p}	Volumetric fraction of pearlite (%)
$\mathrm{f_{DRV}}$	Intensity of dynamic recovery processes related constant ($\mathrm{f_{DRV}} = 1.2$)
F_{c}	Cutting force (N)
F_{c0}	Cutting force measured with fresh tool (N)
F_{f}	Feed force (N)
F_{f0}	Feed force measured with fresh tool (N)
F_{sh2}	Shear forces in the secondary shear zone (N)
$\mathrm{FS_{0.2}}$	Flow stress for a strain level of 20% (MPa)
g	Empirical constant (g=61.7)
h_0	Height of compression specimens (mm)
K	Empirical constant (K=38 GPa)
k_{i}	Thermal conductance ($\mathrm{W{\cdot}m^2{\cdot}K^{-1}}$)
$\mathrm{k_0}$	Latent hardening related constant (-)
K	Thermal conductivity ($\mathrm{W{\cdot}m^{-1}{\cdot}K^{-1}}$)

K_{tool}	Thermal conductivity of the tool ($\text{W}\cdot\text{m}^{-1}\cdot\text{K}^{-1}$)
K_{B}	Crater wear length (μm)
K_{T}	Crater wear depth (μm)
$K_{\text{T,mechanical}}$	Crater wear depth related to mechanical type wear (μm)
K_{sc}	Specific cutting force ($\text{N}\cdot\text{mm}^2$)
K_{sf}	Specific feed force ($\text{N}\cdot\text{mm}^2$)
L	Machined length (m)
l_{c}	Contact length (mm)
m	Temperature sensitivity coefficient (-)
m_{f}	Temperature sensitivity coefficient of ferrite (-)
m_{p}	Temperature sensitivity coefficient of pearlite (-)
m^*	Temperature sensitivity exponent in MSB model (-)
M	Taylor or Smith factor (M=3)
n	Strain hardening coefficient (-)
n_{f}	Strain hardening coefficient of ferrite (-)
n_{p}	Strain hardening coefficient of pearlite (-)
n^*	Strain rate hardening coefficient in MSB model (-)
n_0	Critical density of geometrically necessary dislocations ($\text{n}_0 = 2.82$)
q_{sh}	Heat flux in a shear zone (W)
q_{sh2}	Heat flux in the secondary shear zone (W)
q_{sh3}	Heat flux in the tertiary shear zone (W)
q_{tool}	Heat flux flowing into the tool (W)
r	Temperature related exponent in MSB model (r=6.4)
r_{ε}	Cutting edge radius (μm)
R	Universal gas constant ($\text{R}=8.314\ \text{J}\cdot\text{mol}^{-1}\cdot\text{K}^{-1}$)
s	Interlamellar spacing (μm)
S^*	Temperature related empirical constant in MSB model ($\text{S}^*=0.076$)
t	Cutting time (min)
t_1	Uncut chip thickness (mm)
t_2	Chip thickness (mm)
t_{eq}	Chip thickness ratio (-)
T	Temperature (°C)
T_0	Room temperature (T_0=20°C)
ΔT_{adb}	Temperature increase due to adiabatic heating (°C)
T_{m}	Melting temperature in dynamic compression tests (°C)
T_{r}	Reference temperature in dynamic compression tests (°C)
T_{contact}	Temperature in the mid-plane of the contact section (°C)
T_{side}	Temperature on the side of the tool (°C)
T_{sat}	Saturation temperature in strain rate equation (T_{sat}=1108 K)
UTS	Ulimate tensile strength (MPa)
V_{B}	Length of flank wear land (μm)
V_{H}	Height of flank wear land (μm)
$V_{\text{H,mechanical}}$	Height of flank wear land related to mechanical type wear (μm)

V_{c}	Cutting speed ($\mathrm{m{\cdot}min^{-1}}$)
V_{chip}	Chip velocity ($\mathrm{m{\cdot}min^{-1}}$)
V_{sl}	Sliding velocity ($\mathrm{m{\cdot}min^{-1}}$)
W	Tool wear (μm)
$W_{\mathrm{mechanical}}$	Mechanical type tool wear (μm)
X^{α}	Kinematical hardening of the ferrite (-)
YS	Yield stress (MPa)

Symbols in Greek characters:

α	Clearance angle ($^{\mathrm{o}}$)
α_{n}	Forest dislocation hardening related constant ($\alpha_{\mathrm{n}} = 0.4$)
α^{*}	Heat partition between tool and workpiece (%)
α_{L}	Linear thermal expansion coefficient ($^{\mathrm{o}}\mathrm{C}^{-1}$)
β	Taylor-Quinney coefficient (-)
ε	True strain (-)
$\dot{\varepsilon}$	Strain rate ($\mathrm{s^{-1}}$)
$\dot{\varepsilon}_0$	Reference strain rate in dynamic compression tests ($\mathrm{s^{-1}}$)
η	Fraction of energy converted into heat (%)
η_{adb}	Adiabatic correction for the strain rate sensitivity (%)
γ	Rake angle ($^{\mathrm{o}}$)
κ	Thermal diffusivity ($\mathrm{cm^2{\cdot}s^{-1}}$)
λ	Friction angle ($^{\mathrm{o}}$)
λ_{d}	Density of shear bands ($\lambda_{\mathrm{d}} = 34.5\,\mathrm{b}$)
μ	Friction coefficient (-)
μ_{k}	Dynamic component of friction coefficient (-)
μ_{s}	Static component of friction coefficient (-)
μ_{α}	Shear modulus of ferrite ($\mu_{\alpha} = 80\,\mathrm{GPa}$)
ϕ	Shear angle ($^{\mathrm{o}}$)
ρ	Density ($\mathrm{kg{\cdot}m^{-3}}$)
ρ^{α}	Statistically stored dislocation density in ferrite ($\mathrm{m^{-2}}$)
σ	True stress (MPa)
σ_{SH}	Strain hardening term in MSB flow stress model (MPa)
σ_{TS}	Thermal softening term in MSB flow stress model (-)
σ_{SRH}	Strain rate hardening term in MSB flow stress model (-)
σ_0	Lattice friction (MPa)
σ_0^{α}	Lattice friction of ferrite (MPa)
σ_0^{p}	Lattice friction of pearlite (MPa)
τ_{sh2}	Shear stresses in the secondary shear zone (MPa)
τ_{sh3}	Shear stresses in the tertiary shear zone (MPa)
θ^{IV}	Stage IV hardening of pearlite (MPa)
υ	Poisson coefficient (-)

Abbreviations:

(16)	Steel 16MnCr5
(27)	Steel 27MnCr5
(45)	Steel C45
(60)	Steel C60
ALE	Arbitrary Lagrangian Eulerian
CEL	Coupled Eulerian Lagrangian
CPRESS	Contact pressure (in Abaqus)
DL	Digital levels
DSA	Dynamic strain aging
DRX	Dynamic recrystallization
GND	Geometrically necessary dislocations
FE	Finite element
FEM	Finite element method
FP	Ferrite-pearlite
HB	Brinnel hardness
HV	Vickers hardness
IR	Infrared
IT	Integration time
JC	Johnson-Cook model
MR	Material removed (cm^3)
MRI	Material removal index
NT11	Nodal temperature (in Abaqus)
PSZ	Primary shear zone
SEM	Scanning electro microscope
SHPB	Split Hopkinson pressure bar
SSZ	Secondary shear zone
TSZ	Tertiary shear zone

Chapter 1

Introduction

Manufacturing processes represent an important share of the gross domestic product (GDP) of developed countries. In terms of added value and employment, metal cutting represents a significantly large segment of industry. For example, in 2014 it was estimated that production by machining operations represented approximately 12% of European manufacturing investments, and was the most value added manufacturing process (Eurostat NACE 2017). The car industry, electrical engineering, railways, shipbuilding, aircraft manufacture and the machine tool sector itself, all have large machine shops with many thousands of employees engaged in machining. In these sectors, industrial production has increased by 10% in the European Community and by 12% in the EU28 in the last 5 years (Eurostat NACE 2017). In such a competitive market, shorter product lead-times and cost-reduction are of great importance. The commercial success of a new product is not only influenced by the time to market, but also by the quality of the machined component.

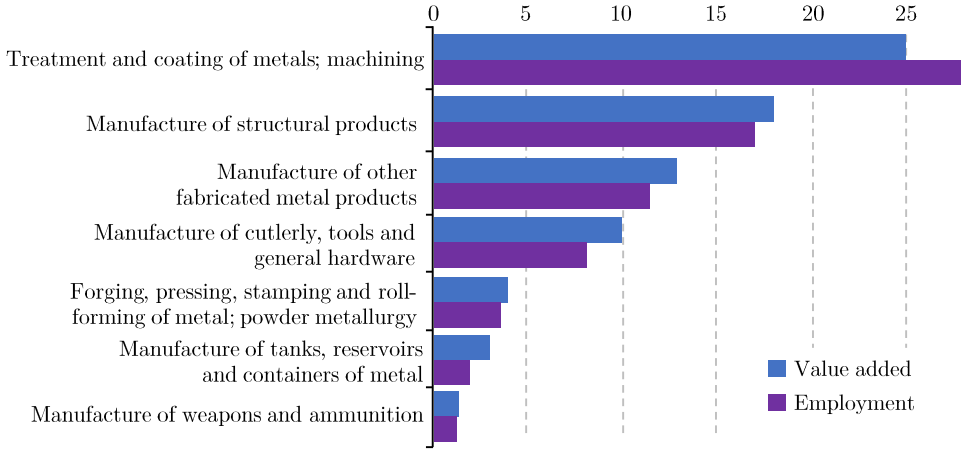

Figure 1.1: Ranking of value added and employment of manufacturing processes in Europe (Eurostat NACE 2017)

In order to further increase efficiency and reduce costs it is necessary to improve the understanding of the metal cutting process. The study of metal cutting focuses on the features of cutting tools, workpiece materials, coolants and fixture systems, as well as in the machine tools themselves. This has led to the improvement of the quality of products, an increase in tool life, and has contributed to cost reduction. For example, the development of cutting tool materials has has been subject of much study. In 70 years productivity has been increased in more than ten times through the replacement of high-speed steels to coated cemented carbides.

Concerning workpiece materials, trends mainly focus on the development of new materials or in the improvement of those existing. In the automotive industry, case-hardening and carbon steels are those materials mostly used in applications such as transmission shafts, camshafts, gear wheels, pinions and gear shafts or wheel hubs (Raabe 2006). These represent more than 40% of the structural materials and nearly a 70% from of the employed materials in automobile production (Fais 2016). Machining processes such as turning, broaching, drilling and tapping are commonly employed operations in the manufacturing of those components. An example of these processes is shown in Figure 1.2.

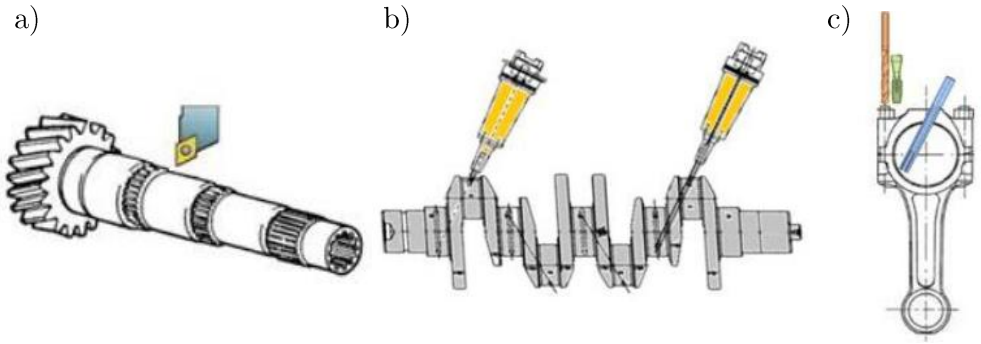

Figure 1.2: Common machining processes employed in automotive industry: a) turning-hobbing of a gear, b) deep drilling for engine passage in a crank pin, c) big eye boring, deep drilling and tapping in a piston (D'Eramo et al. 2017)

Typically, these steels are machined in soft conditions with Ferrite-Pearlite (FP) microstructure. Then a heat treatment is performed (case hardening or quenched and tempered) to obtain the final martensitic microstructure in the component, in which the finishing machining takes place. A lot of work has already been done regarding machining of hardened materials (Rech and Moisan 2003; Bartarya and Choudhury 2012). However, cutting ferrite-pearlite structures has been much less investigated although it remains a real industrial issue.

In the course of studying the influence of workpiece materials on cutting performance, one of the objectives of metal cutting studies is to establish a predictive theory that enables the prediction of process variables such as chip formation, cutting forces, cutting temperature, tool wear and surface integrity. However, the ultimate objective of the

science of metal cutting is to solve practical problems associated with improving the efficiency of industry (Arrazola et al. 2013). Nevertheless, the principles governing the cutting process have first to be understood, prior to developing a predictive theory.

In the same manner as in research areas such as forging or composite materials, efforts have been focused on obtaining models for the prediction of thermo-mechanical states throughout the machining process. Although much work has been done to date, there is still a need to improve the predictions (Arrazola et al. 2013). These existing predictive tools are mostly empirical, analytical and numerical type (for example finite element models). In the context of developing industrially flexible and predictive support tools, and limiting the experimental campaigns, numerical simulation is making a case as a relevant tool.

Finite Element (FE) modeling of the cutting process made its appearance in the 1970s. But it has been in the last two decades however, in which have been the greatest breakthroughs in the scientific field, due to the advances in computing, and the development of meshing and convergence algorithms.

Most numerical research is focused on the calculation of fundamental machining variables (cutting forces, temperatures, strains, strain rates, tool stresses, etc.) during the chip forming process. Mainly they are modeled in a simplified working condition such as orthogonal or 2D machining. Obtaining variables of industrial relevance (wear, surface integrity) is more complex, and in general the results obtained to date are not as effective as industry requires (Arrazola et al. 2013). The reasons for this are several: difficulties in obtaining correctly identified input parameters, very simple material and contact behavior models that do not reflect the real behavior of the process, very high calculation times in 3D models, etc. As a consequence, FE modeling continues to be a developing technique, where aspects of input parameters such as friction and material flow stress laws are of great influence in obtaining fundamental physical results as well as relevant industrial results (Melkote et al. 2017). Obtaining a universal chip formation model capable of obtaining quantitative and qualitative results that relate input parameters to fundamental variables and relevant industrial results is still a challenge today.

In this framework, this research focuses on the development and validation of a procedure to model the chip formation process, capable of predicting the influence that the microstructure of the material has on machinability/tool wear. In order to achieve the objective, modeling based on finite elements is proposed, due to the flexibility and possibilities this offers. To achieve the objective, the required inputs are identified, and an approach linking fundamental variables and industrial outcomes is assessed.

The analysis is focused on the study of carbon steels, where the microstructure type is that of ferrite-pearlite. These are materials widely used in the automotive industry, in which processing by machining is a common operation. The influence that composition and inclusions such as SMn, Ca (favorable) or Al_2O_3 (unfavorable) have on

tool wear have been studied in-depth. However, despite the fact that the influence of microstructure has also been researched with great interest, there are still large gaps about the influence of the quantity, shape, orientation and typology of phases present in the samples. This aspect is relevant since new material developments carried out by steelmakers tend to reduce the amount of additives due to their impact not only on the mechanical properties, but also on the environmental and process costs. Specifically, the role of ferrite and pearlite ratio, grain size, or interlamellar spacing of pearlite is the subject of study in this research.

The comprehensive investigations performed in this thesis contribute to the understanding of the cutting mechanisms and wear behavior of FP steels. The time-consuming empirical analyses, which is a major problem for both steelmakers and end-users, can be reduced due to a developed tool wear prediction strategy. In addition, the study considers the influence of lamellar ferrite-pearlite microstructure properties, which is of great concern for scientific and industrial developments.

The thesis has been developed within the framework of the projects IMMAC - Innovative Method dedicated to the development of a ferrite-pearlite grade regarding its MAChinability (RFCS-EU), MICROMAQUINTE - MICROestructura de aceros y superaleaciones base níquel en la MAQUinabilidad e INTEgridad superficial de componentes mecanizados (Basque Government - Department of Education, Linguistic Policy and Culture) and EMULATE - Un enfoque multiescala para la simulación de problemas termomecánicos en condiciones extremas: aplicación al mecanizado (RETOS-Spanish Government).

1.1 Scientific framework

In the machining process material is subjected to severe thermomechanic conditions, in which severe strains, strain rates, temperatures and heating rates occur (Merchant 1944; Oxley and Young 1989). The influence of these thermo-mechanical loads can generate differences between the bulk material and the material that makes contact with the tool (Courbon et al. 2014), or even affect the machined surface of the component (Ulutan and Ozel 2011). During the cutting operation, the tool is subjected also to severe thermomechanical loads. Pressures on the contact surfaces can be around 2 GPa, combined with shear stresses due to friction, and temperatures above 1000°C (Trent and Wright 2000).

The prediction of these fundamental physical variables (temperatures, strains, stresses, etc.) through the generation of models is the object of study in the field of metal machining. The final objective is to obtain relevant data of industrial parameters with the aim of improving productivity (linked with tool life) and/or quality of the machined components (linked with the surface integrity of machined parts). Figure 1.3 shows a diagram of the current state of modeling.

Input parameters such as cutting tool geometry, material properties and contact behavior are required in the development of models. By means of these inputs the models are able to calculate fundamental variables (*Stage 1*), and through them obtain aspects of industrial relevance (*Stage 2*). A clear example is the calculation of the tool life, where the developed model should reflect correctly the jump from *Stage 1* to *Stage 2*.

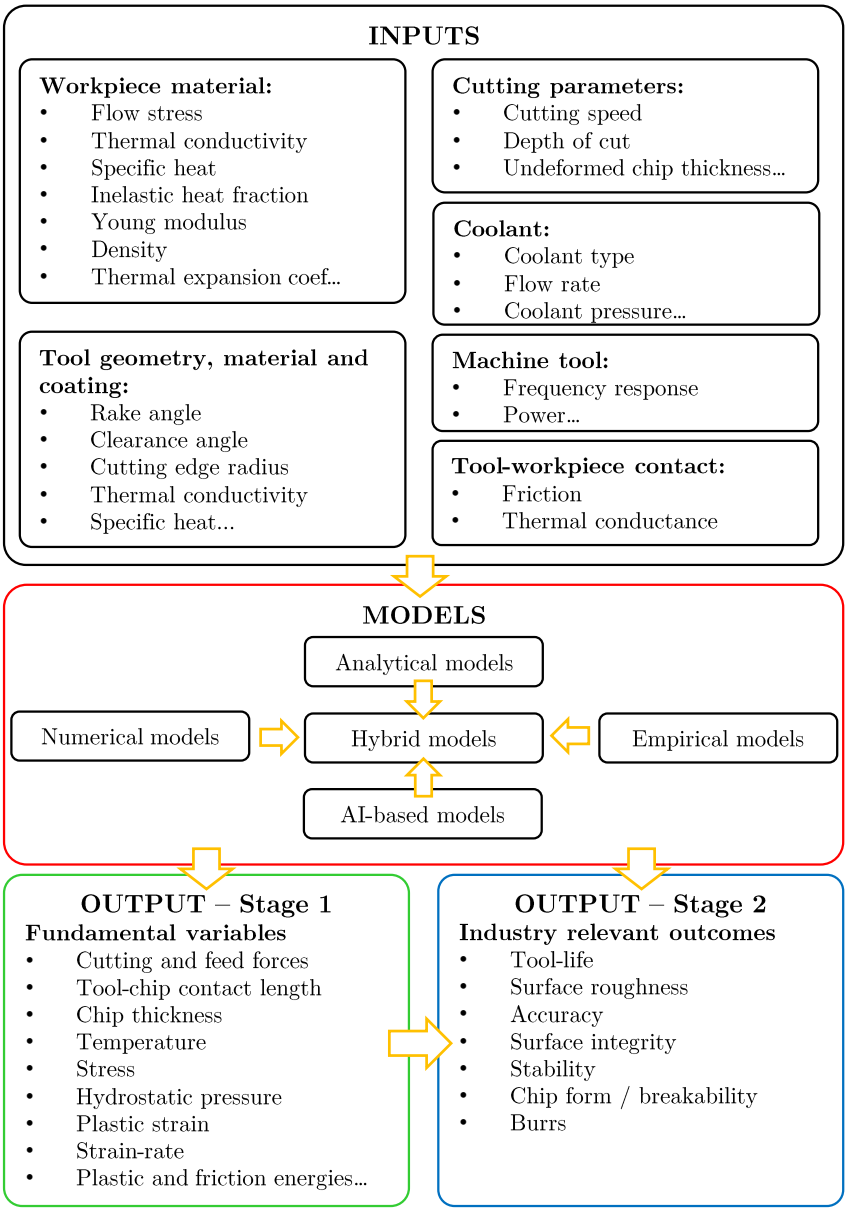

Figure 1.3: Diagram of the machining process modeling, adapted from Arrazola et al. (2013)

The models developed in the field of machining are divided into three main categories: analytical models, numerical models and empirical models. There are also models based on Artificial Intelligence (AI models) or hybrid models that combine those abovementioned. Table 1.1 shows the advantages and disadvantages of these models (Arrazola et al. 2013).

Table 1.1: Capabilities and limitations of modeling approaches

	Analytical	Numerical	Empirical
Principle	Slip-line theory or minimum energy principle	Continuum mechanics using FEM, FDM & meshless FEM	Curve fitting of experimental data
Capabilities	Predicts forces, chip geometry, contact length, stresses, strains, strain-rates and temperatures	Predicts forces, chip geometry, stresses, strain, strain-rates temperatures, wear, surface integrity	Applicable to most machining operations for measurable process variables only
Limitations	Usually limited to 2-D analysis with single and multiple cutting edge	Material model, friction as input, computational limitations (mesh)	Valid only for the range of experimentation
Advant.	Ability to develop fast and practical tools	Connect to industry relevant parameters	Practical, fast and direct estimation of industry-relevant parameters
Disadv.	Unique to each machining problem	Long computation time	Extensive experimentation, time consuming and costly

Due to advances in computational performance, development of convergence algorithms, and mesh management methods, the use of FE models has been increasing since 1990 (Arrazola et al. 2013). Furthermore, as illustrated in Table 1.1, the possibility of connecting to industrial aspects (surface integrity or tool life) and of obtaining fundamental process parameters, makes FE models an ideal tool for the assessment of the problematic proposed in the research.

- Analysis of the inputs of FE models

The input parameters in numerical modeling are of considerable influence when it comes to obtaining representative results (Childs 2010; Sartkulvanich et al. 2005; Melkote et al. 2017). Figure 1.3 shows the fundamental input parameters in relation to the possible results that can be obtained by FE modeling.

Arrazola et al. (2004) carried out a sensitivity study of the input data for FE models, analyzing the material properties (flow stress and thermal properties) and contact behavior. The study concluded that both material and friction modeling play an important role in the predicted results, which can generate up to 120% of variations in cutting forces, 70% in tool temperature and 70% in the contact pressure. In later research, Özel (2006) performed a study with different friction models, and concluded that state variable friction models were more accurate for fundamental variable prediction. Arrazola and Ozel (2008) carried out a second study on the effect of friction,

concluding that not only the selected friction model, but also the parameters of the model itself (e.g. limiting shear stress in the case of a sticking-sliding model) are of great influence in results like tool temperature and contact pressures.

These studies identified flow stress and the contact models as key aspects, and added to them tool and workpiece thermal properties, towards the development of a FE model as close as possible to reality. The correct modeling and characterization of these issues is of such importance that, recently, Melkote et al. (2017) published a keynote dealing only with input parameters.

The material behavior law aims to emulate the physics that occur in the machining process. The phenomena to be considered are strain and strain rate hardening, and the softening of the material due to temperature increase. The selection of these parameters is a result of the high strains, strain rates and temperatures occurring in the process itself. However, as shown in Figure 1.4, these in-process thermomechanical conditions are usually far from the limits of actual characterization methods. Therefore, the fitting of the behavior models at those extreme thermo-mechanical solicitations is still a real issue.

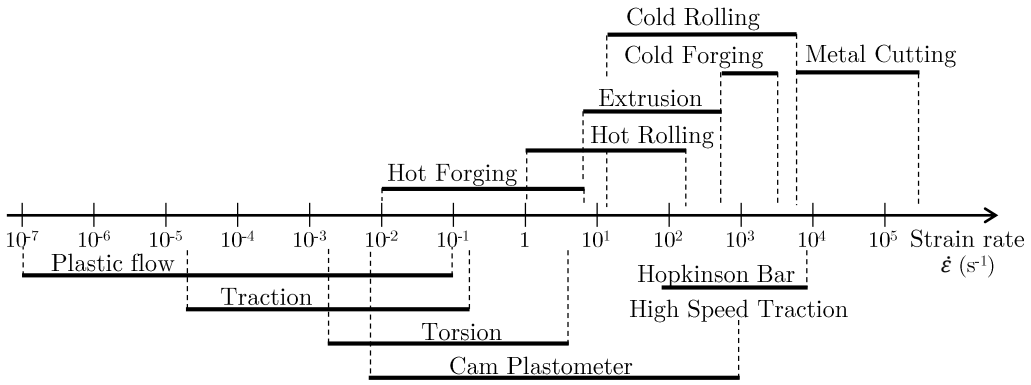

Figure 1.4: Strain rate range reached in metalworking and the limitations of standard mechanical tests, adapted from Wagner et al. (2010)

To date, phenomenological models (models fitted to experimental tests) are those most employed, but currently there is a challenge to include physical aspects to improve the accuracy of predictions. In this context, modified physical-phenomenological models including microstructure evolution such as recrystallizations or phase changes (Kim et al. 2003; Umbrello et al. 2004), or even the development of physical models based on crystal plasticity and dislocation theory are examples of the current state of material modeling (Allain et al. 2009).

Friction models attempt to capture the contact behavior between tool and workpiece. A correct modeling of friction is critical as the contact conditions between tool and chip depend on this factor (Özel 2006). From the experimental point of view, tribological tests are not able to reproduce the real contact conditions at high contact pressures, temperatures and sliding speeds occurring in the tool-chip interface during machining.

For this reason the characterization of friction has been mostly identified mechanistically based on cutting tests (Arrazola 2003; Childs 2000). However, it is possible to find studies that have developed advanced techniques to characterize the contact behavior as close as possible to machining conditions, and those seem to be accurate when applied to the FE codes (Zemzemi et al. 2008).

To accurately model the machining process, thermal properties of work and tool material, including the thermal transfer between the contacting parts, is also critical (Melkote et al. 2017). Temperature-dependent properties include the specific heat or heat capacity, thermal expansion, and thermal conductivity (Arrazola et al. 2013). In addition, the heat partition coefficient must be known to better represent the temperature amplitudes and distributions (Courbon et al. 2013).

- Analysis of the outputs obtained with FE models

As shown in the graph of Figure 1.3, prediction of industry-relevant parameters requires the prediction of fundamental process variables as a prerequisite (Arrazola et al. 2013). For this reason it is necessary to validate first the models with measurable variables such as cutting forces, power or torque, or even empirically measured 2D variables such as strain, strain rate or temperature. For instance, FE models can also provide useful data of non-measurable variables such as stresses on the workpiece or in the cutting tool.

Cutting forces is the most common employed parameter to validate a developed model since it is able to be measured empirically. Temperature prediction is also of critical importance, as it governs thermally activated wear mechanisms (Usui et al. 1984; Takeyama and Murata 1963). Since the measurement of temperatures in machining operations is difficult, the prediction and validation of temperature fields and heat partition still presents a major challenge. Several studies have used FE simulations to predict temperatures for various cutting conditions, tool material, coating and edge geometry (Outeiro et al. 2008; Özel et al. 2010). They concluded that attention should be paid to material data suitable for the heating rate encountered in machining; to ensure that equilibrium thermal state is reached in the simulations; and to account for preheating of the workpiece due to previous cutting.

Stresses, strains and strain-rates are variables that are difficult or not possible to measure. Predicted stresses are highly sensitive to thermo-mechanical loading and tool-workpiece contact conditions, and therefore accurate predictions require precise material behavior and contact models. Predicted strain fields and distribution of strain-rates in the shear zones can be obtained using FE simulations, but validation remains a major challenge (Calistes et al. 2009).

Machining performance outcomes (*Stage 2*) are the next prediction step from the fundamental variables (*Stage 1*). Successful models have as their objective the reduction of expensive experimental testing in the process development. In the context of this project, tool-life modeling is the example of performance modeling able to give the

final user (steelmakers, tool manufacturers) information about the way to develop optimum material microstructures or optimize the cutting conditions, tool geometry, etc. Other performance aspects commonly studied are surface integrity, chip morphology or process stability.

Machinability is usually measured in terms tool-wear or tool-life. The first predictive models were based on empirical tests or analytical expressions (Taylor 1907; Hastings et al. 1980). These models evolved into the well-known wear rate models that are widely employed in FE codes (Usui et al. 1984; Takeyama and Murata 1963). In terms of empirically or numerically obtained variables (temperature, contact stresses, sliding velocities) the generated wear is calculated. According to Xie et al. (2005) and Lorentzon and Järvstråt (2008), the challenging aspects for precise wear/machinability prediction are (i) identification of tool-material wear contact parameters, (ii) friction model identification and (iii) work material model characterization. Once they are overcome, the existing enhanced hardware and software capabilities allows the user to model 2D/3D FE-based models. Given predictions are those of wear patterns or crater and flank wear specific values, tested over a wide range of tool inserts, coatings and workpiece materials (Attanasio et al. 2017; Binder et al. 2015).

1.1.1 Summary of scientific framework

The microstructure of the material and alloying elements during processing play an important role in the machinability of ferrite-pearlite steels. Although the influence of alloying elements is known, and the global effect of the microstructure seems to be clear, microstructural aspects still have some uncertainties. In addition, increasing the empirical knowhow of machinability in relation to the microstructure of the material, and developing a model able to reflect the influence of the microstructure still seems to be a challenge today.

In order to define the global tasks to successfully develop a predictive model, it is necessary to point out some technical remarks from the scientific framework previously presented. Developing a predictive model has to overcome three main steps: (i) input parameter identification and characterization, (ii) model selection and development and (iii) output validation. In this context, some main critical conclusions are extracted:

- Material constitutive or flow stress model and tool-workpiece contact behavior are the input parameters that most influence fundamental variables, and subsequently the industrial relevant results. In both cases, the characterization methodology and the selection of an appropriate model seems to be of great importance. In a second instance, thermal properties of tool and workpiece materials, and the thermal transfer between parts are also significant.
- Numerical FE-type models involve flexibility, reduction of experimental tests and a direct relationship of results to aspects of industrial relevance. This fact gives

an advantage over analytical and empirical models.

- Fundamental variable prediction is the way to obtain reliable industrial results. It is mandatory to first validate the model on aspects related to cutting forces, temperature and other fundamental measurable variables, to later predict machinability or tool life related indexes. The prediction of tool life or tool wear is based on wear behavior laws, that also must be characterized.

1.2 Objectives

The main goal of this Ph.D. work is **the development of a procedure based on finite element modeling to predict machinability and tool wear evolution considering the effect of the microstructure, and additionally contribute to the understanding of the machinability of lamellar ferrite-pearlite steels**. The new knowledge acquired in this work can contribute to the development of steel grades where machinability can be improved by means of a modified microstructure, and to reduce the time-consuming empirical trials due to machinability prediction. The accomplishment of the objective will be of interest to steelmakers, machining workshops, tool manufacturers, etc. The operational objectives that give response to the main goal are listed below:

- To define and characterize the inputs required to develop the numerical model.
  - To characterize the studied steels including chemical composition, microstructure, thermal properties and mechanical behavior.
  - To characterize the contact behavior between tool and workpiece.
- To understand and rate the influence that materials microstructure and cutting conditions have on machinability, and extract necessary output data to validate the models.
  - To analyze the influence that the ferrite-pearlite microstructure has on tool wear.
  - To analyze the influence that ferrite-pearlite microstructure and tool wear have on fundamental variables such as cutting and feed forces, tool temperature, chip morphology and tool-chip contact.
- To determine and develop a numerical modeling procedure to predict machinability and tool wear.
  - To implement and validate the characterized inputs in an appropriate FE-based approach for machining modeling.
  - To characterize and implement a wear rate law in the FE code to predict tool wear evolution.

1.3 Structure of the document

This work consists of three main chapters, apart from the introduction, the conclusions and minor chapters. In addition to the description of the developed work, a technical literature review is detailed in each main chapter. A flowchart of the sections of the document is presented in Figure 1.5.

Chapter 2 concerns the material characterization applied to machining processes. The selected FP steels to be machined in the Ph.D. work are characterized in terms of chemical composition, microstructure, thermal properties and mechanical behavior. These aforementioned properties were selected to meet the needs of the inputs for the FE model, and to give response to the microstructure related machinability analysis. Based on the rheology characterization, a new constitutive model which represents the behavior of FP steels is developed.

In Chapter 3 the orthogonal cutting tests are described. First, the developed specific set-up is presented, in which both the fundamental variables and tool wear are measured synchronized in orthogonal cutting conditions. Moreover, the additionally developed set-up for calibration of the infrared camera to measure tool temperatures is presented. The achieved results are analyzed in-depth: first the wear evolution is described, and secondly the fundamental variables and the evolution that these have with tool wear are set out. Finally, based on the combined results of fundamental variables and tool wear, a wear rate model that describes the wear evolution of the FP steels is proposed.

The development of the predictive numerical model is presented in Chapter 4. A novel procedure is set out to predict the machinability and tool wear evolution based on an Arbitrary Lagrangian Eulerian (ALE) 2D cutting model. The main characteristics and input parameters of the FE model are first described. In a further section, the strategy and implementation of the wear model, based on the empirical test of Chapter 2, is outlined. Moreover, the performance of the model is compared with the experimental machinability tests.

Finally, the main conclusions from this work, publications and future outlook are explained in Chapter 5, 6 and 7, respectively.

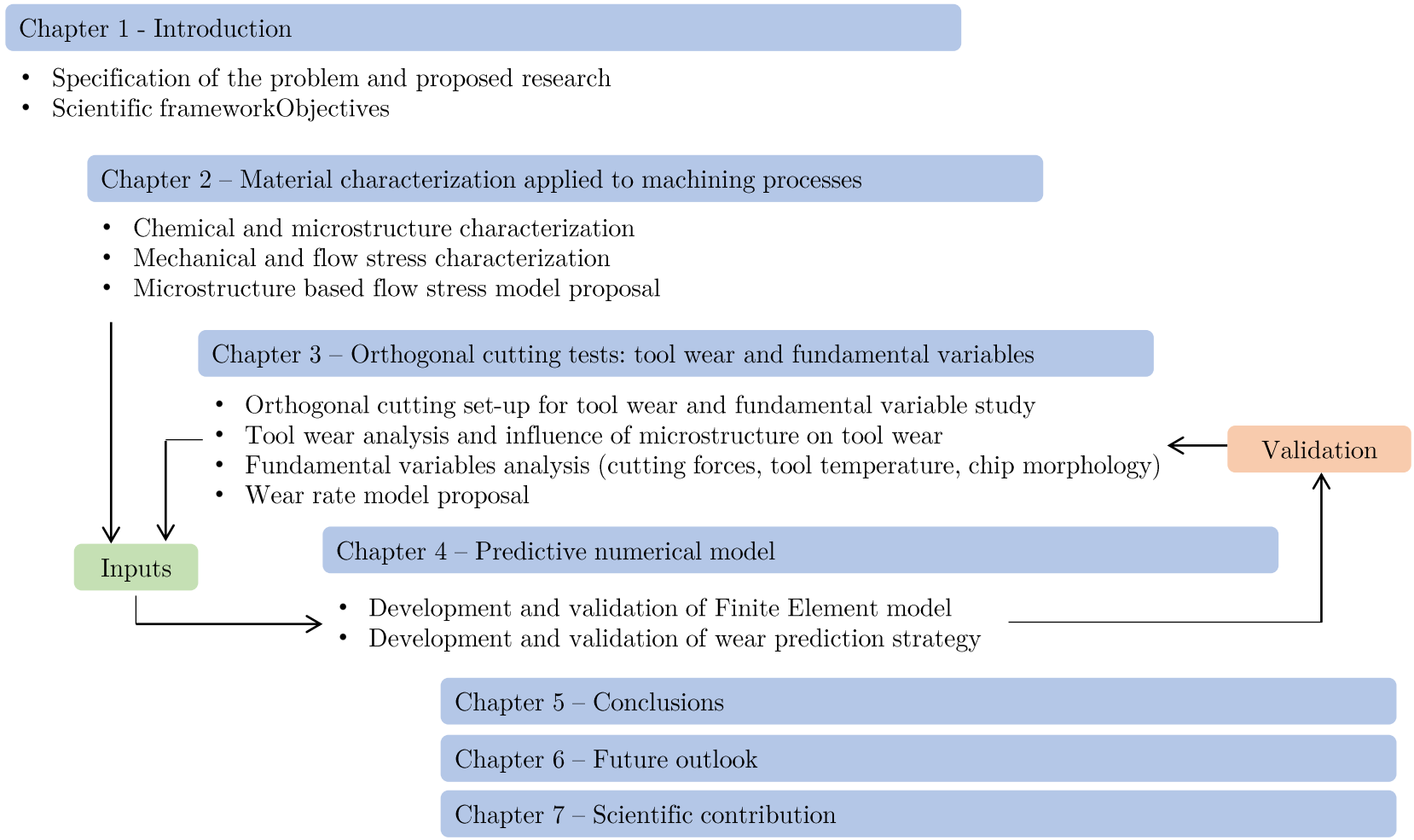

Figure 1.5: Structure of the thesis document

1.4 Original contributions

This research work has produced the following original contributions.

- An extended characterization of four ferrite-pearlite grades utilized in automotive and railway industry has been undertaken. This includes the chemical, microstructural, thermal and mechanical characterization. In this latter, the yield stress is characterized at room and high temperatures and different strain rates close to those found in machining.
- A physical-phenomenological flow stress model is proposed to describe the behavior of the steels at high strains, strain-rates and temperatures. This material behavior introduces strain softening as well as the coupling between the strain-rate and temperature. Furthermore, the strain hardening is described as a function of the interlamellar spacing, ferritic grain size, and ferrite-pearlite ratio. This enables the modeling of the flow behavior of ferrite-pearlite steels where the internal structure is that of lamellar pearlite.
- An innovative methodology to characterize tool wear and fundamental variables synchronously in orthogonal cutting conditions is developed. This records the evolution of tool temperature and cutting forces have with tool wear. In addition, a new methodology to relate the measured tool radiation with the real temperature without the need of an emissivity characterization is proposed. The main contribution is the characterization of the wear behavior of ferrite-pearlite steels, and the development of an empirical wear rate law that can be integrated in numerical or even analytical models.
- A procedure to predict machinability and tool wear based on an Arbitrary Lagrangian Eulerian 2D cutting model was developed. In a first stage, the model was validated over a wide range of cutting conditions and FP steels. Secondly, the previously characterized wear rate law was implemented in the FE code, and tool wear predictions were qualitatively validated through comparison with empirical orthogonal cutting tests.

Chapter 2

Material characterization applied to machining

As explained in the introduction, the material characterization is almost a requirement to obtain reliable input data for the development of a numerical model, and also to enable a more in-depth understanding of experimental results. Considering this, and extended work related to the characterization of ferrite-pearlite steels was carried out in the course of this thesis, and is presented in this chapter.

The chapter is divided into two main sections. First a literature review is carried out regarding the fundamental chemical, microstructural and mechanical properties of common ferrite-pearlite steels. Secondly, the developed work and main conclusions are described.

In the second section, the workpiece materials machined in the course of this research work are introduced and characterized in terms of chemical, microstructural, thermal and mechanical properties. Mechanical characterizations include a complete rheological study over a wide range of temperatures and strain rates. As described in the diagram (Figure 2.1), chemical, microstructure and mechanical data of materials is used to develop a flow stress behavior law. This, together with the thermal properties of workpiece and tool materials, are employed as input data in the numerical code.

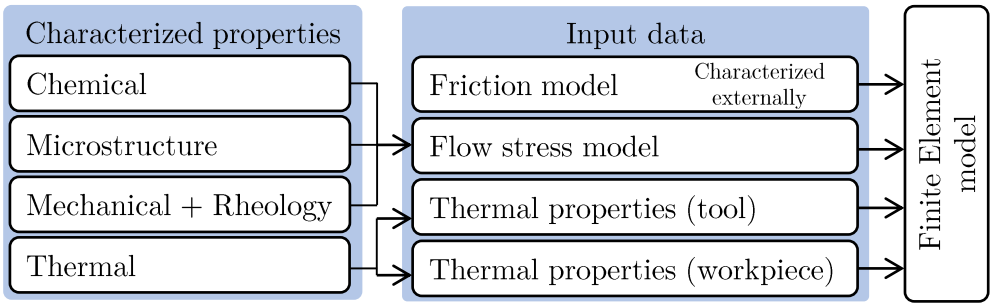

Figure 2.1: Diagram of characterized material properties

2.1 Literature review: Material characterization

This analysis of the literature review is focused on low-medium carbon steels, where the microstructure is that of ferrite-pearlite type. These materials are widely used in the automotive industry, to develop components such as crankshafts and steering racks. Therefore, machining is a common processing operation in their manufacturing route.

Firstly, the main chemical, microstructural and mechanical characteristics of ferrite-pearlite steels are analyzed. Furthermore, the effect that microstructure has on the thermo-mechanical properties is also studied. For numerical modeling purposes, a complete rheological characterization is mandatory to enable the development of a flow stress model that describes the behavior of FP steels. Therefore, the methods to determine the mechanical stress-strain behavior of steels are explained, including the adiabatic heating estimation and correction methodologies. Finally, the main constitutive equations to model the flow stress are presented and discussed.

2.1.1 Metallurgy and mechanical properties of ferrite-pearlite steels

Chemical composition and microstructure

Steel is an iron based alloy with a varying weight of 0.03-1.075% of carbon content, depending on the selected grade. Cooling at hypo-eutectic temperature generates steels of ferrite-pearlite microstructural state. These steels are considered as multiphase materials. They consist of pearlite islands (hard phase) embedded in a ferrite matrix (soft phase). Table 2.1 summarizes the main compositions found in these types of steels.

Table 2.1: Typical chemical compositions found in ferrite-pearlite steels (Handbook 1990)

C (carbon)	Fe (iron)	Mn (manganese)	P (phosphorus)	S (sulphur)	Ni (nickel)	Mo (molybdenum)	Si (silicon)
0.03-1.075	98-99	0.45-0.75	0.01-0.02	0.01-0.025	0-3.5	0-0.25	0-0.25

Ferrite, or so-called α-Fe phase, is a solid solution of carbon (C) with a low carbon content (0.02% by weight). It is one of the stable forms of iron in solid state. It forms a Body-Centered Cubic structure (BCC) (Handbook 1990).

Pearlite is obtained from austenite following a solid state reaction during the cooling process. This reaction is called eutectoid, in which the austenitic phase is transformed into a bi-phasic structure. The pearlite consists of ferrite (α-Fe) and cementite (Fe_3C). If steel or iron cools very slowly, cementite may occur in globules instead of in layers, forming globulized pearlite. In lamellar pearlite, cementite lamellaes are distributed in colonies in a constant orientation. Cementite has an orthorhombic crystal structure (Handbook 1990). Figure 2.2-a shows an example of microscopy of a FP steel, in which

black pearlite grains are distinguished from whiter ferrite grains (Mian et al. 2010). In Figure 2.2-b a lamellar pearlite grain is presented in detail, where the cementite lamellae are distinguished in the ferritic matrix (González et al. 2009). In Figure 2.2-c a globulized pearlite grain is depicted (Dlouhy et al. 2016).

The isothermal transformation diagram of a steel is shown in Figure 2.3. It can be seen that a rapid cooling to temperatures below 727°C and a subsequent incubation, or temperature maintenance, generates the transformation of pearlite. Depending on the cooling temperature, the pearlite may be fine or coarse, in other words, with greater or lesser interlamellar spacing (Krauss 2015). Annealing just below the transformation temperature (about 700°C) spheroidizes the cementite, which is the form in which it has least strengthening effect (globulized pearlite).

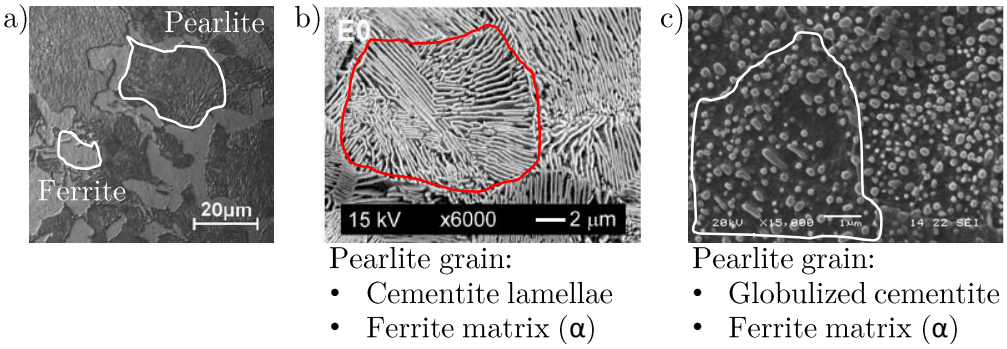

Figure 2.2: a) SEM images of AISI 1045 (Mian et al. 2010), b) lamellar pearlite (González et al. 2009) and c) globulized pearlite (Dlouhy et al. 2016)

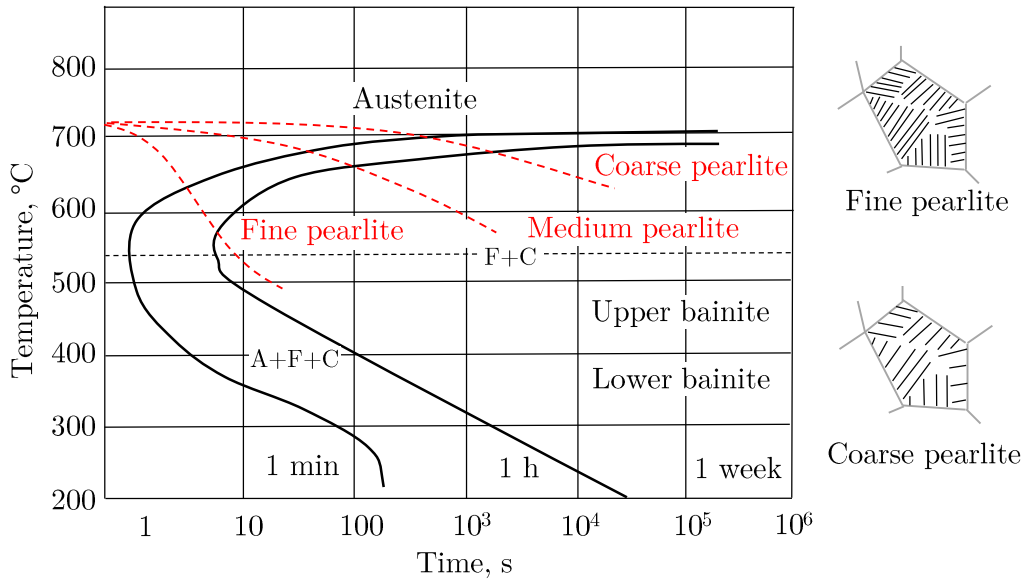

Figure 2.3: Transformation diagram of steels, adapted from Krauss (2015)

Mechanical properties

Mechanical properties of steels are mainly dependent on their microstructural characteristics. The microstructure of carbon steels consists of ferrite and pearlite, where the volume fractions depend primarily on the carbon content. Yield stress, ultimate tensile strength and flow stress of steel are taken as the most common macroscopic mechanical properties. As described by Abouridouane et al. (2012) in Figure 2.4, different volume fractions of ferrite-pearlite lead to variations of yield material behavior.

Concerning the tensile-compression properties, FP steels show a wide variation of yield stress (175-750 MPa from pure ferritic to pure pearlitic steels) and ultimate tensile strength values (600-1300 MPa). The strain hardening, in contrast, does not reflect marked variations regarding the macroscopic microstructural state.

One of the characteristics of FP steels is that their strength decreases when temperature is increased. Thermal activation makes it easier for dislocations to surmount obstacles, and therefore generate a softening in the macroscopic behavior. An example of thermal softening can be observed in Figure 2.5 for a typical ferritic-pearlitic mild-steel with a 0.2% carbon content (Tisza 2001).

Some essential conclusions can be drawn from this diagram. It can be stated that when temperatures increase, a decrease in strength and an increase in ductility occurs. However, a somewhat deviant behavior from this general trend can be observed at the temperatures between 50 and 250°C. In this range, a local minimum of strength and at the same time a local maximum of ductility occur at around 50°C. Above this

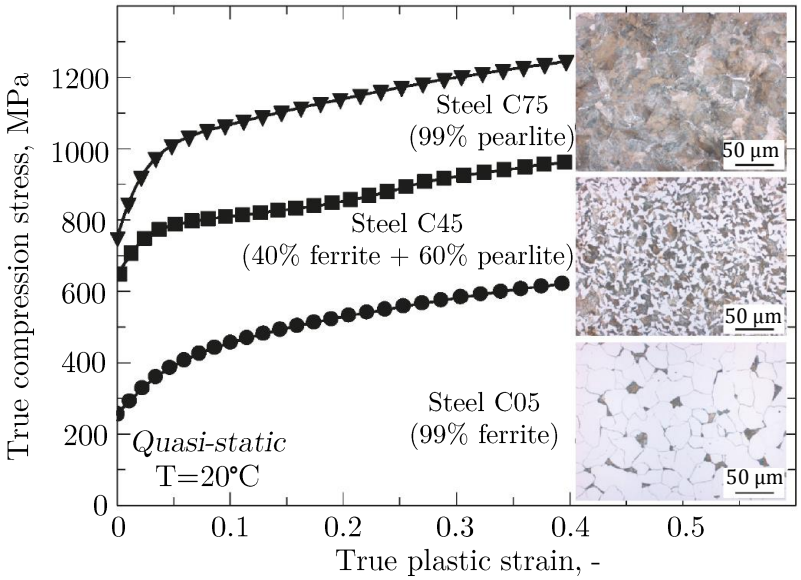

Figure 2.4: Flow stress and microstructures of ferrite-pearlite carbon steels (Abouridouane et al. 2012)

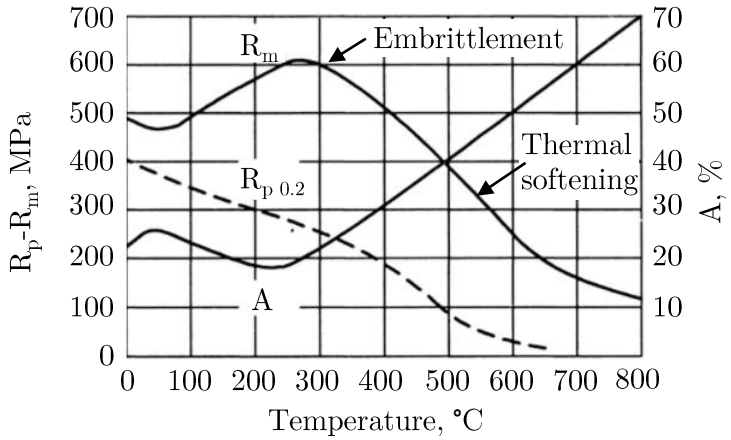

Figure 2.5: Effect of temperature on the mechanical properties of a 0.2% mild steel at quasi-static strain rate (Tisza 2001)

temperature, the strength increases and the ductility lowers. There is another local extreme in the temperature range $200 - 250^{o}$C, which represents a local maximum of strength and a local minimum of ductility. These changes can be considered as a kind of embrittlement, and is due to the interstitial elements of small atomic diameter (usually carbon atoms). These dissolved atoms are located in dislocation-free interstices of the lattice. The occupation of the expanded zones of dislocations by these atoms obstructs free movement. Therefore, an extra amount of energy is required to move dislocations, which is experienced as an increase in strength (Tisza 2001).

Knowledge of the dynamic behavior of steels is critical for machining operations, due to the high strain rates the material is subjected to. This is comprehensively described in the works of Maekawa et al. (1983) and Warnecke and Oh (2002), where the strain rate hardening behavior was assessed for a certain number of steels. As shown in Figure 2.6-a, tests developed at higher strain rate present a increase on the flow stress. The blue brittleness effect was also a characteristic behavior at temperatures of 550-650^{o}C. As the strain rate is rise, the peak on the curve occurs at higher temperatures.

From the microscopic point of view, the effect of pearlitic interlamellar spacing has been widely analyzed in the literature (Dollar et al. 1988; Modi et al. 2001; Q'Donnelly et al. 1984; Ray and Mondal 1991). Investigators agree that yield strength and hardness are function of the inverse of the square root of the interlamellar spacing (Figure 2.6-b). Karlsson and Linden (1975) observed that the hardness ratio in the undeformed state between pearlite and ferrite $K = HV_{pearlite}/HV_{ferrite}$ could be in the ranges of K=1.9-2.4 depending on the interlamellar spacing.

With regards to the grain size, small grains increase the yield strength and toughness of the material. In contrast, a larger grain size offers greater ductility and ductile-brittle transition (Handbook 1990; Q'Donnelly et al. 1984).

In particular, the creep behavior in the case of ferrite-pearlite steels is mostly deter-

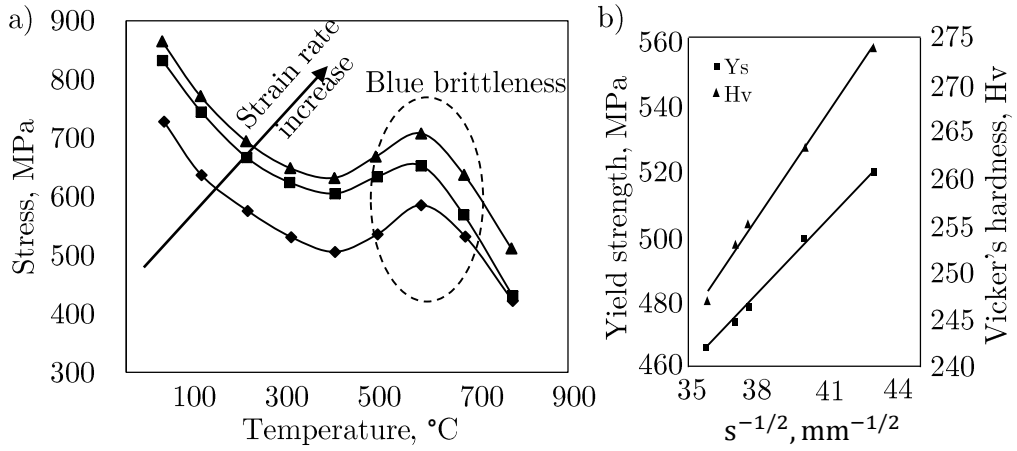

Figure 2.6: a) Relation of stress and temperature at constant strain and strain rates of 200-1200-2000 s^{-1} for a 0.18% C steel, adapted from Maekawa et al. (1983). b) Hardness and yield strength as a function of the inverse of the square root of the interlamellar spacing (Modi et al. 2001)

mined by the interlamellar distance of the pearlite, and becomes more significant as the volumetric fraction of the pearlite increases. With the combination of both phases it is possible to obtain high values of ultimate stress and higher rates of strain hardening than other materials with the same flow strength (Coromant 1994).

2.1.2 Mechanical characterization

In the following section, the methodologies to determine the mechanical behavior of steels are described. These are mainly determined by the characterization of the stress-strain curves, and in the case of machining, close to the manufacturing solicitations. In addition, an analysis of the material behavior models that represent the thermo-mechanical loads which occur during machining is carried out.

Mechanical characterization tests

The main difficulty in characterizing materials under near machining conditions are the high strains, strain rates and temperatures that have to be taken into account. Therefore, the tests undertaken in the literature are markedly different compared to conventional material testing. The most frequently employed tests are summarized in Figure 2.7.

Quasi-static tests are employed to determine the plastic behavior of materials at low strain rates ($\dot{\varepsilon} < 1\,s^{-1}$). These are usually carried out in conventional tensile-compression machines.

The **uniaxial tensile tests** are the main reference tests for steelmakers to provide the mechanical specifications such as strength, ductility, toughness, elastic modulus

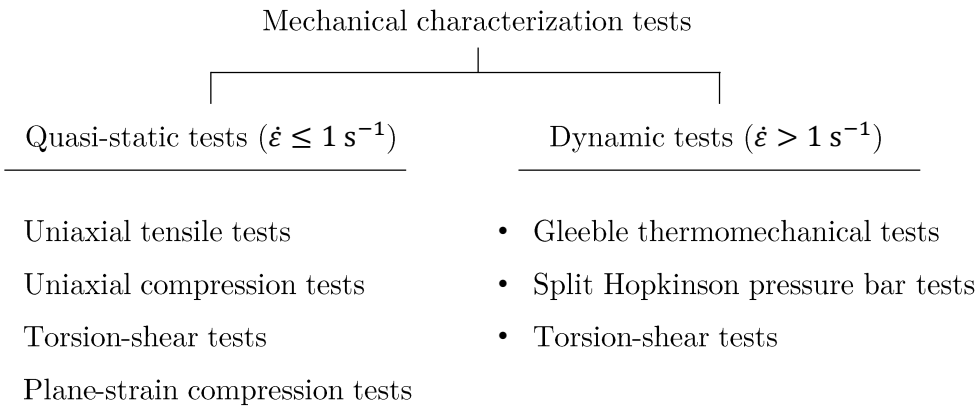

Figure 2.7: The most common mechanical tests for characterization of steels

and strain hardening ratio to the final user. These tests can be performed at room (ASTM E8 / E8M-16a 2016) and high temperature (ASTM E21-09 2009). However, the necking effect occurs in samples, limiting the uniform elongation during tension. Therefore, tensile tests are not appropriate to study the plastic stress-strain relationship at the high strain levels achieved during the manufacturing process (Hosford 2010).

In despite of obtaining higher strain levels, **uniaxial compression tests** are a widely used methodology for characterization. These can also be performed at room (ASTM E9-09 2009) and high temperature (ASTM E209-00 2010). One of the main features of these tests is the sample preparation, usually cylindrical specimens, and the simplicity of the set-up, as they are usually carried out in conventional tensile testing machines. Nevertheless, the process itself presents some difficulties. Tested specimens may undergo barreling or buckling effects, which results in non valid tests. As described in the ASTM E9-09 (2009), buckling is generally reduced by decreasing the height-to-diameter ratio, h_0/d_0. According to the standard, this ratio should not exceed a value of $h_0/d_0 < 1.5$. The barreling effect is mostly generated by the friction between the machine plates and the testing sample. The effect increases together with the diameter of the specimen during the test. To avoid or reduce barreling, the contact surfaces can be lubricated by the use of solid or teflon-based lubricants (Seo et al. 2005), graphite and tantalum foils (Rao and Hawbolt 1992), or by intermittent loading-unloading tests where the surfaces are continuously lubricated (Hosford 2010). Rastegaev-type specimens are another option to reduce friction and barreling effects (Jaspers and Dautzenberg 2002). In this specific case, concentric grooves of 0.1 mm depth are shaped on the top and bottom surfaces in order to trap the lubricant during the tests, as shown in Figure 2.8-a.

During machining, the workpiece is subjected to quasi-pure shear solicitations, combined with a compression state depending on the analyzed deformation region (Trent and Wright 2000). **Shear tests** to determine this behavior are mostly based on torsion tests. The advantage of torsion tests is that very high strains can be reached (up

to strains of 5), even at elevated temperatures. During the test, the specimen shape remains almost constant, and presents negligible necking or barreling instabilities (Hosford 2010). However, although the shear effect occurs throughout the process, torsion tests are less frequently utilized than uniaxial tensile/compression tests, mainly due to the result interpretation complexity and the strain-strain rate variation along the specimen radius (Semiatin and Jonas 2003).

It is possible to characterize the shear behavior by the use of specially designed specimens, in which a compression of this geometry results in a calibrated shear zone. The most common specimens are *Hat* shape samples, such as the work developed by Hor et al. (2013) where different steel microstructures were tested over a wide range of thermal (20-1000°C) and strain rate conditions. Some works have used *Shear Compression Specimens* (SCS). For example Dorogoy and Rittel (2009) have determined the material constitutive parameters using these specimen types. Other models of specimens presented in the literature are *disc* shapes or variations of SCS samples denominated *Compact Force Simple-shear Sample* (CFSS), where the aim is to produce simple-shear behavior along a calibrated section (Gray et al. 2016). Examples of shear specimens are shown on Figure 2.8.

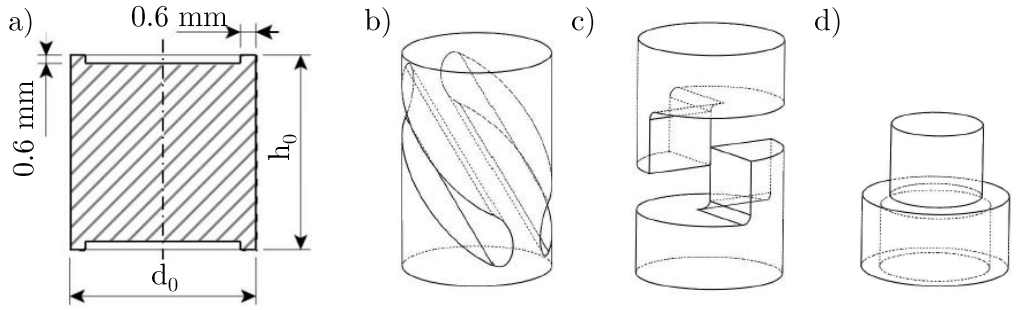

Figure 2.8: a) Rastegaev-type specimen (Jaspers and Dautzenberg 2002). Specially designed shear specimens b) SCS (Dorogoy and Rittel 2009), c) SFSS (Gray et al. 2016), d) Hat-shape (Hor et al. 2013)

Plane-strain compression tests are specially designed to keep the contact area between the samples and the plates constant during deformation. This is achieved by using thin specimens much wider than the breadth of the employed indenter. The elastic constrains of the undeformed shoulders of the material on each side of the indenter prevent the extension of the sample in the width direction, therefore assuming a plane-strain condition (Semiatin and Jonas 2003). These tests allow the performance of compression tests up to higher strain values compared to uniaxial compression tests with cylindrical samples.

Dynamic tests are employed to test the plastic behavior of materials at high strain rates ($\dot{\varepsilon} > 1\,s^{-1}$). The Split-Hopkinson Pressure Bar (SHPB) and Gleeble machines have been widely utilized in the literature to mechanically characterize metal at high strain rates. The above mentioned tensile, compression and shear tests can be executed

under dynamic conditions with these machines.

The **Gleeble** system is a high strain-rate, high temperature testing machine. The system is capable of applying forces of around 100 kN and displacement rates up to 2000 mm·s^{-1}. These machines usually have two configurations, tension and compression, which leads to different jaw shapes. An example diagram of the configuration is shown in Figure 2.9. During the tests, the specimens are held between two tungsten carbide anvils. The desired temperature is generated by Joule effect, and is monitored by thermocouples welded to the specimen. An extensometer, fixed on the jaws, allows measuring the displacement of the mobile jaws and a load cell measures the forces.

When it is necessary to perform tests at higher strain rates than in the Gleeble machine, the **Split Hopkinson pressure bar** is most commonly used. A cylindrical specimen is compressed axially between two instrumented coaxial bars (Hopkinson 1914). Strain gauges mounted on the incident and transmitter bars enable the stress waves to be measured (Wu and Gorham 1997). A striker bar of the same diameter is propelled using a gas gun so that it strikes the incident bar (Figure 2.10). This generates a

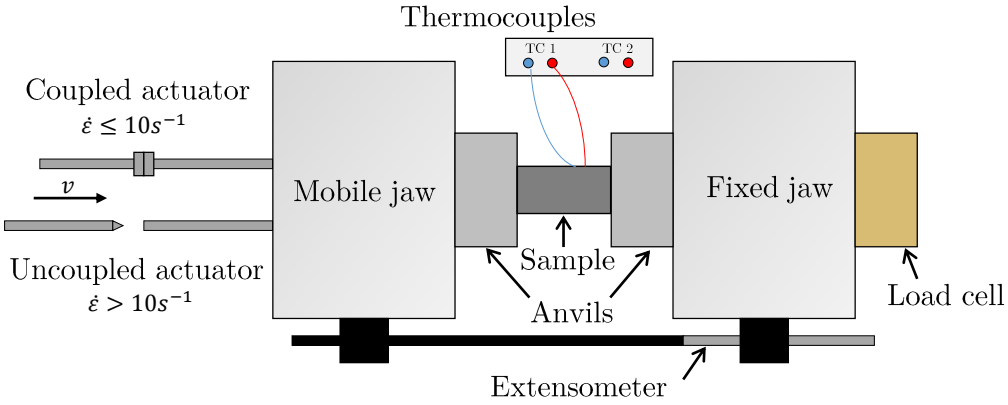

Figure 2.9: Representation of Gleeble testing set-up (Sacristan 2016)

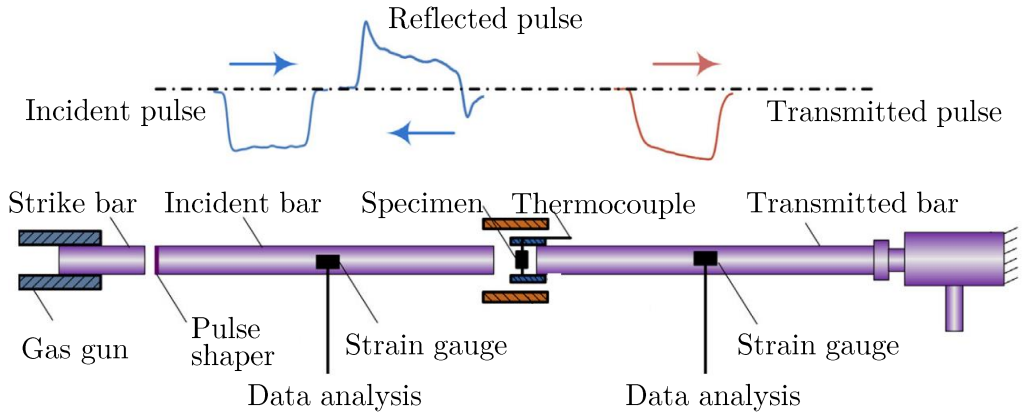

Figure 2.10: Schematic representation of SHPB testing set-up (Chen et al. 2015)

compression wave that travels down from the incident to the transmitter bar. By measuring the stress pulses in real time, the stresses acting on the samples can be calculated (Chen et al. 2015). The bars and the projectile (or striker bar) are typically made of high-strength steels, with a very high yield strength and substantial toughness, in order to remain in the elastic domain during the test. Strain rates up to $10^4 \mathrm{s}^{-1}$ can be achieved in SHPB tests.

Adiabatic heating: effects and correction methodology

When materials are subjected to large plastic deformations, a fraction of work done for plastic flow is almost instantaneously converted into heat, which significantly increases the temperature of the specimen. Experimental studies have estimated the heat energy fraction to be somewhere between 90-95%, depending on the tested material (Soltani 2013). The magnitude of the adiabatic temperature rise can be calculated using Equation 2.1.

$$\Delta T_{\mathrm{ADB}} = \frac{\beta}{\rho \cdot C_{\mathrm{p}}} \cdot \int_0^{\varepsilon} \sigma \mathrm{d}\varepsilon \tag{2.1}$$

where ρ is the density, C_{p} the heat capacity and β the Taylor Quinney coefficient. The latter specifies the fraction of the total energy converted into heat (typical literature values range from 0.9 to 0.95 (Goetz and Semiatin 2001)).

The adiabatic correction factor for the strain rate sensitivity, η, is used when the strain rates are between $10^{-3}\,\mathrm{s}^{-1}$ and $10^{1}\,\mathrm{s}^{-1}$ (Charpentier et al. 1986; Oh et al. 1992). This is defined as:

$$\eta = \frac{\Delta T_{\text{STRAIN RATE CORRECTED}}}{\Delta T_{\text{ADIABATIC}}} \tag{2.2}$$

At strain rates between 10^{-3} and $10^{1}\,\mathrm{s}^{-1}$, η is taken to vary linearly with $\log(\dot{\varepsilon})$, *i.e.*, η is equal to 0.0, 0.25, 0.50, 0.75 and 1.0 for rates of 10^{-3}, 10^{-2}, 10^{-1}, 10^{0} and $10^{1}\ \mathrm{s}^{-1}$, respectively. In general, η is taken to be independent of strain and temperature.

Goetz and Semiatin (2001) derived an analytical expression for η based on a 1-D lumped parameter approach:

$$\begin{aligned} \eta &= 1/[1 + (h\Delta\varepsilon)/(\chi_{\mathrm{w}}\rho C_{\mathrm{p}}\dot{\varepsilon})] \\ h &= 1/[\chi_w/K_w + 1/\mathrm{HTC} + \chi_{\mathrm{D}}/K_{\mathrm{D}}] \end{aligned} \tag{2.3}$$

where χ_w is one-half of the workpiece length, ρ is the density, C_{p} is the specific heat, HTC is the interface heat-transfer coefficient, ε is the strain, $\dot{\varepsilon}$ is the strain rate, χ_{D} is

the distance from the die surface to the interior, and K_{w} and K_{D} are workpiece and die thermal conductivities, respectively.

Once the increase in temperature is calculated, it is possible to convert the measured flow stress into isothermal theoretical values with the first order Taylor Series Expansion of Eq. 2.4 (Xiong et al. 2015). This approach is shown schematically in the graph in Figure 2.11.

$$\sigma(T)\Big|_{\varepsilon,\dot{\varepsilon}} = \sigma(T_{\mathrm{real}}) + \Delta T \cdot \sigma'(T_{\mathrm{real}}) \tag{2.4}$$

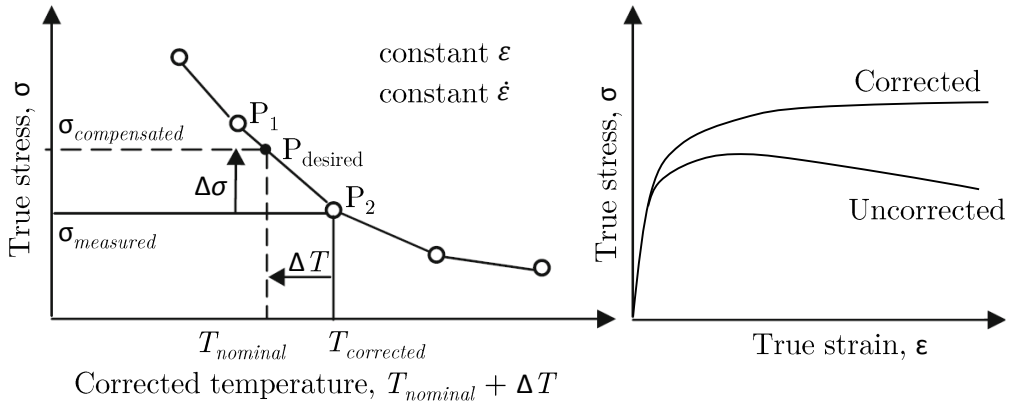

Figure 2.11: Approach to derive isothermal stress (Xiong et al. 2015) and example of adiabatically corrected curve, adapted from Zhao (2000)

2.1.3 Flow stress behavior modeling

The material behavior law aims to reproduce the physics that occur in the machining process. The phenomena that must be considered in machining are strain hardening and strain rate, and the softening of the material due to increase of temperature. The selection of these parameters are a result of the high strains, strain rates and temperatures that occur in the process itself.

The analyzed material or flow stress laws can be grouped into three main categories, as described in Figure 2.12. The first group of material models are named as **phenomenological models**. They reflect the flow behavior on the basis of strain, strain rate and temperature, where the strain hardening and thermal softening are also taken into account. In a second division the **physical-phenomenological models** are grouped, that apart from the abovementioned properties also incorporate material parameters such as hardness, initial grain size and recrystallizations. Finally, the **physical models** that focus on the microstructural properties of the constituents are located in the last group. These models are based on the internal structure of the material phases, dislocation properties, sliding planes, etc.

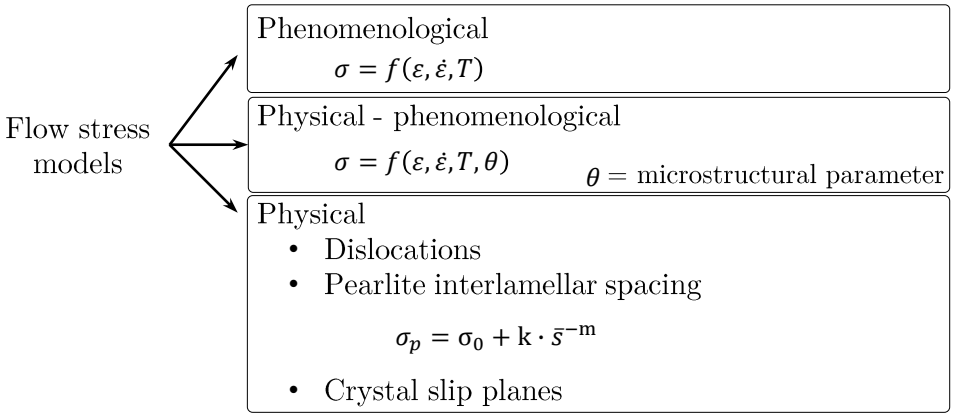

Figure 2.12: Division of flow stress models

Phenomenological models

Oxley (1966) first presented a flow stress behavior model where the strain hardening was dominated by an initial yield stress and an exponential hardening coefficient. The model was temperature dependent, which was determined in turn by the strain rate, and combined into a unique function.

Johnson and Cook (1983) developed the behavior law most used in the chip formation numerical models found in the literature (JC model). Their proposed equation describes the flow stress as a product of strain, strain rate and temperature dependent terms. It considers isotropic hardening, strain rate hardening and thermal softening as three independent phenomena that can be isolated from each other.

A wide range of materials have been described by means of the JC equation. Steel C45 (or AISI 1045) is one of the most modeled materials. Interestingly, several combinations of coefficient values can be found in the literature for this material (Table 2.2), which is a drawback in order to obtain a correctly characterized flow stress model.

Table 2.2: JC flow stress coefficients of C45 - AISI 1045 steel

	A (MPa)	B (MPa)	C (-)	n (-)	m (-)
Ee et al. (2005)	310	815	0.05	0.22	2.624
Abouridouane et al. (2012)	546	487	0.015	0.25	1.22
Jaspers and Dautzenberg (2002)	553	600	0.013	0.23	1
Klocke et al. (2001)	546	487	0.027	0.25	0.631

Over the course of many years, the JC model has received several modifications to improve its accuracy in wider testing conditions. The main limitation is that it describes an increasing strain hardening that diverges to infinity with the strain and, therefore, does not consider any strain stabilization or even strain softening. In this context,

Calamaz et al. (2008) proposed the TANH model, where a softening behavior was modeled under a hypothesis of representing the effects of recrystallization and dynamic recovery. The flow softening is defined as a decreasing behavior in the flow stress with increasing strain beyond a critical strain value. In a further modification of this model, Sima and Özel (2010) introduced an exponent to the hyperbolic function to better control the softening behavior. In Figure 2.13 the resultant flow stresses of JC and TANH models are compared.

Another approximation to consider thermal flow softening was developed by Abouridouane et al. (2016). The difference between this model and the JC equation is that the thermal phenomena is modeled as an exponential function where the ratio between real and melting temperatures are multiplied by a sensitivity parameter β.

In a further study based on the JC model, Iturbe et al. (2017) developed their own empirical model to describe the particular behavior of high strength steels such as nickel based super-alloys. In particular, a coupled empirical model that introduces strain softening as well as the coupling between the temperature and strain rate was developed. The strain hardening-softening term σ_ε was taken from the work of Lurdos et al. (2008), where strain hardening was considered up to an specific strain value, followed by strain softening. The maximum stress was set by the stress saturation parameter σ_s. The strain hardening was controlled by the common A and n parameters, and the strain softening was set by an exponential term where the strain was multiplied by a sensitivity parameter r. To consider the thermal softening as nonlinear, σ_T was proposed as an exponential term where m and B temperature sensitivity parameters were taken from quasi-static tests. The strain rate hardening was considered to be coupled with the temperature. For that reason, the strain rate coefficient was set as $C(T) = C{\cdot}D^T$. Strain rate sensitivity parameters C and D had to be identified from all the temperature-strain rate testing configurations.

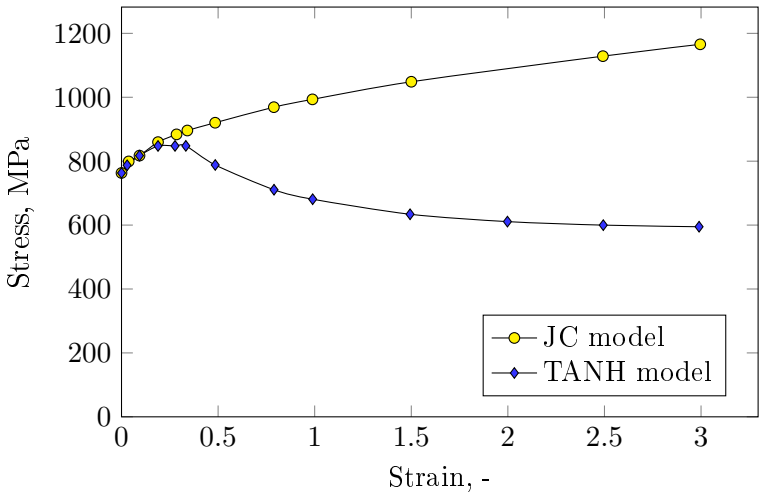

Figure 2.13: Comparison between JC and TANH models (Calamaz et al. 2008)

Table 2.3: Phenomenological models found in the literature

Flow stress equation		Features
Johnson and Cook (1983) $\sigma_{\mathrm{JC}} = (A + B \cdot \varepsilon^n) \cdot \left[1 + C \cdot \ln\left(\frac{\dot{\varepsilon}}{\dot{\varepsilon}_0}\right)\right] \cdot \left[1 - \left(\frac{T - T_\mathrm{r}}{T_\mathrm{m} - T_\mathrm{r}}\right)\right]$	A: yield strength (MPa) B: strain hardening (MPa) C: strain rate sensitivity coefficient n: strain hardening coefficient m: temperature sensitivity coefficient	• Considers the uncoupled effects of strain, strain rate and temperature • Easy to incorporate in FE codes • Does not predict strain softening • Not accurate for $\dot{\varepsilon} > 10^3$
Calamaz et al. (2008) $\sigma = \sigma_{\mathrm{JC}} \cdot \left[D + (1 - D)\tanh\left(\frac{1}{\varepsilon + \varepsilon_0}\right)\right]$ $D = 1 - \left(\frac{\rho \cdot \varepsilon}{1 + \rho \cdot \varepsilon} \cdot \tanh\left(\frac{T - T_\mathrm{r}}{T_\mathrm{rec} - T_\mathrm{r}}\right)^q\right)$	ρ: controls the slope of $\sigma - \varepsilon$ curve after the peak of stress q: temperature range for strain softening T_rec: temperature for strain softening (°C)	• Strain softening occurs due to recrystallization at $T > 0.3T_m$ • Employed to predict chip segmentation • Other variations: Sima and Özel (2010) Özel and Ulutan (2012)
Abouridouane et al. (2016) $\sigma = (A + B \cdot \varepsilon^n) \cdot \left[1 + C \cdot \ln\left(\frac{\dot{\varepsilon}}{\dot{\varepsilon}_0}\right)\right] \cdot \exp\left(\beta \cdot \frac{T - T_\mathrm{r}}{T_\mathrm{m} - T_\mathrm{r}}\right)$	β: temperature sensitivity parameter	• Better reflects the strain softening behavior
Iturbe et al. (2017) $\sigma = \sigma_\varepsilon(\varepsilon) \cdot \sigma_T(T) \cdot \sigma_{\dot{\varepsilon}}(\dot{\varepsilon}, T)$ $\sigma_\varepsilon = \sigma_\mathrm{s} + (\sigma_0 - \sigma_\mathrm{s} + A\varepsilon^n)\exp(-r\varepsilon)$ $\sigma_T = \frac{1}{1 + e^{-m(T-B)}}$ $\sigma_{\dot{\varepsilon}} = 1 + (C \cdot D^T) \cdot \ln(\frac{\dot{\varepsilon}}{\dot{\varepsilon}_0})$	σ_s: steady state stress r: strain sensitivity m, B: stress-temperature sensitivity	• Accounts for strain softening • Non-linear decrease of stress with temperature • Considers the coupled effect of strain rate and temperature

Physical-phenomenological models

Umbrello et al. (2004) modified the JC model for better representing the behavior of hardened materials. As a case study, they machined a workpiece that was heat-treated to 52-64 HRC prior to cutting. The work hardening was represented with a power law in the form of $C\varepsilon^n$, the influence of strain rate was modeled with the logarithmic function $1+[\ln(\dot{\varepsilon})^m - A]$ and the influence of temperature was set as a fifth grade exponent equation. The varying hardness of a given material was represented by a linear function that modifies the work hardening $F+G\varepsilon$. The functions F and G are linear functions of hardness which depend on the material state. The former, F, modifies the initial yield stress and the latter, G, the strain hardening curve. The resultant hardening term was represented as $C\varepsilon^n+F+G\varepsilon$.

Kim et al. (2003) proposed a model considering that deformation is a thermally activated mechanism, linked to a recrystallization phenomena. This model was based on the Zener-Hollomon parameter expressed as $Z = \dot{\varepsilon} \cdot exp\left(\frac{Q}{R \cdot T}\right)$, where Q is the activation energy and R is the Boltzmann constant. Depending on the value of Z, DRX is taken into account in the model once the critical strain ε_c is reached. The work hardening $\sigma_{\text{WH+DRV}}$ calculated by a Voce equation is lowered by a σ_{DRX} stress depending on a recrystallized volume fraction X_{DRX}. The latter directly drives the drop in the flow stress observed when recrystallization is taking place and corresponds to the degree of recrystallization that occurs in the material. In addition to better describe the physical phenomena occurring at high strains, it provides a kinetic equation of the recrystallized volume fraction with the plastic strain in the form of an Avrami type model (Courbon et al. 2013). As described in Figure 2.14, the predicted flow stress taking into account the effect of DRX is similar to the one predicted by the TANH model, but in this specific case the bases are derived from physical equations.

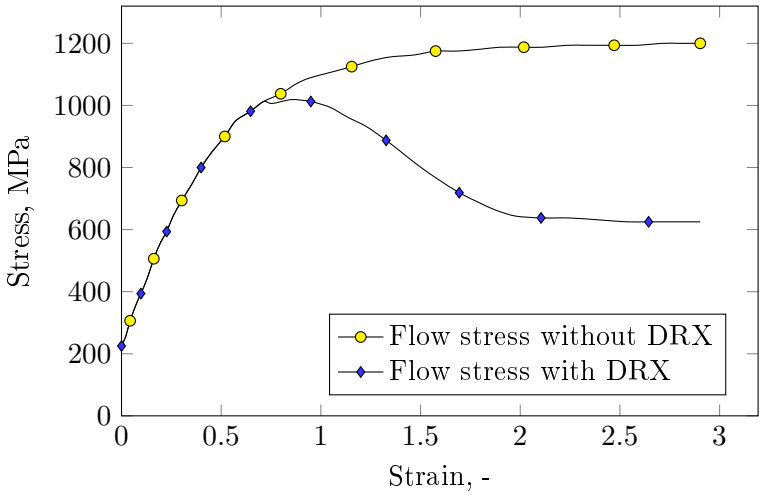

Figure 2.14: Comparison of flow stresses with and without the effect of DRX (Courbon et al. 2013)

Table 2.4: Physical-phenomenological models found in the literature

Flow stress equation	Features	
Umbrello et al. (2004)		
$\sigma(\varepsilon, \dot{\varepsilon}, T, HRC) = B(T) \cdot (C\varepsilon^n + F + G\varepsilon) \cdot [1 + (\ln(\dot{\varepsilon})^m - A)]$	$(F + G\varepsilon)$: linear function to represent the effect of material hardness	• Modifies the elastic limit dependent on material hardness
$B(T) = \exp(aT^5 + bT^4 + cT^3 + dT^2 + eT + f)$	$B(T)$: multiplicative factor for thermal softening	• Resultant flow stress captures the effect of material hardness
Kim et al. (2003) (data from Courbon et al. (2013))		
$\sigma_{\mathrm{y}} = \sigma_{(\mathrm{WH+DRV})} - \sigma_{\mathrm{DRX}}$		
$\sigma_{(\mathrm{WH+DRV})} = \sigma_0 + (\sigma_p - \sigma_0)\left[1 - \exp\left(C\varepsilon_p\right)\right]^m$	$\sigma_{(WH+DRV)}$: YS due to work hardening	• Prediction of DRX occurred during chip formation
$\varepsilon_p < \varepsilon_c, \quad \sigma_{\mathrm{DRX}} = 0$	σ_{DRX}: lowering of YS due to DRX	• Identification of recrystallized regions
$\varepsilon_p > \varepsilon_c, \quad \sigma_{\mathrm{DRX}} = (\sigma_p - \sigma s)\left[\frac{X_{\mathrm{DRX}} - X_{\varepsilon_{\mathrm{pic}}}}{1 - X_{\varepsilon_{\mathrm{pic}}}}\right]$	X_{DRX}: recrystallized volume fraction	• Flow stress modification due to DRX (strain softening)
$X_{\mathrm{DRX}} = 1 - \exp\left[-\left(\frac{\varepsilon_p - \varepsilon_c}{\varepsilon'}\right)^{m'}\right]$		

Physical models

Zerilli and Armstrong (1987) developed a formulation for material constitutive behavior based on dislocation mechanics. One of the main points of the developed law is that each material structure (fcc, bcc) has each own material behavior, depending on the particular characteristics of the structure. The effect of the grain size was also included, modeled with an incremental stress product of a microstructural stress intensity K and the inverse square root of the average grain diameter l ($\Delta\sigma = kl^{-1/2}$). $\Delta\sigma'_{\mathrm{G}}$ refers to the stress increment due to solute.

The abovementioned description of stress components which are combined to determine the plastic flow stress of bcc or fcc metals lead to two expressions. In the fcc case:

$$\sigma = \Delta\sigma'_{\mathrm{G}} + C_2\varepsilon^{1/2}\exp(-C_3T + C_4T\ln\dot{\varepsilon}) + kl^{-1/2} \tag{2.5}$$

A main consideration is that the temperature softening and strain-rate hardening dependence of σ is greater with increased strain hardening. In the case of the bcc structure:

$$\sigma = \Delta\sigma'_{\mathrm{G}} + C_1\exp(-C_3T + C_4T\ln\dot{\varepsilon}) + C_5\varepsilon^{1/2} + kl^{-1/2} \tag{2.6}$$

An uncoupled strain hardening term from the strain-rate hardening and thermal softening was modeled. These latter dependencies as well as the grain size dependence are generally larger than those corresponding dependencies exhibited by fcc metals.

In more in-depth studies of ferritic-pearlitic materials, isolated models for ferrite and pearlite have been developed over the years. These models can be combined into a unique behavior law with the homogenization laws. In this context, one of the most relevant works is the one started by Bouaziz and Le Corre (2003) based on the investigations of Mecking and Kocks (1981), Bergström (1970), and Estrin (1996). In a subsequent study (Allain and Bouaziz 2008), a model based on the homogenization of ferritic and pearlitic phase behavior with an ISO-work assumption was presented. The homogenization equation for ferrite-pearlite lamellar structures was presented as follows:

$$(\sigma_\alpha(\varepsilon_\alpha))\mathrm{d}\varepsilon_\alpha = (\sigma_{\mathrm{p}}(\varepsilon_{\mathrm{p}}) - X_{\mathrm{p}}(\varepsilon_{\mathrm{p}}))\mathrm{d}\varepsilon_{\mathrm{p}} \tag{2.7}$$

where, σ_α is the flow stress for the ferritic phase
ε_α is the strain of the ferritic phase
σ_{p} is the flow stress for the pearlitic phase
ε_{p} is the strain of the pearlitic phase
X_α is the intrinsic kinematical hardening variable of pearlite

The behavior of the pearlitic phase was defined by a modified Hall-Petch relation, derived from the work of Dollar et al. (1988). In this case, the plastic work-hardening was considered as isotropic, and followed a Voce law (saturation law) without any dependence on the microstructure. The initial flow stress was controlled by the interlamellar spacing (Eq. 2.8).

$$\sigma_{\mathrm{p}}(\varepsilon_{\mathrm{p}}) = \sigma_0^{\mathrm{p}} + \frac{\mathrm{M}\mu_\alpha b}{s} + \frac{K}{g}\left(1 - \exp\left(-\frac{g\varepsilon_p}{2}\right)\right) \tag{2.8}$$

where, K and g are empirical parameters
M is the Taylor factor
μ_α is the shear modulus of ferrite
s is the interlamellar spacing of pearlite
ε_{p} is the strain of the pearlitic phase
σ_0^{p} is the lattice friction of ferrite between the cementite lamellae of pearlite

The intrinsic kinematical stress for the specific case of lamellar structures was defined with Eq. 2.9.

$$X_{\mathrm{p}} = \frac{A}{\sqrt{s}}\left(1 - \exp((-B\varepsilon_{\mathrm{p}})\right) \tag{2.9}$$

where, A and B are two empirical parameters

To describe the constitutive behavior of the ferritic phase, Bui-Van et al. (2009) included the effect of strain rate and temperature on the constitutive equations developed by Estrin (1996) and Mecking and Kocks (1981). The formalism to express the flow stress is that of Eq. 2.10.

$$\sigma = \sigma_0^\alpha + \frac{\sigma^*}{2} + \frac{1}{2}\sqrt{(\sigma^*)^2 + 4(\sigma_{\mathrm{i}})^2} \tag{2.10}$$

where, σ_{i} is the effective stress to overcome local obstacles (see Eq. 2.11)
σ^* is the long-range internal stress that hinders dislocation glide (see Eq. 2.12)

The stress to overcome the local obstacles is related to the strain hardening of the constituent. The proposed forest hardening model for a polycrystalline ferritic steel was based on a modified equation derived from Bergström (1970), represented by Eq. 2.11 (Allain and Bouaziz 2008).

$$\sigma_{\mathrm{i}}(\varepsilon_\alpha) = \sigma_0^\alpha + \frac{\alpha M \mu_\alpha \sqrt{b}}{\sqrt{d_\alpha}}\sqrt{\frac{1 - \exp(-f\mathrm{M}\varepsilon_\alpha)}{f}} \tag{2.11}$$

where, α is related to the dynamic recovery of ferrite
d_α is the ferritic grain size
f is an adjustable parameter related to the forest hardening of ferrite
σ_0^α is the lattice friction of ferrite

The long-range internal stresses were directly linked to the strain rate based on the Orowan's relation (Bui-Van et al. 2009):

$$\sigma^* = \frac{k_B T}{V^*} \sinh^{-1}\left(\frac{\dot{\varepsilon}}{2M\rho_m v_{Debye} b^2 \exp\left(-\frac{\Delta G_0}{k_B T}\right)}\right) \tag{2.12}$$

where, k_B is the Boltzmann constant
ρ_m is the density of mobile dislocations
v_{Debye} is the Debye frequency
b is the mean Taylor factor
ΔG_0 is the activation energy
V^* is the activation volume of the mechanism

The performance of the model was evaluated in two publications. First, the quasi-static behavior was tested on four FP steels, where the accuracy of the model was assessed using data employed in the literature (Allain and Bouaziz 2008), as shown in Figure 2.15-a. Next, the dynamic behavior of pure ferrite was validated in two commercial steels (Bui-Van et al. 2009) as shown in Figure 2.15-b.

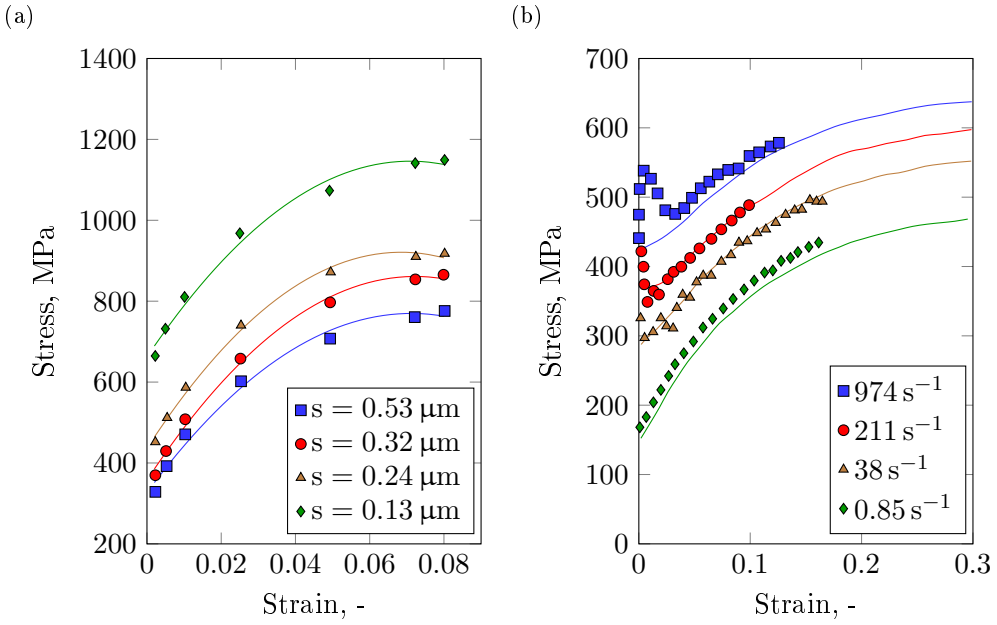

Figure 2.15: a) Modeled behavior of pearlite at quasi-static strain rate and 20°C (Allain and Bouaziz 2008). b) Modeled behavior of ferrite at different strain rates and 20°C (Bui-Van et al. 2009)

2.1.4 Critical analysis

In general terms, the mechanical properties of FP steels with lamellar-type pearlite structures are mostly dependent on the ferrite-pearlite ratio, grain size and interlamellar spacing. While the %C controls the ferrite-pearlite ratio, the thermal treatment defined in the TTT diagram controls the grain size and interlamellar spacing.

The strengthening effect that finer interlamellar spacing has on the yield strength and hardness is well documented. Analyzed to a far lesser extent, however, is the combined effect of lower-bigger grain size with finer-coarser pearlite.

In this context, it should be noted that a microstructure dependent flow stress model should, at least, reflect the effect of ferrite-pearlite ratio and interlamellar spacing of pearlite.

Concerning the current thermo-mechanical characterization methods, it was observed that tests employed to define material dynamic behavior are far from providing similar conditions to those encountered in machining: high strains (2-5), strain rates ($10^3 - 10^5\,s^{-1}$), temperatures (800-1200°C) and temperature rates ($10^5 - 10^6\,°C{\cdot}s^{-1}$). Thus, flow stress models that account for the thermo-mechanical states reached during cutting are needed. These models, at the very least, should represent the empirically obtained high temperature dynamic data.

Characterizing the yield behavior for developing a flow stress model is mostly derived from dynamic compression tests such as SHPB or Gleeble. These types of tests are selected due to their simplicity of sample preparation and results interpretation compared to shear tests. Nevertheless, the conditions reached during torsion-type shear tests and specially designed shear tests are closer in behavior with that of cutting. This represents a challenge for the near future in material modeling.

Flow stress models can be grouped into three main categories. The main advantages and disadvantages are shown in Table 2.5.

In this context, most of the material flow stress laws applied in the FE codes are based

Table 2.5: Advantages and disadvantages of flow stress models

	Phenomenological	Physical-phenomenological	Physical
Advant.	Strain hardening Thermal softening High strains and strain rates High temperatures	Material advanced parameters Microstructure variations such as DRX	Internal structure of phases (dislocations, sliding planes) Individual behavior of constituents
Disadv.	Microstructure not considered Characterization of parameters	Microstructure not considered Extensive parameters	Not suitable for high dynamics and temperatures Structure characterization

on phenomenological models, where the JC model (Johnson and Cook 1983) and variations of this (Calamaz et al. 2008; Abouridouane et al. 2016) prevail as the most widely used. Nevertheless, recently developed physical-phenomenological models demonstrate a more accurate tendency by including parameters related to microstructure.

Physically based models (microstructure or phase level) are still a challenge today. As an example, in the case of ferrite-pearlite steels, it enables the modeling of the individual behavior of ferrite and pearlite, which can imply an advance for the material forming process. At the time of writing, the models were not tested for the specific case of machining, so their validity under extreme thermomechanical conditions are still unknown.

2.2 Specification of workpiece materials

Four different ferrite-pearlite steel grades were selected to develop this research: 16MnCr5, 27MnCr5, C45 and C60. These were selected to cover a wide range of microstructure variants. The manufacturing of the grades was carried out by two steelmakers. ASCOMETAL manufactured the 16MnCr5 and 27MnCr5, and SIDENOR the C45 and C60 grades. All the grades were processed by isothermal annealing, in order to obtain an homogeneous as possible ferrite-pearlite structure without any banding, and a minimum globulization of pearlite. A schematic representation of the heat treatment performed is shown in Figure 2.16.

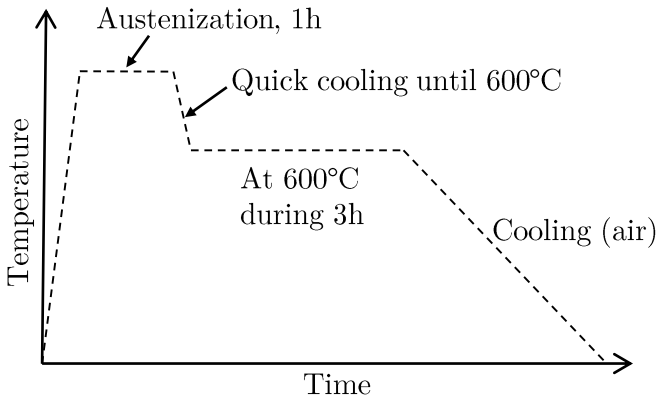

Figure 2.16: Isothermal heat treatment of steels

In the case of 16MnCr5 and 27MnCr5, austenization at 910°C (1h) and isothermal annealing at 600°C (3h) was performed. For the C45 and C60 grades the austenization temperature was set to 860°C. All the material was received in rolled bars of 60-65 mm diameter and 1 m length.

2.3 Chemical and microstructure properties

2.3.1 Chemical composition

The chemical composition of the different grades was measured by the manufacturer. Table 2.6 summarizes the composition data.

Table 2.6: Chemical composition of steel grades, provided by D'Eramo et al. (2017)

Grade	C	Si	Mn	S	P	Ni	Cr	Mo	Cu	Al
16MnCr5	0.19	0.17	1.23	0.028	0.016	0.19	1.03	0.07	0.17	0.020
27MnCr5	0.25	0.24	1.19	0.033	0.009	0.09	1.06	0.04	0.11	0.032
C45	0.45	0.33	0.78	0.025	0.014	0.09	0.12	0.02	0.11	0.007
C60	0.61	0.28	0.65	0.027	0.016	0.14	0.11	0.04	0.24	0.005

The carbon content in the 16MnCr5 sample was a little higher and in the 27MnCr5 a little lower than expected. The C45 and C60 grades presented the expected carbon balance. The differences in Al content are worth noting. These were due to the different deoxidation methods used to manufacture the steels. C45 and C60 were deoxidized with Si, while 16MnCr5 and 27MnCr5 with Al (this is the reason for the higher Al content). This higher Al content may lead to different inclusion populations which may affect the steel machining performance (Trent and Wright 2000).

2.3.2 Microstructure studies

A complete microstructural evaluation of the different steel variants was performed, including microstructure assessment, determination of the ferrite-pearlite ratio, determination of the pearlite globulization ratio and ferrite and pearlite grain size. The measurement of the interlamellar spacing and an inclusion study was carried out by the steelmakers using SEM-EDS technique.

Samples were extracted from both the longitudinal and transversal directions in the billets. From the transversal section three samples were extracted: core, mid-radius and surface. The standard sample preparation procedure was carried out by etching, grinding and polishing. Then nital reagent (1-5 mL HNO_3, 100 mL ethanol-95%) was employed to reveal the microstructure. Micrographs were captured with a Leica DM-IR optical microscope.

Microstructure observations

Homogeneity and the banding level was evaluated for the selected steels. The latter was performed by steelmakers, based on the testing method Renault 1194 (1969), in which banding level of the grades was cataloged from A to C from the lower to higher level of banding, comparing microstructures with reference pictures.

Figure 2.17 shows the microstructure for the tested FP steels in the transversal direction. The microstructures were mainly composed of homogeneous ferrite-pearlite structure in the whole section for all the steels. However, once the longitudinal direction was evaluated, a presence of bands was clearly seen in the 16MnCr5, and slightly visible in the 27MnCr5. These were cataloged as grade B, while the C45 and C60 were cataloged as A. An example of banding on the 16MnCr5 and homogeneous structure of C45 are shown in Figure 2.18.

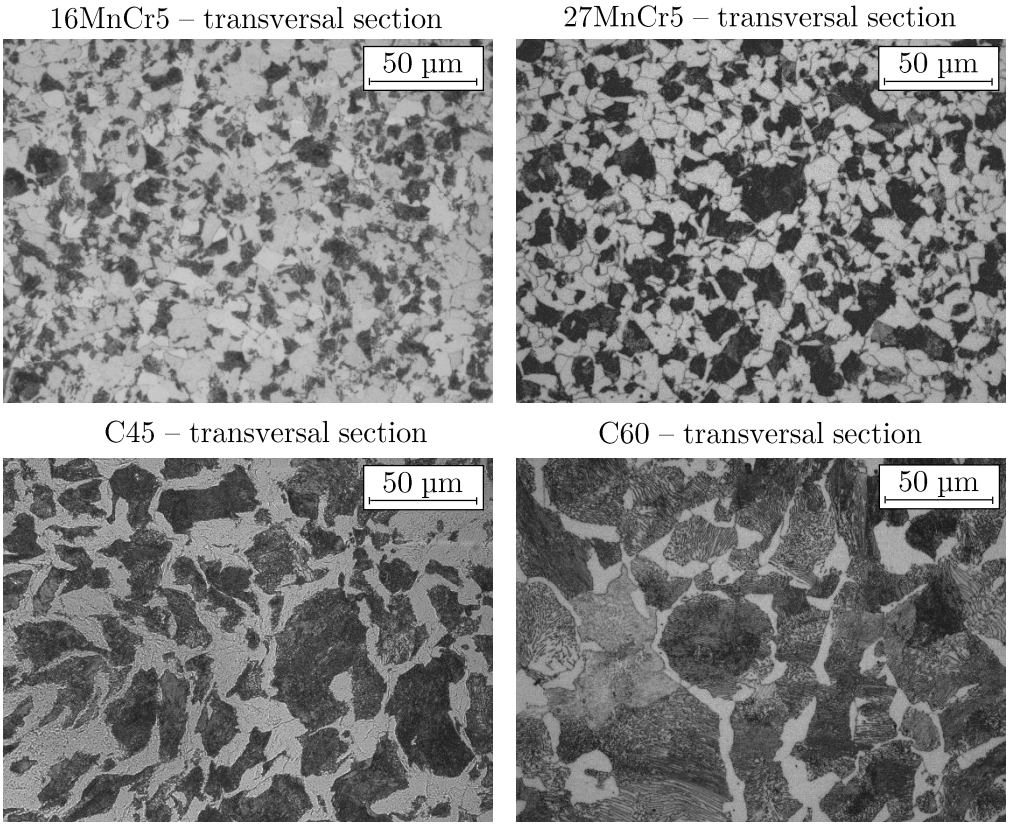

Figure 2.17: Optical microstructures of steels at 50x (mid-radius, transversal direction)

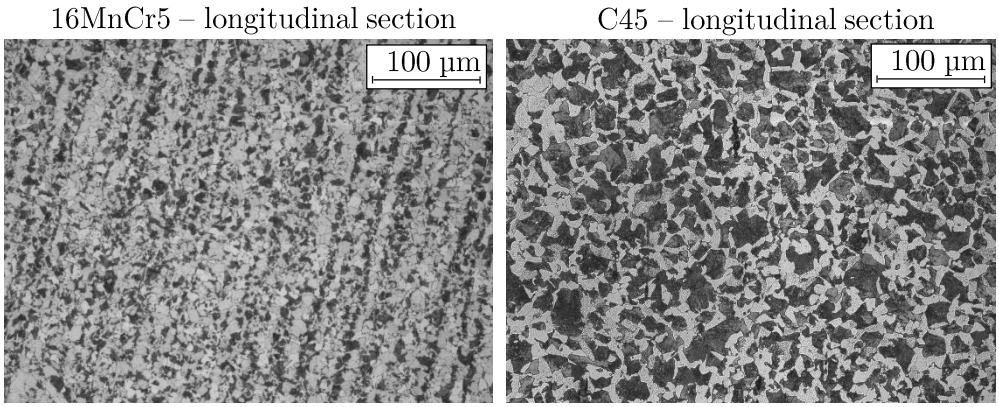

Figure 2.18: Optical microstructures of 16MnCr5 and C45 at 20x (mid-radius, longitudinal direction)

Ferrite-pearlite fraction

To establish the fraction of ferrite-pearlite, a statistical image analysis based on Matlab software was developed. It distinguishes between the RGB-color of both grains, and accounts for the number of pixels that refer to each grain to determine the FP ratio. This was performed for each material in the four extracted samples (three transversal and one longitudinal) at magnifications of 50x and 100x. The proportion of lamellar pearlite was evaluated by the steelmakers using the method Renault 1193 (1969). Etched pictures at a magnification of 500x were compared with reference pictures to determine the ratio of globular pearlite.

From the results of the RGB analysis (see Table 2.7), medium to low fraction of ferrite was found in the samples. High concentration of pearlitic structure was found in the C60, but in contrast, 16MnCr5 was found to be far from pure ferritic steel. Not all pearlitic fraction corresponded to lamellar pearlite. Figure 2.19 shows an example of lamellar and globular pearlite in the C45 grade at a magnification of 100x.

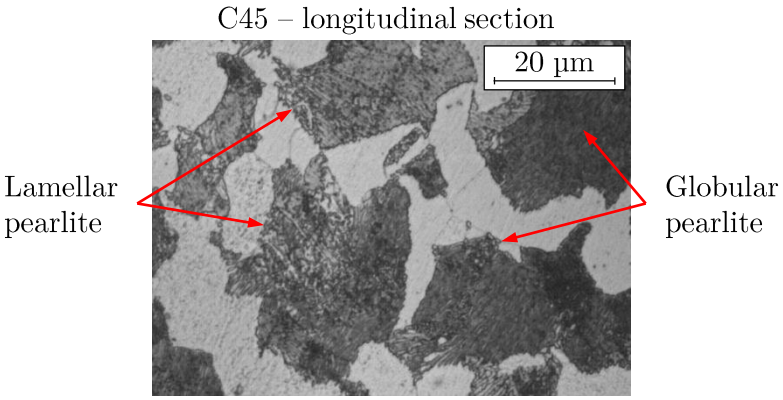

Figure 2.19: Lamellar and globular pearlite grains on C45 grade

In Table 2.7 the proportion of lamellar and globular pearlite is given for all the variants. 16MnCr5 and 27MnCr5 presented an almost lamellar pearlitic structure, while the micrographs of C45 and C60 revealed 25% of globulized pearlite. As is explained in the literature review of Chapter 3, the effect that globular or lamellar pearlite has on machinability might be determinant in terms of tool wear (Björkeborn et al. 2010).

Table 2.7: Quantitative analysis of ferrite-pearlite ratio (%ferrite/%pearlite) and proportion of lamellar/globular pearlite (%). Uncertainty ±5%

	16MnCr5	27MnCr5	C45	C60
%ferrite / %pearlite	58 / 42	40 / 60	25 / 75	14 / 86
%lamellar / %globular	90 / 10	90 / 10	75 / 25	75 / 25

Ferritic and pearlitic grain size

The ferritic and pearlitic grain sizes have been qualitatively measured following the standard ASTM E112-13 (2013) by means of the intercept method. For the case of ferrite, the measurement was performed only when proeutectoid ferrite exhibited nodular aspect. The average grain sizes are set out in Table 2.8.

Table 2.8: Ferritic and pearlitic grain size (μm). Uncertainty ±5μm

	16MnCr5	27MnCr5	C45	C60
Ferrite	10	14	17	11
Pearlite	13-15	15	22-27	31

Pearlite interlamellar spacing

Referring back to the analyzed literature review, it was concluded that pearlite interlamellar spacing has a determinant effect on the mechanical properties of FP steels. This interlamellar spacing might be decisive when analyzing the machinability of these steels.

The interlamellar spacing was measured by ASCOMETAL on the 16MnCr5 and 27MnCr5 variants, and by SIDENOR the C45 and C60. The statistical method consisted of measuring the distance between 5 lamellaes on SEM (Scanning Electron Microscope) images at a magnification of 10000x. This operation was repeated on about 70 images, and involved up to 16 measures per image. The schematic representation of the method is reported in Figure 2.20. An example of lamellar pearlite for the 27MnCr5 is shown in Figure 2.21.

Average interlamellar spacing, as well as standard deviation, is given for each grade in Table 2.9. A lowering of the interlamellar spacing was found when the carbon content

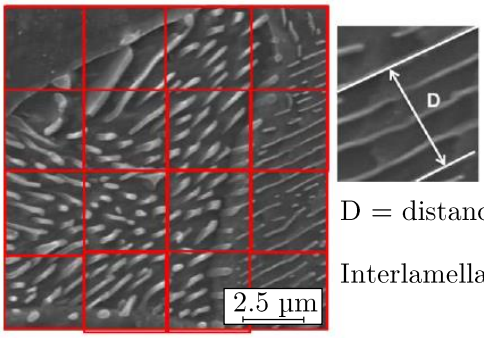

Figure 2.20: Method used by steelmakers for measuring the interlamellar spacing

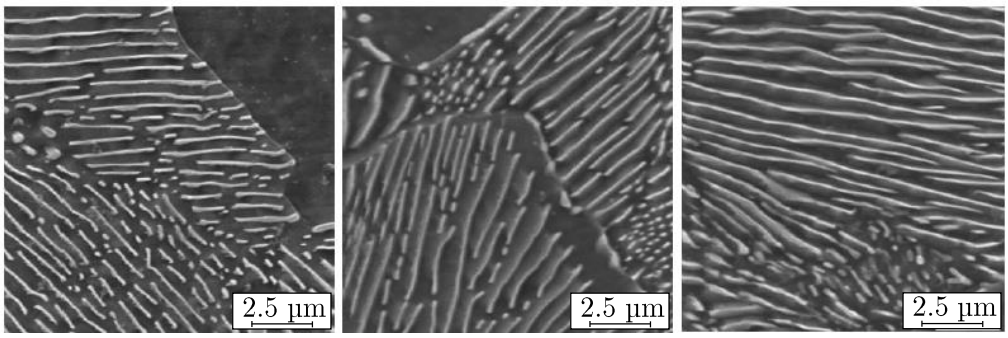

Figure 2.21: Example of the lamellar pearlite on the 27MnCr5 variant

decreased. This could also be linked to the smaller pearlite grains found in the 16MnCr5 and 27MnCr5 samples. A maximum deviation of 35% was found in the 16MnCr5 and C60 grades.

Table 2.9: Interlamellar spacing - average ± standard deviation (nm)

16MnCr5	27MnCr5	C45	C60
190 ± 65	285 ± 74	293 ± 82	372 ± 135

Inclusion studies

The inclusion studies were reported by steelmakers using SEM-EDS technique. The inclusions population showed that about 90% of the total amount were MnS. However, as a consequence of the different deoxidation methods used by the steelmakers, greater amount of Si content in the inclusions was present in the steels manufactured by SIDENOR, and higher Al content in the inclusions of those produced by ASCOMETAL. In those of the latter, aluminum oxides Al_2O_3 where found on the slag, an important aspect to be aware due to its negative influence in tool-life, increasing tool wear (Trent and Wright 2000).

2.4 Thermal characterization

In this section the thermal characterization of 16MnCr5, 27MnCr5, C45 and C60 is presented. In addition, due to numerical modeling requirements, a carbide H13A grade tool material was also analyzed. The following properties were tested:

- Specific heat (C_{p}) depending on temperature was determined with a Differential Scanning Calorimeter Netzsch Jupiter STA 449 (samples of Ø4 x 3 mm).
- Density (ρ) according to temperature was characterized with a Vertical Dilatometer Linseis L75PT (samples of Ø6 x 15 mm).
- Thermal diffusivity (κ) depending on temperature was determined with a Laser Flash Linseis LFA 1000 (samples of Ø10 x 3 mm).
- Thermal conductivity (K) for each material, after the previous three thermal properties, was calculated with Eq. 2.13.

$$K(T) = \kappa(T) \cdot C_{\mathrm{p}}(T) \cdot \rho(T) \tag{2.13}$$

Sample preparation was carried out by milling and wire-EDM cutting operations. Three repetitions for each defined property were measured, except in the case of specific heat, where a single test for each material was realized. In Figure 2.22 the thermal properties of the steels are given.

Measured density values did not represent big differences between the selected grades. A decrease in density with respect to temperature was found, which correlated with literature (Brooks 1996). The assessed values ranged between 7800-7450 kg·m^{-3}. A sudden increase at around 700-800°C was noticeable, which was linked to a phase change in the material (austenite transformation) (Brooks 1996).

Differences in measured specific heat between steels were nearly null. The specific heat increased together with temperature from 370-630 J·kg^{-1}·m^{-3} when moving from 20-600°C. Over 600°C an instability occurred, where sudden increases and decreases in specific heat were observed. This event was linked to the material reaching the vicinities of the Curie temperature. At this point energy is absorbed (or released) in destroying (or creating) the magnetic domains when heating (cooling). In other words, the material transforms from the paramagnetic to the ferromagnetic state (Kop et al. 2001). The peak in specific heat produced a corresponding dip in thermal diffusivity at the Curie temperature.

Diffusivity presented the widest differences between steels. The highest diffusivity was found in 16MnCr5, with rates around 50-100% higher compared to the other materials. This was followed by 27MnCr5, C45 and C60 in decreasing order. The lowering trend with the increasing temperature was assessed for all cases. Some machinability studies

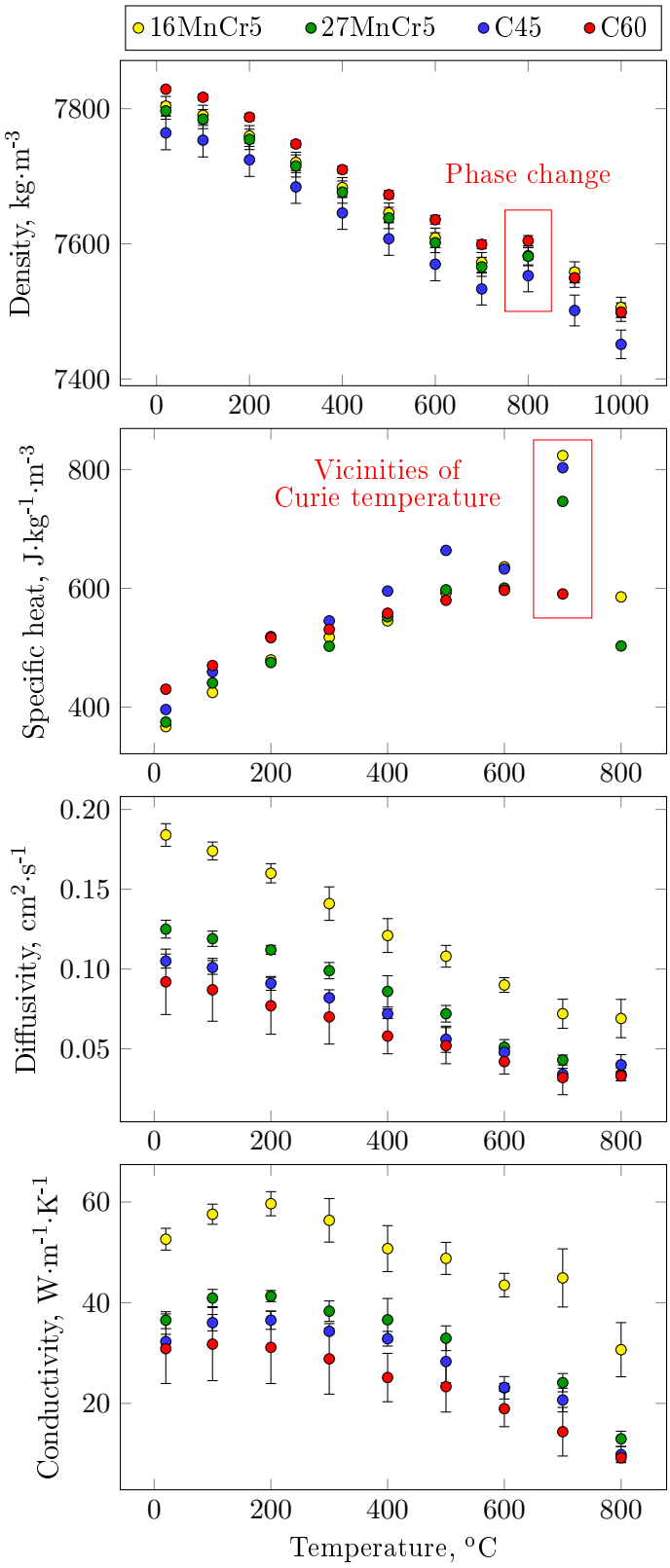

Figure 2.22: Thermal properties of steels depending on temperature

attribute the obtained results to diffusivity, noting that best machinability is obtained with higher diffusivity steels, as the variation in temperature with cutting speed can behave in different manner (Childs 2000).

Thermal conductivity was calculated based on Eq. 2.13. Observed differences in the steels were mostly due to the variations in diffusivity. Consequently, the 16MnCr5 grade presented higher conductivity than other tested grades, with differences up to 45-75%. Conductivity reduced from 52 to 30 $W \cdot m^{-1} \cdot K^{-1}$ in the case of 16MnCr5, and around 32 to 20 $W \cdot m^{-1} \cdot K^{-1}$ in the other steels in the temperature range of 20-800°C.

Figure 2.23 summarizes the thermal properties of H13A carbide. The density of the tool material showed a slight decreasing trend when temperature was increased. Density varied from 14970-14675 $kg \cdot m^{-3}$. The specific heat remained nearly constant at 200 $J \cdot kg^{-1} \cdot m^{-3}$ until 500°C, after which it started decreasing gradually. Then, at 700°C a sudden drop to 100 $J \cdot kg^{-1} \cdot m^{-3}$ occurred. This might be linked to a phase change

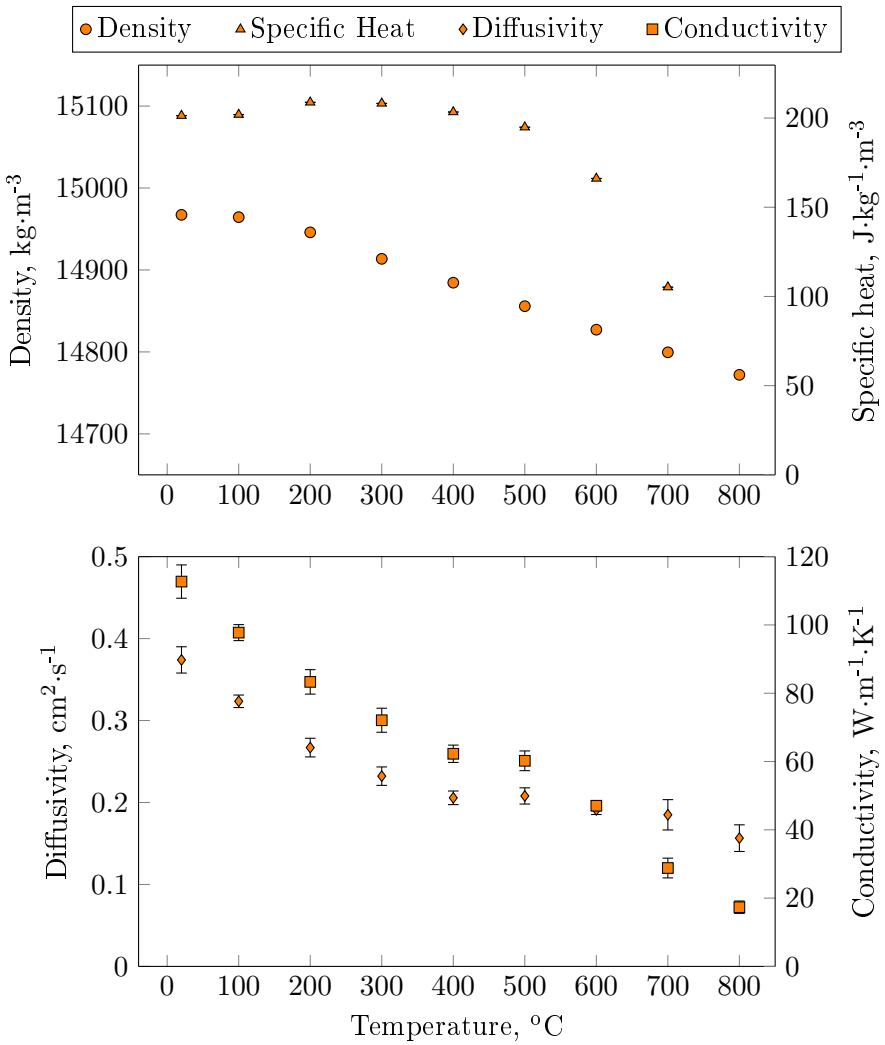

Figure 2.23: Thermal properties of carbide H13A depending on temperature

in some of the constituents (Humphry-Baker et al. 2017). Diffusivity values showed a slight decreasing trend that varied from 0.37 to 0.16 $cm^2 \cdot s^{-1}$. The calculated conductivity presented values in the range of 112-17 $W \cdot m^{-1} \cdot K^{-1}$. Therefore, at 800°C the conductivity was 90% lower than that at room temperature.

2.5 Mechanical properties

In this section, the mechanical properties required for input data, and others that can facilitate the understanding of machining tests are characterized. These are the material mechanical characteristics (Brinell hardness- HB, ultimate tensile strength-UTS, yield strength-YS, elastic elongation-El, elongation to fracture-A and toughness-KU) and the plastic behavior of FP steels.

2.5.1 Material standard mechanical characteristics

The data reported in Table 2.10 was provided by the steelmakers. Tensile, hardness and toughness tests at room temperature were carried out in their own laboratories. In general, reported results were in line with the fracture mechanics. Toughness was lower for the highest UTS values. The hardness of 16MnCr5 and 27MnCr5, as well as for the C45 and C60 was similar despite the different percentage of pearlite.

Table 2.10: Results of tensile, toughness and hardness tests (D'Eramo et al. 2017)

Steel variant	UTS (MPa)	YS (MPa)	El (%)	A (%)	KU (J)	Hardness (HB)
16MnCr5	544	306	30	72	76	162
27MnCr5	610	367	33	66	60	163
C45	667	361	18	48	20	185
C60	699	372	17	34	12	188

2.5.2 Plastic behavior: Rheological characterization

For all the steel variants, a matrix of tests was defined at different temperatures and strain rates, using different mechanical testing methods (Table 2.11). On the one hand uniaxial compression tests at quasi-static and low dynamic strain-rate conditions were carried out. On the other hand, medium-to-low strain-rate tests and high dynamic strain-rate tests were performed by the steelmakers, in a Gleeble and SHPB machines respectively. From these tests, the mechanical properties of the materials were compared under different conditions and the experimental curves to determine material constitutive laws were extracted.

Table 2.11: Matrix of rheology tests

Test method	T (°C)	$\dot{\varepsilon}$ (s^{-1})
Uniaxial compression	20, 500, 680	0.5, 5
Gleeble tests	20, 500, 680	50, 500
SHPB tests	20, 500, 680	2000, 4000

Experimental procedure

- Experimental setup

Uniaxial compression loading of the FP steel specimens was accomplished using an MTS 810 actuator. This was equipped with a 100kN load cell and FlexTest SE control program. Coupled with an induction system Iberinduction SMJRG-15, it enables high temperature material testing under compressive loading. The linear displacement between the compression plates was ensured with a specific die clamped on the hydraulic grips of the MTS 810. The contact surfaces between the plates and the specimens were lubricated prior to each test with CONDAT-Condaero 228 graphite-based paint to reduce friction effects. A diagram of both the MTS 810 and the compression plates is depicted in the Appendix A.

- Determination of the adiabatic-heating and flow stress correction methodology

In the literature review it was clearly observed that flow stress curves are affected by the self heating effect. This generates an increase in the specimen temperature related to the work done for plastic deformation. In the scope of determining real isothermal curves (at constant temperature), the temperature increase during the deformation process was estimated by utilizing Eq. 2.14.

$$\Delta T_{\mathrm{adb}} = \eta_{\mathrm{adb}} \cdot \frac{\beta}{\rho \cdot C_{\mathrm{p}}} \cdot \int_0^{\varepsilon} \sigma \mathrm{d}\varepsilon \tag{2.14}$$

where ρ is the density, C_{p} the heat capacity and β the Taylor Quinney coefficient. The latter specifies the fraction of the total energy converted into heat. Typical literature values range from 0.9 to 0.95 (Goetz and Semiatin 2001). The adiabatic correction factor for the strain rate sensitivity, η_{adb}, was used between the isothermal conditions at strain rates $\leq 10^{-3}\,s^{-1}$, where η_{adb}=0, and the adiabatic conditions at rates $\geq 10^{1}\,s^{-1}$, where η_{adb}=1 (Charpentier et al. 1986; Oh et al. 1992). Thermal data needed for Eq. 2.14 was taken from the characterization section.

Once the increase in temperature was calculated, measured flow stresses were converted into isothermal theoretical values with a first order Taylor Series Expansion, as shown in Eq.2.4 and explained in Figure 2.11 (Xiong et al. 2015).

Flow stress behavior: Analysis of results

This subsection is divided into two parts: Firstly the analysis of the adiabatic heating is analyzed. Secondly, the influence that temperature and strain rate have on flow stress is presented and discussed.

In Table 2.12 and Table 2.13 a summary of adiabatic temperature increase and corrected yield properties are presented for the developed tests.

- Influence of the adiabatic-heating

The ΔT_{adb} is calculated based on the plastic work, which is the area below the strain-stress curve. In general, it increased with the strain rate, and decreased with the deformation temperature for each tested material.

Comparing the adiabatic heating temperatures in all the steels, a consistent dependence on the mechanical properties was observed. The grades that showed greater flow stress resulted in greater temperature increments. The highest ΔT_{adb}, therefore, was occurred in the C60, followed by C45, 27MnCr5 and 16MnCr5.

Calculated temperatures were compared to those found in the literature. For example, Laasraoui and Jonas (1991) found that the increase in temperature at the conditions of 800°C and 10 s^{-1} of a low carbon steel was 20°C. Tests developed in the present research in close conditions achieved 15-18°C. Taking the work of Samanta (1968) as reference, a maximum ΔT_{adb} of 60-70°C was found when testing plain carbon steels up to 430 s^{-1}. The maximum ΔT_{adb} of 78°C achieved in the C60 grade (4000 s^{-1}, 20°C) was close to the reported values. Thus, the values calculated in this study were in line with those found in the literature.

It is important to note that the effect of ΔT_{adb} decreasing with the increase of temperature did not strictly occur under all conditions. In the case of C45 and C60, when analyzing the dynamic tests at 2000 and 4000 s^{-1}, at the temperature of 500°C a drop in the adiabatic temperature occurred, followed by an increase at 680°C. This was linked to a DSA phenomena of these materials at those specific conditions. As is discussed in the following pages of this section, the material showed softer behavior at 500°C than at 680°C. The outcome was less plastic work and, therefore, less adiabatic temperature increase. In the case of 16MnCr5 and 27MnCr5, the DSA effect was less pronounced. It was possible to detect lower ΔT_{adb} values at 2000 and 4000 s^{-1} than at 50 s^{-1}. A dipper drop on the strength due to DSA was the cause of this lower adiabatic heating.

Table 2.12: Adiabatic heating at plastic strain of 0.2 and yield properties of 16MnCr5 and 27MnCr5 steels (uncertainty ±2-3%)

	$\dot{\varepsilon}$ (s^{-1})	T (°C)	ΔT_{adb} (°C)	YS (MPa)	$FS_{0.2}$ (MPa)	UTS (MPa)
16MnCr5	0.5	20	31	280	678	742
		500	16	224	554	594
		680	6	208	316	339
	5	20	49	346	728	769
		500	25	224	592	639
		680	11	208	362	390
	50	20	55	392	753	806
		500	27	267	580	668
		680	15	273	441	458
	2000	20	55	676	960	965
		500	22	292	615	620
		680	18	294	700	700
	4000	20	78	703	1029	1062
		500	30	308	619	698
		680	24	271	684	769
27MnCr5	0.5	20	33	312	737	785
		500	16	225	569	597
		680	8	191	327	345
	5	20	55	382	820	851
		500	26	238	614	647
		680	13	228	382	403
	50	20	62	430	805	851
		500	31	294	653	709
		680	18	314	471	490
	2000	20	60	682	1026	1027
		500	23	287	649	665
		680	21	286	715	736
	4000	20	73	681	1059	1118
		500	30	282	656	733
		680	28	287	717	795

Table 2.13: Adiabatic heating at plastic strain of 0.2 and yield properties of C45 and C60 steels (uncertainty ±2-3%)

	$\dot{\varepsilon}$ (s^{-1})	T (°C)	ΔT_{adb} (°C)	YS (MPa)	$FS_{0.2}$ (MPa)	UTS (MPa)
C45	0.5	20	28	339	818	863
		500	21	249	605	606
		680	11	196	315	321
	5	20	43	359	839	864
		500	34	271	681	685
		680	19	246	391	402
	50	20	49	416	882	919
		500	41	348	751	779
		680	28	321	498	516
	2000	20	48	662	1103	1106
		500	34	316	744	771
		680	38	319	834	836
	4000	20	65	687	1139	1179
		500	39	350	722	813
		680	47	300	888	909
C60	0.5	20	34	355	865	926
		500	20	271	650	655
		680	10	211	337	342
	5	20	53	377	895	928
		500	32	284	729	734
		680	18	256	416	444
	50	20	64	456	960	988
		500	40	376	794	849
		680	26	348	546	566
	2000	20	75	691	1171	1180
		500	33	311	770	796
		680	40	300	851	851
	4000	20	78	728	1174	1217
		500	35	379	777	857
		680	44	324	882	936

- Influence of the material, temperature and strain rate

Yield data extracted from the curves is reported in Table 2.12 and Table 2.13. The results showed the expected impact of microstructure and composition on yield behavior. The higher the carbon content or % of pearlite the material contained, the greater the strength of the material. This was significant when analyzing the UTS and the $FS_{0.2}$. In these cases, the differences between grades were more marked (see Figure 2.24). In the case of initial yield stress (YS) differences between grades were less noticeable.

As shown in Figure 2.24, at quasi-static and room temperature testing conditions, differences between grades are appreciable. The flow stress increased 190 MPa when comparing the 16MnCr5 with the C60. The strain hardening was almost the same for the four studied steels. With regards to the YS, up to 75 MPa of variation were found.

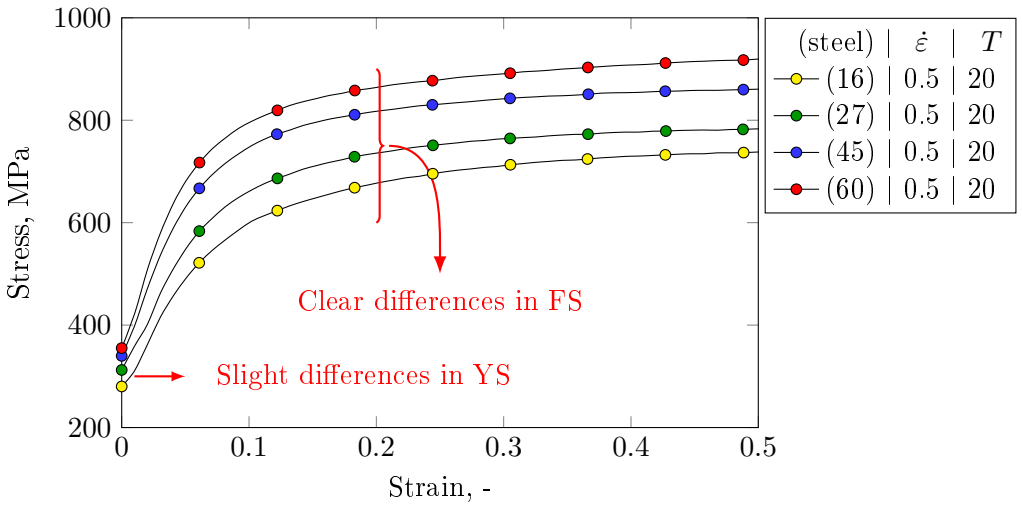

Figure 2.24: Flow stress curves of FP steels at strain rate of 0.5 s^{-1} and 20°C

Stress-strain curves of the steels over a wide range of temperatures (20-680°C) for a given strain rate of 0.5 s^{-1} are shown in Figure 2.25. It can be seen that for a given strain rate, as the temperature rose the strength of the material decreased. The strain hardening of the tested grades, which at first glance appeared to be similar, presented some narrow differences at medium-to-high temperatures. In this range, 16MnCr5 and 27MnCr5 seemed to react against the strain showing greater hardening. The curves of C45 and C60 behaved flatter, in contrast, tending to stabilize at a saturation stress.

The effect of temperature increase is observed in detail when plotting UTS against temperature (see Figure 2.26). Thermal softening on C45 and C60 was not very pronounced until the temperature of 500°C was exceeded. In contrast, 16MnCr5 and 27MnCr5 reflected a more constant thermal softening up to 500°C, although over 680°C adopted a similar decrease to the other steels. At the temperature of 680°C, the UTS of all the tested materials converged to nearly the same stress value.

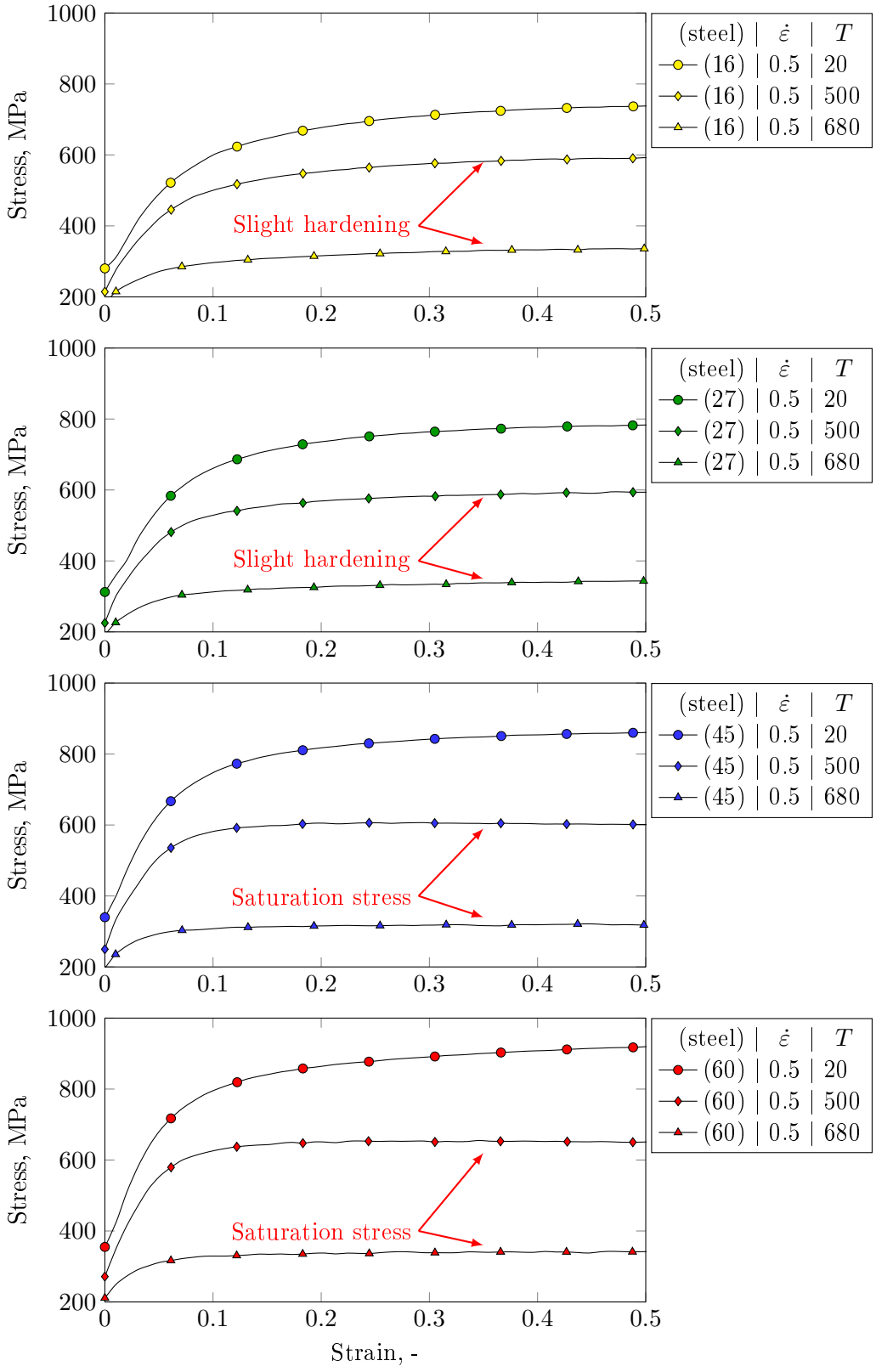

Figure 2.25: Influence of temperature on the compressive flow stress behavior of FP steels at a strain rate of 0.5 s^{-1}

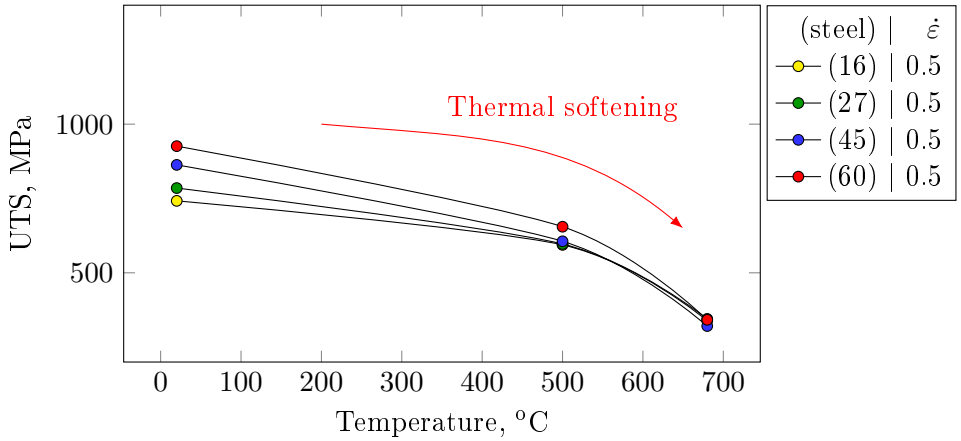

Figure 2.26: Influence of temperature on the UTS at 0.5 s^{-1} and 20°C

The influence that temperature had on UTS for each strain rate condition is plotted individually in Figure 2.27. Solid lines represent the compression tests at low-medium strain rates, dotted lines the ones developed on the Gleeble machine at medium strain rates, and dashed lines report the results of the SHPB dynamic tests.

The influence of temperature on the mechanical properties can be divided into two different behaviors: low strain rate and high strain rate. At low strain rates (results of compression tests), the UTS reduced a small degree until the temperature of 500°C was reached. From this critical temperature on, the drop in strength was more pronounced. This reduction in strength was more significant in the case of the C45 and C60.

The results in the high strain rate domain (2000-4000 s^{-1}) were influenced by the DSA effect. From 20 to 500°C the UTS presented a dip, followed by a sudden increase at 680°C. Although no results were reported by the steelmakers above 680°C, it was expected that the UTS should represent a softening similar to that achieved at low strain rates.

DSA is due to recurrent pinning of dislocations while arrested at obstacles during their motion that results in plastic straining (Nemat-Nasser and Guo 2003). The phenomenon is attributed to the additional resistance of dislocation motion produced by the mobility of solute atoms (e.g., C and N for steels) that can diffuse to dislocations above a certain temperature while the dislocations are waiting at their short range barriers. As the solutes catch up with moving dislocations and pin them down, the flow stress increases. With increasing strain rates, higher temperatures are required to drive the solute atoms to dislocations at sufficient speeds. Thus, the plastic deformation behavior and DSA are dependent on both temperature and strain rate (Wang et al. 2015).

Results in Figure 2.27 illustrate that the peak point of the flow stress was shifted to higher temperatures with increasing strain rate. This phenomena was thus not visible in the low strain-rate range since it should appear in the range between 200-300°C.

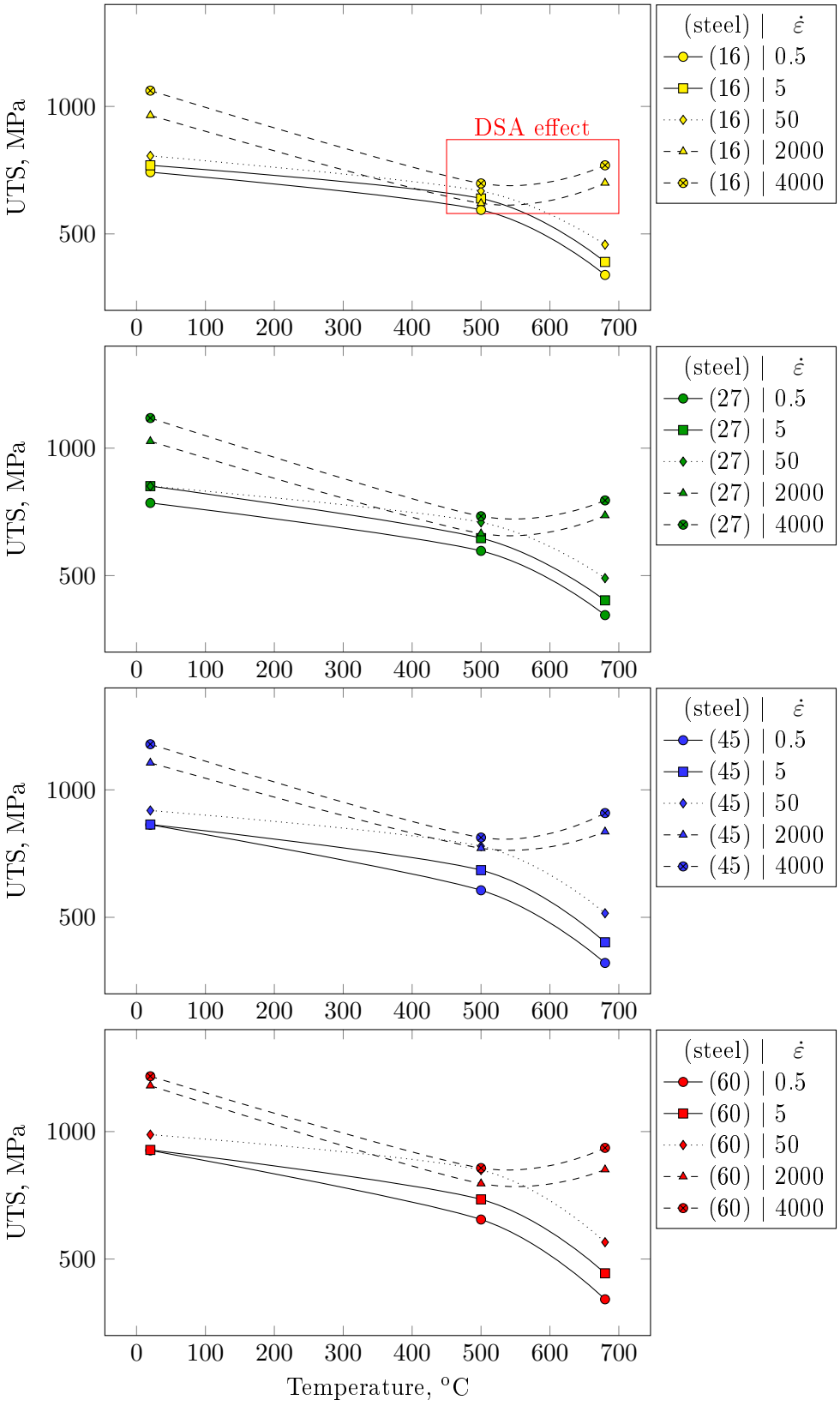

Figure 2.27: Influence of temperature on the UTS values at all tested strain rates

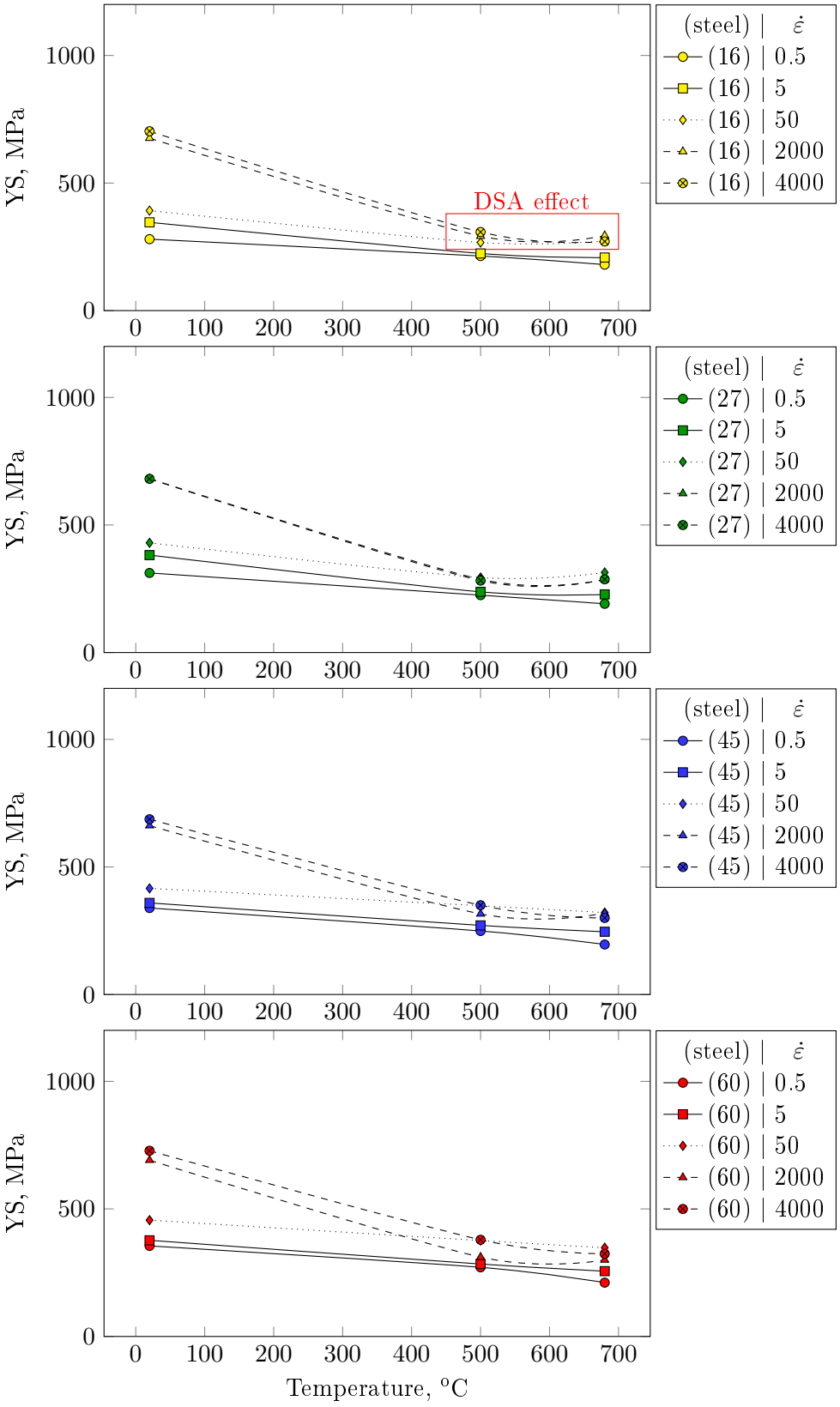

Figure 2.28: Influence of temperature on the YS values at all tested strain rates

The effect of temperature on the YS is shown in Figure 2.28. The effect of the DSA was also evident at high strain rates, although was less aggressive since the stress values were lower. At low strain rates YS decreased almost in line with the temperature increase.

In Figure 2.29 and Figure 2.30 the stress-strain curves for 0.5-4000 s^{-1} and temperatures of 20°C and 680°C are depicted. The results at the intermediate temperature of 500°C followed the same trend, and are plotted in the Appendix A.

It was observed that for a given temperature, the strength of the material increased with increasing strain rate. Strain rate increase promotes the accumulation of dislocations (increase of the dislocation density), generating dislocation pileups, and therefore hardening the material (Tisza 2001).

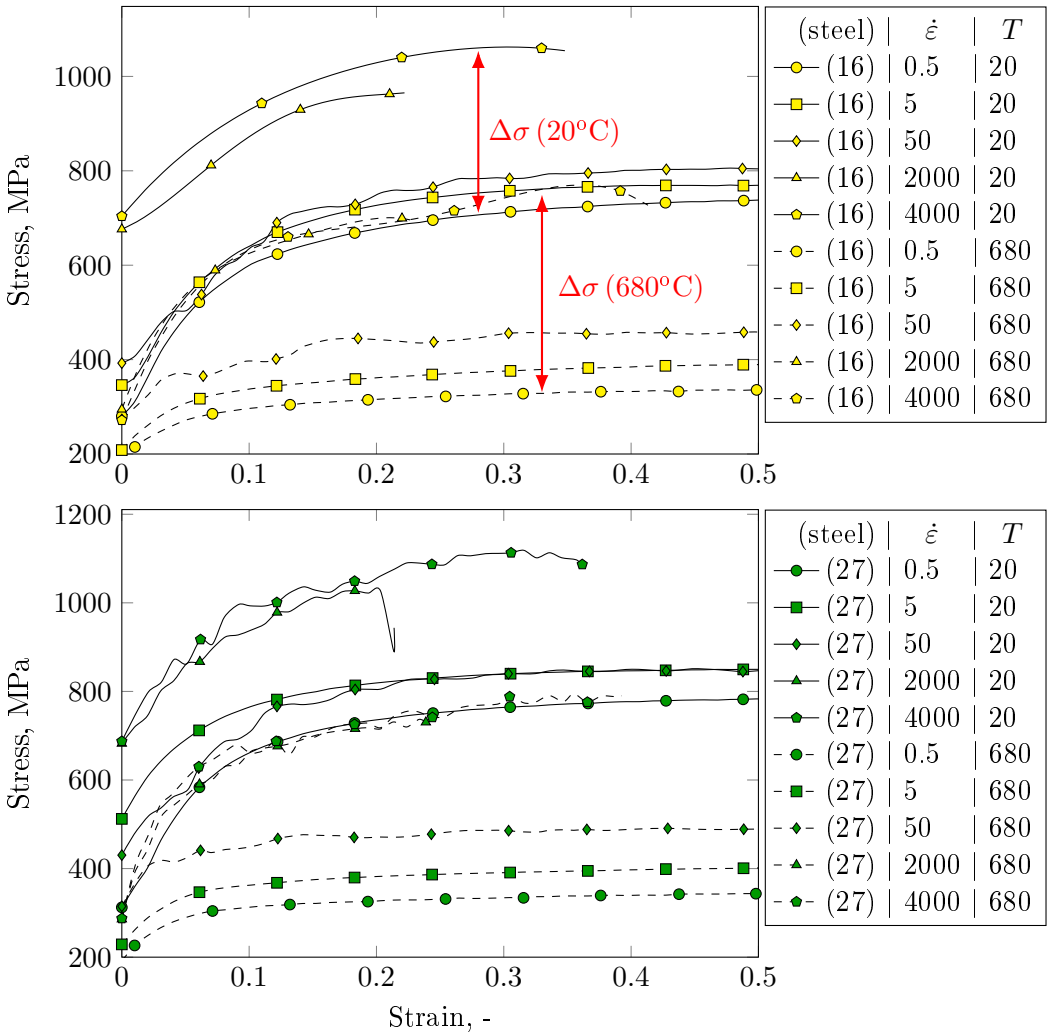

Figure 2.29: Influence of temperature on the compressive flow stress behavior of 16MnCr5 and 27MnCr5 steels at the temperatures of 20 and 680°C

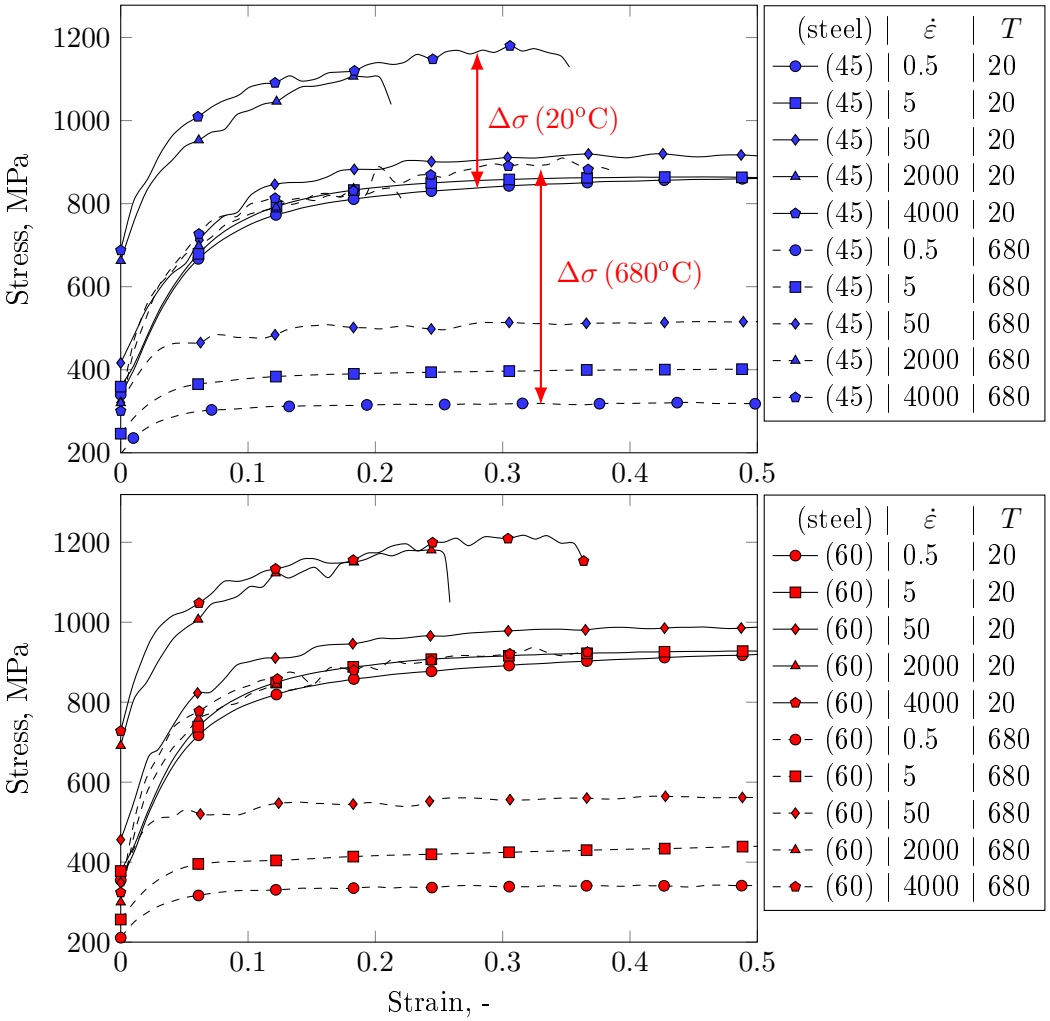

Figure 2.30: Influence of temperature on the compressive flow stress behavior of C45 and C60 steels at the temperatures of 20-680°C

The hardening effect of strain rate was more sensitive in the range of high temperatures. This is observed when comparing the differences on flow stress between 0.5 and 4000 s^{-1} at room temperature, $\Delta\sigma$ (20°C), and 680°C, $\Delta\sigma$ (680°C). In the low temperature domain, material strengthening occurred at strain rates over 2000 s^{-1}. Between 0.5-50 s^{-1}, differences in the curves were hardly noticeable. Stresses in the high temperature range (T>500°C) were more sensitive to the strain rate. It was possible to appreciate greater differences in the curves at 0.5-50 s^{-1}. In addition, there was also a marked difference in the flow stress between low and high rate tests (2000-4000 s^{-1}). From these tests it was concluded that the influence of the strain rate on the flow stress behavior of analyzed FP steels was temperature dependent.

To ensure the reliability of compression tests, results were compared to experimental data sets found in the literature. Quasi-static tests at room temperature were taken as reference from the work developed by Abouridouane et al. (2012). Yield values at

the strain of 0.2 varied from 530 to 1120 MPa from a nearly pure ferritic to a nearly pure pearlitic steel. For a C45 steel they reported a $FS_{0.2}$ of 850 MPa. Characterized FP steels in the same conditions presented $FS_{0.2}$ values in the range of 749-858 MPa, and for the specific case of C45 was 818 MPa. Therefore, the characterized data of this research was in line with the work of Abouridouane et al. (2012).

Maekawa et al. (1983) analyzed the flow stress behavior of a 0.18 %C steel at the rates of 200-2000 s^{-1}, similar to the 16MnCr5 tested in this study. They reported that the flow stress depended on the histories of the temperature and the strain rate to which the steel had been subjected in straining. For example, at the rate of 2000 s^{-1} the $FS_{0.2}$ decreased from 720-500 MPa when the material was heated from 20 to 400°C. At 600°C the $FS_{0.2}$ increased to 600 MPa. The same behavior was observed in the comparable case of 16MnCr5, and also in the other FP steels tested. At the temperatures of 20, 500 and 680°C, the measured stresses were 977, 622 and 706 MPa respectively. This behavior was linked by Maekawa et al. (1983) to the blue-brittleness effect in that specific temperature range. In this document, this phenomena is denoted as DSA.

- Microstructural analysis of the tested samples

To extract additional information with reference to microstructural changes, the metallurgy of the deformed specimens was analyzed through optical microscopy. As an example, Figure 2.31 shows the deformed micrographs of C45 grade compared to the base material, at different temperatures and strain rates. The analysis region was selected at the mid radius of the specimen, thus, avoiding the highly deformed mi-

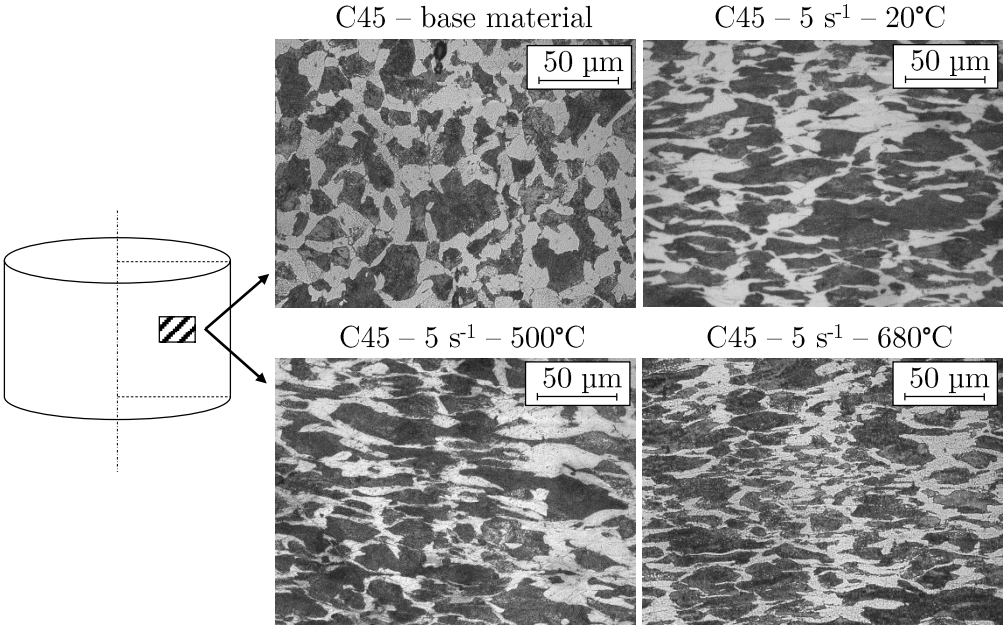

Figure 2.31: C45 steel micrographs of compressed specimens at strain rate of 5 s^{-1} and temperatures in the range 20-680°C

crostructure found in the middle of the samples, which was a consequence of the shear effects.

The evolution of the microstructure with the temperature increase did not show any type of grain refinement or recrystallization for any of the FP steels. It was possible to distinguish deformed grains due to compression and shearing in the structure, but the size of the grains seemed to remain nearly constant, compared to the base material.

The methodology used in this study was selected to avoid generating microstructure changes during sample heating prior to the compression tests, and the results with heating rates of 300-400°C·min^{-1} indicated that this was the case. In addition, the results were in accordance with the reported flow stress data. There was no symptom of any severe strain softening that could be a consequence of a recrystallization or grain refinement, which correlated with the microstructure observations.

2.6 MicroStructure Based flow stress model proposal

The reliability of FE models is contingent on the employed inputs. In this context the way of representing the material flow behavior was identified as one of the most influencing input parameters (Arrazola et al. 2004; Özel 2006). Thus, a constitutive model representing the behavior during machining process is necessary.

The model should represent the following aspects:

- Material behavior under high strain, strain rates and temperatures.
- Distinguish the behavior of FP steels based on microstructure input.

To accomplish these defined objectives, this research project identified and tested the most representative models in the literature. Taking into account the advantages and disadvantages of these models, a new model is proposed with the aim of improving the predictions when referring to FP steels.

2.6.1 Analysis of representative flow stress models from the literature

The model developed by Abouridouane et al. (2012), which is an extension of the behavior law developed by Johnson and Cook (1983), is the most frequently used model for simulating FP steels in metal cutting processes. The model describes the behavior based on the ferrite-pearlite ratio. First, specific flow stress data was calculated for pure pearlitic and ferritic steels (the parameters A, B, C, n and m were calculated for pearlite and ferrite). Then, an homogenization law based on the f_{p} is applied to calculate the resultant flow stress. Eq. 2.15 represents the flow behavior.

$$\sigma = (A + B \cdot \varepsilon^n) \cdot \left[1 + C \cdot \ln\left(\frac{\dot{\varepsilon}}{\dot{\varepsilon}_0}\right)\right] \cdot \left[1 - \left(\frac{T - T_\mathrm{r}}{T_\mathrm{m} - T_\mathrm{r}}\right)\right] \tag{2.15}$$

where,
$$A = A_\mathrm{f} + f_\mathrm{p}(A_\mathrm{p} - A_\mathrm{f})$$
$$B = B_\mathrm{f} + f_\mathrm{p}(B_\mathrm{p} - B_\mathrm{f})$$
$$nB = n_\mathrm{f}B_\mathrm{f} + f_\mathrm{p}(n_\mathrm{p}B_\mathrm{p} - n_cB_c)$$
$$CA = C_\mathrm{f}A_\mathrm{f} + f_\mathrm{p}(C_\mathrm{p}A_\mathrm{p} - C_\mathrm{f}A_\mathrm{f})$$
$$mA = m_\mathrm{f}A_\mathrm{f} + f_\mathrm{p}(m_\mathrm{p}A_\mathrm{p} - m_\mathrm{f}A_\mathrm{f})$$

Based on the data reported by Abouridouane et al. (2012) for pearlite and ferrite, and the characterized f_p of pearlite, the parameters of the JC model were calculated for each of the selected FP steels. These are summarized in Table 2.14.

Table 2.14: Parameters of JC equation based on homogenization law presented by Abouridouane et al. (2012)

	A (MPa)	B (MPa)	n (-)	C (-)	m (-)
16MnCr5	416	580	0.341	0.016	1.28
27MnCr5	520	584	0.338	0.014	1.2
C45	606	587	0.334	0.012	1.15
C60	663	589	0.332	0.011	1.13

The validity of the model was tested by comparing the measured and predicted flow stress curves (Section 2.5.2). Figure 2.32 compares the resultant flow stresses at room temperature and quasi-static condition.

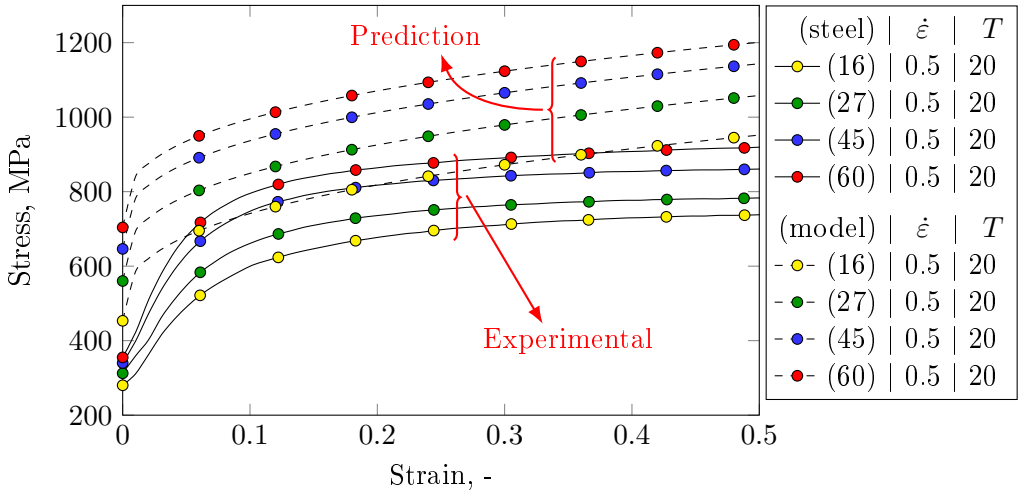

Figure 2.32: Comparison of predicted (dashed line) and experimental (solid line) flow stress curves at 20°C and 0.5 s^{-1}

The material model predicted higher flow stress than the experiments. As a consequence, the predicted curves shifted to a position of 120-180 MPa above the experimental data. Moreover, the experimental curves presented strain hardening up to a saturation stress (UTS), and from this strain level on the stresses remained nearly constant. In contrast, although isotropic hardening is considered in the model, it highly overestimated material flow stress as this diverged to infinity with increasing strain.

Taking the C45 grade as a reference, the influence that temperature had on flow stress curves can be examined in Figure 2.33.

The results demonstrated that temperature did not affect strain hardening. Experiments tend to saturate when reaching the UTS, whereas the model diverged to infinity at all the tested temperatures. Furthermore, the thermal softening seemed to be underestimated. This is better described in Figure 2.34.

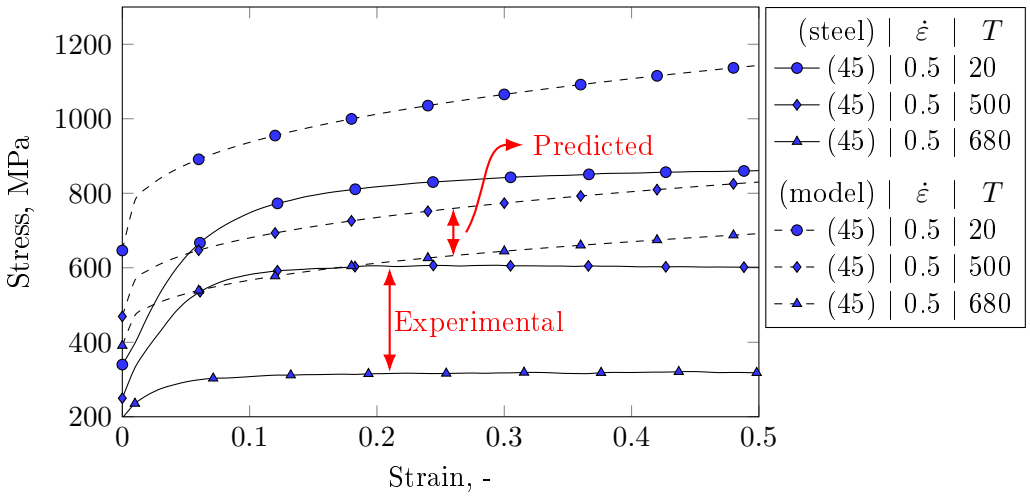

Figure 2.33: Influence of temperature on predicted (dashed line) and experimental (solid line) flow stress curves at 20, 500 and 680°C and 0.5 s^{-1}

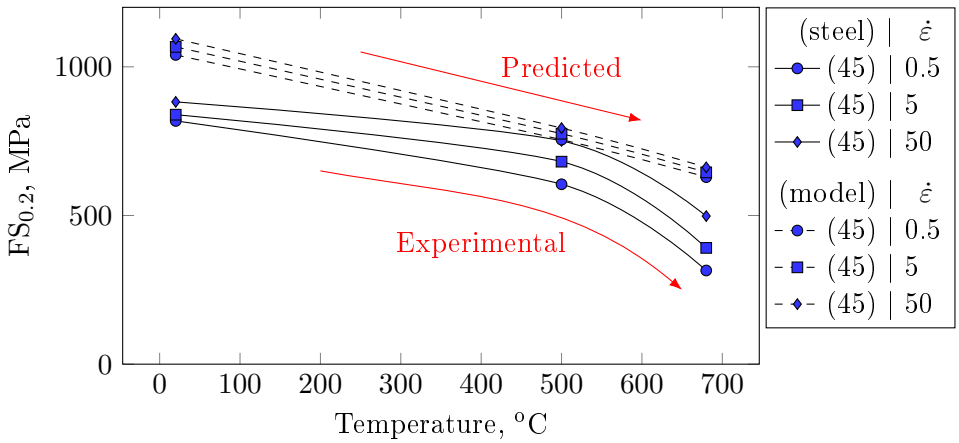

Figure 2.34: Influence of temperature on the $FS_{0.2}$ on predicted (dashed line) and experimental (solid line) results

Considering only the tendency of the flow stress it is clear that the modeled linear behavior of the thermal softening did not correspond to the real behavior of the C45. Therefore, it is difficult to accurately capture the softening effect with the model proposed by Abouridouane et al. (2012).

The sensitivity the model had to the strain rate is plotted against the experiments in Figure 2.35. The predictions were not in line with the experiments, since did not show marked differences between 5 and 4000 s^{-1}. As a result, the predicted stresses lie between the characterizations. This might be a consequence of the logarithmic relation of $\ln(\dot{\varepsilon}/\dot{\varepsilon_0})$ which could be underestimating the strengthening due to the increase in strain rate.

In summary, the proposed JC flow stress model did not accurately represent the behavior of the selected range of FP steels. This could be for two reasons. Firstly, the equations of the conventional JC law that represent the physics of strain hardening, thermal softening and strain rate hardening did not behave in the same manner as the tested materials. Secondly, the methodology published by Abouridouane et al. (2012) to obtain the parameters of the flow stress law gave stress values far from the experimental data obtained in the present research.

With regards to modeling material behavior based on microstructure properties, the works of Allain and Bouaziz (2008) and Bui-Van et al. (2009) were also found to be relevant. The former described the isolated behavior of ferrite and pearlite in terms of dislocation density physics. The mixing of these constituents was accomplished by an ISO-work homogenization law. The model successfully described the behavior of different ferritic-lamellar pearlitic materials at room temperature and quasi-static conditions. Bui-Van et al. (2009) modeled the behavior of ferritic materials at high strains coupled with temperature. Although the possibility of modeling the individual

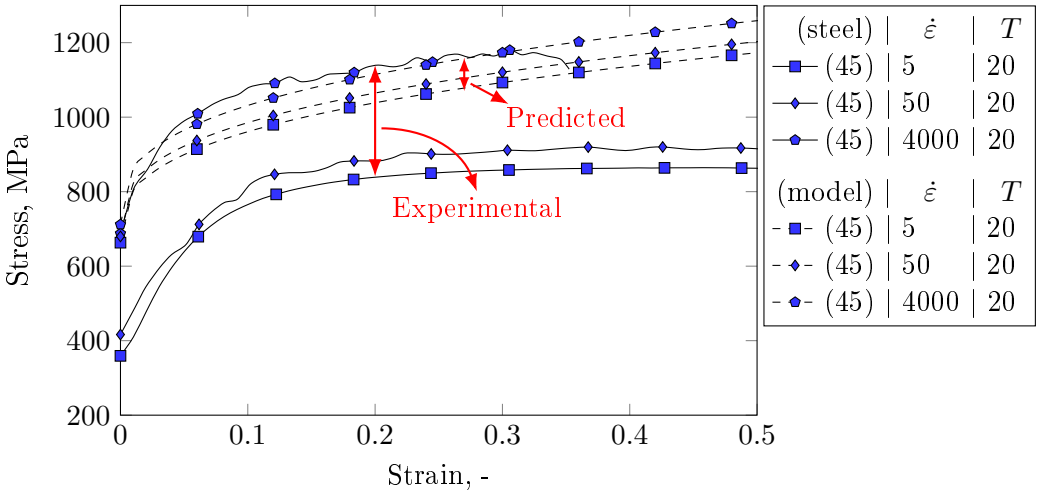

Figure 2.35: Influence of strain rate on predicted (dashed line) and experimental (solid line) flow stress curves at 20°C and 5, 50 and 4000 s^{-1}

influence that ferrite and pearlite had on flow stress seemed interesting, an equation describing the dynamic behavior of pearlite was still lacking.

2.6.2 Description of the MicroStructure Based model

Considering the limitations of the current constitutive models that model the behavior of FP steels, a new model was proposed in the present thesis. This model combined the physical quasi-static behavior of FP steels described by Allain and Bouaziz (2008), with the phenomenological methodology of individually coupling the effects of thermal softening and strain rate hardening presented in the JC model (Johnson and Cook 1983).

The developed MicroStructure Based flow stress model (MSB model) can be expressed as described in Eq. 2.16. The influence of strain hardening (σ_{SH}), thermal softening (σ_{TS}) and strain rate hardening (σ_{SRH}) were modeled separately and integrated into this equation.

$$\sigma = \sigma_{\mathrm{SH}}(\varepsilon) \cdot \sigma_{\mathrm{TS}}(T) \cdot \sigma_{\mathrm{SRH}}(\dot{\varepsilon}, T) \tag{2.16}$$

As the physics were modeled as independent terms, it was assumed that the microscopic behavior of thermal softening and strain rate hardening were identical for ferrite and pearlite. Taking into account this hypothesis, these phenomena could be represented as macroscopic, and therefore modeled separately.

In the following lines the steps undertaken to characterize the terms of the equation are explained.

Strain hardening

The comparisons between the measured and predicted results using the conventional JC model with the parameters proposed by Abouridouane et al. (2012) did not successfully described the real behavior of FP steels. According to the analysis previously described, some objectives were determined to develop a more realistic strain hardening prediction:

- Modeled flow stress should reflect the quasi-static behavior of FP steels at room temperature.
- The input parameters should be set dependent on microstructure parameters.
- Strain hardening should be considered up to a certain strain level followed by a strain stabilization (or reduce the slope of the strain hardening).

The work of Allain and Bouaziz (2008) captured successfully the quasi-static behavior of FP steels, and for this reason their flow stress law was incorporated into the model developed in this research. The macroscopic flow behavior of the FP steels was achieved by means of specific dislocation models for ferrite and pearlite, combined with and ISO-work assumption. The proposed forest-hardening model for a polycrystalline ferritic steel was based on a modified equation derived from Bergström (1970), expressed by Eq. 2.17.

$$\sigma_\alpha(\varepsilon_\alpha) = \sigma_0^\alpha + X^\alpha + \alpha_\mathrm{n} \mathrm{M} \mu_\alpha \mathrm{b} \sqrt{\rho^\alpha} \tag{2.17}$$

where, α_n is a constant related to the forest dislocation hardening ($\alpha_\mathrm{n} = 0.4$)
M is the mean Taylor or Smith factor ($\mathrm{M} = 3$)
μ_α is the shear modulus of ferrite ($\mu_\alpha = 80\,\mathrm{GPa}$)
b is the Burger's vector ($\mathrm{b} = 2.5\,\mathrm{x}\,10^{-10}\,\mathrm{m}$)
ρ^α is the statistically stored dislocation density in ferrite
X^α is the kinematical hardening of the ferrite
σ_0^α is the lattice friction of ferrite

The kinematical hardening of the ferritic constituent increases with the density of geometrically necessary dislocations. It is also related to the ferritic grain size d_α. This can be described with Eq. 2.18.

$$X^\alpha = \frac{\mathrm{M} \mu_\alpha \mathrm{b}}{d_\alpha} \left(\mathrm{n}_0 \left(1 - \exp\left(-\frac{\lambda_\mathrm{d} \varepsilon^\alpha}{\mathrm{n}_0} \right) \right) \right) \tag{2.18}$$

where, d_α is the ferritic grain size
n_0 is the critical density of geometrically necessary dislocations ($\mathrm{n}_0 = 2.82$)
λ_d refers to the density of shear bands ($\lambda_\mathrm{d} = 34.5\,\mathrm{b}$)

Work hardening models for ferrite considers that the evolution of the dislocation density with strain is a result of the competition between the rate of production of dislocations, and their annihilation rate (Gutiérrez and Altuna 2008). This eventually leads to a unified phenomenological formulation or Mecking & Kocks model $\frac{d\rho}{d\varepsilon} = \mathrm{M}\left(\frac{1}{\mathrm{b}L} - \mathrm{k}_2 \rho^\alpha\right)$ (Mecking and Kocks 1981), where k_2 is the dislocation annihilation constant and L the dislocation mean free path, defined as the mean spacing between obstacles to dislocation motion (glide) (Gutiérrez and Altuna 2008). Assuming the grain boundaries contribute to the work-hardening in terms of $L = d_\alpha \cdot \mathrm{f}_\mathrm{DRV}$, where f_DRV is an adjustable parameter related to the dynamic recovery, and $\mathrm{k}_2 = \frac{\lambda_\mathrm{d}}{\mathrm{n}_0}$, the Mecking & Kocks equation can be written as 2.19.

$$\frac{\mathrm{d}\rho^{\alpha}}{\mathrm{d}\varepsilon^{\alpha}} = \mathrm{M}\left(\frac{1}{\mathrm{b}\cdot d_{\alpha}\cdot \mathrm{f_{DRV}}} + \frac{\mathrm{k_0}}{\mathrm{b}}\sqrt{\rho^{\alpha}} - \frac{\lambda_{\mathrm{d}}}{\mathrm{n_0}}\right) \tag{2.19}$$

Assuming that the dislocation-dislocation interaction can be disregarded, leading to a strain-independent dislocation mean free path, the integration of the equation leads to Eq. 2.20.

$$\rho_{\mathrm{i}}^{\alpha} = \rho_{\mathrm{i-1}}^{\alpha} + \mathrm{M}\left(\varepsilon_{\mathrm{i}}^{\alpha} - \varepsilon_{\mathrm{i-1}}\right)\left(\frac{\exp\left(-\frac{\lambda_{\mathrm{d}}\cdot\varepsilon_{\mathrm{i}}^{\alpha}}{\mathrm{n_0}}\right)}{\mathrm{b}\cdot d_{\alpha}} + \frac{\mathrm{k_0}\sqrt{\rho_{\mathrm{i-1}}^{\alpha}}}{\mathrm{b}} - \mathrm{f_{DRV}}\cdot\rho_{\mathrm{i-1}}^{\alpha}\right) \tag{2.20}$$

where, $\mathrm{f_{DRV}}$ is an adjustable parameter related to the intensity of dynamic recovery processes ($\mathrm{f_{DRV}} = 1.2$)
$\mathrm{k_0}$ is a constant related to latent hardening

The law used to describe the behavior of polycrystalline pearlite is more empirical and makes the strong assumption that only the ferrite between the cementite lamellae deforms plastically. It was derived from the work of Dollar et al. (1988) and followed a Voce-type law as described in Eq. 2.21.

$$\sigma_{\mathrm{p}}(\varepsilon_{\mathrm{p}}) = \sigma_0^{\mathrm{p}} + \frac{\mathrm{M}\mu^{\alpha}\mathrm{b}}{s} + \frac{\mathrm{K}}{\mathrm{g}}\left(1 - \exp\left(-\frac{\mathrm{g}\varepsilon_{\mathrm{p}}}{2}\right)\right) + \theta^{\mathrm{IV}}\varepsilon_{\mathrm{p}} \tag{2.21}$$

where, s is the interlamellar spacing
K and g are two empirical constants (K=38 GPa, g=61.7)
θ^{IV} is the stage IV hardening of pearlite

The connection of ferrite and pearlite heterogeneous media was calculated by a classical mean field approach. The resultant stress (σ) was, respectively, the average value of the local stresses. Both mean values (σ_{p} and σ_{f}) were weighted with the respective fractions of the components (Eq. 2.22).

$$\sigma = (1 - f_{\mathrm{p}})\sigma_{\alpha}(\varepsilon_{\alpha}) + f_{\mathrm{p}}\sigma_{\mathrm{p}}(\varepsilon_{\mathrm{p}}) \tag{2.22}$$

The ISO-work localization law was proposed to describe the transfer of load and deformation between the components (Allain and Bouaziz 2008). This concept involves an equal dissipation of the plastic work in each of the phases (Eq. 2.23).

$$\sigma_{\alpha}(\varepsilon_{\alpha})\mathrm{d}\varepsilon_{\alpha} = \sigma_{\mathrm{p}}(\varepsilon_{\mathrm{p}})\mathrm{d}\varepsilon_{\mathrm{p}} \tag{2.23}$$

In the work of Allain and Bouaziz (2008), the friction stresses for ferrite and pearlite were considered as identical ($\sigma_0^{\mathrm{P}} = \sigma_0^{\alpha} = \sigma_0$), assuming the non-partition of substitutional elements between ferrite and austenite before pearlitic transformation. Within this framework, the equation of σ_0 could be expressed as dependent on materials composition taking into account the different solutes and interstitials in solid solution (Allain and Bouaziz 2008; Allain et al. 2009; Bui-Van et al. 2009). The contribution that the elements in solution have on the lattice friction was initially suggested by Pickering and Gladman (1963). This equation was adjusted by D'Eramo et al. (2017) to better reflect the influence of the solutes and is expressed in Eq 2.24 (concentrations are expressed in wt.%, $\sigma_{00} = 52\,\mathrm{MPa}$). The calculated friction stresses are summarized in Table 2.15.

$$\sigma_0 = \sigma_{00} + 33\mathrm{Mn} + 91\mathrm{Si} + 8\mathrm{Cu} + 4.5\mathrm{Ni} + 5230\mathrm{B} + 8\mathrm{Mo} + 4\mathrm{Al} \tag{2.24}$$

Table 2.15: Calculated σ_0 based on composition

	16MnCr5	27MnCr5	C45	C60
σ_0 (MPa)	145	135	123	128

Considering this friction stress data, the resultant flow stress curves were calculated for each of the FP steels. The comparison with the experimental curves is depicted in Figure 2.36 at the temperature of 20°C and 0.5 s^{-1} strain rate.

The model showed considerable accuracy when reproducing the experimental results. The modeled strain hardening reflected the behavior of almost all the FP steels, although some deviations were found on the C60 grade. These were mostly at strains

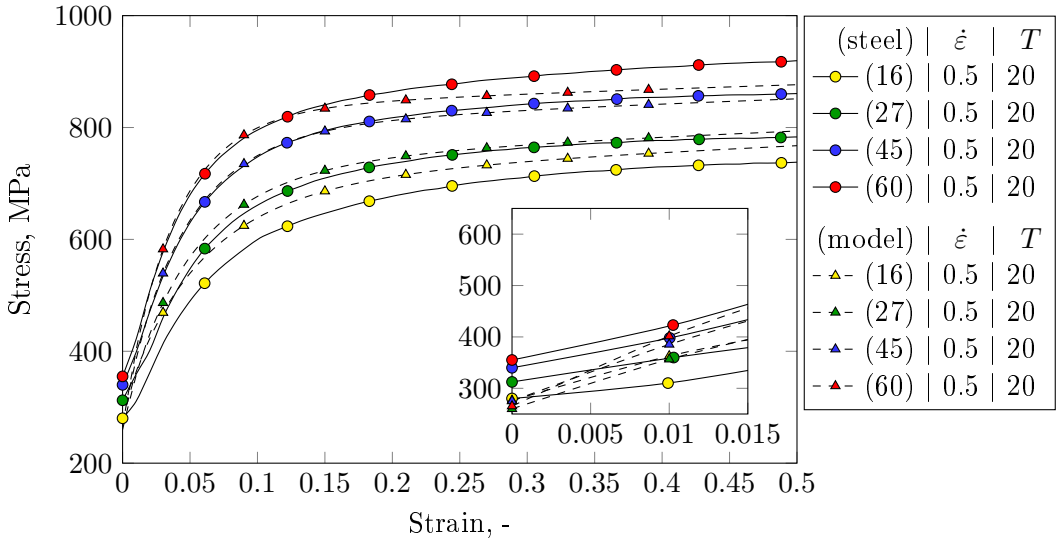

Figure 2.36: Comparison of predicted (dashed line) and experimental (solid line) flow stress curves at 20°C and 0.5 s^{-1}

over 0.2. As shown in the detail of the plot, the agreement was not exact for small deformations lower than 2%. Nevertheless the predictions showed good correlation above this strain.

The predicted UTS are compared with those of experiments in Table 2.16, which in turn presented good agreement. Results were almost the same for the 27MnCr5 and C45. The C60 steel presented a higher deviation due to the differences in the strain hardening, and the results for the 16MnCr5 where overestimated throughout the analyzed strain range. In spite of those deviations, however, the maximum error was less than 5%.

Table 2.16: Empirical and predicted UTS values with the proposed model

	Predicted UTS (MPa)	Empirical UTS (MPa)
16MnCr5	777	742
27MnCr5	802	785
C45	859	863
C60	883	926

In an in-depth analysis, the influence that each constituent, ferrite and pearlite, had on the resultant flow stress of the bulk material was checked for each of the FP steels (Figure 2.37). For example, for the C45 (f_{p}=75%) at a strain of 0.3 the contribution of ferrite was approximately 115 MPa and that of pearlite 715 MPa. In the case of the 16MnCr5 (f_{p}=42%) the influence of ferrite was half of that of pearlite. Considering the differences in pearlite ratio the materials had, results coincided with what was expected.

Therefore the proposed physical theory to model strain hardening was considered accurate. It should also be noted that it satisfied the initial objective of representing material behavior considering only with microstructural parameters. According to the established equations, the input parameters are material composition (in order to calculate lattice friction), interlamellar spacing (s), ferritic mean grain size (d_{α}) and pearlite fraction (f_{p}). The required parameters are summarized in Table 2.17 at the end of this section.

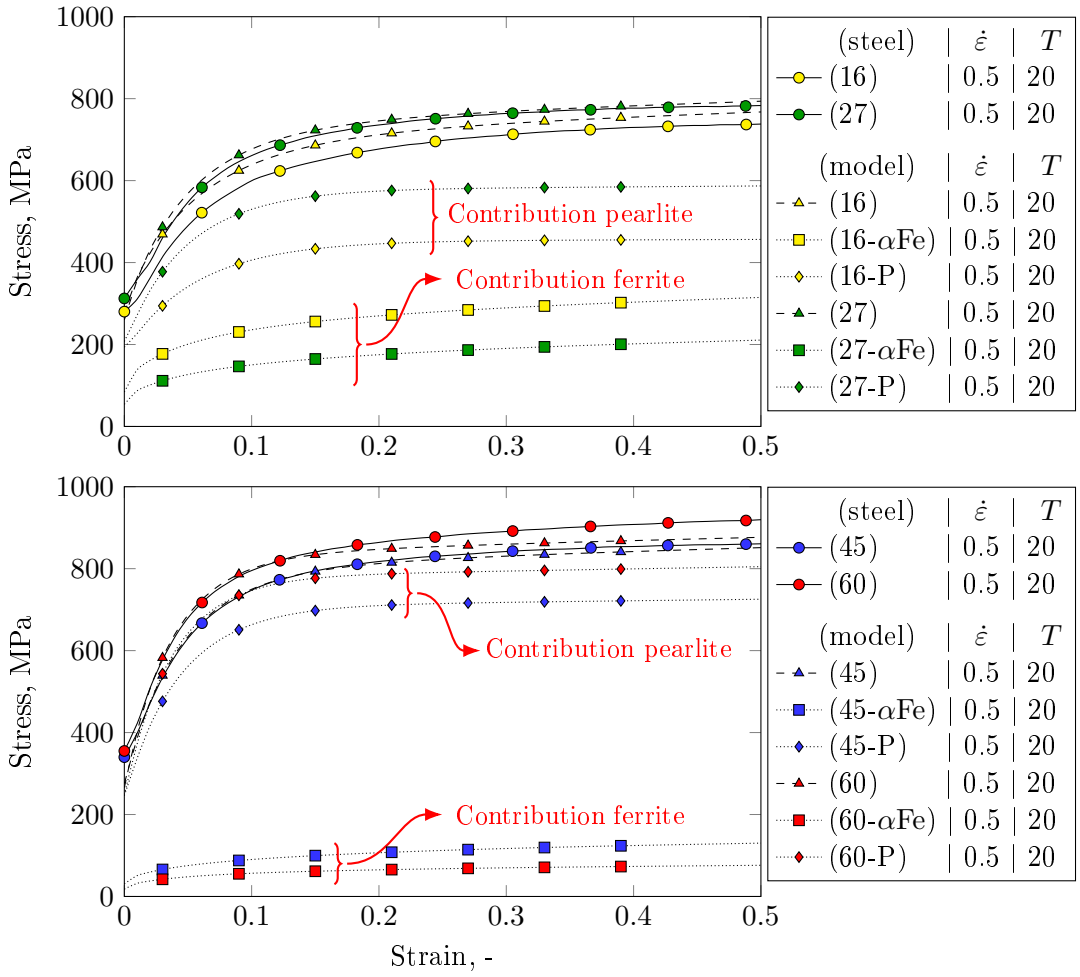

Figure 2.37: Comparison of predicted (dashed line) and experimental (solid line) flow stress curves at 20°C and 0.5 s^{-1}. Contribution of ferritic and pearlitic constituents (dotted line)

Thermal softening

Experimentally, the decrease in the flow stress as a result of temperature increase was observed at different strain rates (Figure 2.27 and Figure 2.28). At medium-to-low strain rates (0.5-50 s^{-1}) the yield stress decreased nonlinearly, presenting a higher drop at temperatures above 500°C. A similar behavior was modeled by Iturbe et al. (2017) for the case of Inconel 718. At high strain rates, DSA influenced the flow thermal softening. At an specific temperature, dependent on the strain rate, the material suffered a sudden hardening followed by a softening. As this usually occurs in the low strain levels (Wang et al. 2015), it was assumed that its influence in the performance of the machining model would be negligible.

With regards to the thermal softening equation, the analysis of Figure 2.34 clearly denoted that the linear decrease of stress with temperature rise presented in the JC model did not represent the real material behavior. Therefore, to consider the thermal

softening phenomenon as nonlinear, the exponential term proposed by Iturbe et al. (2017) was empirically adjusted to reproduce the experimental results. As described in the hypothesis at the beginning of this section, the same thermal softening was considered for all the FP steels. Thermal softening was governed by Eq. 2.25.

$$\sigma_{\mathrm{TS}}(T) = \frac{1}{1 + \mathrm{e}^{\mathrm{m}^*(T - \mathrm{B}^*)}} \tag{2.25}$$

The fitting of the empirical m^* and B^* parameters is described in Figure 2.38. The numerical values obtained are 0.00844 and $913.6^{\mathrm{o}}\mathrm{C}^{-1}$ respectively. The results demonstrated not only an accurate fitting but also that the softening did not differ much between steels, justifying the hypothesis of a unique σ_{TS} for all the materials.

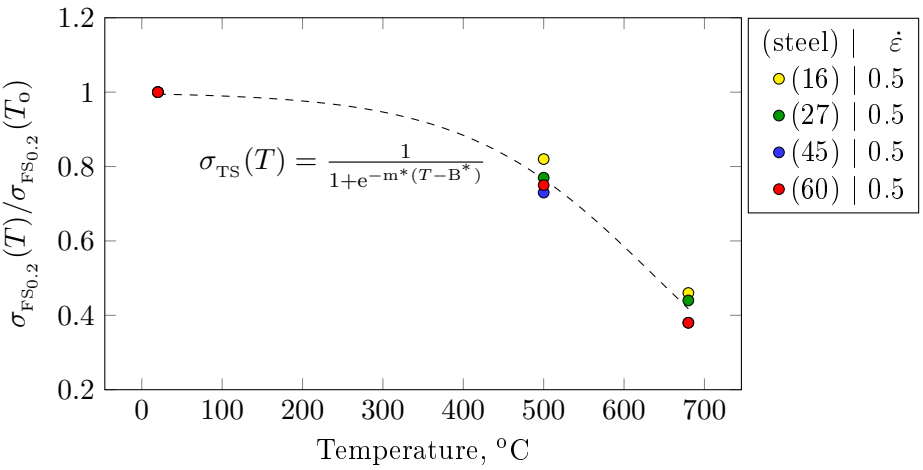

Figure 2.38: Characterization of the thermal softening term based on the flow stress at strain of 0.2 and strain rate of 0.5 s^{-1}

Figure 2.39 shows the comparison between the model and the experimental datasets after the fitting procedure. The proposed thermal softening greatly improves the JC model predictions. In the range of tested temperatures (available experimental data), the model reproduces the drop from 500 to $680^{\mathrm{o}}\mathrm{C}$ with a high degree of accuracy in all the materials. The error found in the C45 and C60 was negligible, however, for the 27MnCr5 and 16MnCr5 greater differences were observed. In the latter two, a maximum error of 12% was observed at $680^{\mathrm{o}}\mathrm{C}$. However, the deviations were lower than in the original study of Iturbe et al. (2017), and the accuracy of representing the thermal softening was considerably more accurate than in the JC model.

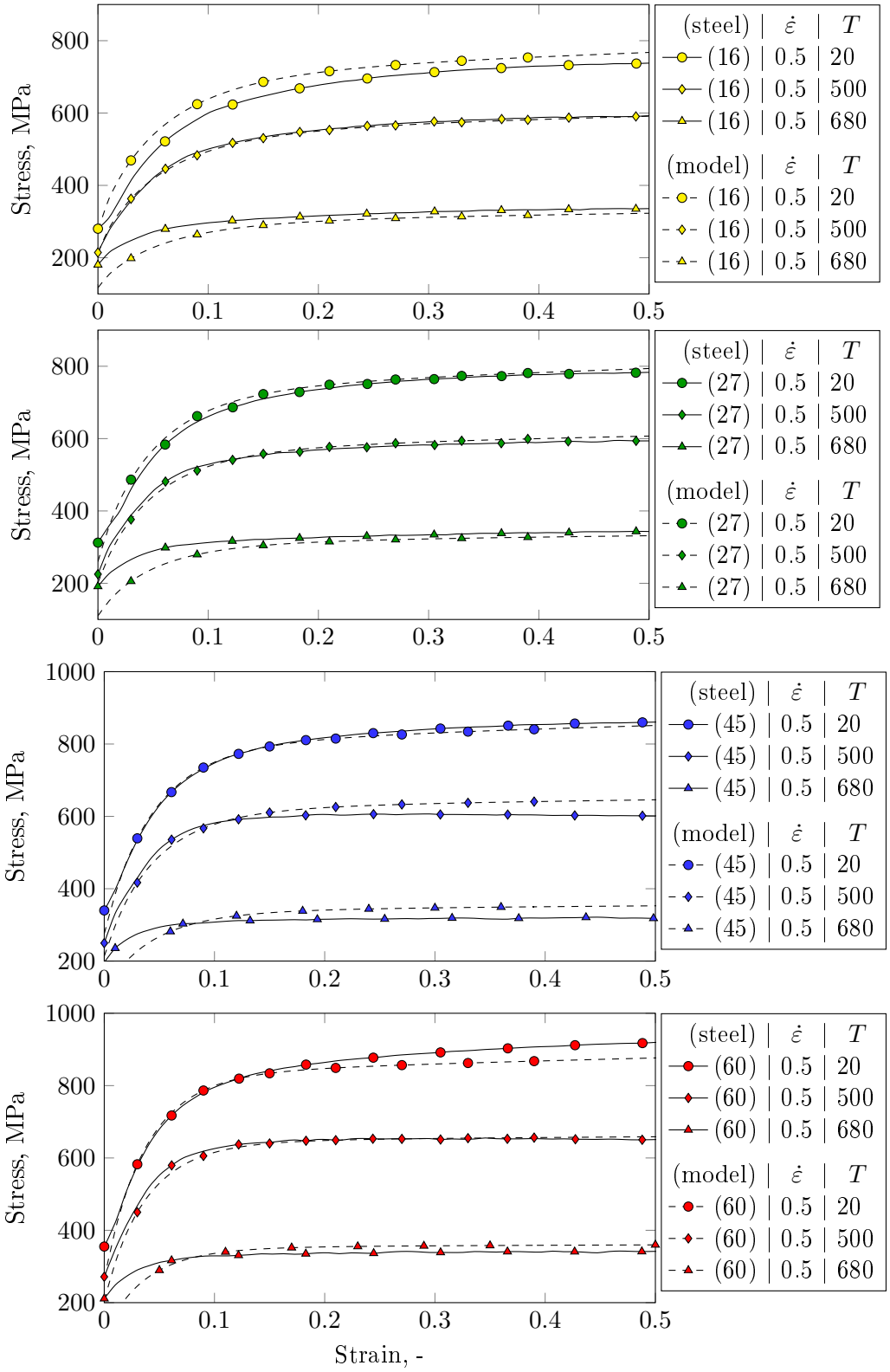

Figure 2.39: Comparison of predicted (dashed line) and experimental (solid line) flow stress curves at 20, 500 and 680°C and 0.5 s^{-1}.

Strain rate hardening

From the uniaxial compression tests carried out at different temperatures and strain rates, it was concluded that the influence of the strain rate on the flow behavior of the FP steels was temperature dependent. In the low temperature domain (T<500°C), the influence of the strain rate on the material strength was found to be lower than at higher temperatures (T>500°C). Therefore, the need for a model representing the coupling between strain rate and temperature was clear. The JC model does not take into account the coupling between temperature and strain rate, as demonstrated with the poor predictions depicted in Figure 2.35. Iturbe et al. (2017) proposed a coupled model for strain rate, where the sensitivity parameter was set as $C(T) = C{\cdot}D^T$. At first this model was taken as an example, but the results gave a non-realistic strain rate influence as $C(T)$ diverged to infinity at high temperatures (the increase of temperature generated a higher increase on the strain rate sensitivity rather than a thermal softening). Another characteristic of these cited models was the linear-logarithmic relation between the reference and the tested strain rate in terms of $\ln(\dot{\varepsilon}/\dot{\varepsilon_0})$. As is presented in the following lines, the analyzed FP steels presented a logarithmic relation of the type $\ln(\dot{\varepsilon}/\dot{\varepsilon_0})^{n^*}$.

Taking into account the abovementioned considerations, a new strain rate sensitivity equation was proposed. This was established with the following steps: (1) calibration of the exponential-logarithmic relation between strain rates and (2) development of the function relating the strain rate sensitivity to temperature. The proposed equation to represent the strain rate hardening is summarized in Eq. 2.26.

$$\sigma_{\mathrm{SRH}}(\dot{\varepsilon}, T) = 1 + C(T){\cdot}\ln\left(\frac{\dot{\varepsilon}}{\dot{\varepsilon_0}}\right)^{n^*} \tag{2.26}$$

The fitting procedure to characterize the strain rate hardening coefficient (n^*) was developed taking into account all the studied steels. The relation between the tested strain rate and the reference was established using the tests carried out at room temperature (20°C). The fitting described in Figure 2.40 obtained an exponent n^*=1.848, and demonstrated the exponential relationship between strain rates. Some slight differences were observed between grades, but these were disregarded as the obtained regression was close for all the FP steels.

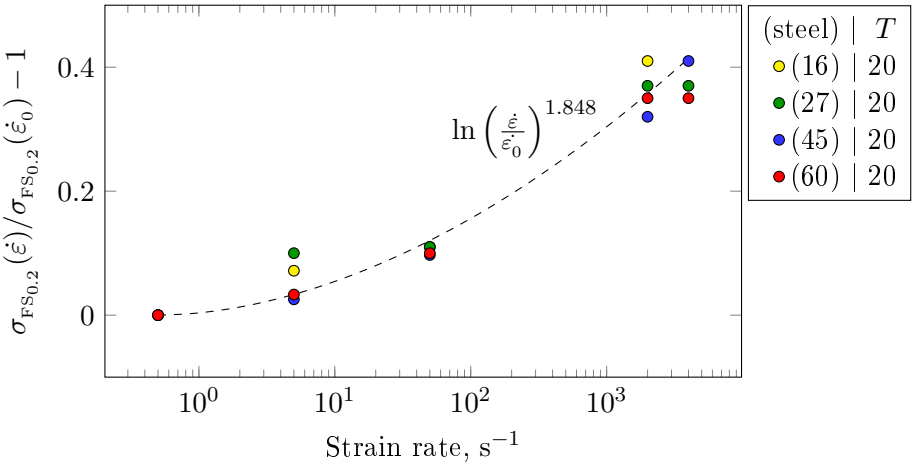

Figure 2.40: Characterization of the strain rate hardening exponent based on the yield stress at strain of 0.2 and temperature of 20°C

Once the strain rate hardening coefficient was calibrated, the next step consisted of determining the equation to couple the strain rate with temperature. The connection between strain rate hardening and temperature was modeled in terms of Eq. 2.27. For each FP steel, the SRH value was extracted for all temperatures and strain rate combinations. The resultant SRH plotted against temperature is shown in Figure 2.41 (note that only average values of SRH at each temperature are plotted).

$$\text{SRH} = \frac{\sigma_{FS_{0.2}}(\dot{\varepsilon})/\sigma_{FS_{0.2}}(\dot{\varepsilon}_0) - 1}{\ln\left(\frac{\dot{\varepsilon}}{\dot{\varepsilon}_0}\right)^{1.848}} \tag{2.27}$$

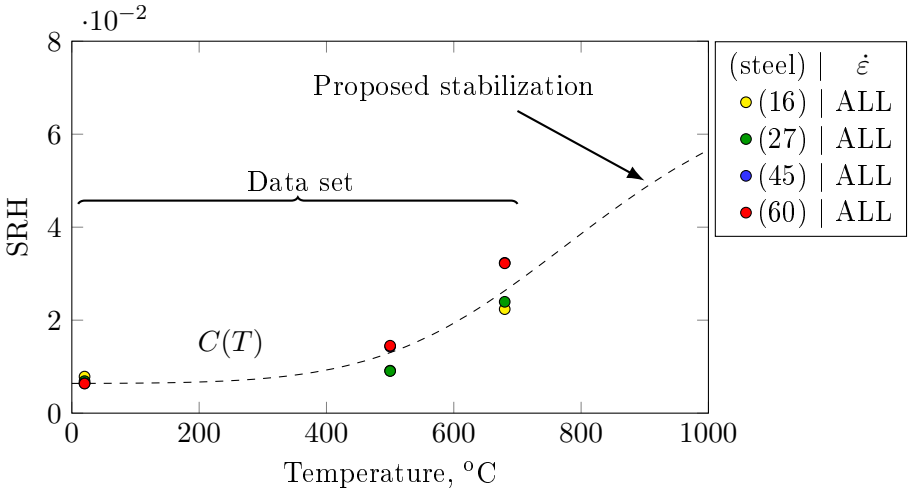

Figure 2.41: Characterization of the relationship between strain hardening term and temperature based on the yield stress at strain of 0.2 and related with $\ln(\dot{\varepsilon}/\dot{\varepsilon}_0)^{1.848}$

The empirically fitted equation $C(T)$ was divided into two sections. The first reproduced the experimental data set. The second part was the proposed stabilization of the influence that temperature had on the strain rate, which introduced a constant slope on the fitted curve. The latter was necessary, according to the preliminary results obtained when testing the exponential equation proposed by Iturbe et al. (2017). As a consequence of this extrapolation, the influence that temperature had on strain rate hardening did not diverge to infinity, and therefore overcome the thermal softening. $C(T)$ was calculated using Eq. 2.28.

$$C(T) = \mathrm{S}^{*} + \frac{\mathrm{D}^{*} - \mathrm{S}^{*}}{1 + \left(\frac{T}{\mathrm{T_{sat}}}\right)^{\mathrm{r}}} \tag{2.28}$$

where, S^{*} is an empirical constant (0.076)
D^{*} is an empirical constant (0.0064)
r is a temperature related exponent (6.4)
$\mathrm{T_{sat}}$ is the saturation temperature in absolute values (1108 K)
T is the testing temperature in absolute values

The performance of the model was evaluated with the four selected FP steels. The predictions are plotted against the experiments in Figure 2.42 for the temperatures of 20 and 680°C, and strain rates of 5 and 4000 s^{-1}. The agreement between experimental results and modeled behavior showed a high degree of accuracy for the C45 and C60, obtaining nearly the same results across the temperature and strain rate range. Only at the beginning of the curves did some deviations occur, where in some cases a lower yield stress was predicted. The predictions of the 27MnCr5 were more precise at high strain rates than at lower. This could be linked to the established logarithmic relation between strain rates, as some deviations can be observed in Figure 2.40 at the rate of 5 s^{-1}. Nevertheless, the differences were about 10%. The performance of the 16MnCr5 revealed a high deviation at 4000 s^{-1} and 20°C. In particular, this experimental condition presented a higher than expected strength, achieving higher stress values than the 27MnCr5. Therefore, it seemed reasonable to have such differences in the case of 16MnCr5. For the other conditions, the tendencies were similar to the 27MnCr5. Based on these results, the proposed approach assessed the objectives of representing the behavior of FP steels at high strains and high temperatures.

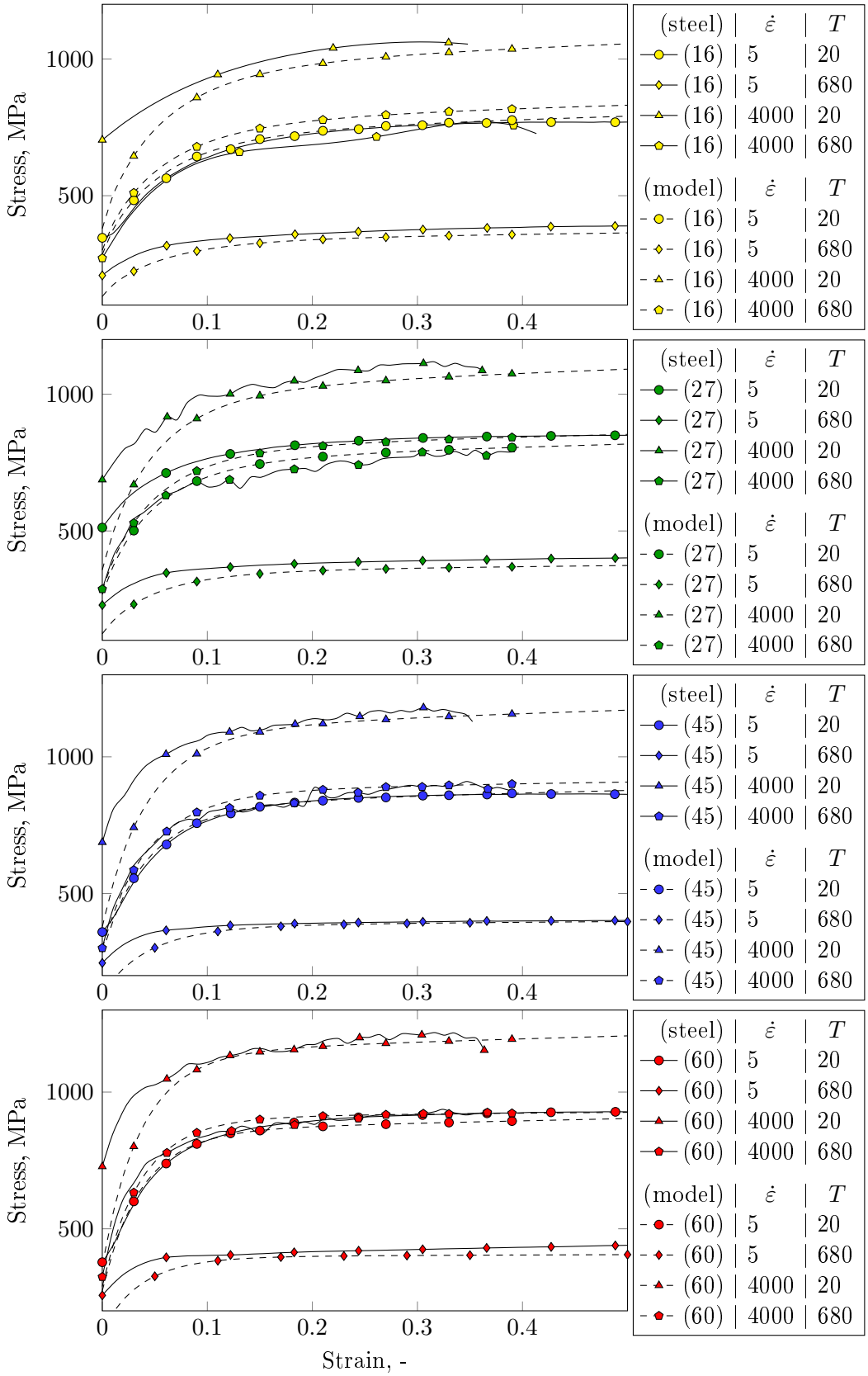

Figure 2.42: Comparison of predicted (dashed line) and experimental (solid line) flow stress curves at temperatures of 20 and 680°C and strain rates of 5 and 4000 s^{-1}.

Table 2.17: Proposed parameters of MSB model. Parameters of strain hardening term are obtained from Allain and Bouaziz (2008) and D'Eramo et al. (2017)

Parameters of strain hardening term			
μ_α	Shear modulus of ferrite	MPa	80000
M	Taylor factor		3
b	Burgers vector	m	$2.5x10^{-10}$
α_n	Forest hardening		0.4
f_{DRV}	Dynamic recovery		1.2
k_0	Latent hardening		$5.63x10^{-3}$
n_0	Critical density of GND		2.82
λ_d	Density of shear bands	b	34.5
K	Empirical parameter (pearlite)	MPa	22000
g	Empirical parameter (pearlite)		61.7
θ^{IV}	Stage IV hardening (pearlite)		100
Parameters of thermal softening term			
m^*	Temperature sensitivity exponent		0.0084
B^*	Thermal sensitivity coefficient	$^oC^{-1}$	913.6
Parameters of strain rate hardening term			
S^*	Empirical constant		0.076
D^*	Empirical constant		0.0064
r	Temperature related exponent		6.4
T_{sat}	Saturation temperature		1108 K

2.6.3 Conclusions of the MicroStructure Based model

Using the rheological and microstructural study of the four FP steels, a new flow stress model was proposed. The model described the particular behavior of FP steels based on microstructure properties, at conditions of high temperature and strain rate.

The model introduces strain hardening behavior as a function of the pearlite ratio, interlamellar spacing and ferritic grain size. The composition of the material allows the calculation of the lattice friction of ferrite. Once these are characterized, the behavior of FP steels with lamellar type pearlitic grains can be modeled. However, in the development of the model it must be noted that some hypotheses were made. The most significant of which is that only the ferrite between the cementite lamellae deforms plastically.

Thermal softening and strain rate hardening were considered identical for both ferrite and pearlite constituents. For this reason, a non-linear thermal softening was modeled to represent the macroscopic behavior of FP steels. The coupling between strain rate and temperature was also introduced, represented by a temperature dependent formulation. The multiplicative effect that thermal softening and strain rate hardening had on the resultant yield behavior for each temperature and strain rate condition is repre-

sented in Figure 2.43. The figure shows that at strain rates below $10^4\,s^{-1}$ the increase in temperature generates a softening of the material. This softening is divided into two steps. Initially a slight lowering occurs, followed by a dip in the material strength over 500°C. When the material is subjected to strain rates over $10^4\,s^{-1}$, at temperatures below 500°C a slight hardening of the material occurs with the temperature increase, followed by a sudden drop on material strength. This hardening can be linked to thermal softening fighting against the increase in strain rate as a result of temperature. In the temperature range of 400-600°C, material is mostly hardened by the high strain rates rather than thermally softened. In the majority of cases, prediction matched experimental data sets of all the FP steels, and presented a maximum error in the range of 10-12%.

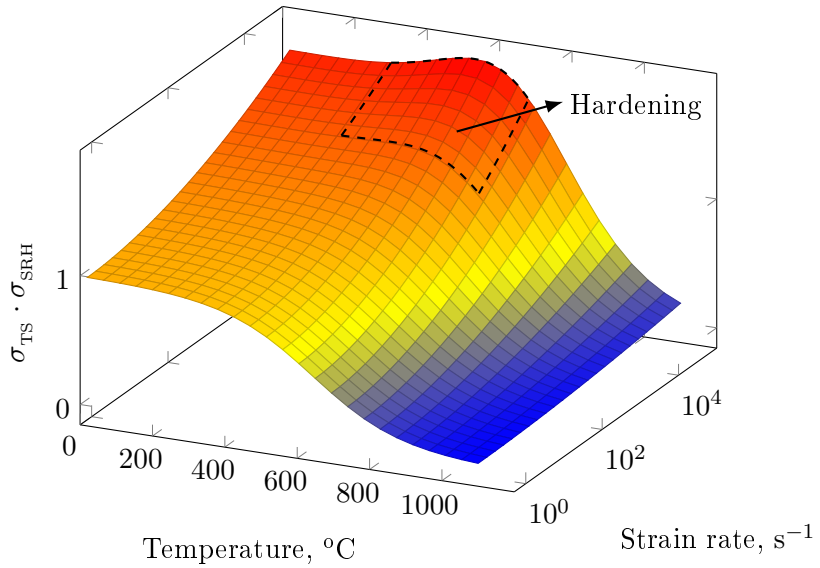

Figure 2.43: Multiplicative effect of thermal softening and strain rate hardening

2.7 Conclusions of the chapter

In this chapter, 16MnCr5, 27MnCr5, C45 and C60 steels were microstructurally and mechanically characterized. A comprehensive experimental study of the rheology of these ferrite-pearlite steels was conducted over a wide range of temperatures and strain rates, characteristic of machining processes. The flow stress behavior was reproduced by the microstructure based model. The conclusions derived from this chapter are listed below:

- The steels were selected to cover wide range of microstructure variants. The main differences in microstructures were found to be the ferrite-pearlite ratio, grain size, and interlamellar spacing. A range of 42% to 85% of pearlite was measured in the steels, which was directly linked with the carbon content of the

grades. The steels were well differentiated by means of the pearlitic grain size. 16MnCr5 and 27MnCr5 presented small pearlitic grains of 13-15 μm, while measurements of C45 an C60 gave values between 22-31 μm. Ferritic grain size did not show such variations, with values in the range of 10-17 μm. The interlamellar spacing of pearlite was the most challenging property to be established for two reasons. First, large deviations were found in the results, as a consequence of the high variations found when measuring different grains of each material. Secondly, noticeable differences appeared between grades. 16MnCr5 had an average interlamellar distance of 190 nm, while that of the C60 was nearly double. The latter presented the highest deviations of all the tested samples. The measurements on 27MnCr5 and C45 were situated in the mid-range, with 285 and 293 nm respectively.

- Identified thermal properties did not represent remarkable variations between the FP steels. Only the calculated conductivity of 16MnCr5 was found to be 50-60% higher, a direct effect of the greater diffusivity this steel presented. However, the obtained results gave some information about the physics that occur at the microstructure level. Density decreased together with temperature, but at around 700-800°C a sudden increase occurred in all the steels. This was attributed to an austenitic phase transformation, which was confirmed by the specific heat measurements. This presented severe instabilities in the abovementioned temperature domain, related to the energy absorbed or released when the magnetic properties of constituents vary. With regards to the thermal properties of the carbide H13A, it is worth highlighting that thermal conductivity drops by 90% when temperature is increased from 0 to 800°C. Thermal conductivity varies from 112 to 17 $W \cdot m^{-1} \cdot K^{-1}$.

- From the reported mechanical characteristics, it is important to note that no hardness differences were found between 16MnCr5 and 27MnCr5 (162-163 HB), and between C45 and C60 (185-188 HB) despite the differences in percentage of pearlite.

- Rheology results gave important knowledge about the flow characteristics of the analyzed steels. In general, the flow stress behavior was in agreement with what was expected. The steels with higher carbon content performed with higher flow strength, therefore presenting higher yield stress and ultimate tensile strength. In all the samples, 500°C was identified as the critical temperature at which the mechanical properties of these FP steels significantly reduce. Above this temperature, thermal softening was found to be more severe. However, this occurred only at the medium-to-low strain rates (0.5-50 s^{-1}). The flow behavior at high strain rates (2000-4000 s^{-1}) demonstrated that the selected steels were affected by DSA. This caused a sudden hardening of material at some specific temperatures, related to the pinning of dislocations arrested at obstacles during their motion. Regarding the influence of strain rate on material hardening, this was found to be more significant at the high temperature domain.

- Based on these mechanical characterization tests, a new material constitutive model was proposed to represent the behavior of FP steels. The strain hardening behavior was modeled as function of the microstructure parameters of pearlite fraction, interlamellar spacing and ferritic mean grain size. Thermal softening as well as the coupling between the temperature and the strain rate were also introduced, as they are known to occur experimentally. The proposed material constitutive model showed significant improvement in terms of flow stress prediction compared to the widely employed conventional JC model (Johnson and Cook 1983; Abouridouane et al. 2012).

Chapter 3

Orthogonal cutting tests: Analysis of tool wear and fundamental variables

Considering the significant influence that the microstructure of steel has on machinability, this chapter intends to expand the knowledge base of this subject based on purpose designed experimental tests. Specific tests were designed for the development of a wear rate law that represented the wear behavior of FP steels, and to obtain the required empirical data sets for the validation of the FE model described in Chapter 4 (Figure 3.1). The findings from this experimental procedure were also employed in the understanding of the machinability of FP steels in terms of material microstructure, tool wear, and the evolution that fundamental variables undergo with tool wear. To accomplish this abovementioned, two advanced setups were designed, one focused on the orthogonal cutting process and the other on obtaining realistic tool temperatures without the need to characterize the emissivity of the tool.

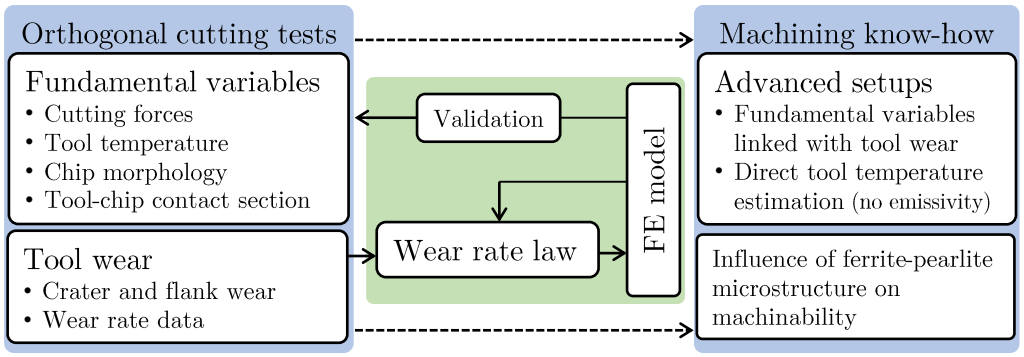

Figure 3.1: Flowchart of the chapter

This chapter is divided into two main sections. First a literature review sets out the fundamentals of machining processes, and the influence that ferrite-pearlite microstructures have on machinability. Secondly, the developed work and main conclusions are described.

3.1 Literature review: Machining fundamentals and machinability of ferrite-pearlite steels

The first section of the literature review examines the fundamentals of the process itself, where simplistic orthogonal cutting is analyzed. Taking as example this cutting procedure, the main physics of the process are explained in terms of material deformation behavior, heat generation and heat partition, pressures and cutting forces. Once these abovementioned fundamental or scientific variables are detailed, the industrial relevant outcomes are enumerated. With regards to the scope of the research, the different tool wear modes and mechanisms are summarized.

In the second section of the review, the influence that ferrite-pearlite steels have on machinability is presented. Based on the knowledge acquired in the first section, the fundamental variables and the tool wear are analyzed in terms of alloying elements and ferritic-pearlitic microstructure.

3.1.1 The orthogonal cutting process

All metal-cutting operations can be likened to the process shown in Figure 3.2, where the tool is constrained to move relative to the workpiece in such a way that a layer of metal is removed in the form of a chip (Boothroyd 1988). A special case of cutting, where the cutting edge of the tool is arranged to be perpendicular to the direction of relative work-tool motion is known as orthogonal cutting. It is described as the "ideal" model of machining, and represents a two-dimensional rather than a three-dimensional problem. Therefore, it lends itself to research investigations where it is desirable to eliminate as many of the independent variables as possible. A process can be determined as orthogonal once it follows the set out below (Shaw and Cookson 2005):

- Plane strain criteria: The chip does not flow towards the sides of the thickness (edge effect), and the width of material and workpiece are assumed to be infinite.
- The undeformed chip thickness (or feed) is constant throughout the entire process.
- The deformation is homogeneous along the material thickness.
- The cutting speed is perpendicular to the cutting edge.

- The process is isolated from the third dimension, and thus the passive force or penetration force is annulled.

In Figure 3.2 an orthogonal cutting diagram with the geometric parameters of the tool and workpiece is observed. The wedge-shaped cutting tool consists of two surfaces intersecting to form the cutting edge. The surface along which the chip flows is known as the rake face, and the surface on the back is known as the flank face. The depth of the material to be removed by the action of the tool is named as the undeformed chip thickness, or in the specific case of orthogonal cutting could be called the feed. In the industrial market several types of rake face geometries can be found, which are commonly designed with chip breakers in order to prevent continuous chip formation.

The angle between the rake face and the line perpendicular to the workpiece surface is known as the rake angle. This angle can be positive (as shown in Figure 3.2) or negative (opposite direction as the one represented in the figure) depending on the requirements of the process. The rake angle is one of the most important variables in metal cutting (Boothroyd 1988). Increasing the rake angle usually involves a reduction in forces, however this reduces the area of the tool edge and tool life can be affected. The tool flank face is not directly involved in the process of chip removal, but the angle it forms with the line parallel to the workpiece surface (relieve angle) plays a part in the contact friction between tool and workpiece. Its minimum value must be set not to make contact with the machined surface of the workpiece, and should not be increased in such a manner that tool life is compromised. Commonly found relieve angles are

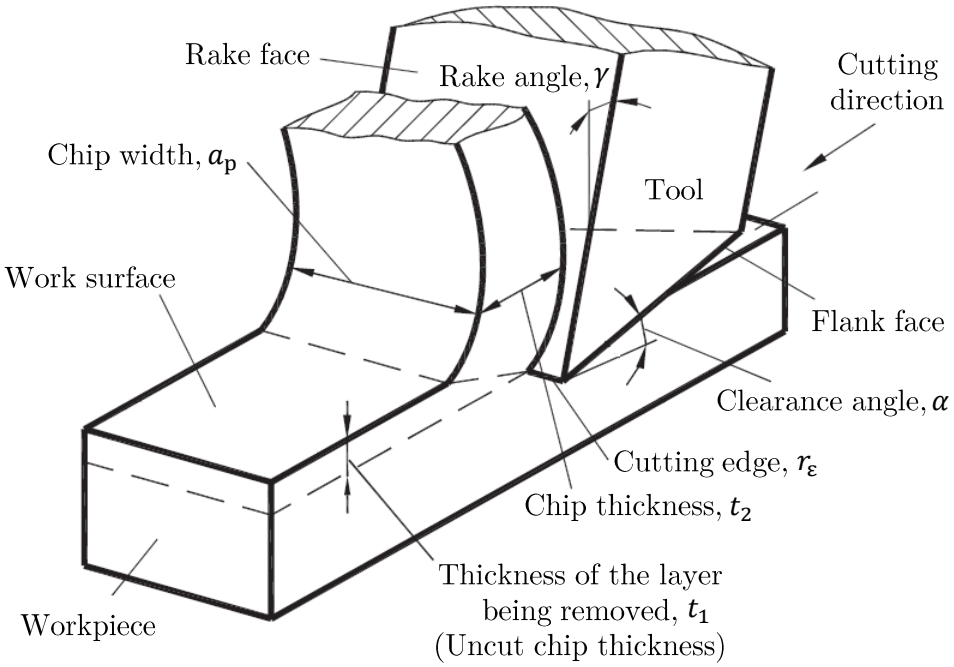

Figure 3.2: Schematic representation of orthogonal cutting

in the range of 5-6°. The cutting edge, which is a rounded edge in the intersection between the rake and flank faces, is also determinant in the cutting operation. A sharp cutting edge can contribute to reduce the feed or passive forces acting on the tool, but in contrast may reduce the tool life as the stresses are concentrated in a smaller region (Trent and Wright 2000). In addition, it is known to have significant influence in the surface integrity of the machined components (Pawade et al. 2008).

3.1.2 The physics of the orthogonal cutting process

In the machining process the material is subjected to severe thermomechanic conditions localized in three shear zones, in which deformations of up to 400%, deformation rates of 10^5 s^{-1} and temperatures up to 1000°C can occur (Merchant 1944; Oxley and Young 1989). Figure 3.3 shows in detail the abovementioned shear zones.

The primary (PSZ) and secondary shear zones (SSZ) generate high pressures on the material and tool. The strains generated in the primary zone are caused by the shearing effects when dividing the material, and are around 100-200%. In the secondary zone the effect of the strain is caused by the intense friction between the rake face and the chip. It is the zone of maximum strain, reaching values of up to 200-400%. The tertiary shear zone (TSZ) is caused by the interaction between the cutting edge and the machined material. Deformation values of 50-100% can be reached in the machined surface of the workpiece, which are enlarged in conjunction with the increase in flank wear (Oxley and Young 1989).

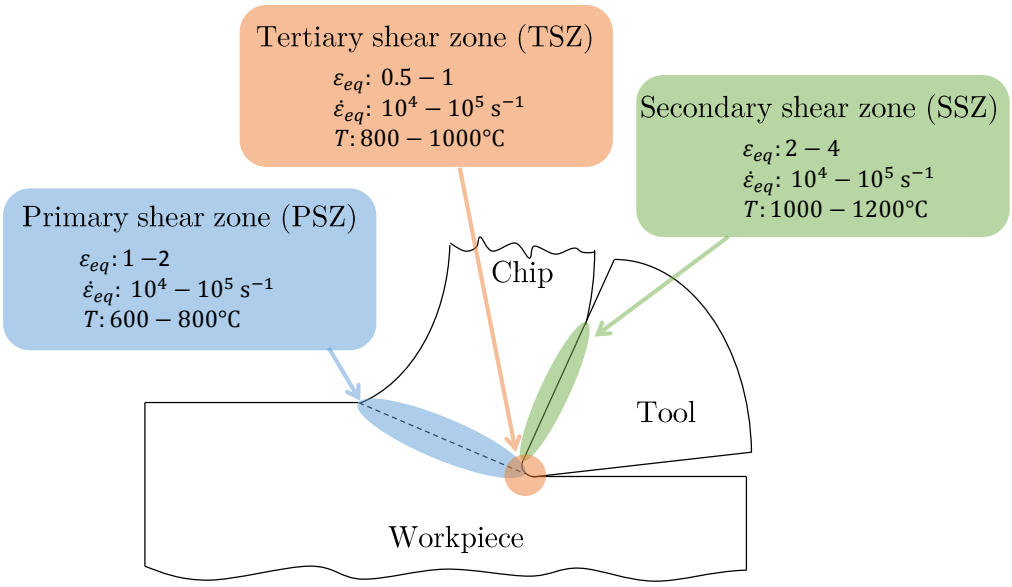

Figure 3.3: Schematic representation and physics of the shear zones, adapted from Oxley and Young (1989)

The strain rates during the machining process can reach values of $10^4 - 10^5\,s^{-1}$. These are usually maximum in the TSZ due to the stagnation-sliding transition occurring in this region. When the material is flowing at the height of the uncut chip thickness and reaches the cutting edge, it suffers a sudden stagnation in which the sliding velocity relative to the tool becomes null. After that, the particle of material that goes to the workpiece begins to slide until reaching again a relative velocity equal to the cutting speed (Hamann et al. 1994). The high strain rates and strains found in this TSZ are a consequence of this stagnation-sliding effect.

The rate of temperature increase during the process is worth noting, and can reach values of 10^5-10^6 $^oC{\cdot}s^{-1}$. For example, when cutting at 300 $m{\cdot}min^{-1}$ (i.e. 5 $m{\cdot}s^{-1}$), 5 mm are run in a millisecond. Along this 5 mm length of cut, the temperature of the material rises from room temperature to 500°C, taking as an example the average temperatures that can be found in the PSZ. This temperature increase involves heat rates of $5{\cdot}10^5$ $^oC{\cdot}s^{-1}$. The influence of these thermo-mechanical loads can generate differences between the bulk material and the material that makes contact with the tool (Courbon et al. 2014), or even affect the machined surface of the component (Ulutan and Ozel 2011).

Heat in the machining processes

Almost all the mechanical energies generated in the cutting process are transformed into heat (Coromant 1994). These are mainly generated by two physical phenomena: plastic deformation and friction. The heat generated in the PSZ is due to the plastic work done by shearing the material. In the SSZ the heat is caused by the plastic-work and by the friction in the tool-chip interface. Finally, the heat in the TSZ, which is located in the interface tool-workpiece, is formed by the friction existing in this area and increases together the wear on the flank face.

Concerning the heat transfer (Figure 3.4), the heat during the process is largely evacuated by the chip, with values around 80%. Another 10% approximately is evacuated through the workpiece and the remaining is transferred to the tool (Kronenberg 1966). Childs (2000) concluded that the amount of heat transferred to the tool had a strong dependence on the thermal number (or Pecklet number) and the ratio between tool and work conductivity $K^* = K_{tool}/K_{work}$. Based on this theory, Soler et al. (2015b) published that about 7-10% of friction heat flows into the tool when machining an AISI 4140 alloy at a cutting speed of 200 $m{\cdot}min^{-1}$ and 0.2 mm feed. In general, is of high interest a rapid evacuation of the heat from the cutting area in order to decrease the temperature in the contact zone and avoid wear.

The temperature in the cutting zone depends on the contact between the chip and tool, the magnitude of the shearing forces and the type of friction between the workpiece and the tool material (Shi et al. 2002). Figure 3.5 shows the thermal distribution of a low carbon steel alloy machined with an M34 high speed steel insert at a cutting speed of

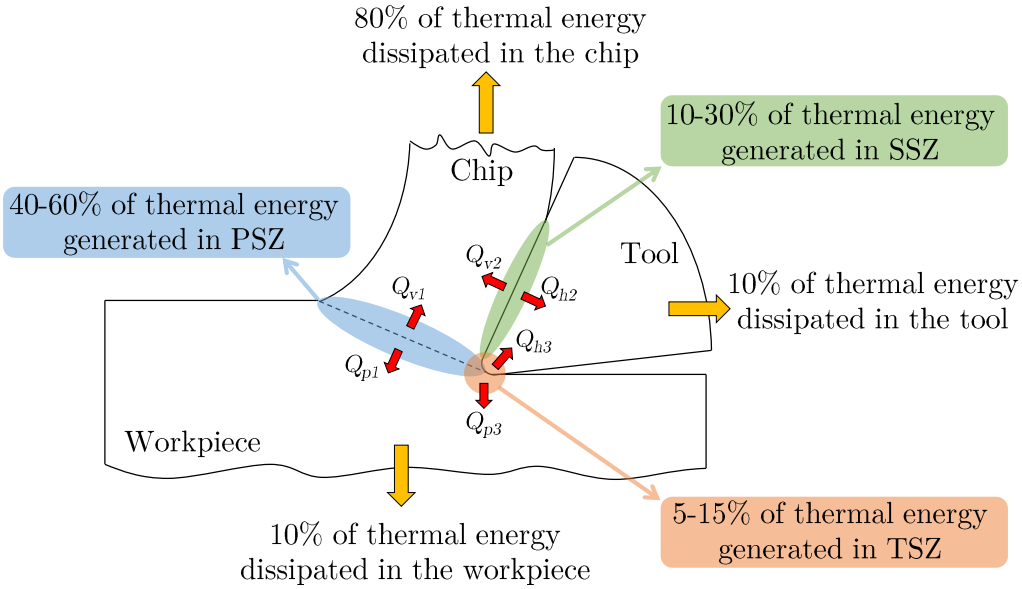

Figure 3.4: Schematic representation of heat generation and distribution in the shear zones (Kronenberg 1966)

180 m·min^{-1} and a feed of 0.25 mm. The figure shows that the SSZ, in which the shear effects are more severe, is where higher thermal concentration is generated. This was tested experimentally by analyzing the microstructure variations in high speed steel (Trent and Wright 2000).

Kurimoto et al. (1982) machined a low-alloy engineering steel using a cemented carbide tool over a range of speeds and feeds. They recorded the maximum rake face temperature with the use of a thermocouple inserted in the carbide. Figure 3.6 shows the temperature plotted against cutting speed for three different values of feed. Results indicate an increase in temperature with increments in speed and feed. Temperatures over 1000°C were recorded for speeds of 120 m·min^{-1} and above, conditions commonly used in industry.

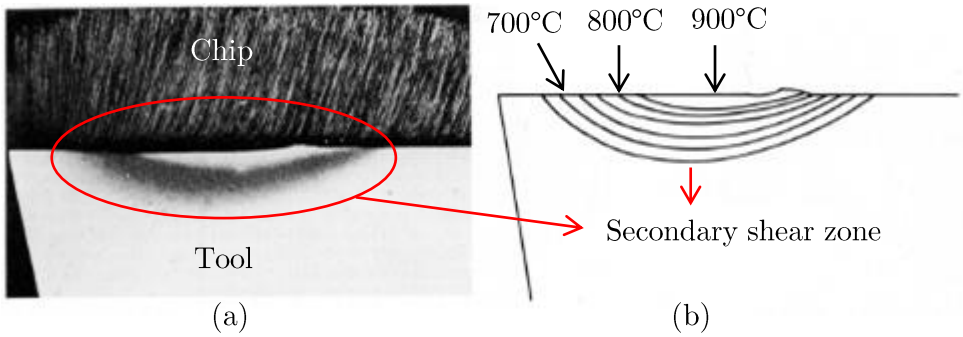

Figure 3.5: a) Experimental view of thermally affected zone. b) Thermal contours extracted from microstructure analysis (Trent and Wright 2000)

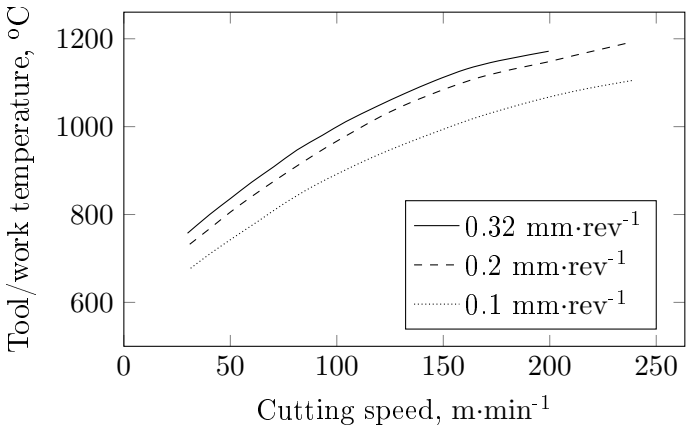

Figure 3.6: Tool temperature (tool/work thermocouple) when machining a low alloy engineering steel (Trent and Wright 2000)

At the time of writing other advanced set-ups were gaining relevancy in the field of machining. Armendia et al. (2010) and Arrazola et al. (2008) recorded tool temperatures when machining materials such as Ti6Al4V and AISI 4140 alloys with the use of thermal infrared (IR) cameras. In their experiments, a flat surface for radiation measurement was ground on the edge of each insert perpendicular to the optical axis of the IR camera. This flat surface was situated at distance shorter than 1 mm from the initiation of the tool-chip contact area. Arrazola et al. (2008) obtained the higher tool side temperatures in the tool-chip interface (see Figure 3.7-a), which was in line with the statements of Trent and Wright (2000). They also confirmed that increasing the cutting speed and the feed when machining an AISI 4140 alloy caused an increase in temperature. In detail, when the cutting speed was increased from 100 to 300 m·min^{-1} the tool side temperature varied from 650 to 800°C, and increasing the feed from 0.1 to 0.3 mm resulted in a variation from 650 to 875°C. Tool side temperature seemed to be slightly more sensitive to feed variation than to cutting speed, contrary to that measured by Trent and Wright (2000) with the thermocouple method. This measured tool side temperatures can also be transformed to those in the contact section between chip and tool based on analytical theories of heat transfer (Soler et al. 2015b).

In a further study, Arrazola et al. (2015) recorded tool rake face temperatures during orthogonal cutting of the abovementioned alloys. They followed the same procedure as in their previous publication, but in this case the optical axis of the IR camera was pointing over the rake face. Circumferential slots were cut in the orthogonal tube, so that the rake face became visible each time the cut was interrupted. In the analysis of contact temperature when machining AISI 4140, they observed that the temperature variation from mid to edge of contact increased together with cutting speed and feed (see Figure 3.7-b). These experiments showed that tool side face temperature was less than the maximum contact temperature by an amount increasing from 120 to 380°C.

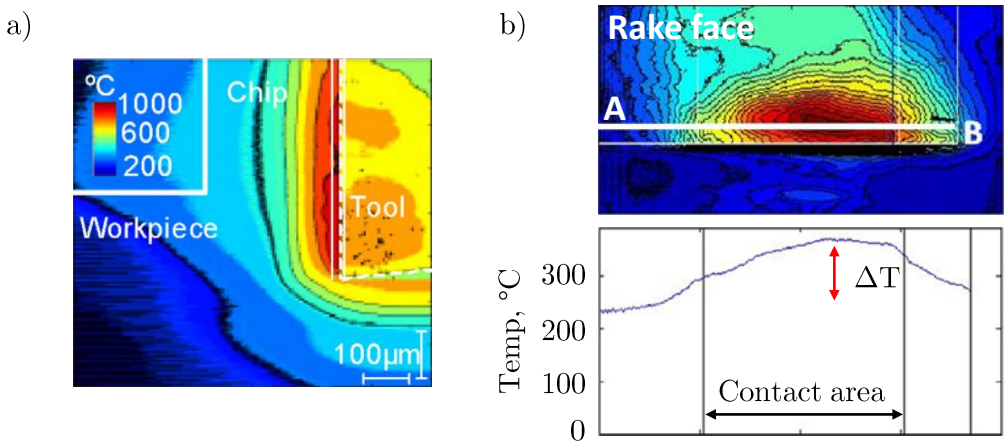

Figure 3.7: a) Thermal tool side maps when cutting AISI 4140 at 400 m·min^{-1} and 0.2 mm b) Infrared rake face image and radiation temperature along AB when cutting AISI 4140 at 75 m·min^{-1} and 0.1 mm (Arrazola et al. 2015)

Pressures and cutting forces

Two main forces are differentiated in the orthogonal cutting process: cutting force and feed force (see Figure 3.8-a). Both forces are generated by the intense friction and pressures on the contact faces. The pressures applied on the rake and flank face, together with the cutting edge, are mainly compressive with values that can be around 2GPa. Shear stresses due to friction also appear on the contact surfaces. The pressure is maximal in the region of the cutting edge and is reduced as it advances in the direction of the rake face. The normal pressure generated on the rake face and the shear forces on the flank face are directly related to the cutting force. These reactions in turn are linked to the shearing of the material in the primary shear zone. The feed force is related to the shear stress at the rake face and the normal pressure on the flank face. The cutting edge has a great influence on the distribution of cutting and feed forces. Its influence on the feed force is more noticeable the bigger the cutting edge radius is, and also with the increase in flank wear (Albrecht 1960).

Figure 3.8-a shows a diagram of the stresses at the cutting edge, where the reaction generated is caused by the shear and compressive effects of the material. Figure 3.8-b shows the area of adhesion and sliding of the chip, and its subsequent relationship with the compressive and shear stresses on the rake face.

Pressures, and the resulting cutting forces, are influenced by the workpiece material, tool geometry and the selected cutting conditions. The influence that FP steels have on cutting forces is analyzed in Section 3.1.4. An analysis of the literature related to the force/cutting speed curves shows that for nearly all metals a decrease in both F_c and F_f occurs when cutting speed is increased. This is usually more significant in the low speed range (Figure 3.9-a). This drop in forces is partially caused by a decrease in the tool-chip contact area and by a drop in shear strength in the flow-zone, as the

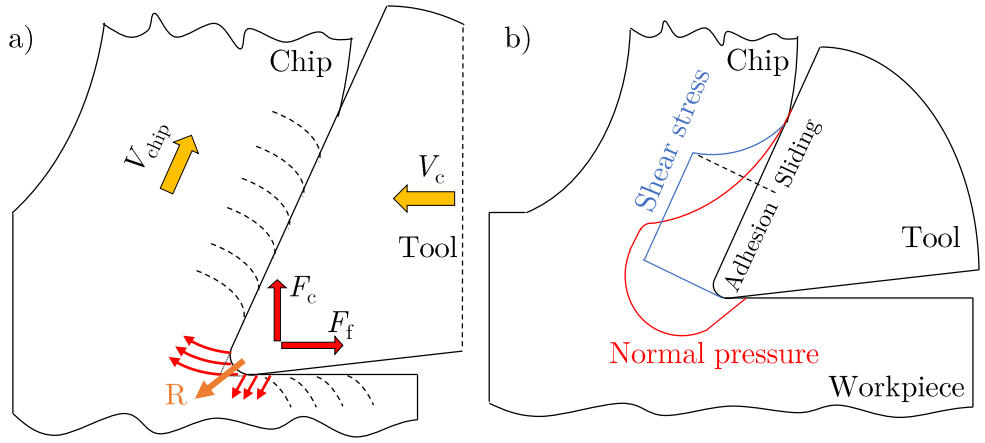

Figure 3.8: a) Reaction forces in the cutting edge, adapted from Albrecht (1960) b) Stresses in the contact surfaces, adapted from Trent and Wright (2000)

temperature of the workpiece rises with increasing speed (Trent and Wright 2000). Increasing the uncut chip thickness directly drives an increase of F_c and F_f, as the area of work material perpendicular to the direction of motion increases. Concerning the tool geometry, the influence of the rake angle is worth noting. As shown in Figure 3.9-b, increasing the rake angle lowers both the cutting force and feed force, but reduces the strength of the tool edge, which may lead to edge fracture (Trent and Wright 2000).

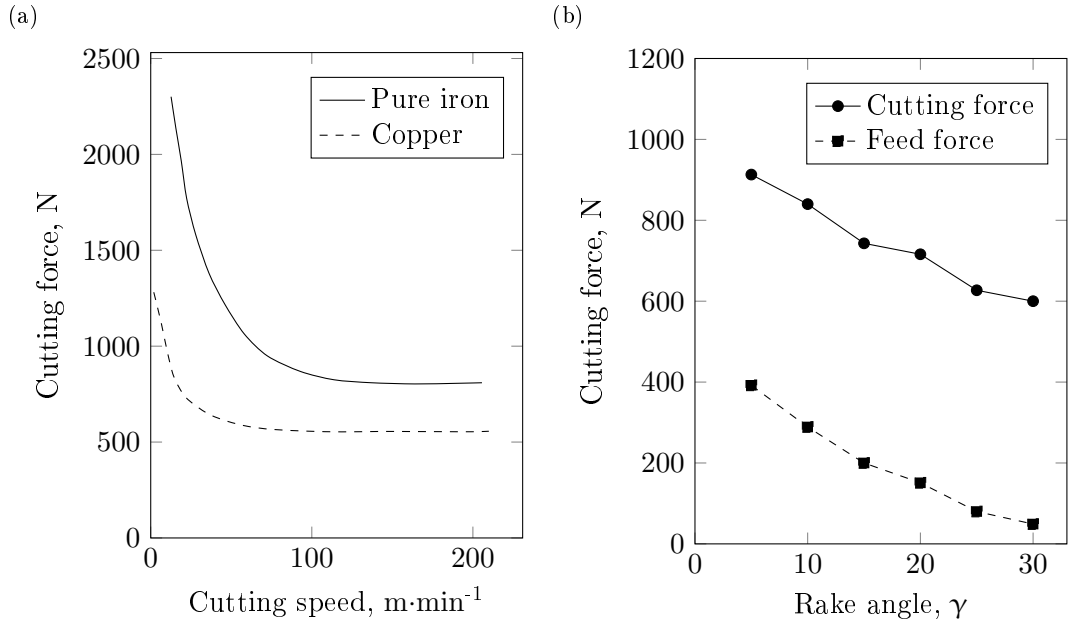

Figure 3.9: a) Cutting force vs cutting speed for pure iron and copper b) Effect of rake angle on cutting forces for low carbon steel (0.1 mm·rev^{-1}, 27 m·min^{-1}) (Trent and Wright 2000)

3.1.3 Tool wear: modes and mechanisms

Depending on the location and morphology of wear, three principal types can be distinguished (Figure 3.10): flank wear (flank face), crater wear (rake face) and notch wear (nose or end of the cutting depth). These and the criteria to define the end of tool-life are described in the standard ISO 3685 (1999).

- *Flank wear* (V_B). This is a flat surface located on the flank face, usually parallel to the machined surface of the workpiece. It is mainly attributed to (i) friction and rubbing of the tool along the machined surface causing adhesion and abrasion and (ii) high temperatures. It is generally used as the tool life criterion due to the ease of which it can be measured.

- *Crater wear* (K_T-K_B). This is a concavity located in the rake face. It normally occurs when there is a large and continuous sticking-sliding contact between the chip and the rake face of the tool. The most significant factors influencing crater wear are (i) the temperature at the tool-chip interface and (ii) the chemical affinity between the tool and workpiece materials. It is commonly associated with the combination of diffusion, attrition and adhesion mechanisms.

- *Notch wear* (V_N). This is a single groove that occurs simultaneously on the rake and flank faces, located at the nose or the end of the depth of cut. It usually occurs due to oxidation and attrition phenomena when machining materials (i) with poor thermal properties, (ii) with the presence of a hard oxidized surface, or (iii) with high work-hardening characteristics. It is usually a sign of premature tool wear.

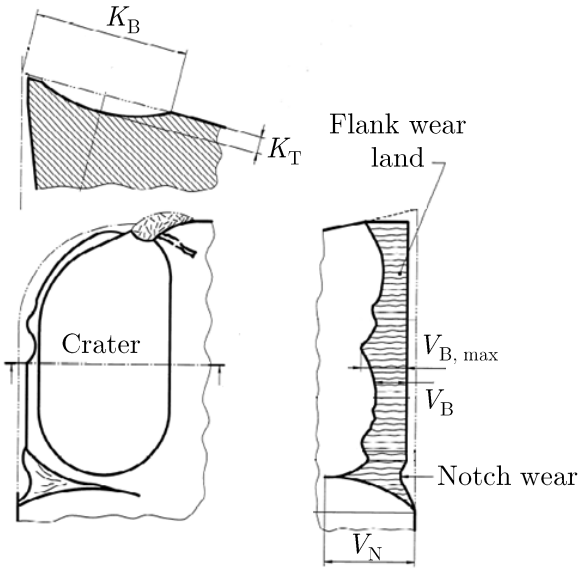

Figure 3.10: Wear mode characterization according to ISO 3685 (1999)

When machining carbon steels various tool wear mechanisms and tool failure modes can occur simultaneously. Tool wear is generated as a result of the chemical, thermal and mechanical interactions between tool and workpiece. Depending on tool and workpiece material, dominant tool wear mechanisms change with the cutting conditions. Mainly, these changes occur due to the variations of temperature in the cutting zone. The main wear mechanisms which occur when machining FP steels are adhesion, abrasion, diffusion and oxidation (see Figure 3.11). Other mechanisms such as chipping, cracking, thermal and mechanical fatigue can also be found (Coromant 1994).

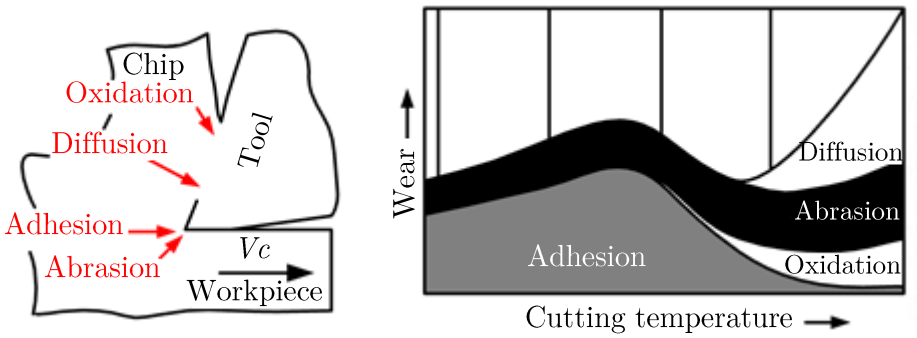

Figure 3.11: Wear mechanisms, adapted from Li (2012)

In the following lines, the main tool wear mechanisms and failure modes are explained.

- *Adhesion.* This is caused by the formation and fracture of the welded asperities of work material between the cutting tool and the workpiece. The periodical detachment of the adhered material causes the removal of grains of tool material. A certain range of temperatures (usually low) increase the affinity between the tool and workpiece, which combined with the action of high contact pressures provoke this wear phenomenon (Coromant 1994). The adhesion in carbon-alloys reaches its maximum degree at around 300°C, as demonstrated by Gåård (2008). In addition, Padilla Montes (2011) suggested that the limiting temperature for adhesion could be around 900°C. A diagram of the adhesion wear phenomenon is shown in Figure 3.12.

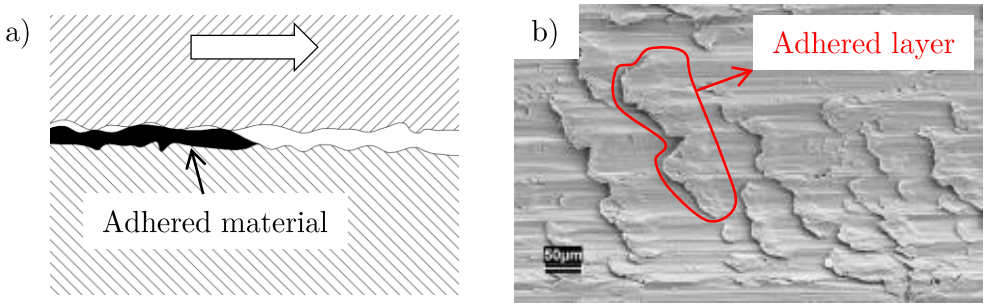

Figure 3.12: a) Adhesive wear mechanism (Coromant 1994). b) Example of adhesive wear in the rake face (Gåård 2008)

Low deformation rates are commonly linked to low temperatures within the deformation process, favoring the effect of adhesive wear. An example of this commonly occurs in forging processes, which can be likened to machining processes at low cutting speeds (Gåård 2008). An example of wear by adhesion is shown in Figure 3.12, in which layers of material adhered on the flank face of the tool are observed. In machining operations such as broaching, drilling or sawing, where cutting speeds are low, the risk of adhesion increases.

- *Abrasion.* This is damage that occurs due to the relative movement of hard particles of workpiece material on the surfaces of the tool. Hard inclusions of the workpiece material are pressed against the surface of the tool and then the relative slip displacement generates channel-shaped indentations in the direction of motion. At cutting temperatures above 800°C, abrasion becomes less significant compared to diffusion wear (Takeyama and Murata 1963; Mathew 1989; Yen et al. 2004). Figure 3.13 shows a diagram of the abrasion wear phenomenon and a micrograph image in which the channel-shaped indents generated on the flank face of the tool are visible.

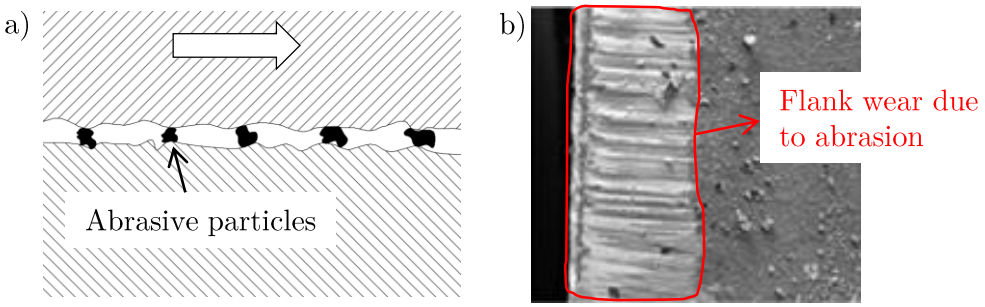

Figure 3.13: a) Abrasive wear mechanism (Coromant 1994). b) Flank face worn by abrasion (Zhu et al. 2013)

- *Diffusion.* This is tool damage that is affected by the chemical action that occurs during the cutting process. The chemical properties of the tool material and its affinity with the workpiece material determine the development of the diffusion wear phenomenon. During the operation, an atomic exchange takes place in two opposite directions, atoms are diffussed from the tool to the workpiece and vice-versa. This phenomenon is highly sensitive to temperature, growing exponentially at temperatures over 900-1200°C (Padilla Montes 2011). Furthermore, diffusion wear can be the most severe wear mechanism at high cutting speeds. In Figure 3.14 a diagram of the diffusion wear phenomenon and the identification of the diffusion region by SEM-EBSD measurement of the concentration of carbon atoms is shown (Zhu et al. 2013).

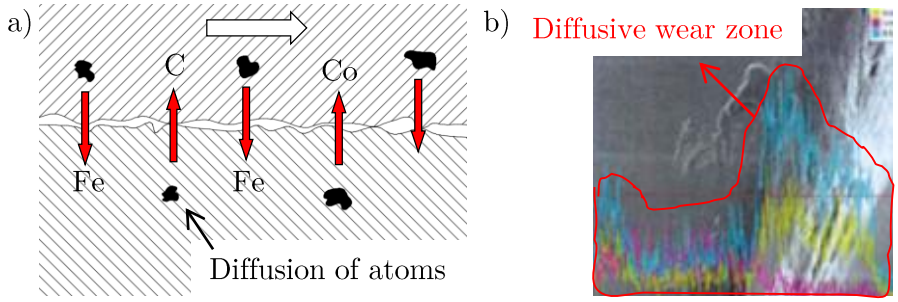

Figure 3.14: a) Diffusion wear mechanism (Coromant 1994). b) Experimental measurement of diffusive wear by SEM-EBSD (Zhu et al. 2013)

- *Oxidation.* High temperatures combined with the presence of oxygen promote the oxidation for most metals. Some cutting materials are more susceptible than others to this type of wear. Oxidation causes notches that are usually formed on the cutting edge. A diagram of the oxidation wear phenomenon and an experimental wear measurement obtained by SEM-EBSD microscopy is analyzed in Figure 3.15. The figure shows that the concentration of oxygen is higher where the oxidation occurs (Xu et al. 2013).

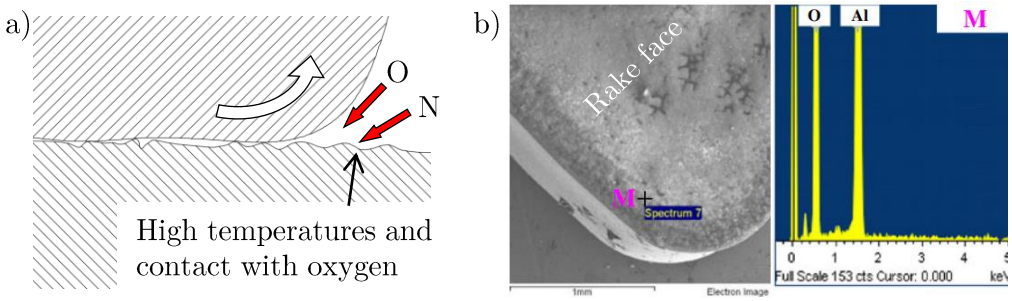

Figure 3.15: a) Oxidation wear mechanism (Coromant 1994). b) Analysis of the oxidized region (Xu et al. 2013)

3.1.4 Machining of ferrite-pearlite steels

In this section, the main factors affecting the machinability of ferrite-pearlite steels, as well as the influence that workpiece material has on tool life, cutting forces, cutting temperature and chip form are explained.

Input parameters affecting machinability

Machinability depends upon the dynamic reactions which occur in the workpiece material. Although the term machinability is attributed to the work material itself, machinability is not a unique material property which can be clearly defined and measured

(Bhattacharya 1987). For example, for a particular person, the machinability of a work material can be measured in terms of the number of components produced per hour, the cost of machining the component, or the final quality of a critical surface (Trent and Wright 2000). Indeed, aspects such as the machine tool, the geometry of the tool, the lubricant employed and the operating conditions influence the definition of machinability of the material. Despite the lack of universal metric, machinability may be assessed by one or more of the following criteria:

- *Tool life.* The amount of material removed by a tool before the tool performance becomes unacceptable or the tool is worn by a standard amount.
- *Limiting material removal rate.* The maximum rate at which the material can be machined for a standard short tool life.
- *Cutting forces.* The forces acting on the tool (measured by dynamometers) or the power consumption.
- *Tool temperature.* Temperatures generated in tools are a major influence on the rate of tool wear and on the limit of material removal rate.
- *Surface finish and burr formation.* The finished surface and geometry state of the machined workpiece achieved under specified cutting conditions.
- *Chip shape.* The chip shape influences the clearance of the chips from around the tool.

Figure 3.16 summarizes the main input material properties and the commonly measured output parameters affecting machinability. For practical considerations, the criteria adopted in this Ph.D. dissertation are classified as (i) industrial output parameters, in this case considered as tool life or tool wear, and (ii) scientific output parameters, related to the fundamental variables such as cutting forces, tool temperature and chip morphology.

During processing, external variables also interfere with the output results that define the machinability of the work. The characteristics of the turning lathes or milling machines have a significant influence on the process. Similar occurs with the cooling methods, tool materials and tool coatings, which clearly affects outputs such as tool wear, cutting forces or tool temperatures. However, taking into account that this research is constrained to develop basic knowledge, the study of these aspects are out of scope.

Although steels with a ferrite-pearlite structure are one of the most commonly machined materials, they are not those with the best machinability. This can be attributed to their high melting-point. With these higher melting-point metals, the heat generated while cutting becomes a controlling factor. It imposes constraints on the tool performance, and hence on the tool life (Trent and Wright 2000). The stresses acting on

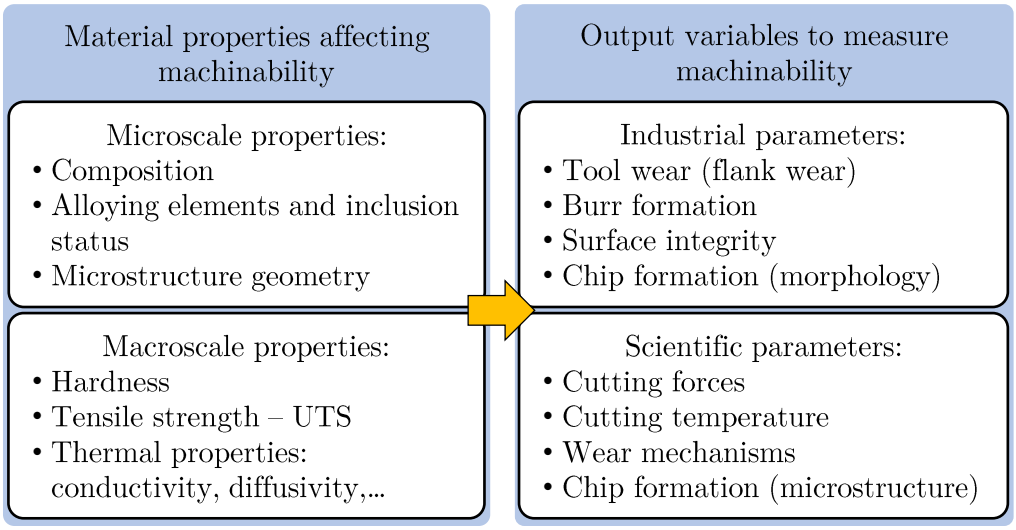

Figure 3.16: Material properties and industrial and scientific output parameters in machinability analysis

the tool are of significant relevance in tool performance too, as they are commonly linked to deformation of the edge and tool failures. Alloying elements in steel (carbon, manganese, chromium, etc.) usually increase their strength, which influences both the stresses acting on the tool and the temperatures generated. To date, the experimental study of the influence of alloying elements on the tool wear been effectively investigated to assess machinability.

To permit higher metal removal rates, steel work-materials are often heat treated to reduce the hardness to a minimum. In the machining of low carbon steels containing mostly pro-eutectoid ferrite, slow cooling from the annealing temperature is essential. This ensures that the carbon is not present in solution inside the ferrite grains, nor as very finely dispersed particles. Heat treatments are necessary to make sure that the carbon is not redissolved with the natural heating of the process, thereby accidentally returning the steel to a more-difficult-to-machine state (Dearnley and Trent 1982). Of equal or greater importance is the heat treatment performed to modify the microstructure. The heat treatment for medium or high carbon steel often consists of annealing just below the transformation temperature (about 700°C). This spheroidizes the cementite, which is the form in which it has least strengthening effect, rather than obtaining lamellar type structures which tend to strengthen the material. For some operations, a coarse pearlite structure is preferred, which is obtained by a full annealing treatment in which the steel is slowly cooled from above the transformation temperature. In fact, the performance of the machining process is highly dependent on the microstructural parameters of these materials (Demir 2008; Klocke and Kuchie 2011), and more specifically in the microstructure of the pearlite or alloying elements (Brunzel and Fomin 1997; Cohen and Voigt 2003).

Influence of alloying elements in tool wear

During the last decades, several authors have already studied the influence that alloying elements or inclusion status have on machinability. These are included during casting not only to modify the mechanical properties, but also to improve the machinability in terms of wear reduction or tool life increase. Although the objective of this work is far from the study of the effect of alloying elements, the results presented in Chapter 2 found that the steels analyzed showed different inclusion status that could later affect on machinability results. Therefore, a summary of the effect that most common inclusions have on machinability is set out in the following lines.

- *Lead (Pb).* In proportions of 0.1-0.35% lead improves the machinability due to the lubricating effect that it generates on the rake face. It was commonly added to pearlitic structures to increase productivity (Tata and Sampsell 1973), but nowadays its use is forbidden due to its polluting effects.

- *Chromium (Cr).* Chromium forms wear resistant carbides that decrease machinability.

- *Nickel (Ni).* Nickel alloyed steels have lower machinability because nickel increases the resistance to decohesion without decreasing ductility. Ni-inclusions generate a decrease in the thermal conductivity which also involves a negative effect from the productive point of view, due to the increase in diffusive wear generated by the higher temperatures occurring in the interface of the tool. Nevertheless, the machinability of nickel treated ferritic and austenitic steels can be improved by annealing. Authors such as Medvedeva et al. (2011) analyzed the influence of grain size and percentage of nickel on Ni-alloyed steels. They conclude that a smaller grain size, with even higher percentage of nickel, resulted in

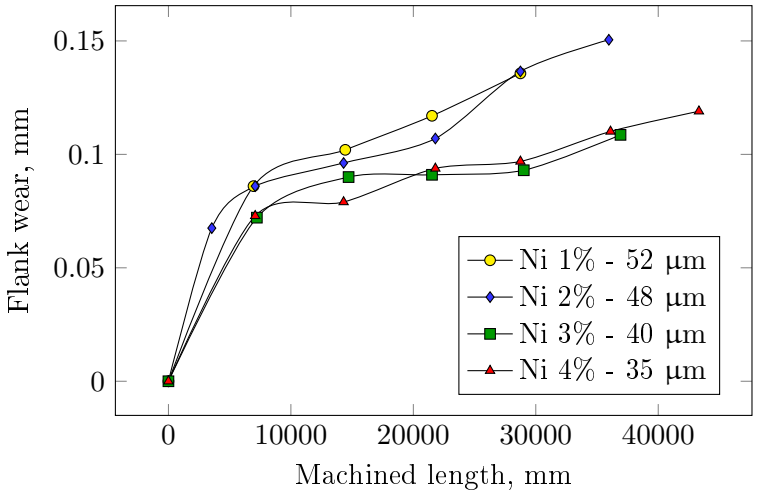

Figure 3.17: Flank on Nickel-based alloys with different grain sizes (Medvedeva et al. 2011)

a reduction of flank wear and, therefore, an increase in tool life (Figure 3.17).

- *Sulphur (S).* Sulfides contribute to lubricating the cutting area and, hence, protect the tool. This is the case of manganese sulphides (MnS), in which their high capacity for plastic deformation generates this protecting layer. They also facilitate decohesion, substantially improving chip formation. Not only the amount of MnS, but also the distribution of this constituent in the steel structure is important (Trent and Wright 2000). In general, a globulized morphology is preferred rather than lamellar-shape MnS. In contrast, calcium sulphides (CaS) generate wear by dissolution, adversely affecting the life of the tool (Nordgren and Melander 1990).

- *Selenium (Se) and Tellurium (Te).* These are alloying elements that together with sulfur generate sulfides that improve machinability. They are more effective increasing machinability than lead-treated steels, and have the advantage of being non-polluting (Tata and Sampsell 1973; Zaslavsky et al. 1969). A tool-life comparison can be seen in Figure 3.18 for different % Se.

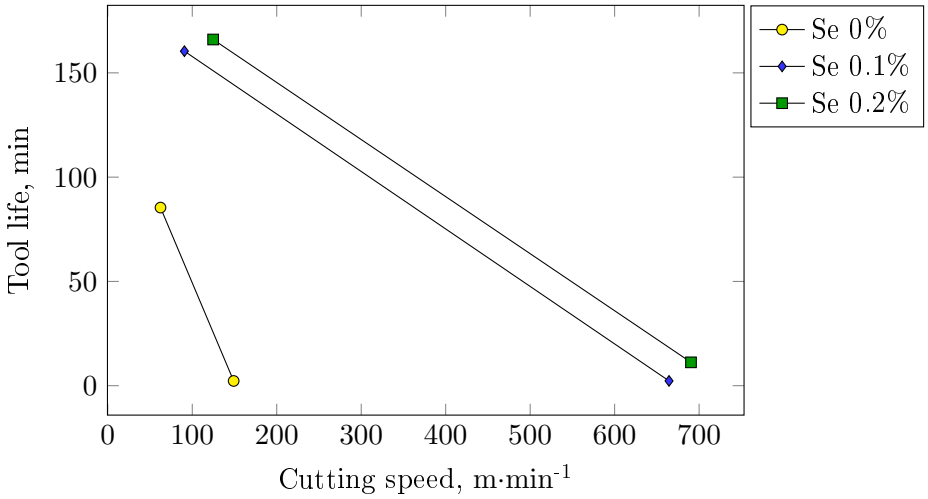

Figure 3.18: Tool life in function of % Se (Gol'dshtein and Morozov 1980)

- *Phosphorus (P) and Nitrogen (N).* These are used in proportions of less than 0.015% in order to reduce wear without substantially increasing brittleness (Coromant 1994).

- *Bismuth (Bi).* Materials treated with bismuth enable the chips to be more readily broken into small segments (Trent and Wright 2000). It also favors the formation of a material layer that is adhered to the tool surface, providing a positive lubricant action, similar to that of calcium and copper (Davim 2013).

- *Aluminum (Al) and Silicon (Si).* These are common deoxidizers employed for the removal of excess oxygen from molten metal. Aluminum forms aluminas

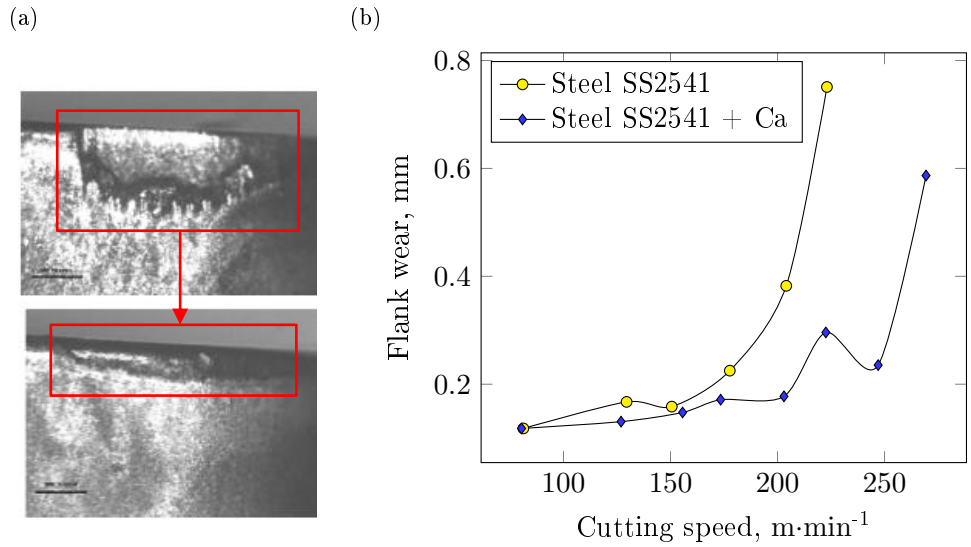

Figure 3.19: Flank wear for different calcium treated steels (Gol'dshtein and Morozov 1980)

(Al_2O_3) which generate a very abrasive effect on the tool, causing high crater wear. Silicon is also detrimental to tool life and surface quality in low carbon and free machining steels. It increases the strength and hardness of the steels, and forms hard abrasive particles which increase tool wear (Trent and Wright 2000).

- *Calcium (Ca).* Calcium forms inclusions that reduce the negative effect of aluminas, reducing abrasive wear (Nordgren and Melander 1990). In proportions of around 0.005-0.05% it reduces the shear forces (Hamann et al. 1996), and generates a continuous film (BUL or whitening) decreasing the wear of the tool (Gol'dshtein and Morozov 1980). Figure 3.19-a shows the influence of calcium aluminates in the decrease of the abrasive effect of the alumina shown in flank wear. Nordgren and Melander (1989) analyzed flank wear for the case of a SS2541 steel with calcium treatment and another without treatment, machined with cemented carbide tools. In the ISO 3685 wear tests they obtained a higher wear ratio in the untreated steel, as shown in Figure 3.19-b.

Influence of FP microstructure on tool wear

The machinability of FP steels, in terms of tool wear, is greatly influenced by the morphology of the pearlitic phase and its internal structure. Globally, pearlite has a negative effect on tool wear. This is linked to the reduced deformability and high hardness of the constituent, that generates significant abrasive wear and high shear and cutting forces (Doane 1988; Ebrahimi and Moshksar 2009).

When the machinability of FP steels is analyzed in terms of microstructure, in general, the most influential aspects are the amount of ferrite or pearlite found in the steels, the size of the pearlite nodules (pearlite colonies with typically spherical form) and the internal geometry of pearlite grains which can be of lamellar or globulized (or spheroidized) type (Björkeborn et al. 2010).

Even without taking into account the effect of lamellar, globular or the nodule size of pearlite, in general terms, a higher percentage of pearlite generates greater abrasive wear (Björkeborn et al. 2010; Trent and Wright 2000). With the increase of pearlite ratio, the adhesive effect of ferrite is reduced, converting into an abrasive effect (Mian et al. 2010). Figure 3.20 depicts the reduction in adhesion when machining an AISI 1045 steel compared to AISI 1005.

Verdeja et al. (2009) evaluated the machinability through various heat treatments to modify the microstructure in a SAE 8620 low-carbon alloyed steel. Figure 3.21 compares the machinability rate index (MRI) with respect to the lamellar pearlite fraction obtained in those heat-treated steels (S: spheroidized, F: ferritic structure, CC: controlled cooling, A: annealed, IA: isothermal annealing, N: normalized, SR: stress relieved). Although the amount of pearlite compared to that of ferrite was much lower, the authors showed that as pearlite fraction increases, the machinability generally diminishes. In contrast, they didn't find any correlation between the machinability index and ferrite grain size. For example, when comparing samples S and F, ferritic grain size decreased and MRI diminished. While comparing samples F and N, the opposite trend was found as MRI lowered with increasing ferritic grain size. They also concluded that hardness could not be directly linked to machinability. Comparing samples S and F, increasing hardness provoked an improvement in MRI, while comparing F with the other samples, increasing HV worsens the machinability. Other authors such as Lane et al. (1967), Björkeborn et al. (2010), Chen et al. (1985), and Ozcatalbas and Ercan (2003) also concluded that hardness alone is not sufficient to predict machinability of steel.

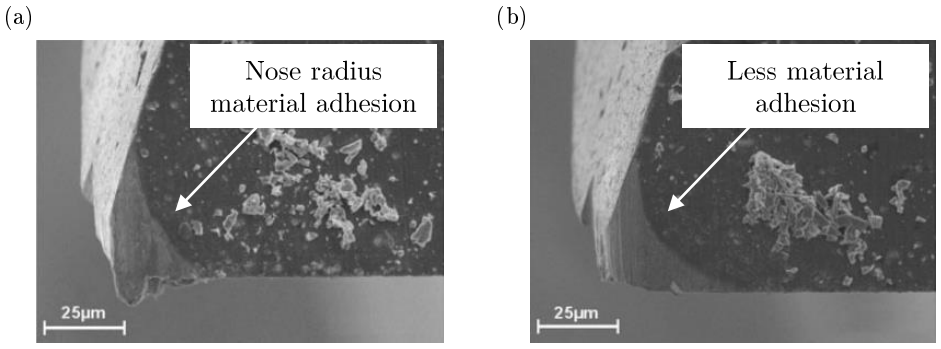

Figure 3.20: a) Adhesive wear by machining AISI 1005. b) Less adhesive wear by machining AISI 1045 (Mian et al. 2010)

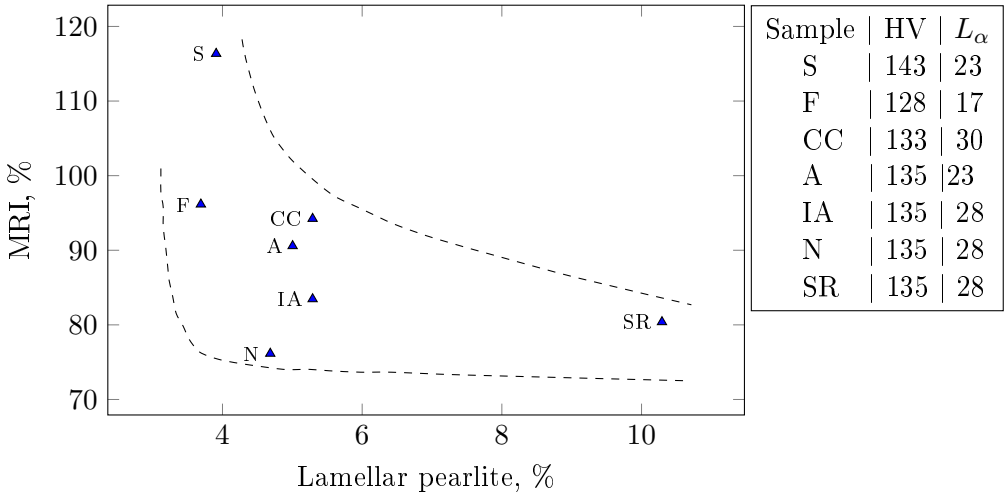

Figure 3.21: MR index in function of % of lamellar pearlite for various heat treated steels. Hardness (HV) and mean ferritic grain size (µm) are specified in the legend (Verdeja et al. 2009)

Björkeborn et al. (2010) analyzed the impact of globular and lamellar pearlite in tool flank wear. Different microstructures were produced in steel 20MnCr5, which led to different pearlite structures with an amount of 41-47% of pro-eutectoid ferrite. They recorded the evolution of flank wear depending on the amount of material removed at different cutting speeds. In the comparison between globulized or lamellar pearlite type structures, their results presented different trends depending on the cutting speed. At the lower cutting speed, machining the globulized pearlite steels achieved lower flank wear. In contrast, at high cutting speed achieved similar flank wear to those which occurred when cutting the lamellar steels. Therefore, it was difficult to conclude that globulized (or partially globulized) pearlite was optimum or detrimental in terms of flank wear. Comparing both lamellar steels, differences were observed in flank wear. The results suggest that a smaller interlamellar spacing generates greater flank wear,

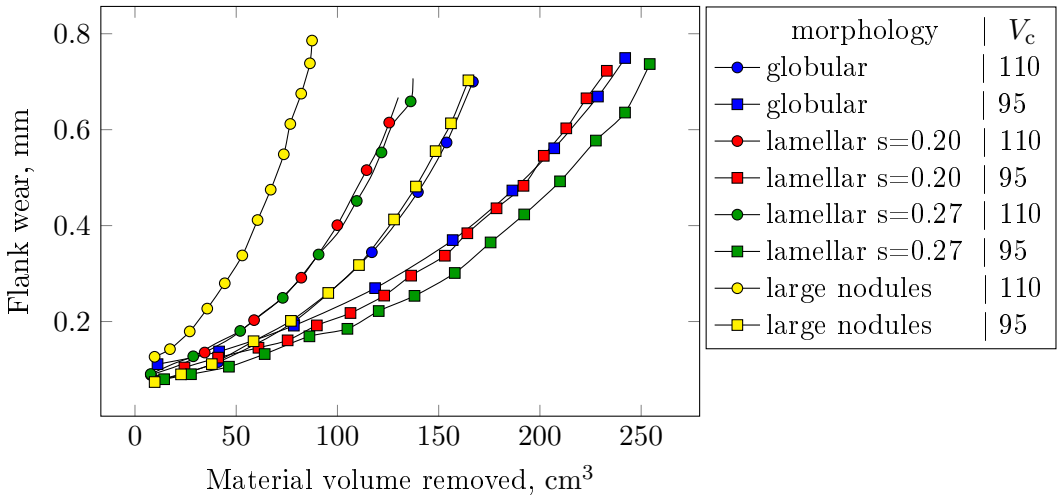

Figure 3.22: Effect of morphology of pearlite on flank wear (Björkeborn et al. 2010)

and is more noticeable when cutting speed is increased (Figure 3.22). However, it must be taken into account that these two steels differ in hardness values, with 163 HV measured for the coarser one and 180 HV for the finner lamellar steel.

The same authors also compared these abovementioned steels to another heat treated steel with a microstructure composed of large pearlite nodules, and an amount of pro-eutectic ferrite of 15%. They indicated that pearlite nodular size affects machinability more than pearlite morphology, i.e., lamellar spacing and the degree of globulization, in spite of the lower ferrite content (Figure 3.22). Steels with larger pearlite nodular size can lead to a decrease in the machinability in the form of increased tool wear (Björkeborn et al. 2010; Björkeborn et al. 2008). This was in line with the research developed by Brunzel and Fomin (1997).

The effect that grain size has on tool wear is better known. Researches in this field argue that the best tool life is obtained when non-alloy low-carbon steels are machined in the ferritic-pearlitic state with a uniformly coarse grain (Opitz and Gappisch 1962; Trent and Wright 2000). In this context, the research of Ozcatalbas and Ercan (2003) was found relevant. An as-rolled SAE 1050 steel was heat treated by normalizing, in which the pearlite grain size was reduced from 27 to 11 μm, while the amount of pearlite was maintained at 65% and the hardness at 204-207 HV. According to flank wear criterion, the V20 of the as-rolled steel was 261 m·min^{-1}, while that of the normalized sample was 147 m·min^{-1}. The flank wear in both steels was dominated by an abrasive mechanism. In addition, not only was the wear on the flank increased when reducing the grain size, but also the wear on the rake face. In the crater the diffusion wear was more obvious than the adhesion mechanism. In the case of the normalized steel they observed that the binding material was diffused across the chip as the tool reinforcing particles came forward almost completely. An example of SEM images comparing the SAE 1050 as-rolled and nominalized steels is shown in Figure 3.23. In the case of the normalized steel it can be seen that less adhesion is occurred in the crater, as the tool reinforced particles are more visible.

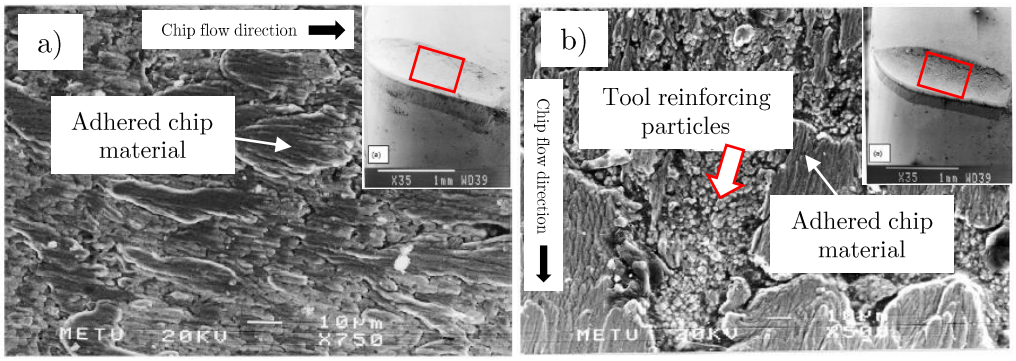

Figure 3.23: a) SEM analysis of rake face when cutting AISI 1050 as-rolled b) SEM analysis of rake face when cutting AISI 1050 normalized, adapted from Ozcatalbas and Ercan (2003)

However, in the same study of Ozcatalbas and Ercan (2003), another SAE 1050 steel was tested after annealing treatment. The microstructure of the latter was formed by coarser pearlite grains with partially globulized cementite (pearlite grain size of 38 μm), and the hardness of the material was decreased to 171 HV. Besides the increasing grain size, and the reduction of material hardness, the V20 was lowered to 159 $m \cdot min^{-1}$. This was lower compared to the as-rolled steel. It can be concluded, therefore, that depending on the internal geometry of pearlite, coarser grains do not always achieve a better machinability. The same trend was also observed by prior researchers such as Okusa et al. (1978) and Araki and Yamamoto (1978).

Influence of FP microstructure on fundamental variables

In this section the scientific parameters or the so-called fundamental variables are analyzed in terms of FP microstructure. These are the cutting forces, chip morphology and tool temperature.

- Cutting forces

Alloying a pure metal normally increases its yield strength but often reduces the tool forces because the contact length on the rake face becomes shorter.(i.e.the area of contact is reduced). For example, in Figure 3.24-a force/cutting speed curves for pure iron and a medium carbon steel are compared. Tool forces are lower for the alloy than for the pure metal across the whole speed range, the largest differences being at low speeds (Trent and Wright 2000). Similar conclusions were obtained by Korkut and Donertas (2007) when face milling two FP steels. They found that AISI 1020 achieved longer contact length and higher cutting forces than AISI 1040. This in turn was also linked to the feed forces being reduced together with the increase of pearlite ratio.

In contrast, some authors have published opposite tendencies from that stated by the previous authors. This is the case of the research done by Obikawa et al. (2009), in which four steels from pure ferritic to pure pearlitic were machined. They found that the higher the pearlite content, the higher the cutting and feed forces measured (Figure 3.24-b). This was also corroborated by Milovic and Wallbank (1983) when testing two alloyed FP steels with 0.14% and 0.11% carbon content. An increase in %C caused cutting forces to increase by 30%.

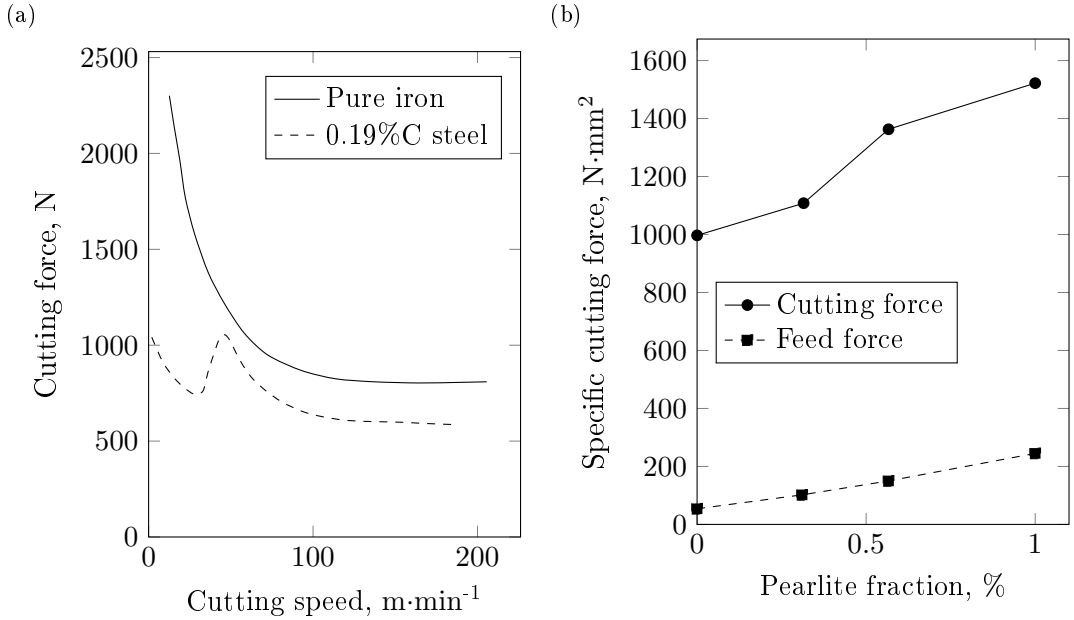

Figure 3.24: a) Cutting force vs cutting speed for pure iron and alloyed steel (Trent and Wright 2000) b) Cutting and feed forces vs pearlite fraction (Obikawa et al. 2009)

- Cutting temperature

Most of the experimental studies found in the literature examine the tool cutting temperature from the point of view of varying cutting conditions or tool geometry. Few focus their study on the influence that carbon content or microstructure have on tool temperature.

The research of Milovic and Wallbank (1983) is worth noting. They analyzed the tool temperatures of various steels at cutting speeds of over 100 m·min^{-1}. They observed that increasing carbon content caused an increase in tool temperature. They also reported that alloying the steels with lead (Pb) generated a decrease in the measured rake face temperatures. These results are described in Figure 3.25-a.

In the abovementioned work of Ozcatalbas and Ercan (2003), tool/chip interface temperatures in function of cutting speed of the as-rolled, annealed and normalized AISI 1050 specimens were recorded during turning (Figure 3.25-b). The temperatures of the normalized steel were higher than that of the as-rolled. This was in line with their observations of higher diffusive wear on the rake face in the former. In contrast, the interface temperature of the annealed steel was lower than that of the as-rolled, in spite of its higher degree of flank and crater wear. Therefore it was not possible for increasing crater wear to be directly linked to an increase in temperature. Other aspects such as abrasion or adhesion had to be taken into account. Additionally, although it could have been a coincidence, the smaller the pearlitic grain size of the material, the higher the temperature in the interface.

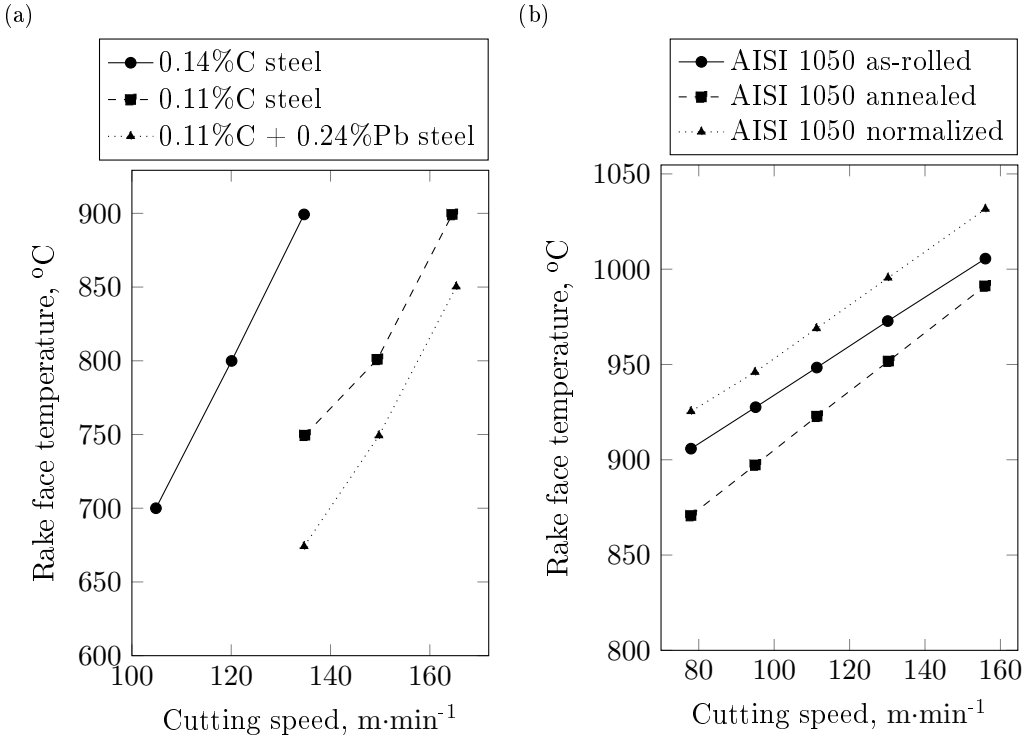

Figure 3.25: a) Variation in maximum rake face temperature with cutting speed for 0.14% and 0.11%C steels, and steel alloyed with Pb (Milovic and Wallbank 1983) b) Tool-chip interface temperatures of AISI 1060 in as-rolled, annealed and normalized states (Ozcatalbas and Ercan 2003)

- Chip morphology

In the existing knowledge it is well-known that chip morphology has a direct relationship with the cutting forces. Commonly, an increase of chip thickness generates a reduction on the shear angle, and therefore the cutting forces increase. On the contrary, a reduction in chip thickness generates a drop in the forces (Merchant 1944). However, this statement does not fully apply to FP steels.

Trent and Wright (2000) and Korkut and Donertas (2007) stated that increasing %C or f_p caused a reduction on chip thickness and therefore a drop in the cutting forces. The opposite was concluded by Milovic and Wallbank (1983), who published that cutting forces and chip thickness increase together with %C or f_p.

Buchkremer et al. (2016) tested normalized and quenched-tempered AISI 4140 ferritic-pearlitic steels. The carbon content was of 0.41% in both cases, but the pearlite grain size of the latter was much more refined than that of the former. As a consequence of the thermal treatment the hardness increased from 203 HV to 468 HV. Measured chips showed that grain refinement (or hardness increase) resulted in thinner chips, but higher cutting and feed forces were still measured when cutting.

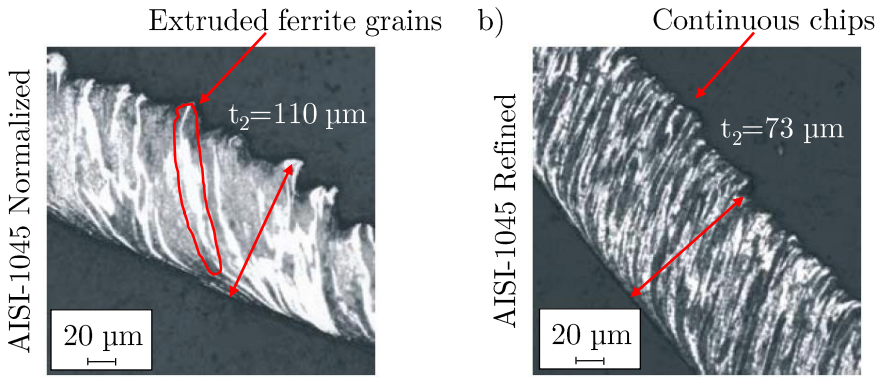

Figure 3.26: a) Chip formation when cutting normalized AISI 1045 at 50 µm uncut chip thickness b) Chip formation when cutting refined AISI 1045 at 50 µm uncut chip thickness, adapted from Simoneau et al. (2007)

As regards the microstructure scale effect, Simoneau et al. (2007) analyzed the influence that uncut chip thickness and grain size had on chip morphology. Two sets of heat treatments were conducted on an AISI 1045 steel, obtaining normalized (grain size $\sim 100\,\mu m$) and refined (grain size $\sim 8\,\mu m$) structures. From the micrographs of their publications it was possible to extract that a grain refinement resulted in slightly thicker chips, as is observed when comparing Figure 3.26-a and 3.26-b. From the morphology of the chips, it was also significant that continuous chip formation eventually gave way to shear-extruded type chips as the grain size of steel was increased. While in the case of the refined AISI 1045 the pearlite ferrite and pearlite are deformed in a similar manner, in the normalized steel, the ferrite grains are evidently extruded and sheared between the pearlite grains.

3.1.5 Tool wear prediction empirical models

Over the years, the prediction of tool wear has followed two different lines: empirical tool life models and physically-based tool wear rate models. Empirical type wear models gives the relationship between tool life and cutting parameters or process variables. For example, Taylor's tool life equation (Taylor 1907), reveals the exponential relationship between tool life and cutting speed, and Hastings tool life equation describes the effect of cutting temperature on tool life (Hastings et al. 1980). In various sizes of cutting database, Taylor's tool life equation and its extended versions under different cutting conditions appear most frequently. However, empirical tool life equations are suitable to very limited range of cutting conditions (Colding 1961). As the new machining technologies, e.g. high-speed-cutting or dry cutting, are getting spread in manufacturing industry, the existing empirical equations need to be updated with new constants and a lot of experimental work has to be done. In addition, in spite that tool life can be predicted by these equations, it is difficult to get further information about the tool wear progress, tool wear profile or tool wear mechanisms that are sometimes important for tool designers (Xie et al. 2005).

Tool wear rate models are derived from one or several wear mechanisms. They provide the information about wear growth rate due to certain wear mechanisms. In these models, the wear growth rate can be related to several cutting fundamental variables that have to be measured experimentally or obtained by analytical methods (Kwon 2000). The complex approach to this problem stems from the research carried out by Shaw and Dirke (1956) for abrasive-adhesive wear and Trigger and Chao (1956) for diffusion wear.

In the attempt carried out by Takeyama and Murata (1963), the wear of the tool was attributed to two types of mechanisms, mechanical (abrasion) and physic-chemical (diffusion). The authors related the abrasive wear with the cutting distance and deduced it independent from temperature, while associated the diffusive wear directly to a thermal activated phenomena modeled with a Boltzmann-type canonical distribution (Eq. 3.1).

$$\frac{dW}{dt} = \frac{dW_{\text{abrasion}}}{dt} + \frac{dW_{\text{diffusion}}}{dt} = V_{\text{c}}(T, f) \cdot C + D \cdot e^{\frac{-E_{\text{a}}}{R \cdot T}} \tag{3.1}$$

When determining the constants C and D, it is necessary to use experimental data sets of wear tests, as shown in Figure 3.27. The coefficient C represents the constant abrasion wear along the temperature and the coefficient D is the multiplier factor of the exponential curve representing diffusion.

Takeyama & Murata's model presented several variations among the years. For example, Luo et al. (2005) described the sliding coefficient function of the hardness of tool material. This was represented with the Eq. 3.2, where A_L is the abrasive-adhesive wear constant and H_T is the hardness of tool material.

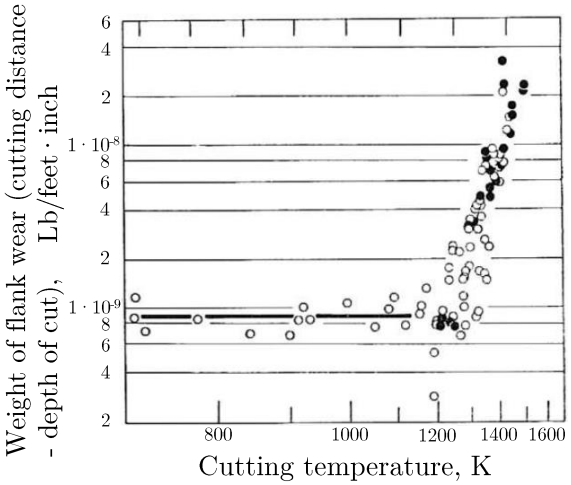

Figure 3.27: C and D parameter identification from experimental tests (Takeyama and Murata 1963)

$$\frac{dW_{\text{abrasion}}}{dt} = \frac{A_{\text{L}}}{H_{\text{T}}} \cdot \frac{F_{\text{n}}}{V_{\text{c}} \cdot f} \tag{3.2}$$

In another modification, Attanasio et al. (2008) characterized the D coefficient function of temperature for AISI 1045 steel. Using both experimental and simulation tests, they obtained a polynomial equation of the form of Eq. 3.3.

$$D(T) = 1.6735{\cdot}10^{-9}T^3 - 5.5376{\cdot}10^{-6}T^2 + 0.00611T - 2.251 \tag{3.3}$$

Usui et al. (1984) extended the work of Shaw and Dirke (1956) to represent the behavior for the adhesive wear, taking into account the contact pressure, sliding velocity and interface temperature (Eq. 3.4).

$$\frac{dW}{dt} = A \cdot \sigma_{\text{c}} \cdot V_{\text{s}} \cdot e^{-\frac{B}{T}} \tag{3.4}$$

where A and B are the contact parameters between tool and workpiece, σ_{c} is the contact pressure, V_{s} is the relative sliding velocity between tool and chip and T is the interface temperature. The wear rate data ($\frac{dW}{dt}$) is obtained experimentally, and the values of V_{s}, σ_{n} and T experimentally, theoretically or numerically.

In the study of Usui et al. (1984) the wear behavior of the crater and flank wear was characterized for different steels with a carbon content ranging from 0.15% to 0.45% machined with P20 grade carbide inserts. The wear characteristic concerning the crater wear (Figure 3.28-a) was almost identical for all tested steels, although in the lower temperature rage the agreement was worst than that of the higher temperatures. For the case of flank wear (Figure 3.28-b) the wear characteristic curve was also the same for all the steels, but the constant A and B differed between the high and low temperature range. In the high temperature range, coefficients A and B for both crater and flank wear were identical (A=0.01198 MPa^{-1}, B=21950 K^{-1}).

Numerous authors have implemented the Usui's law in their finite element models, such as Özel (2009), Haddag and Nouari (2013), Yen et al. (2004), Xie et al. (2005), Klocke and Frank (2006).

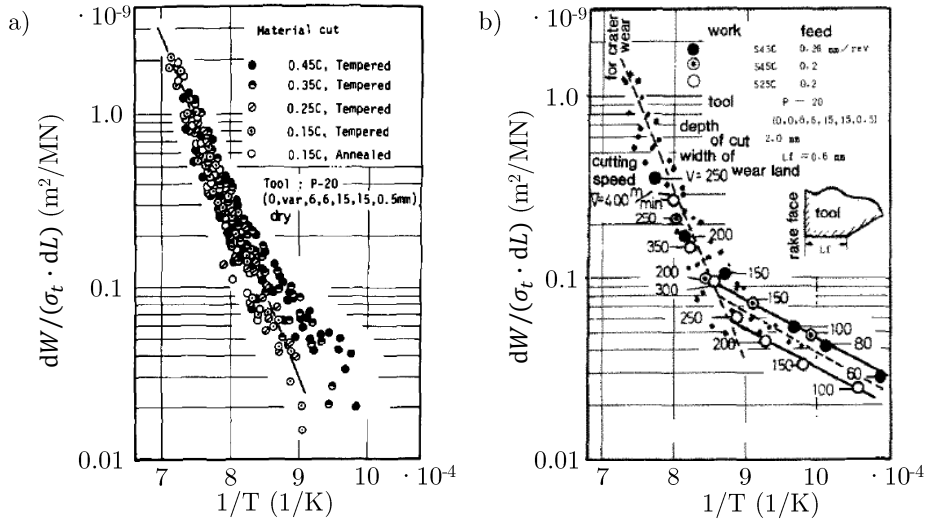

Figure 3.28: Wear characteristic curves for (a) crater and (b) flank wear (Usui et al. 1984)

Recently, Pálmai (2013) deduced a new formula to describe the flank wear as a consequence of abrasion, adhesion and diffusion phenomena. The proposed formula (Eq. 3.5) integrates the concepts of Takeyama & Murata and Usui, with the additional feature of including the relationship between temperature and wear with a Taylor-type equation. In addition, the formula also takes into account the effect of cutting length for both mechanically and thermally activated wear processes.

$$\begin{aligned} \frac{dW}{dt} &= \frac{V_\mathrm{c}}{W}\left[A_\mathrm{a} + A_\mathrm{th}\cdot e^{-\frac{B_\mathrm{a}}{V_\mathrm{c}+K\cdot W}}\right] \\ B_\mathrm{a} &= \frac{E_\mathrm{a}}{R\cdot T} \\ K &= \frac{C_\mathrm{w}}{C_\mathrm{v}} \end{aligned} \tag{3.5}$$

where V_c is the cutting speed, A_a is the abrasion-adhesion wear constant, A_th is thermal activated wear constant, E_a is the activation energy, C_w and C_v are a constants related to temperature and K is a fitting constant.

Based on similar as abovementioned concepts, Huang and Liang (2004), Chinchanikar and Choudhury (2015), and Zhao et al. (2002) proposed a number of physical-based models to combine the abrasion, adhesion and diffusion mechanisms into a single relation. These models, however, suffer some limitations due mainly to the large amount of data needed to calibrate the wear rate equations (Malakizadi et al. 2016). In addition, aspects like the hardness of the tool or even the hardness of the abrasive particles must be known within the entire range of cutting temperature. For this reason the uncertainties in the material data may introduce additional concerns regarding the reliability of tool wear estimations, leading to hindering the predictions rather than improving (Wassdahl 2008).

3.1.6 Critical analysis

Numerous studies have analyzed the machinability of FP steels in terms of microstructure and/or mechanical properties. The properties listed below were found to be the most relevant, and their effect (positive, negative or non-determined) is described:

- *Alloying elements.* The negative effect that calcium sulphides (CaS), aluminum oxides (Al_2O_3), silicon (Si) and nickel (Ni) have on tool wear is note worthy. The use of selenium (Se), tellurium (Te) and bismuth (Bi) contribute to lubricating the contact surfaces, reducing abrasive wear. Additives such as phosphorous (P), nitrogen (Ni) and bismuth (Bi) are employed to facilitate the breakability of the chip, which in turn improves the machinability. Calcium (Ca) is included in the molten metal to reduce the abrasive effect of the aluminas formed during deoxidation.

- *Pearlite content and nodule size of pearlite.* Large nodules of pearlite (i.e. large colonies of pearlite grains) have a negative effect on tool wear. These are usually linked to higher pearlitic content in most of the studies, which is also detrimental for tool wear. Pearlite grains have an abrasive effect due to the high hardness of the cementite phase. Although in some cases the increase in pearlite content generates lower adhesion, which may lead to an improved surface quality, from the point of view of tool wear this has a negative effect.

- *Geometry of cementite inside pearlite.* This can be found in the form of lamellae, in globules, or in a partially globulized state. Concerning lamellar type pearlite, a lowering in the interlamellar spacing drives the increase of the abrasive effect of pearlite. This is caused because it increases the hardness of the pearlite grains, and as a consequence the average hardness of steel. The influence that globulized pearlite has in machinability has not been clearly observed. For example, Verdeja et al. (2009) observed an improvement when annelaing a steel with a 5% pearlite content, as opposed to normalizing it. In the study of Björkeborn et al. (2010), depending on the cutting speed, globulizing had a positive or negative effect compared to that of lamellar type pearlitic steels. Ozcatalbas and Ercan (2003) observed that annealing (transforming from lamellar to globular pearlite) worsened the machinability of an SAE 1050 steel, compared to the as-rolled bars which were of lamellar type. However, normalizing the steel produced very fine lamellar pearlite, which in turn obtained lower machinability than that of the annealed state. For this reason it was not possible to obtain clear conclusions from the comparison of globular or lamellar cementite morphology that can be found in pearlite grains.

- *Ferrite grain size.* In the majority of studies that analyzed this microstructure property, it was concluded that ferrite grain size played no important role in machinability. The influence that the pearlite nodular size or even the inter-

lamellar spacing had in tool wear was significantly more relevant compared to that of ferritic grain size.

- *Pearlite grain size.* No clear trend was observed, as most of the authors conclude that the most determinant effect is not the grain size of pearlite itself, it is the size of the pearlite colonies or nodular size (Brunzel and Fomin 1997; Björkeborn et al. 2010).

- *Hardness.* The majority or researchers concluded that hardness alone is not sufficient to predict machinability of steel (Okusa et al. 1978; Ozcatalbas and Ercan 2003; Björkeborn et al. 2010).

With regards to the influence that FP steels had on fundamental variables, the following was concluded:

- *Cutting forces.* Discrepancies were found between the analyzed studies. Some authors stated that increasing pearlite content generated an increase in the cutting forces(Obikawa et al. 1997; Milovic and Wallbank 1983), while others found that increasing ferrite content generated longer contact and therefore greater cutting forces (Korkut and Donertas 2007; Trent and Wright 2000).

- *Tool temperature.* In the analysis of tool temperatures it was almost accepted that increasing carbon content, which directly drives an increase in pearlite ratio, generated a temperature rise in the tool. The geometry of the cementite phase, and the grain size of pearlite also influences tool temperatures. The results suggested that smaller grains or thinner interlamellar spacing caused temperatures to rise. However, the latter conclusion might not be completely certain.

- *Chip thickness.* Although in general terms increasing ferrite content is supposed to increase the chip thickness (Trent and Wright 2000; Korkut and Donertas 2007), two steels with the same amount of ferrite can generate chips of different thickness if the grain size is varied (Buchkremer et al. 2016). In general, a grain refinement contributes to obtain thinner chips (Simoneau et al. 2007), but the hardness of the material has also to be taken into account (Buchkremer et al. 2016). In addition, although thinner chips are commonly linked to a lowering in the cutting forces (Merchant 1944), depending on grain size and material hardness this condition might not always be fulfilled (Buchkremer et al. 2016).

The needs for industry concerning tool life prediction are mostly solved by empirical and physical wear models. Those models developed under empirical methods require a large amount of trials, and are limited to the range of cutting conditions analyzed. In contrast, physically based models predict tool wear based on the evolution of certain number of fundamental variables such as tool temperature, contact pressures and sliding distance. However, these models also require the calibration of an amount of

parameters, which are commonly identified by on wear tests. Although the amount of tests might be reduced compared to that empirically assessed laws, these parameters are usually unique for an specific tool-work material pair. In addition, most of the recently developed models incorporate difficult to establish properties such as the hardness of asperities which may introduce additional concerns in wear estimations. Thus, the models developed by Takeyama and Murata (1963) and Usui et al. (1984) are still those most widely employed (Lorentzon and Järvstråt 2008; Attanasio et al. 2008; Ceretti et al. 2009).

The machinability of materials is determined by means of fundamental variables, tool wear, or other indicators that best suits to the final user. On the techniques to measure these variables, it is well established that measurement of cutting forces is usually carried out with piezoelectric dynamometers, due to their level of precision and ease which they can be integrated into the process chain (Céspedes 2011; Shaw and Cookson 2005).

To assess tool temperatures a greater number of methodologies are found in the literature. Thermocouples or infrared cameras are the equipments most widely employed. Although thermocouples are inexpensive, they have several disadvantages: they interfere with the heat flow, have a limited transient response, and are difficult to use in order to obtain temperature gradients (Ay and Yang 1998; Stephenson 1993). Other techniques reported are those using thermosensitive paints (Rossetto and Koch 1970), or metallurgical methods (Trent and Wright 2000).

Infrared Radiation (IR) thermometers have received great attention in recent years as devices for temperature measurement in machining processes (Pujana et al. 2007; Arrazola et al. 2008; Davies et al. 2003; Arriola et al. 2011; Armendia et al. 2010). The principal advantages of this technology are (i) it is non intrusive, i.e., the IR radiation technique does not interfere with the heat flow as thermocouples do, (ii) it enables direct determination of temperature fields and (iii) it has near real-time response. However, it has some drawbacks such as (i) the difficulty to measure temperature when lubricants are employed, (ii) the equipment cost and (iii) defining an appropriate methodology to obtain accurate measurements. In fact, due to the difficulty of using IR techniques for measuring temperature with lubricants, dry cutting is the only choice considered in nearly all research works. However, Cuesta et al. (2016) were able to record the temperature on a side face of a workpiece when dry and wet drilling Inconel 718. This was achieved by integrating the camera into an specially designed box, which isolated the camera and the recording work surface from the coolant.

When infrared thermometers are used, the calibration technique and emissivity estimation is as important as the experimental set-up. Basically, the accuracy of all known infrared techniques depends on the estimation of this parameter (Herve et al. 2012) which is the major uncertainty source (Davies et al. 2003). Arrazola et al. (2008) estimated that the uncertainty of the measurement may be attributed to the calibration ($\pm 10^{o}$C), experimental fluctuations ($\pm 25^{o}$C) and emissivity variations ($\pm 10^{o}$C), which

could lead to an average uncertainty of $\pm 45^{o}$C.

Optical microscope and optical profilometry are those most widely employed methodologies to establish tool wear. Direct optical microscopic measurement techniques allow measurement of tool wear with high accuracy. Nevertheless, they are limited to measure distances on a plane perpendicular to the focusing direction. Therefore, this technique is widely employed on flank wear measurements, which is the most common criteria to establish tool-life end (Yen 2004; Sacristan 2016). Optical profilometry is a highly precise optical technique for measuring surface height and shape with great speed and accuracy (resolutions lower than 1 μm). Several parameters, including width, length, depth and volume from the worn regions can be measured (Devillez et al. 2004; Sacristan et al. 2016). In addition, 2D surface topology profiles can be extracted from the worn regions, allowing the accurate identification of the geometry of the worn tool.

3.2 Developed procedures and experimental set-ups

The objective of the tests undertaken in this study is to provide the necessary data to validate the numerical FE models described in Chapter 4, and to develop a wear rate law to be implemented in the FE codes. In addition, the selected outputs also give support for the understanding of the machinability of FP steels.

Although ISO 3685 (1999) tests are carried out in nose turning operations, the selected procedure in this research was the orthogonal cutting operation, as it is defined as the most appropriate cutting operation to develop basic knowledge. In order to establish the orthogonal cutting methodology to be employed, the main input and output parameters were identified (Figure 3.29). The workpiece material was already defined by the scope of the project. Four low-medium carbon FP steels were selected, which are already described in Chapter 2. The influence of the cutting conditions was selected as an input parameter. These inputs led to a more in-depth analysis of the machinability of the steels, and to the validation of the developed FE cutting model over a wider range of cutting conditions. Other common inputs in the analysis of machining processes such as different tool geometries, tool materials and coatings, or even the use of coolant are out the scope of the project.

The main outputs to assess machinability, to extract the required data to define a wear rate law and validate the models is depicted in Figure 3.29. The main variable to be recorded was the geometry of the worn tool. Based on the standard ISO 3685 (1999) three main wear regions were identified: crater wear depth (K_{T}), crater wear length (K_{B}) and flank wear land (V_{B}). Commonly, wear tests and machinability analysis only refer to V_{B}. In the present work however, all three of those cited variables are identified as this lends to a better understanding of the wear behavior of FP steels. It is widely reported that tool wear is caused by the combination of certain fundamental variables, and are these variables in turn that vary with the increase in tool wear. Hence, the

evolution that fundamental variables had with tool wear were also identified. Those selected were the cutting and feed force, tool temperature, tool-chip contact length and chip thickness.

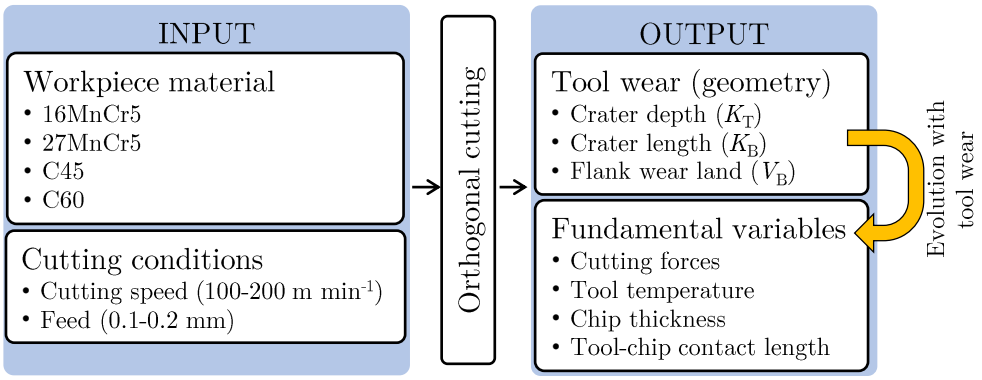

Figure 3.29: Inputs and outputs to be analyzed in orthogonal cutting tests

3.2.1 Orthogonal cutting procedure and set-up definition

The experimental methodology was designed to fulfill the requirements cited previously. These were:

- The machining procedure was simplified to orthogonal cutting in conditions close to turning operations.
- The geometry of the worn tool was recorded at previously defined time increments.
- Fundamental variables were recorded at the beginning of the tests (with a new tool) and with the evolution of tool wear at previously defined time increments.

The experimental procedure was divided into three main stages: (1) fundamental variable measurement in an orthogonal tube, (2) tool wear generation in slotted bars and (3) tool wear measurement. A diagram of the methodology is shown in Figure 3.30.

For fundamental variable measurement, the employed set-up is detailed in previous publications (Arrazola et al. 2015; Arrazola et al. 2009; Arrazola et al. 2008). This was mounted on a CNC vertical milling machine as shown in Figure 3.30. The tool and tool holder were clamped on a dynamometer (Kistler 9121) to measure cutting and feed forces. These and the infrared (IR) camera (FLIR Titanium 550M) were fixed on the moving table of the machine-tool. The orthogonal cutting specimens in tubular form were held on the spindle, which gave the rotation movement and the vertical feed. These specimens were of 58±0.05 mm diameter and 2±0.02 mm wall thickness (width of cut). A ground surface was machined on the inserts to generate a perpendicular

surface for IR measurements, enabling the capture of the thermal field on a side face of the tool. To directly link the measured tool radiation with the real tool temperature, a specially designed setup was developed. This is detailed in the further pages of this chapter. Chips were also collected during tests to analyze the chip morphology.

For the case of tool wear tests, orthogonal cutting on slotted bars was carried out on a CNC lathe (Figure 3.30), similar to the work developed by Hosseinkhani and Ng (2015). This approach was selected to reduce the amount of material required for the tests in comparison to those carried out in the milling machine. The width of both the slot and the material left between the slots (width of cut) was 2±0.02 mm.

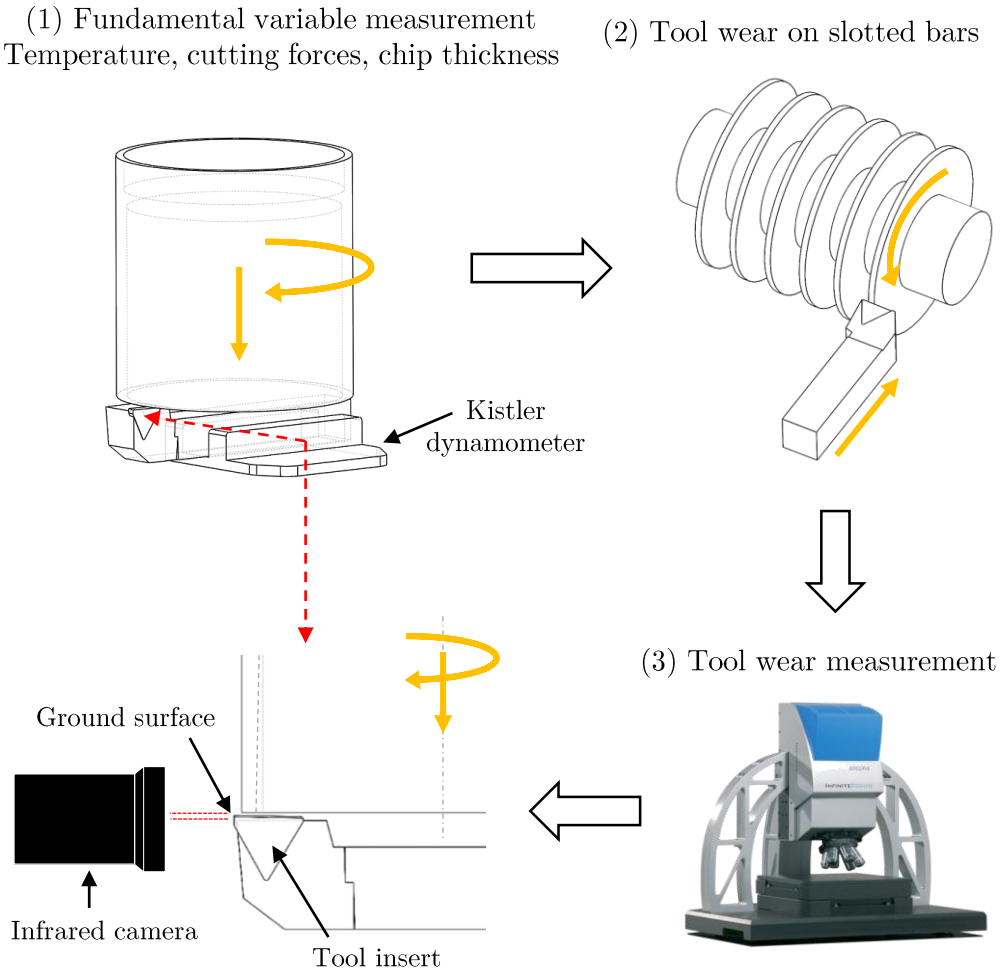

Figure 3.30: Schematic representation of the orthogonal cutting methodology

At defined time increments, the 3D geometry of the worn tool (i.e. crater wear depth K_T, crater wear length K_B and flank wear land V_B) was measured with a confocal profilometer (Alicona Infinite Focus G4). Prior to its measurement, tool inserts were submerged in a 48% hydrofluoric acid solution for 10-15 minutes to remove the accumulation of oxides and material adhesions.

Tests were developed in four different cutting conditions (cutting speeds of 100-200 m·min^{-1}, and feeds of 0.1-0.2 mm). Due to the limitations of measuring tool temperatures with an IR camera, the tests were constrained to dry cutting conditions. To simplify the study, an uncoated P25 grade carbide (WIDIA TPUN-160308-TTM) was selected to develop the whole text matrix. For each tested conditions and material, at least three repetitions were carried out to ensure reliability of results.

The predefined time increments to measure the fundamental variables and tool wear were selected based on the amount of Material Removed (MR). At specific MR, tool wear and/or cutting forces and tool temperature were recorded. Depending on the cutting condition, the cutting time is different in order to assess an established MR. The same occurs with the cutting length. In Table 3.1 the correlation between MR, cutting length and cutting time is described. In all defined MRs, tool wear was measured. Fundamental variables were only recorded at the times marked in colored cells.

The process parameters and output variables of these orthogonal cutting experiments are summarized in Table 3.2 and Table 3.3 respectively.

Table 3.1: Correlation between MR, cutting length and cutting time depending on the cutting condition. In colored cells are specified the MRs in which fundamental variables were also recorded

	MR (cm^3)	0	80	160	240	320	400	480
V_c=100 m·min^{-1}	Time (min)	0	4	8	12	16	20	24
f=0.1 mm	Length (m)	0	400	800	1200	1600	2000	2400
V_c=100 m·min^{-1}	Time (min)	0	2	4	6	8	10	12
f=0.2 mm	Length (m)	0	200	400	600	800	1000	1200
V_c=200 m·min^{-1}	Time (min)	0	2	4	6	8	10	12
f=0.1 mm	Length (m)	0	400	800	1200	1600	2000	2400
V_c=200 m·min^{-1}	Time (min)	0	1	2	3	4	5	6
f=0.2 mm	Length (m)	0	200	400	600	800	1000	1200

Table 3.2: Process parameters utilized in orthogonal tests

Machine Tool	Fundamental variable	Type	Vertical CNC Milling machine
		Reference	Lagun
		Power	15 kW
		Part Clamping	Special HSK tool holder
		CNC	Fagor 8070 T
		Holding System	HSK 63
	Tool wear	Type	Horizontal CNC Lathe
		Reference	Danobat-Danumeric 2
		Power	30 kW
		Part Clamping	Hard chuck jaws
		CNC	Fagor 8070 T
		Holding System	VDI 40
Cutting Tools		Tool holder (mill)	WIDIA - CTGPR2020K16
		Tool holder (lathe)	WIDIA - CTFPL2525M16
		Insert Tool reference	WIDIA - TPUN160308TTM
		Grade	P25
		Coating	No
		Clearance Angle	6
		Rake Angle	5
		Tip radius	0.4 mm
		Cutting edge radius	40 μm
Workpiece		Geometry	Slotted bar - Orthogonal tube
		Material	16MnCr5, 27MnCr5, C45, C60
		Condition	Isothermal annealed
Cutting Conditions		Operation	Orthogonal turning
		Cutting speed	100-200 $m \cdot min^{-1}$
		Feed	0.1-0.2 mm
		Depth of cut	2 mm

Table 3.3: Output variables measured in orthogonal tests

Fundametal variables	Cutting force	Kistler 9121 dynamometer
	Feed force	Kistler 9121 dynamometer
	Tool temperature	FLIR Titanium 550 IR camera
	Chip thickness	Leica DM IRM microscope
	Contact length	Alicona Infinite Focus G4
Tool wear	Crater depth (K_T)	Alicona Infinite Focus G4
	Crater length (K_B)	Alicona Infinite Focus G4
	Flank wear land (V_B)	Alicona Infinite Focus G4

3.2.2 Procedure to estimate tool surface temperature

Infrared cameras do not directly measure temperature. Each camera detector, depending on the amount of photons received, returns an electrical voltage expressed by default in Digital Levels (DLs), using a transfer function known as Non Uniform Correction (NUC) (Bünger et al. 2015).

The use of a blackbody makes it possible to link DLs with radiation temperature (Soler et al. 2015a). However, a machining tool rarely can be treated as a blackbody, therefore, to obtain real temperature from radiation temperature the emissivity of the radiation surface is commonly characterized (Saunders 2007). This approach involves an uncertainty source for precise IR measurements (Herve et al. 2012; Davies et al. 2003).

In the present case a new calibration method was developed in order to directly relate DLs with real temperature (T) without the need for emissivity correction.

A setup that allows heating tool inserts up to 1000°C in a controlled argon atmosphere was designed. This consisted of a hermetic box, inside which a clamping system for tool inserts was placed. An induction system was employed to heat the insert to the desired temperatures, and was controlled with two thermocouples placed on the measuring surface of the insert. An argon inlet was fixed into the hermetic box to prevent the tool from oxidation and the level of oxygen was controlled with a LuminOx SST sensor. Tool temperatures were recored with a FLIR Titanium 550M camera, placed perpendicular to the surface of the insert on a positioning table. A schematic representation of the setup is shown in Figure 3.31.

The methodology was defined to establish the relationship between surface radiation and real temperature, and fit an interpolating function of (DL,T). This function corresponded to the calibration curve.

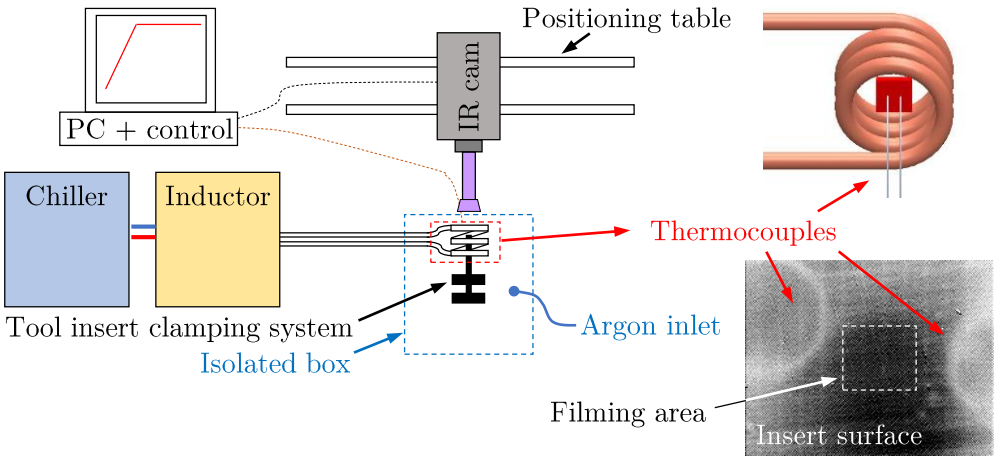

Figure 3.31: Schematic representation of the calibration setup

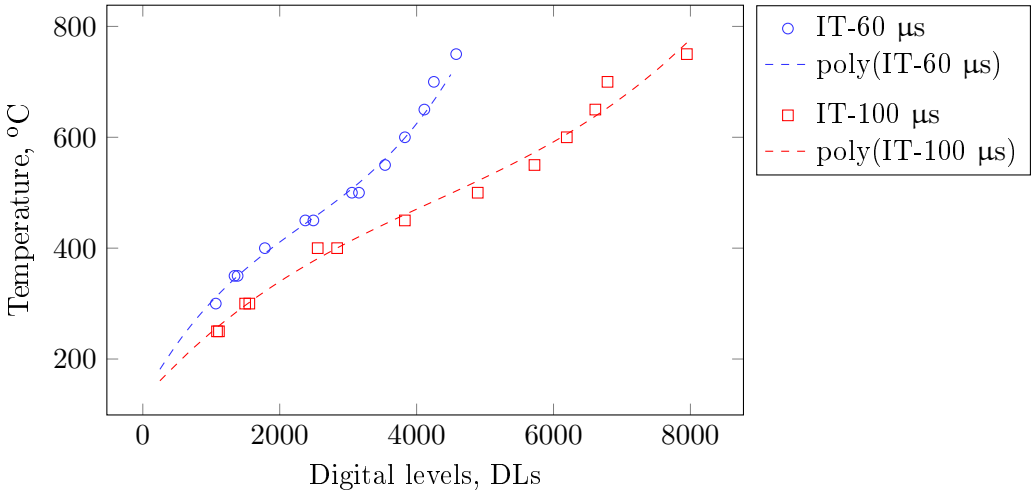

Figure 3.32: Experimental data and fitted polynomials of (T, DLs) for each employed IT

In this procedure the calibration was performed under the same experimental conditions (integration time-IT, optical path, field of view) as those used during the cutting process. Thus, the introduction of new uncertainty sources was prevented.

The procedure was applied to characterize the employed insert WIDIA TPUN-160308-TTM. The calibration procedure was carried out on the two ITs employed in the IR measurements of the orthogonal tests, 60 and 100 µs. The resultant data and fitted polynomials are shown in Figure 3.32.

The obtained results showed almost no deviation between the two repetitions that were carried out for each of the ITs. The fitted polynomials are presented in Eq. 3.6 and Eq. 3.7.

$$T_{\mathrm{IT60}} = 8.15 \cdot 10^{-9} DL^3 - 5.74 \cdot 10^{-5} DL^2 + 0.22\, DL + 129.13 \tag{3.6}$$

$$T_{\mathrm{IT100}} = 1.51 \cdot 10^{-9} DL^3 - 1.93 \cdot 10^{-5} DL^2 + 0.13\, DL + 127.16 \tag{3.7}$$

3.3 Analysis of tool wear

This section analyses the influence that workpiece materials and selected cutting conditions have on tool wear. First, an overview of the obtained results is described. Second, the evolution of the most relevant wear modes, flank wear and crater wear, are presented and discussed. In the case of crater wear another two modes were distinguished, the crater depth and the crater length.

3.3.1 Methodology for tool wear analysis

To establish K_T, K_B and V_B, from each captured 3D geometry of the worn tool the profile of the mid plane of the contact section was extracted. The localization and an example of a profile is shown in Figure 3.33. The measured wear modes are specified in the profile.

To establish the wear rate the same criteria presented by Klocke and Frank (2006) was adopted. As discussed in the following, when plotting the evolution of wear depending on time or depending on the length of cut, three regions were distinguished. First, a large increase in wear occurred, usually linked to the first asperities contacting with the surface of the fresh tool. This sudden increase was followed by a constant wear increase, which was named the steady state tool wear. It is this region in which the wear rate was established. Finally, another severe wear increase before reaching the tool life end occurred. These differentiated regions are described in Figure 3.34. To calculate the wear rate, the slope of the wear evolution in the steady state range was calculated.

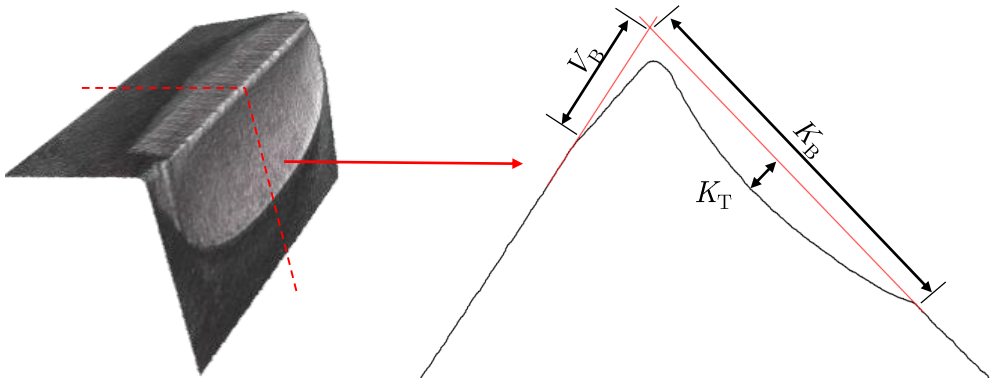

Figure 3.33: Example of the localization and the wear modes of a wear profile

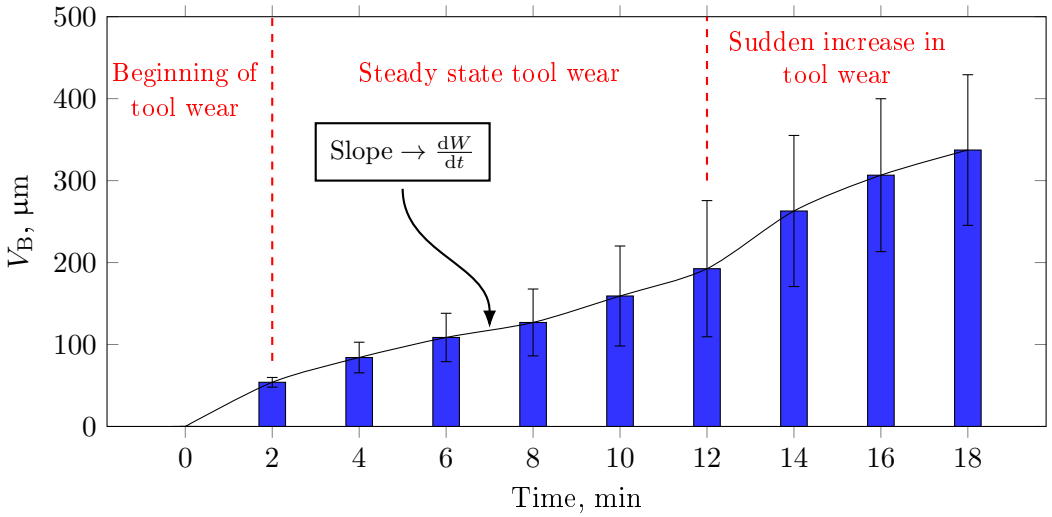

Figure 3.34: Evolution of flank wear for the C45 steel at V_c=200 m·min^{-1} and f=0.1 mm

The influence that feed and cutting speed had on tool wear was also analyzed. The individual influence of a variable, or the effect a variable has on a predefined output, is defined as the variation that is generated on a established output when changing a variable from one value to another value (in this case the variables are the feed and cutting speed). An example to calculate the effect that cutting speed has on V_B is presented in Eq. 3.8. This procedure was applied for both V_B and K_T in the analysis.

$$\begin{aligned} Ef(V_c \rightarrow V_B) &= \text{avg}(200\,\text{m·min}^{-1}) - \text{avg}(100\,\text{m·min}^{-1}) = \\ &= \tfrac{423+351}{2} - \tfrac{253+244}{2} = 139\,\mu\text{m} = 43\% \end{aligned} \tag{3.8}$$

3.3.2 Overview of tool wear results

In Appendix B, in Figures B.1, B.2, B.3 and B.4, the images from the profilometer showing the top view of flank and crater wear are depicted at different Material Removed (MR) states for each of the tested cutting conditions and materials. In addition, the evolution of the profile of the worn tool is also plotted for each condition.

From the whole test matrix, only those of the C45 an C60 were successfully assessed. In all tested conditions, the wear on the tool did not present any severe notching or catastrophic tool breakage. Examples of wear evolution in 2D and the evolution of the worn profiles are shown in Figure B.3 and B.4 for the C45 and C60 steels respectively.

In contrast, 16MnCr5 and 27MnCr5 presented severe difficulties when machining at the condition of V_c=100 m·min^{-1}. At both selected feeds of 0.1 and 0.2 mm, notching and catastrophic edge breakage occurred in nearly all the trials. At V_c=100 m·min^{-1} and f=0.1 mm it was possible to extract information from at least one repetition, whereas

in the case of V_c=100 m·min^{-1} and f=0.2 mm no data was obtained. An example of notch or fragile rupture of the tool insert is shown in Figure 3.35. This type of wear could be caused by a severe chattering effect (primary chatter) which probably was due to the higher friction and shear forces occurred at this cutting condition (Siddhpura and Paurobally 2012).

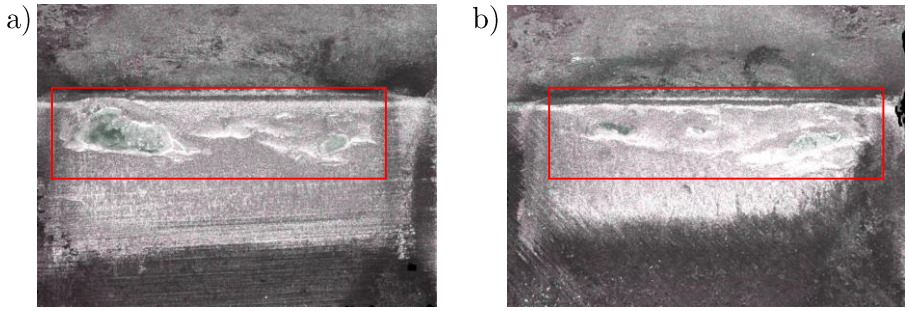

Figure 3.35: Notch or fragile rupture of tool insert at V_c=100 m·min^{-1} and f=0.2 mm when machining (a) 16MnCr5 and (b) 27MnCr5 at a MR of 320 cm^3 or 4 min of cutting

3.3.3 Analysis of flank wear

Flank wear analysis is set out as follows: First, the morphology of the flank wear pattern is described. Next, the flank wear is discussed in terms of FP steels and cutting conditions. Then, the analysis of wear rate is presented, and finally the main results are discussed.

- Morphology of the flank wear

The flank wear presented a rectangular shape in all tested cases, as shown in Figures B.1, B.2, B.3 and B.4. This was slightly wider than the width of cut (5-10%) due to the increase of chip width when cutting. In contrast, the length of the flank wear land (V_B) varied depending on the cutting condition and tested material. An exam-

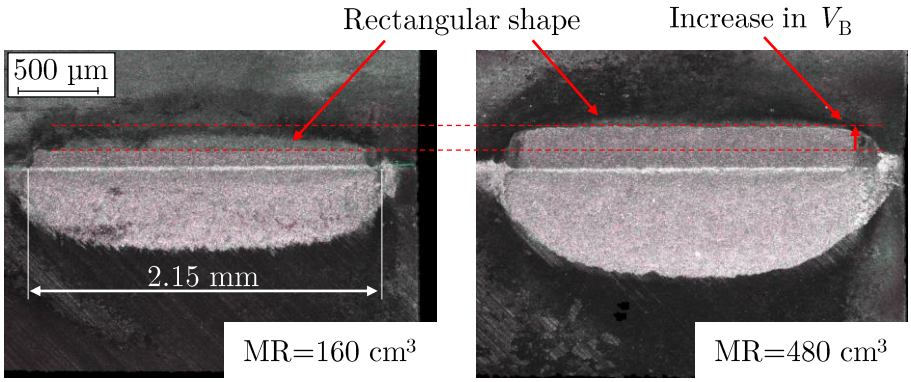

Figure 3.36: Evolution and geometry of flank wear when cutting the C45 steel at V_c=200 m·min^{-1} f=0.2 mm

ple of the geometry and the evolution of the flank wear when machining the C45 at V_c=200 m·min^{-1} and f=0.2 mm is shown in Figure 3.36.

Another relevant geometric data is the angle that is formed between the worn and the original flank surfaces. This was found to be the same for all the FP steels, and independent of the cutting condition. The angle converged to a value of 8-9°once it was stabilized. This was better observed when machining at the conditions in which a large amount of flank wear occurred. A comparison after removing 480 cm^3 at V_c=200 m·min^{-1} and f=0.2 mm is depicted in Figure 3.37. Although the degree of V_B is clearly different, the worn surfaces of all the materials are parallel. Taking into account that the real clearance angle during the process is 6°, the generated worn flank face is almost parallel to the machined surface.

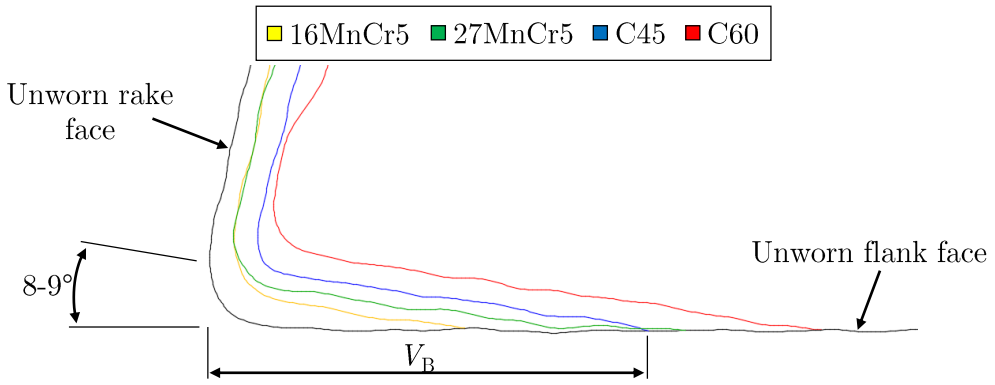

Figure 3.37: Comparison of tool wear profiles at V_c=200 m·min^{-1} and f=0.2 mm (MR=480 cm^3)

- Influence of FP steels on flank wear

The evolution of V_B depending on the amount of material removed for all the steels and cutting conditions is plotted in Figure 3.38.

Qualitatively, up to the selected MR (or cutting time) the V_B evolution was almost constant, and did not reach the limit at which a sudden increase is occurred (Klocke and Frank 2006). The deviations of the repetitions were considerably high compared to other variables tested in this research. Depending on the material, it was observed that the commonly established maximum V_B of 300 µm was overcome but, as discussed previously, the wear evolution was still constant and therefore those results were included in the analysis.

Concerning the influence that workpiece material had on V_B, at all comparable cutting conditions nearly the same pattern was found. In the first stage of the tests, at the MR of 80 and even 160 cm^3, the V_B of the 16MnCr5 and 27MnCr5 steels was greater than or similar to the C45 and C60. This is specified with green arrows in Figure 3.38. Once the amount of MR was increased (or cutting time was increased) the resultant V_B when cutting the C45 and C60 steels began to be greater than that of 16MnCr5 and 27MnCr5 (orange arrows). The greatest wear was achieved in the case of the C60, followed by

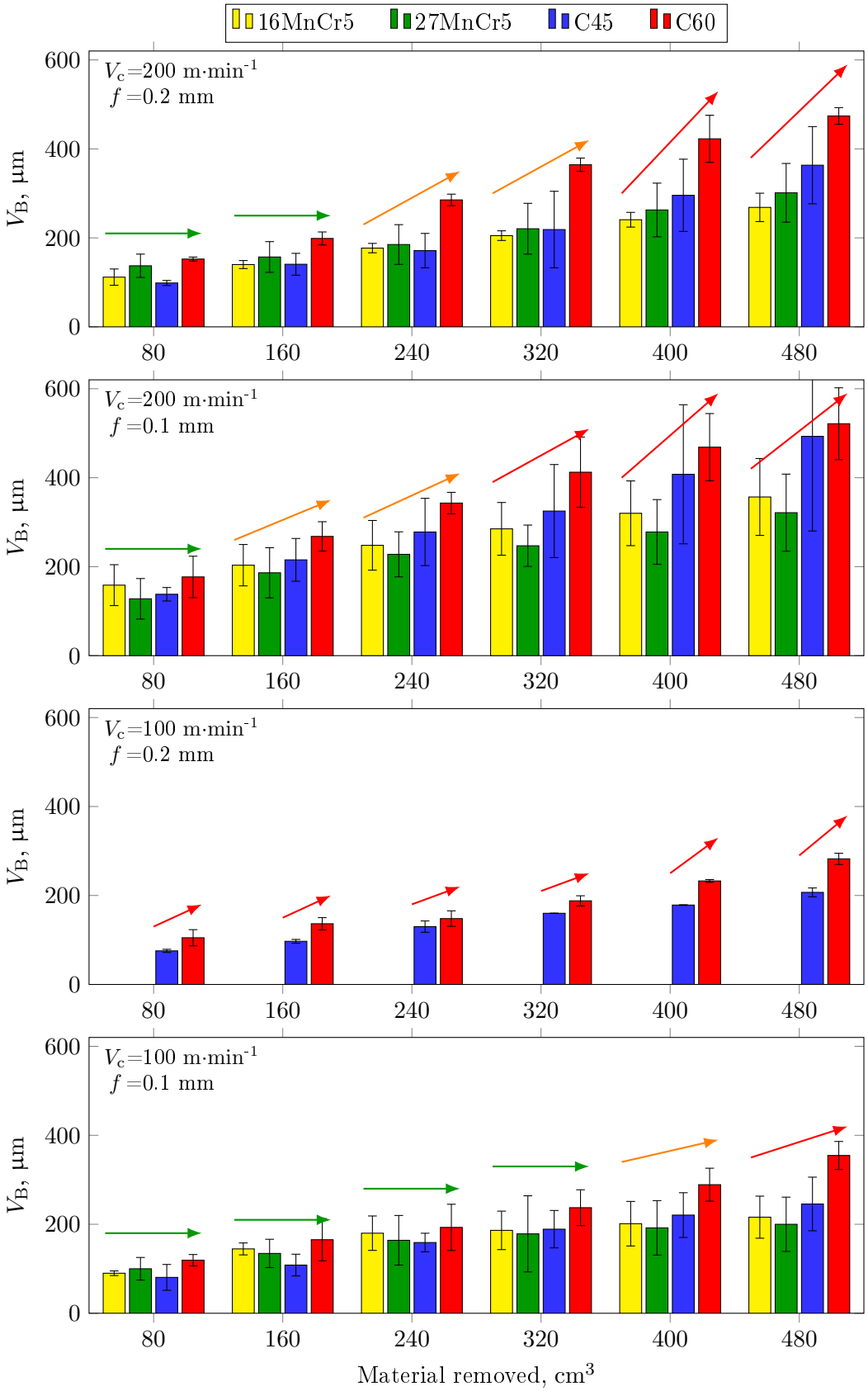

Figure 3.38: Evolution of V_B for all FP steels at all tested cutting conditions

the C45 (red arrows). The maximum V_B by the end of the tests (MR=480 cm^3) was observed at V_c=200 m·min^{-1} and f=0.1 mm. The V_B when machining the C60 was 520 µm, followed by the C45, the 16MnCr5 and the 27MnCr5. The maximum V_B of these latter three steels was 495, 355 and 320 µm respectively.

An in-depth analysis of the wear of 16MnCr5 and 27MnCr5 revealed an unexpected behavior. At V_c=100 and 200 m·min^{-1} and f=0.1 mm the V_B was higher in the 16MnCr5, in spite of its lower pearlite content and the same inclusion status. However, the difference between these two steels was less than 40 µm in the worst of the cases.

Regarding the results of C45 and C60, in all tested conditions the V_B of the C60 was higher than the C45. These results were in line with the literature, which stated that an incresae in pearlite directly drives an increase in flank wear (Opitz and Gappisch 1962; Ozcatalbas and Ercan 2003; Björkeborn et al. 2010). The greatest difference between these two steels was 90 µm.

Table 3.4 summarizes the V_B results at the end of the trials, when an MR of 480 cm^3 was reached. Two data sets are given, the V_B value and the relative % compared to the C45 steel. This latter was selected as the reference steel for all the comparisons presented in this research, as it is one of the most widely used and investigated materials in machining processes. In summary, the C60 steel experienced a 39% greater V_B than the reference C45 steel. The greatest difference was found at V_c=100 m·min^{-1} and f=0.1 mm. In contrast, 16MnCr5 and 27CrMn5 achieved a lower V_B, with an average ratio of 22% and 23% respectively.

- Influence of cutting conditions on flank wear

In order to define in general terms the individual influence that feed and cutting speed had on V_B, the average values of V_B for each cutting condition were calculated. These are shown in the colored cells in Table 3.4.

Table 3.4: V_B results (µm) and comparison with C45 reference steel (%) after an MR of 480 cm^3. In colored cells: Average V_B value (µm) for each tested cutting condition

	16MnCr5	27MnCr5	C45	C60	Average
V_c=100 m·min^{-1} f=0.1 mm	215±45 -12%	200±60 -18%	245±60 *Ref.*	355±30 +44%	255±50
V_c=100 m·min^{-1} f=0.2 mm	—	—	205±10 *Ref.*	280±10 +36%	245±10
V_c=200 m·min^{-1} f=0.1 mm	355±85 -28%	320±85 -35%	495±210 *Ref.*	520±80 +6%	425±115
V_c=200 m·min^{-1} f=0.2 mm	270±30 -26%	300±65 -17%	365±85 *Ref.*	475±20 +30%	350±50
Average	-22%	-23%	*Ref.*	+39%	315±55

It was calculated that increasing the cutting speed from 100 to 200 m·min^{-1}, generated an overall increase of 43% in V_B. In contrast, increasing the feed from 0.1 to 0.2 mm, caused a decrease of 13% in V_B. Thus, it was possible to conclude that flank wear was more sensitive to the cutting speed. However, it is important to note that the influence that cutting conditions had on V_B was established after machining the same amount of material in each of the tests. When the comparison was made after machining a length of cut of 1200 m, increasing the cutting speed caused V_B to increase by 40%, and increasing the feed also provoked a rise in V_B of 28%. Therefore, the results from both cases showed that V_B was consistently more sensitive to cutting speed, but for an specific length of cut increasing the feed was also detrimental.

- Flank wear rate depending on cutting time and length of cut

Following the methodology explained at the beginning of this section, for each material $\frac{dV_B}{dt}$ and $\frac{dV_B}{dL}$ were obtained by calculating the slope of the regression of (V_B, t) and (V_B, L) in the steady state wear range.

The wear rate of the C45 and C60 was in line with what was expected. At nearly all cutting conditions, $\frac{dV_B}{dt}$ and $\frac{dV_B}{dL}$ of the C60 were greater than the other steels, followed by the C45. The maximum wear rates occurred at V_c=200 m·min^{-1} and f=0.2 mm. Machining the C60 resulted in a $\frac{dV_B}{dt}$=68 µm·min^{-1}, followed by the C45, 27MnCr5 and 16MnCr5 with rates of 52, 34 and 32 µm·min^{-1} respectively. The rate of wear when cutting the 16MnCr5 and 27MnCr5 presented diverse results depending on the tested condition. Unexpectedly, at the feed of 0.1 mm, the wear rates of the former were greater than that of the latter.

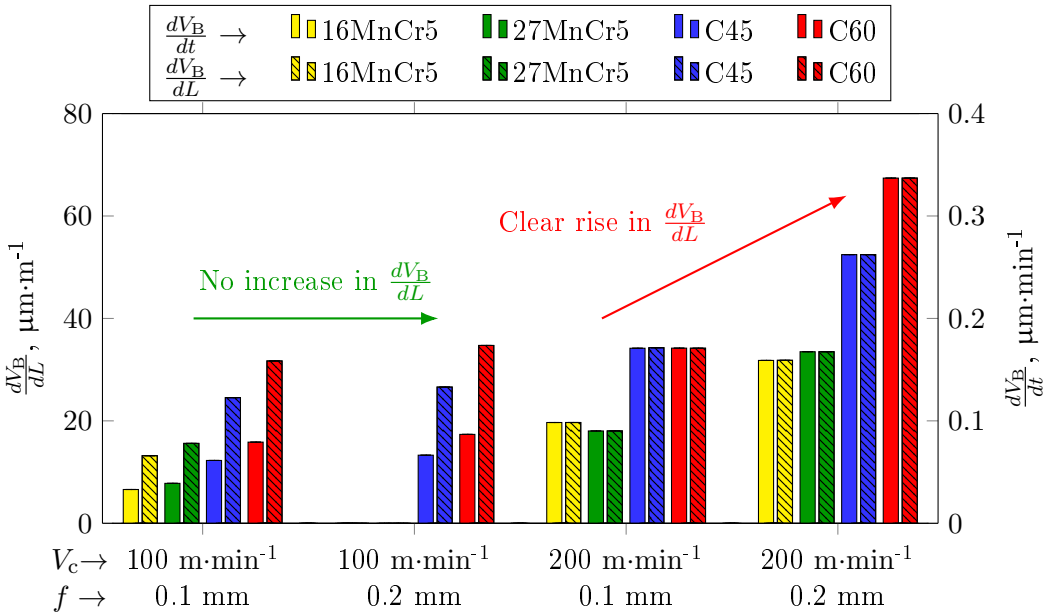

Figure 3.39: Flank wear rate at all tested cutting conditions

As shown in Figure 3.39, when the cutting speed was increased in the tests at f=0.1 mm a slight increase in $\frac{dV_B}{dL}$ occurred. Furthermore, when the tests developed at f=0.2 mm were analyzed, increasing the cutting speed caused a significant rise in $\frac{dV_B}{dL}$. The rise in $\frac{dV_B}{dL}$ was the greatest in the case of the C60, with $\Delta\frac{dV_B}{dL}$=33 $\mu m \cdot m^{-1}$. This was followed by the C45, 27MnCr5 and 16MnCr5.

- Discussion of V_B results

In general, V_B results were in line with those reported in the literature. By the end of the trials, the steels with higher pearlite content, or higher strength, provoked a greater degree of wear in almost all cases (Björkeborn et al. 2008; Ozcatalbas and Ercan 2003; Trent and Wright 2000).

The unexpected results observed at the beginning of the tests, in which the V_B of 16MnCr5 and 27MnCr5 was higher than that of the C45 and C60, could be linked to various hypothesis. At the first stage, the adhesive effect of ferrite and the abrasive effect of the Al_2O_3 inclusions found on the 16MnCr5 and 27MnCr could be overcoming the abrasive effect of pearlite (Trent and Wright 2000; Mian et al. 2010). Therefore, the initial V_B was higher in the 16MnCr5 and 27MnCr5, although those were the steels with lower pearlite content. Nevertheless, as the wear rate of C45 and C60 was higher than that of the 16MnCr5 and 27MnCr5, above a certain amount of MR the V_B of the two former steels became higher.

Linked to the conclusions drawn from the literature, a lower interlamellar spacing was directly related to an increase in tool wear (Björkeborn et al. 2010; Ozcatalbas and Ercan 2003). Thus, the short interlamellar spacing of pearlite and the extremely high degree of pearlite banding found in the 16MnCr5 (see Section 2.3.2) could be one of the reasons the 16MnCr5 presented greater V_B and wear rate than that of the 27MnCr5. The effect was more severe when machining at 0.1 mm feed, as the ratio grain size-uncut chip thickness was increased, which probably derived in more significant interactions between the grain structure and the tool.

The wear rate depending on length of cut, $\frac{dV_B}{dL}$, gave remarkable results from the point of view of wear phenomena. If the wear type had been purely mechanical, affected by an abrasive mechanism, $\frac{dV_B}{dL}$ should have had the same value when comparing the tests at a specific feed and different cutting speeds. However, when cutting at the feed of 0.2 mm, increasing the cutting speed caused a significant rise in $\frac{dV_B}{dL}$. These results suggest that V_B was not only affected by an abrasive mechanism, but also by other mechanisms such as thermal diffusivity. Increasing cutting speeds and increasing feeds are usually linked to higher tool-workpiece contact temperatures (Trent and Wright 2000). A high degree of temperature may produce enough energy to activate a thermal wear mechanism, and therefore rapidly increase the wear rate (Takeyama and Murata 1963).

3.3.4 Analysis of crater wear

In the following lines a qualitative analysis of the morphology of the crater wear is presented. Then, the results of the crater depth (K_T) and crater length (K_B) are analyzed and discussed as related to workpiece material and selected cutting conditions.

- Morphology of the crater wear

The crater presented as a type of concavity on the rake face of the tool. The depth of this concave is the crater depth (K_T), and length refers to the crater length (K_B). This is observed in the profiles depicted in Appendix B (Figures B.1, B.2, B.3 and B.4). Depending on the tested material, cutting condition and amount of MR, the crater had a rectangular or semicircular form. This shape was linked to the amount of wear generated on the rake face. When the wear was low, the morphology was similar to a rectangle, which turned into a semicircular form as the wear increased. In Figure 3.40 a comparison between the rounded crater of C45 steel and the rectangular crater of the 16MnCr5 is shown.

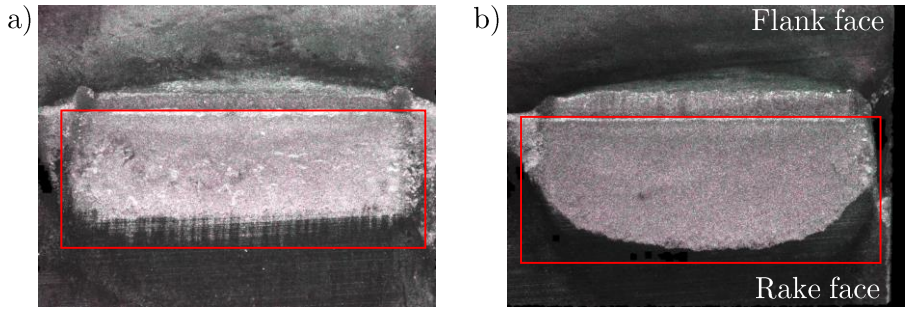

Figure 3.40: Comparison of crater wear between (a) 16MnCr5 and (b) C45 at V_c=200 m·min^{-1} and f=0.2 mm (MR=480 cm^3)

A comparison of the worn profile between the FP steels is shown in Figure 3.41. From these profiles it was possible to extract some general conclusions. Three main regions

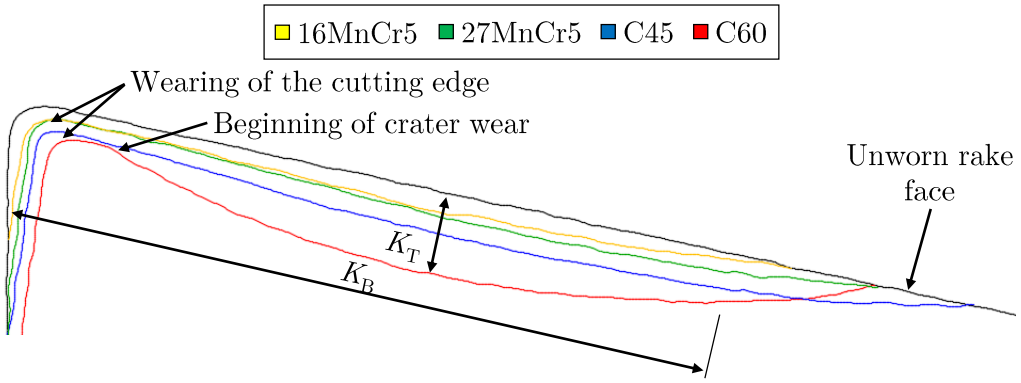

Figure 3.41: Comparison of crater wear profiles at V_c=200 m·min^{-1} and f=0.2 mm (MR=480 cm^3)

were distinguished, the cutting edge (or the new formed cutting edge), the concave form of the crater, and the unworn rake surface. In all the cases, a new cutting edge was formed due to wear. The location of this new cutting edge depended on the amount of flank wear and the amount of wear on the rake face. Moving from this new cutting edge towards the rake face, the concave shape of the crater was localized, in which K_T and K_B are distinguished. Once the end of the crater is reached, the unworn surface of the rake face can be observed.

- Influence of FP steels on crater wear depth

The evolution of the K_T function of the amount of material removed for all the steels and cutting conditions is plotted in Figure 3.42

Qualitatively, the evolution of K_T was stable in all cases, without reaching any sudden rise in wear. The deviations in K_T between repetitions were lower compared to those of V_B. Only at V_c=100 m·min^{-1} and f=0.1 mm were the deviations higher compared to the other tested conditions. As mentioned in the overview, it was not possible to extract results from V_c=100 m·min^{-1} and f=0.2 mm for the 16MnCr5 and 27MnCr5, and in the case of 16MnCr5 the crater was almost negligible at V_c=100 m·min^{-1} and f=0.1 mm.

Concerning the influence that workpiece material had on K_T, the same trend occurred in all analyzed cutting conditions. From the beginning to the end of the tests, the greatest K_T was found when machining the C60, followed in decreasing order by the C45, 27MnCr5 and 16MnCr5. To analyze in more depth the achieved results, the K_T values at the end of the trials are summarized in Table 3.5. Two data sets are given, the K_T value and the relative % compared to the C45 steel.

The greatest K_T was found at the condition of V_c=200 m·min^{-1} and f=0.2 mm when cutting any of the steels. The measured K_T in the case of the C60 was 123 µm, followed

Table 3.5: K_T results (µm) and comparison with C45 reference steel (%) of K_T (MR=480 cm^3). In colored cells: average K_T result for each tested cutting condition

	16MnCr5	27MnCr5	C45	C60	Average
V_c=100 m·min^{-1} f=0.1 mm	∼0	15 -40%	25±8 *Ref.*	35±10 +40%	25±9
V_c=100 m·min^{-1} f=0.2 mm	—	—	15±5 *Ref.*	25±5 +35%	20±5
V_c=200 m·min^{-1} f=0.1 mm	25±5 -60%	30±5 -48%	60±5 *Ref.*	80±5 +37%	50±5
V_c=200 m·min^{-1} f=0.2 mm	30±5 -40%	40±10 -33%	70±15 *Ref.*	120±15 +57%	65±10
Average	-50%	-40%	*Ref.*	+42%	40±10

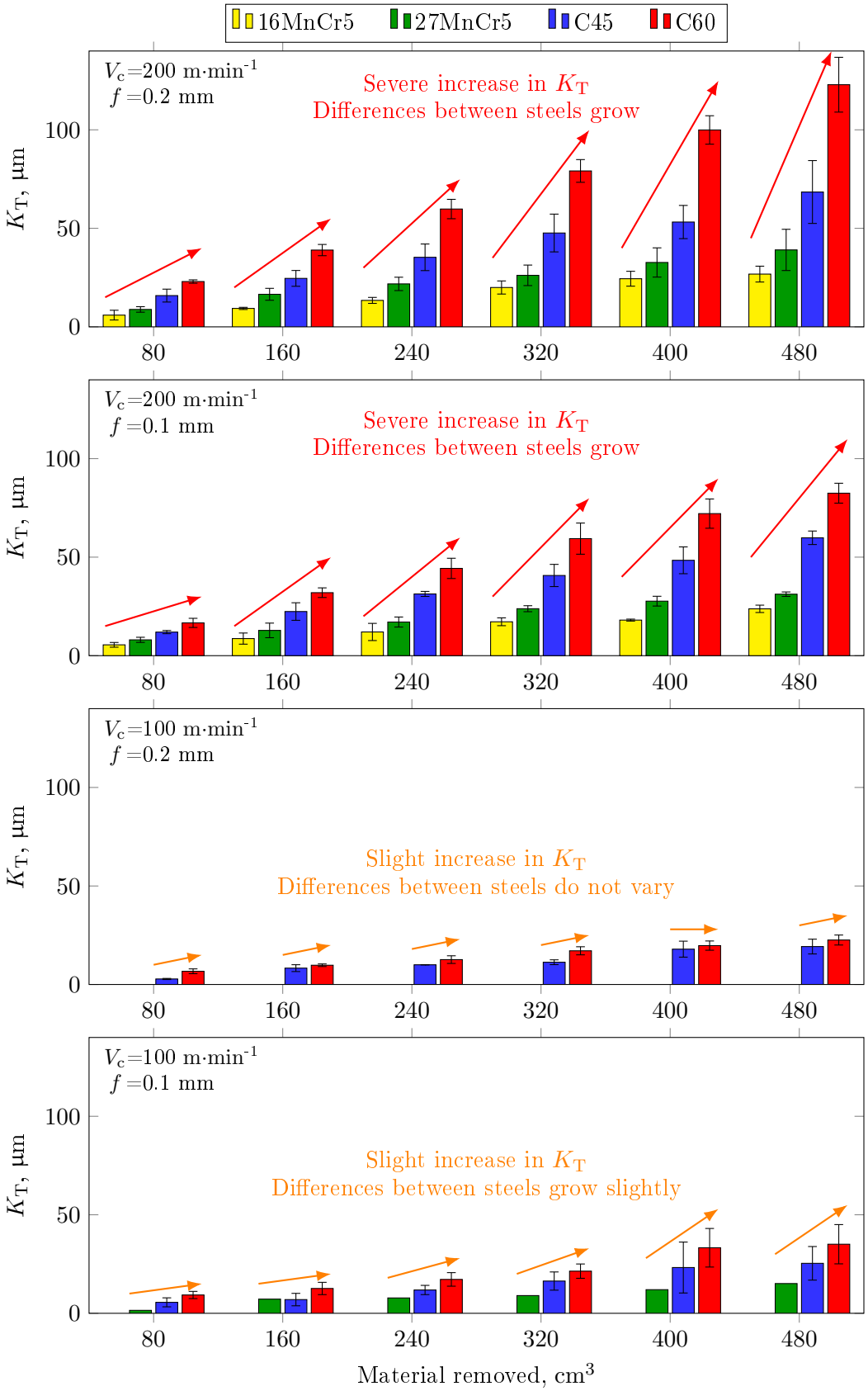

Figure 3.42: Evolution of K_T for all FP steels at all tested cutting conditions

by the C45, 27MnCr5 and 16MnCr5. The K_T of these latter were 68, 39 and 27 µm respectively. The lowest or even negligible K_T was achieved for the 16MnCr5 when cutting at V_c=100 m·min^{-1} and f=0.1 mm. In this latter condition the maximum K_T achieved in the case of the C60 was 35 µm.

Comparing the results with the reference C45 steel, the average difference with the C60 was a 42% greater K_T. This ratio was similar in all conditions, except at V_c=200 m·min^{-1} and f=0.2 mm in which the difference was higher, with values of K_T up to 57% greater. The 27MnCr5 presented an average K_T with depths 40% less than the C45. In the measurable conditions when comparing the C45 with the 16MnCr5, the average difference was 50% lower.

- Influence of cutting conditions on crater wear depth

The individual effect of feed and cutting speed was calculated following the same procedure presented in Eq. 3.8 with the data summarized in the colored cells in Table 3.5. Increasing the feed from 0.1 to 0.2 mm generated an increase of 13% in K_T, whereas varying the cutting speed from 100 to 200 m·min^{-1} achieved an increase of 85%. From these results it was concluded that K_T was much more sensitive to the cutting speed than to the feed after machining 480 cm^3. If the same comparison is done in terms of length of cut, after machining 1200 m of workpiece material, it was concluded that increasing the cutting speed provoked an increase of 23% in K_T, while increasing the feed a 18%. The results demonstrated therefore, that K_T was still more sensitive to cutting speed, but its influence compared to that of feed was lesser.

- Crater depth rate depending on cutting time and length of cut

The wear rate of K_T depending on time and length of cut was calculated ($\frac{dK_T}{dt}$ and $\frac{dK_T}{dL}$) in the range of steady state wear.

From the regressions it was gathered that C60 was the steel that provoked the highest rate of increase in K_T, followed by the C45, 27MnCr5 and 16MnCr5. This was assessed at all tested conditions, which is described in Figure 3.43. At V_c=200 m·min^{-1} and f=0.2 mm the maximum $\frac{dK_T}{dt}$ and $\frac{dK_T}{dL}$ was found to occur in all the steels. A maximum $\frac{dK_T}{dL}$=0.1 µm·m^{-1} was measured in the case of C60. At this specific condition, machining C60 caused a greater K_T rate of 93% compared to machining the C45, while the 27MnCr5 and 16MnCr5 steels obtained a 44% and 56% lower rate, respectively. The rates between the steels differ to a lower degree in the other cutting conditions.

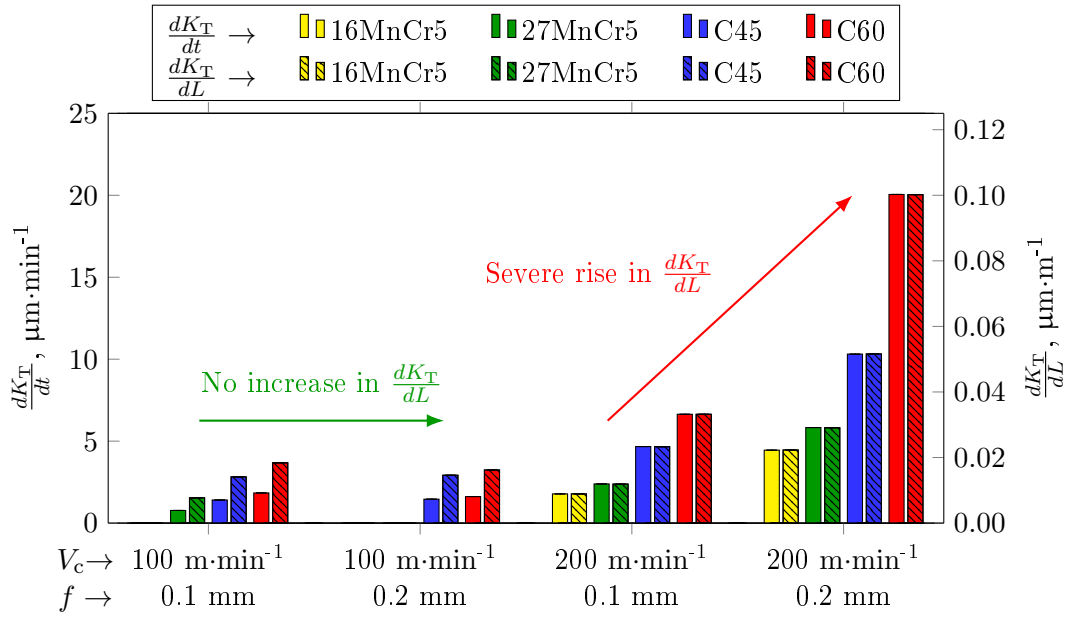

Figure 3.43: Crater depth rate at all tested cutting conditions

- Discussion of K_T results

In general, the greater the amount of pearlite, or the greater the %C the material had, the grater the K_T, $\frac{dK_T}{dt}$ and $\frac{dK_T}{dL}$. This was in line with the literature (Ozcatalbas and Ercan 2003), and might be related to the temperature generated in the rake face (Padilla Montes 2011). Steels with higher carbon content tend to reach greater temperature when cutting (Milovic and Wallbank 1983), therefore promoting the generation of diffusive wear.

Results of $\frac{dK_T}{dL}$ were in line with the abovementioned statements, and suggested that K_T did not only depend on a mechanical type of wear such as abrasion but also to other thermal mechanisms. This was concluded as the increase in cutting speed at 0.2 mm feed generated an increase in $\frac{dK_T}{dL}$. It could also be concluded that K_T was more affected by thermal activated mechanisms such as diffusion than V_B was. This is consistent with the literature, as the temperatures in the rake face are usually higher than in the flank face due to the intense friction stresses taking place in the tool-chip interface (Trent and Wright 2000).

- Influence of FP steels on crater wear length

The evolution of K_B depending on the MR for all steels and cutting conditions is shown in Figure 3.44

In general terms, the results were consistent as they did not present large deviations between the repetitions carried out. As in the other analyzed wear variables, at V_c=100 m·min^{-1} and f=0.2 mm it was not possible to extract reliable data for the 16MnCr5 and 27MnCr5.

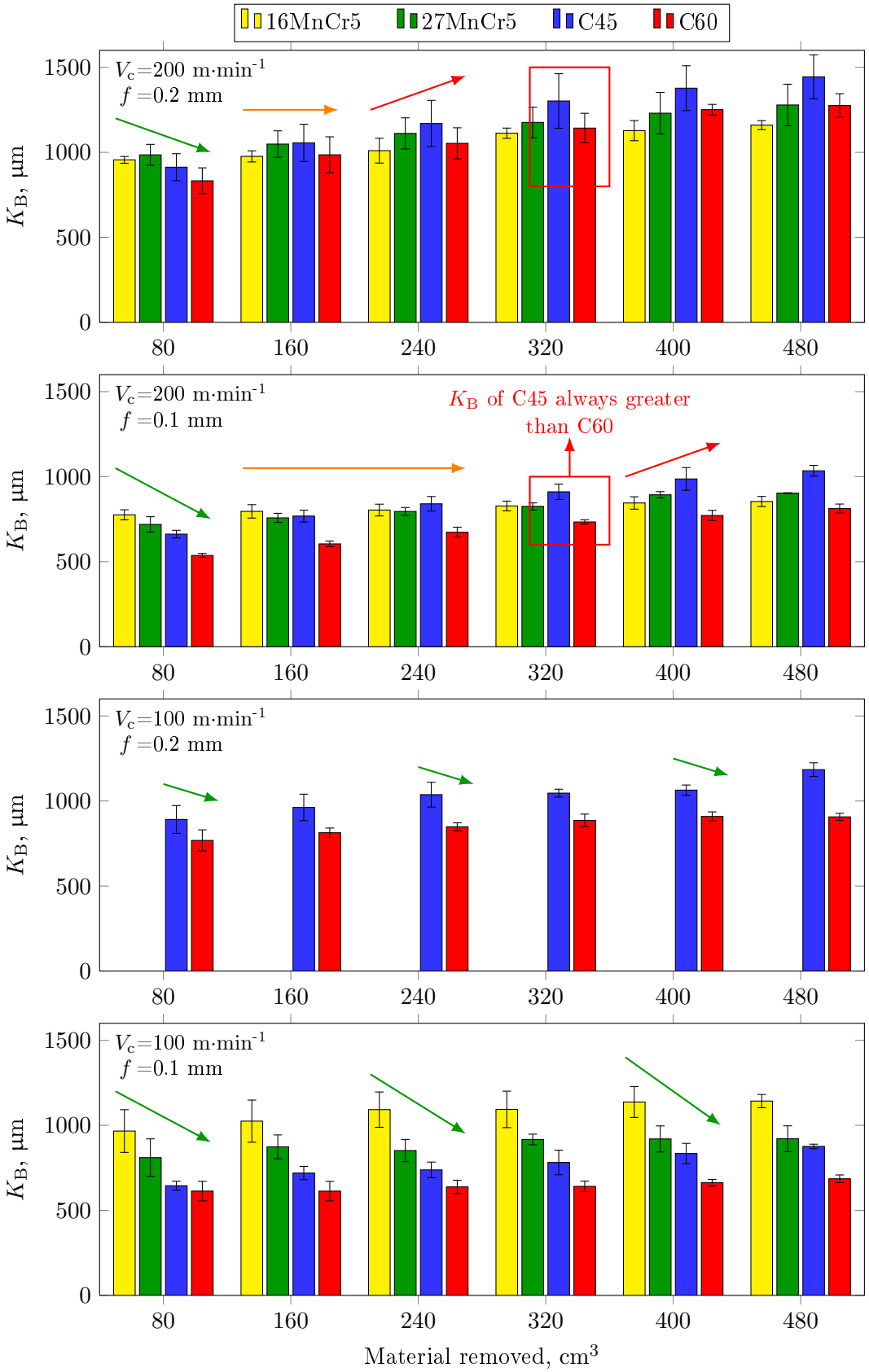

Figure 3.44: Evolution of crater wear length for all FP steels at all tested cutting conditions

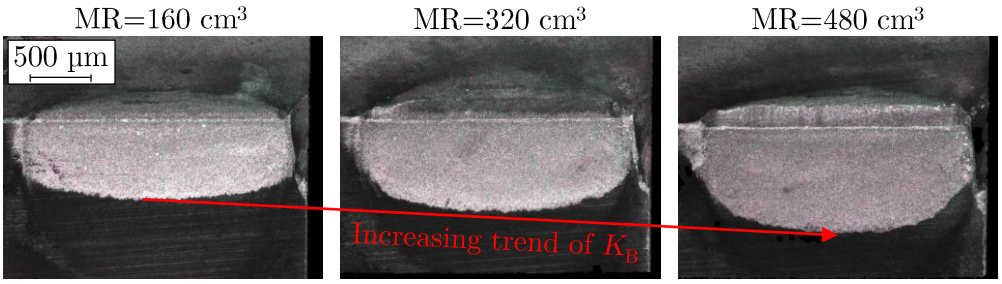

Figure 3.45: Increasing trend of K_B in the case of the C45 steel at V_c=200 m·min^{-1} and f=0.2 mm

In general, K_B presented an increasing trend during the wear tests. This varied depending on the material and cutting condition, and tended to stabilize by the end of the tests. An example of increasing K_B is shown in Figure 3.45 for the C45 steel when machined at V_c=200 m·min^{-1} and f=0.2 mm. It was at this specific cutting condition and in this material where the longest contact was found, with a value of 1.44 mm after removing 480 cm^3 of workpiece material. In addition, all the tests showed a remarkably long K_B, which were between 5.3 to 10 times the uncut chip thickness.

The influence that FP steels had on K_B varied depending on the cutting condition, and also seemed to be dependent on the depth of the crater rather than on the amount of material removed (or cutting time). Thus, different behaviors were observed during the tests. When K_T was not severe, the highest K_B was mostly occurred when cutting the 16MnCr5, followed in decreasing order by the 27MnCr5, C45 and C60 (green arrows in Figure 3.44). Such was the case when cutting at V_c=100 m·min^{-1} and f=0.1 mm up to the MR of 480 cm^3. In contrast, when cutting at V_c=200 m·min^{-1} and f=0.1 and 0.2 mm, conditions in which a severe K_T occurred, the abovementioned trend almost reversed above a certain point. When the MR was increased, K_B tended to result in the same value when cutting any of the steels (orange arrows in Figure 3.44). After that, the steels with greater K_T developed the greatest K_B (red arrows in Figure 3.44). This new trend continued when cutting the 16MnCr5, 27MnCr5 and C45, achieving the greatest K_B in the case of the latter. When machining the C60, an increase in K_B was also observed with increasing MR. For example at the condition of V_c=200 m·min^{-1} and f=0.2 mm the K_B of the C60 was greater than that of 16MnCr5 and 27MnCr5, but not of the C45. The largest increase in K_B occurred at V_c=200 m·min^{-1} and f=0.2 mm for the C45 steel. When machining this steel, the K_B varied from 0.91 to 1.44 mm, which is an increase of 58%. Under the same condition, the increase in K_B of C60, 27MnCr5 and 16MnCr5 was of 53%, 29% and 21% respectively. When the condition of V_c=100 m·min^{-1} and f=0.1 mm was analyzed, although the trends of longer or shorter K_B did not vary between the steels, the K_B still increased during the tests. The ratio of K_B increase was 18% for the 16MnCr5, 13% for the 27MnCr5, 36% for the C45 and 12% for the C60.

- Influence of cutting conditions on crater wear length

It is well known that increasing feed provokes a direct increase on the contact length. For this reason, the K_B was normalized with the uncut chip thickness or feed (t_2) in order to permit a comparison between the different cutting conditions. In Table 3.6 the K_B/t_2 are summarized for each cutting condition when a MR of 480 cm^3 was reached. On the whole, increasing the cutting speed involved in an increase of 8% of the ratio K_B/t_2. The feed had a greater influence, decreasing the ratio by 42%.

Table 3.6: Influence that cutting conditions have on K_B/t_2

V_c (m·min^{-1})	100	100	200	200	
f (mm)	0.1	0.2	0.1	0.2	
16MnCr5	11.4+0.4	—	8.5+0.3	5.8+0.1	
27MnCr5	9.2+0.8	—	9+0.1	6.4+0.6	
C45	8.8+0.1	5.9+0.2	10.3+0.3	7.2+0.6	
C60	6.9+0.2	4.5+0.1	8.1+0.3	6.4+0.3	
Average	9.1+0.4	5.2+0.15	9+0.3	6.5+0.4	7.5+0.3

- Discussion of K_B results

It was almost certain that, in the first stage of the tests, K_B (or contact length) was linked to the ferrite content in all the cutting conditions. As described by Trent and Wright (2000), and also addressed in this study, the contact length increased together with the ferrite content of the material. However, the variation observed in trends at the most severe conditions showed that K_B (or contact length) was not always linked to ferrite content, but also to the degree of wear on the rake. No studies were found in the literature in which similar phenomena were observed.

The K_B achieved when machining the C60 was always lower than the C45. It is believed that the K_B results when processing the C60 were limited by the extremely high degree of K_T, as the deep concavity formed on the rake face did not allow the K_B to increase as in the case of the other materials.

Moreover, all the tests showed a remarkably long K_B, which could be attributed to the high friction stresses on the tool-chip interface due to the selected uncoated carbide insert, as measured experimentally by Rech and Courbon (2017).

3.3.5 Summary of wear results

A summary of wear results is presented in Table 3.7.

Table 3.7: Summary of wear results

	Trends and morphology	Influence of material Analysis of wear rate	Influence of cutting conditions
Flank wear (V_B)	• Rectangular shape in all cases • Worn flank face almost parallel to machined surface • $V_B \Rightarrow$ mechanical and thermal mechanisms	• MR<80-160 cm^3: $\uparrow f_f \Rightarrow \uparrow V_B$ MR>80-160 cm^3: $\uparrow f_p \Rightarrow \uparrow V_B$ • V_B compared to C45: ↑39% C60, ↓22% 27MnCr5, ↓23% 16MnCr5 • $\frac{dV_B}{dL} \Rightarrow$ C60 followed by C45 $\frac{dV_B}{dL}_{16MnCr5} \simeq \frac{dV_B}{dL}_{27MnCr5}$	• After MR=480 cm^3: $\uparrow V_c \Rightarrow \uparrow 43\% V_B$ $\uparrow f \Rightarrow \downarrow 13\% V_B$ • After L=1200 m: $\uparrow V_c \Rightarrow \uparrow 40\% V_B$ $\uparrow f \Rightarrow \uparrow 28\% V_B$
Crater depth (K_T)	• Concave shape which depends on the degree of K_T • $K_T \Rightarrow$ mechanical and severe thermal mechanisms	• Up to MR=480 cm^3: $\uparrow f_p \Rightarrow \uparrow K_T$ • K_T compared to C45: ↑60% C60, ↓40% 27MnCr5, ↓50% 16MnCr5 • $\uparrow f_p \Rightarrow \uparrow \frac{dK_T}{dL}$	• After MR=480 cm^3: $\uparrow V_c \Rightarrow \uparrow 85\% K_T$ $\uparrow f \Rightarrow \downarrow 13\% K_T$ • After L=1200 m: $\uparrow V_c \Rightarrow \uparrow 23\% K_T$ $\uparrow f \Rightarrow \downarrow 18\% K_T$
Crater length (K_B)	• Rectangular or semicircular form depending on the degree of K_T • K_B trends depend on K_T: $\downarrow K_T$: $\uparrow f_\alpha \Rightarrow \uparrow K_B$ $\uparrow K_T$: $\downarrow f_\alpha \Rightarrow \uparrow K_B$	• Seems to be related with f_α	• $\uparrow V_c \Rightarrow \uparrow 8\% K_B/t_2$ $\uparrow f \Rightarrow \downarrow 42\% K_B/t_2$

3.4 Analysis of fundamental variables

This section analyses the influence that workpiece materials, cutting conditions and tool wear had on fundamental variables. Specifically, these latter are the chip thickness, contact length, cutting and feed forces, and tool temperature. The analysis is presented in the following manner: (1) general overview of the trends and evolution with MR and tool wear, (2) the influence that FP steels had on fundamental variables and (3) the influence that cutting conditions had on fundamental variables.

In order to enable a comparison between the tests at different uncut chip thickness, the chip thickness results were compared in terms of chip thickness ratio, t_{eq} (Eq. 3.9). The results of cutting and feed forces were also converted on specific cutting and feed forces, being K_{sc} and K_{sf} respectively (Eq. 3.9). These two latter were calculated as the average forces once the steady state was reached. Tool temperature values were also assessed during the steady state.

$$t_{\mathrm{eq}} = \frac{t_2}{t_1};\ K_{\mathrm{sc}} = \frac{F_{\mathrm{c}}}{t_1 \cdot a_{\mathrm{p}}};\ K_{\mathrm{sf}} = \frac{F_{\mathrm{f}}}{t_1 \cdot a_{\mathrm{p}}} \tag{3.9}$$

As was described in the previous section, fragile tool breakage occurred when cutting the 16MnCr5 and 27MnCr5 steels at V_{c}=100 m·min^{-1} and f=0.2 mm. For this reason at this specific condition, only results from tests with fresh tools were possible to be extracted.

3.4.1 Analysis of chip thickness and contact length

In the following lines the results of chip thickness are analyzed. Then, the results of the contact length between chip and tool are described.

- Evolution of chip thickness

To evaluate the chip thickness, the cross section of the chips was analyzed. Chips were etched, ground and polished. Nital reagent (1-5 mL HNO_3, 100 mL ethanol-95%) was employed to reveal the microstructure and micrographs were captured with a Leica DM-IR microscope. An example of a micrography of each steel machined at the condition of V_{c}=200 m·min^{-1} and f=0.2 mm with fresh tools is shown in Figure 3.46. The complete analysis is summarized in the Appendix B.

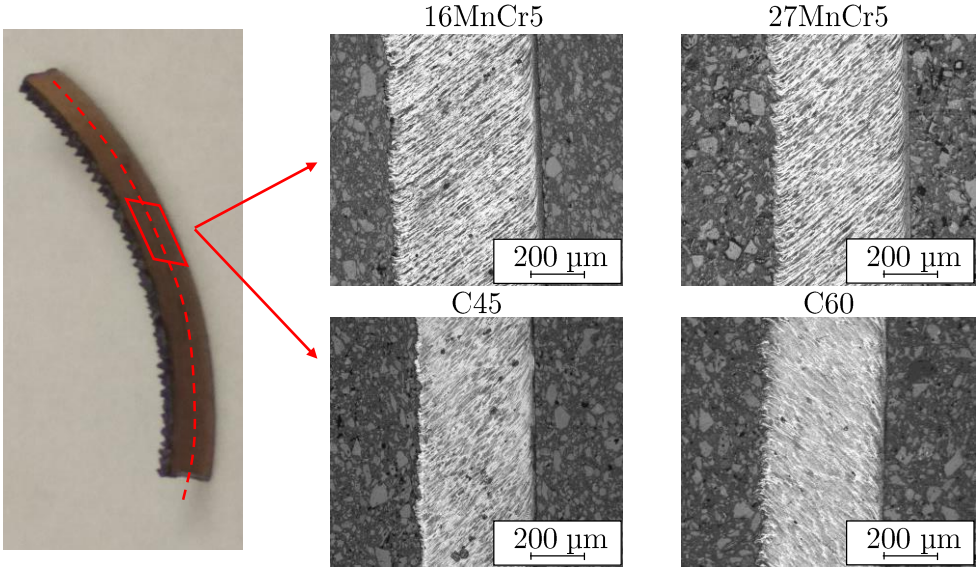

Figure 3.46: Example of chip thickness for all FP steels machined at V_c=200 m·min^{-1} and f=0.2 mm with fresh tools

The evolution of t_{eq} depending on MR is depicted in Figure 3.47. Values of t_{eq} were found in the range of 2-4.3, which means that during the process the chip thickness increased up to 4.3 times the uncut chip thickness. In general, it showed an increasing trend when MR increased. The maximum increase ratio was observed in the C60, followed in decreasing order by the C45, 27MnCr and 16MnCr5. This was maximum when cutting at V_c=200 m·min^{-1} and f=0.1 mm. The increase in t_{eq} was 43% for the C60, 34% for the C45, 29% for the 27MnCr5 and 20% for the 16MnCr5. At the condition of V_c=100 m·min^{-1} and f=0.1 mm, the 16MnCr5 and 27MnCr5 chips became thinner when MR increased, which was the opposite to the rest of the analyzed cases (marked with a red rectangle in Figure 3.47).

- Influence that materials had on chip thickness

The influence that FP steels had on t_{eq} followed nearly the same trend in all the cutting conditions. With fresh tools the steels with higher ferrite content obtained greater t_{eq} (marked with green arrows in Figure 3.47). The trend was mostly followed with increasing MR or tool wear, but the differences between steels decreased (marked with orange arrows). It was also observed in some cases that increasing tool wear generated greater t_{eq} in the C60 than in the C45, and also greater in the 27MnCr5 when compared with the 16MnCr5. Nevertheless, the t_{eq} of C45 and C60 never were greater than those of the 16MnCr5 and 27MnCr5. To assess a relative relation between materials, the average t_{eq} along with the tests for each steel and cutting condition was calculated. These results are summarized in Table 3.8.

The greatest t_{eq} was found at V_c=100 m·min^{-1} and f=0.1 mm when machining the 16MnCr5, with a calculated ratio of 4.15. The lowest ratio was achieved when machin-

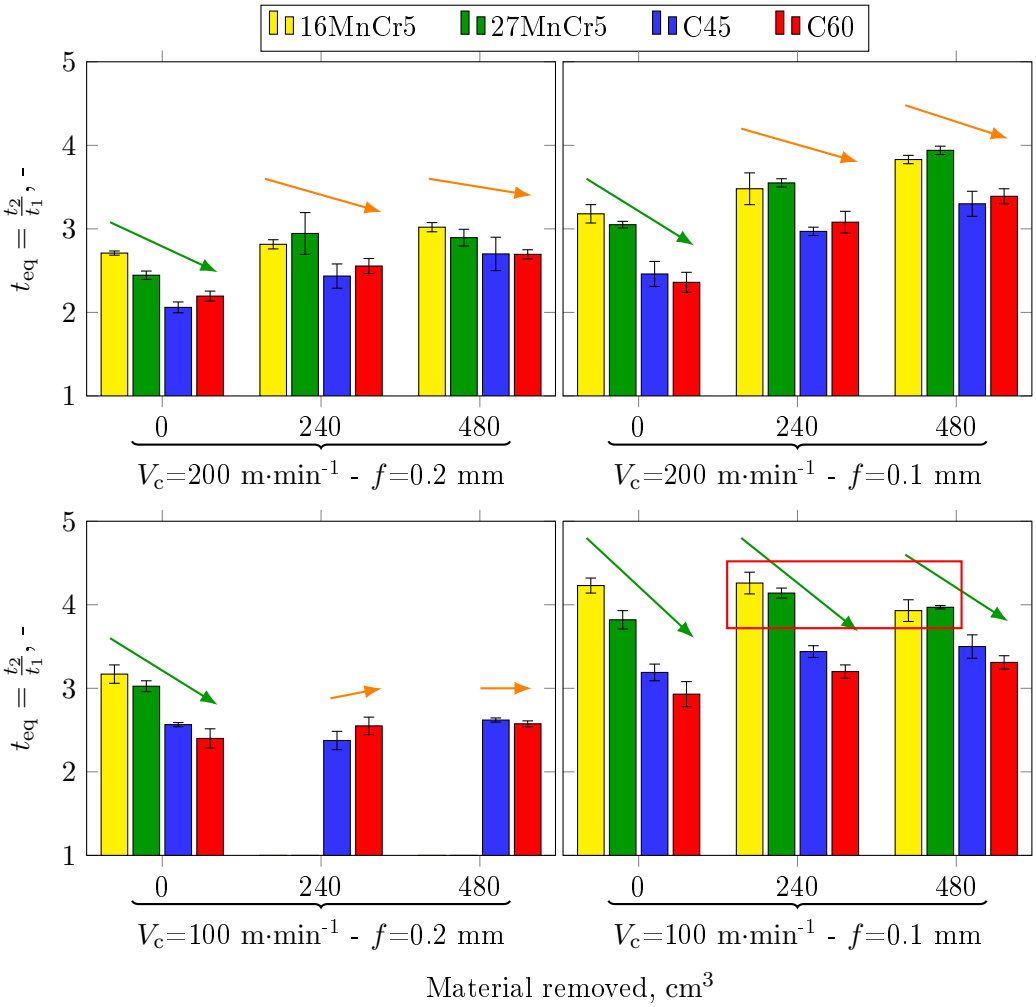

Figure 3.47: Evolution of t_{eq} ratio for all FP steels at all tested cutting conditions

ing the C45 at V_c=200 m·min^{-1} and f=0.2 mm, with an average value of 2.4. Comparing the results with the reference C45 steel, the average difference with the 16MnCr5 was 22% greater. In the case of the 27MnCr5 the difference was slightly lower, with a ratio 18% greater. The average difference between the C60 and the C45 was of only 3%.

- Influence of cutting conditions on chip thickness

In the colored cells in Table 3.8 the average t_{eq} achieved during the tests are summarized for each cutting condition. To calculate the effect that cutting speed and feed had on t_{eq} the same procedure explained in in the beginning of this section. On the whole, increasing cutting speed involved in decrease of 11% in t_{eq}, while the effect of increasing the feed generated a decrease of 24%.

Table 3.8: Average t_{eq} results and comparison with C45 reference steel (%) after a MR of 480 cm^3. In colored cells: average t_{eq} result for the tested cutting conditions

	16MnCr5	27MnCr5	C45	C60	Average
V_c=100 m·min^{-1} f=0.1 mm	4.15±0.15 22%	3.95±0.05 18%	3.40±0.1 *Ref.*	3.15±0.1 -7%	3.65±0.1
V_c=100 m·min^{-1} f=0.2 mm	3.15±0.10 26%	3±0.10 19%	2.50±0.05 *Ref.*	2.50±0.1 -1%	2.8±0.10
V_c=200 m·min^{-1} f=0.1 mm	3.50±0.10 20%	3.50±0.05 20%	2.90±0.10 *Ref.*	2.95±0.10 1%	3.2±0.1
V_c=200 m·min^{-1} f=0.2 mm	2.85±0.05 19%	2.75±0.15 15%	2.40±0.15 *Ref.*	2.50±0.10 4%	2.6±0.1
Average	22%	18%	*Ref.*	-3%	3.05±0.1

- Analysis of contact length

The contact length (l_c) was considered identical to the crater length (K_B). Therefore, the evolution, values and tendencies with increasing MR and with increasing tool wear are explained in Section 3.3.4. To complete that analysis, the contact length was also measured at the beginning of the tests, with fresh tools (when the MR was 0 cm^3). The results for each of the tested conditions are plotted in Figure 3.48.

At the feed of 0.1 mm, the contact length was mostly longer when machining the 16MnCr5, followed in decreasing order by the 27MnCr5, C45 and C60. Machining at a feed of 0.2 mm the l_c obtained in the 27MnCr5 was longer than that of the 16MnCr5 (marked with a red rectangle in Figure 3.48). Similar results occurred at

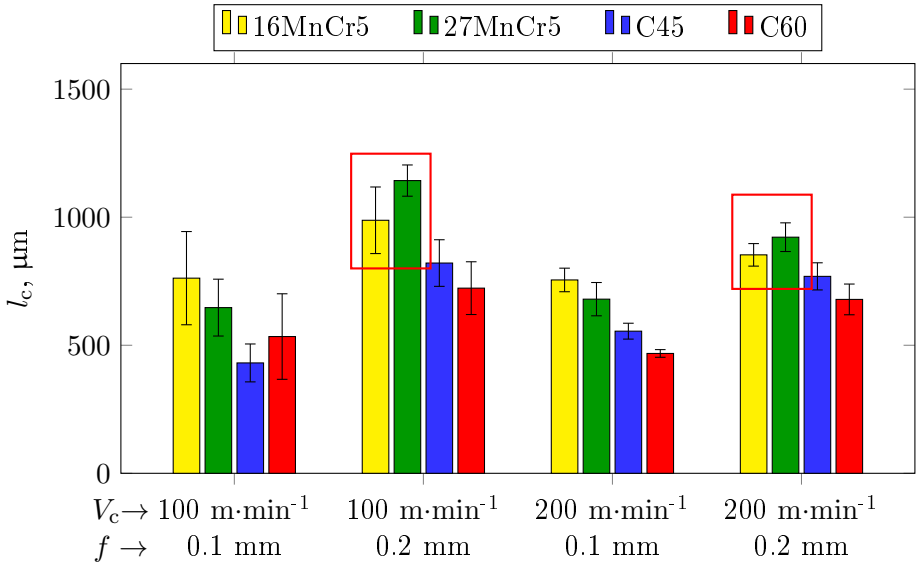

Figure 3.48: Contact length for all tested conditions with fresh tools (MR=0 cm^3)

V_c=100 m·min^{-1} and f=0.1 mm when comparing C60 and C45. The former achieved longer l_c than the latter. A maximum l_c=1.14 mm was achieved when cutting the 27MnCr5 at V_c=100 m·min^{-1} and f=0.2 mm, while the shortest l_c=0.53 mm occurred at V_c=100 m·min^{-1} and f=0.1 mm when machining the C45, in spite of the differences in uncut chip thickness. When comparing the average l_c results with those of the C45 steel (reference steel), the differences were 33% and 32% greater, and 7% lower for the 16MnCr5, 27MnCr5 and C60 respectively.

- Discussion of the results of chip thickness and contact length

In general, the results of chip thickness were in line with the literature. Steels with a higher ferrite content achieved thicker chips, increasing cutting speed provoked a reduction of chip thickness and increasing feed reduced the chip thickness ratio (Trent and Wright 2000; Korkut and Donertas 2007; Simoneau et al. 2007). To date, the variation that thickness experiences with the evolution of tool wear has not been fully analyzed by other researchers. Under the cutting conditions at which the tool wear was relevant, chip thickness increased to a greater degree. Increasing chip thickness commonly causes a reduction of the shear angle, which directly drives an increase in the cutting forces, and a reduction in the sliding velocity of the chip (Merchant 1944; Childs 2000). An increase in forces was assessed in this study, as is set out in the following section, which can be related to this increase in chip thickness.

The obtained contact length trends were in line with those of K_B. Globally, increasing ferrite content provoked an increase in l_c, which is in line with the literature (Trent and Wright 2000).

3.4.2 Analysis of cutting and feed forces

This section analyses the results of cutting and feed forces. These are compared in terms of specific forces.

- Overview of specific cutting and feed forces

Figures 3.49 and 3.50 show the specific cutting and feed forces depending on the MR for each cutting condition and FP steel. The standard deviation of the measurements of K_{sc} was very low, although it increased with increasing MR and tool wear. The standard deviation of K_{sf} was also very low when cutting with fresh tool, but also increased with MR. This was slightly higher than that of K_{sc}, which in some specific cases (i.e. machining the 27MnCr5 at V_c=200 m·min^{-1} and f=0.2 mm after a MR=480 cm^3) the deviation represented about 22% of the average K_{sf} value.

The general trends showed an increase in K_{sc} and K_{sf} with increasing MR, which was directly caused by the increase in tool wear. This was more relevant at the conditions of V_c=200 m·min^{-1} and f=0.1 and 0.2 mm. Moreover, it was at these cutting conditions in which greater V_B, K_T and K_B occurred. In detail, the average increase of K_{sc} was

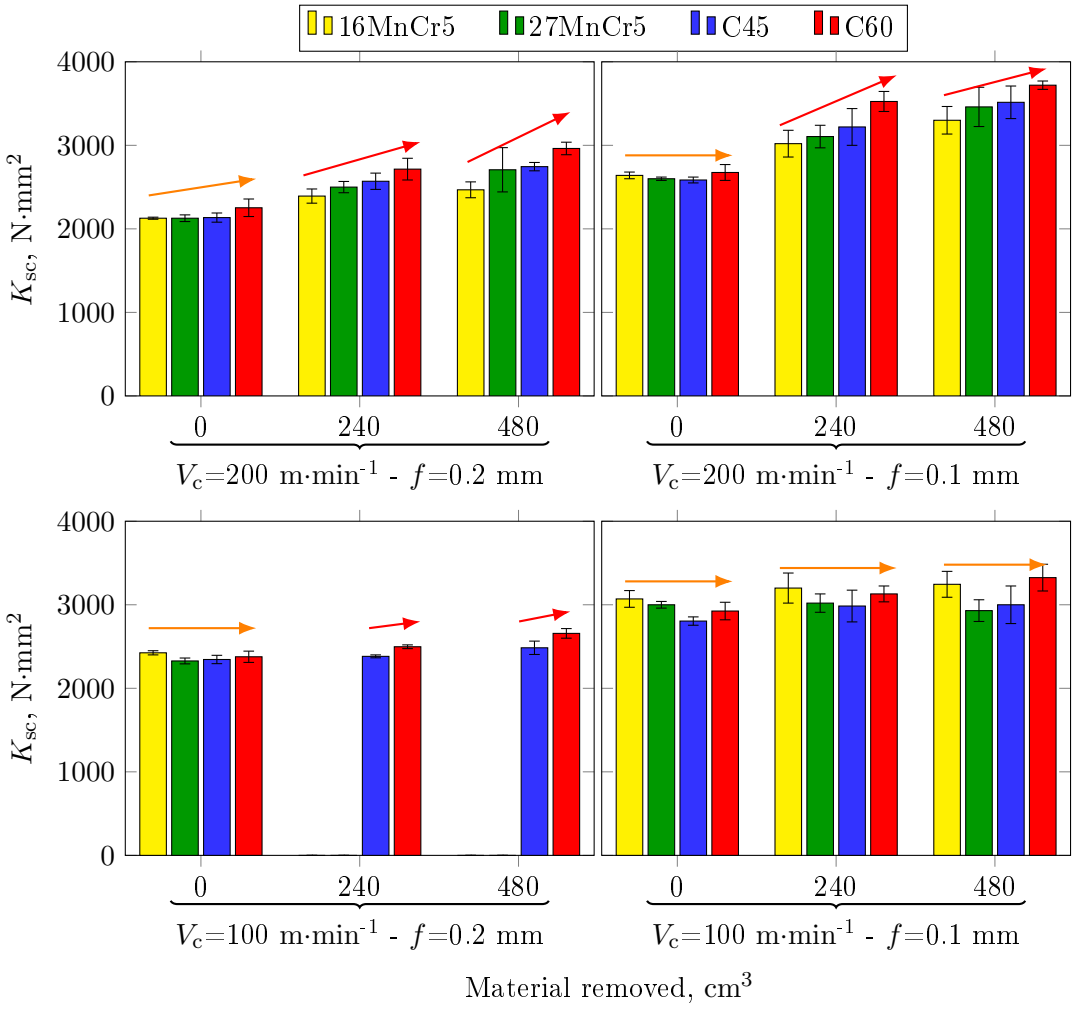

Figure 3.49: Evolution of specific cutting force for all FP steels at all tested cutting conditions

26% at V_c=200 m·min^{-1} and f=0.2 mm, and 33% at V_c=200 m·min^{-1} and f=0.1 mm. The values of K_{sc} were found in the range of 2200-3700 N·mm^2.

The increase of K_{sf} was more sensitive to tool wear. The average calculated increase ratios were 54% and 45% at V_c=200 m·min^{-1} and f=0.1 and 0.2 mm respectively. The values of K_{sf} were in the range of 1100-3100 N·mm^2.

- Influence of FP steels on specific forces

In general terms, the differences between steel grades were only observed with increasing MR or tool wear when analyzing K_{sc}. With fresh tools, the K_{sc} of all steels held the same value under all the tested conditions (marked with orange arrows in Figure 3.49). At V_c=100 m·min^{-1}, the low amount of wear generated in the tools did not cause significant differences in results between the steels. In contrast, at V_c=200 m·min^{-1}, the differences between the steels were noticeable once the tool started to wear (marked with red arrows in Figure 3.49). Comparing the average results of K_{sc} (Table 3.9), an

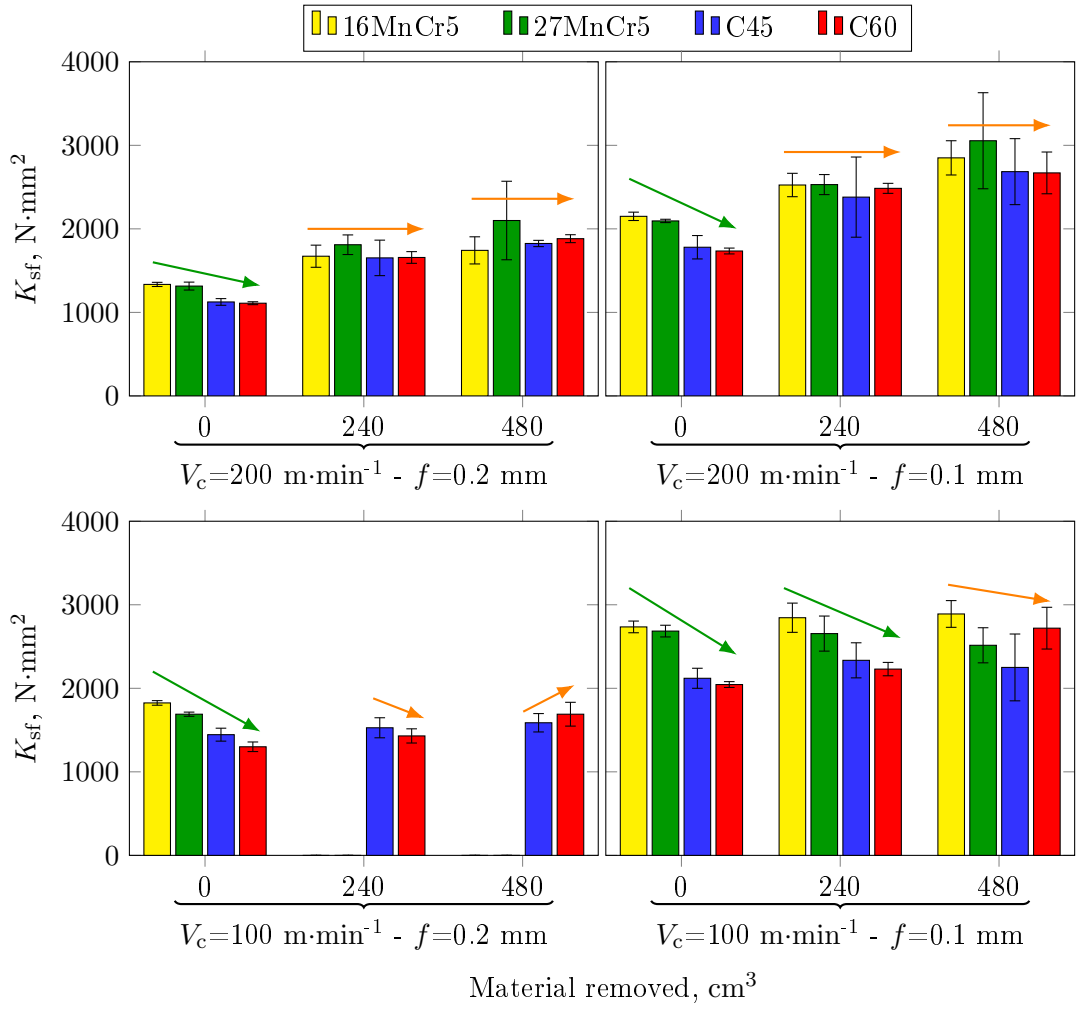

Figure 3.50: Evolution of specific feed force for all FP steels at all tested cutting conditions

increase of 6% was obtained in the C60 compared to the C45. A maximum difference of 8% was obtained between all the tested cases.

Concerning the general influence that the FP steels had on the K_{sf}, the main differences between grades were observed when cutting with fresh tools (MR=0 cm^3), contrary to what occurred in the K_{sc}. In all tested cutting conditions K_{sf} was greater when machining the steels with higher ferrite content (marked with green arrows in Figure 3.50). These were the 16MnCr5 and 27MnCr5 followed by the C45 and C60 in decreasing order. Under all the cutting conditions except the V_c=100 m·min^{-1} and f=0.1 mm, the K_{sf} tended to converge at the same value by the end of the tests (marked with green arrows in Figure 3.50). The average difference achieved machining the 16MnCr5 and 27MnCr5 compared to C45 was 15% and 13% respectively. The K_{sf} of the C60 was almost similar to that of C45 under nearly all conditions.

Table 3.9: Average K_{sc} and K_{sf} results (N·mm^2) and comparison with C45 reference steel (%). In colored cells: average K_{sc} and K_{sf} result (N·mm^2) for the tested cutting conditions

		16MnCr5	27MnCr5	C45	C60	Average
K_{sc} (N·mm^2)	V_c=100 m·min^{-1} f=0.1 mm	3170±145 8%	2985±95 2%	2930±155 *Ref.*	3125±120 7%	3055±125
	V_c=100 m·min^{-1} f=0.2 mm	2425±25 1%	2325±35 -3%	2405±50 *Ref.*	2510±50 4%	2417±40
	V_c=200 m·min^{-1} f=0.1 mm	2985±120 -4%	3055±130 -2%	3105±150 *Ref.*	3305±90 6%	3115±120
	V_c=200 m·min^{-1} f=0.2 mm	2330±65 -6%	2445±125 -2%	2485±65 *Ref.*	2645±105 6%	2475±90
	Average	0%	-1%	*Ref.*	6%	2765±95
K_{sf} (N·mm^2)	V_c=100 m·min^{-1} f=0.1 mm	2825±135 26%	2620±165 17%	2235±245 *Ref.*	2330±120 4%	2500±165
	V_c=100 m·min^{-1} f=0.2 mm	1825±30 20%	1690±25 11%	1520±100 *Ref.*	1475±95 -3%	1625±65
	V_c=200 m·min^{-1} f=0.1 mm	2510±130 10%	2560±240 12%	2280±340 *Ref.*	2295±115 1%	2410±205
	V_c=200 m·min^{-1} f=0.2 mm	1585±105 3%	1740±210 13%	1535±95 *Ref.*	1550±45 1%	1600±115
	Average	15%	13%	*Ref.*	1%	2035±135

- Influence of cutting conditions on specific forces

The average specific forces for each cutting condition are summarized in the colored cells in Table 3.9. Increasing cutting speed had an appreciably low influence on specific forces. An increase of 2% and a decrease of 3% was calculated for K_{sc} and K_{sf} respectively. In contrast, increasing the feed was significant, obtaining a reduction of 23% in K_{sc} and 41% in K_{sf}.

- Discussion of the results of specific forces

In the literature review diverse trends were found in cutting force results when cutting FP steels. Some authors concluded that increasing pearlite content involved in increase in F_c (Obikawa et al. 1997), while others concluded almost the opposite (Trent and Wright 2000). In this research no differences in K_{sc} were found between the steels when cutting with fresh tools. When the tool has no wear, cutting forces are commonly linked to the normal pressures on the rake face (Merchant 1944), and the contact area which is defined by the contact length (l_c) and the width of cut (a_p). Taking into account that the steels with higher ferrite content achieved longer l_c, in spite of their lower strength and possibly lower normal pressures, their F_c or K_{sc} was the same as

the C45 and C60 steels.

Increasing K_{sc} with increased tool wear has been assessed by several authors in the literature not only for steels (Chinchanikar and Choudhury 2016; Huang and Liang 2005), but also for other alloys (Arrazola et al. 2014). This was also observed in this research. The increase in K_{sc} is commonly linked to the increase in shear stresses generated by the increase in V_B. In the present work this may have been also affected by the increase which occurred in the contact length or K_B, and probably by the concave shape of the crater. Another important cause of increasing K_{sc} is the increase in t_2, as this directly drives a reduction in the shear angle and therefore increases the reactions acting on the rake face. This was clearly observed at the conditions at which tool wear was relevant in all the studied steels. The highest increase in K_{sc} was observed in the C60, followed by C45, 27MnCr5 and 16MnCr5, which in turn was linked with the higher increase in wear.

With regards to the results of K_{sf}, the greater values measured with fresh tools in the steels with higher ferrite content were in line with the literature (Trent and Wright 2000; Obikawa et al. 2009). Increasing K_{sf} with increased tool wear was also observed in previous studies, and was assessed as being more sensitive to tool wear (Chinchanikar and Choudhury 2016; Huang and Liang 2005). This K_{sf} increase was linked to the increase in the normal stresses in the flank face, due to the growth in V_B. These were also attributed to the increase in the shear stresses generated in the rake face, as a result of the increase in contact length or K_B. Therefore, as was concluded in the case of K_{sc}, the higher the rate of increase in tool wear, the greater the increase in K_{sf}. As a consequence, at V_c=200 m·min^{-1}, machining the steels with greater pearlite content (C45 and C60) had a greater increase in K_{sf}, to finally achieve a similar K_{sf} to the 16MnCr5 and 27MnCr5.

3.4.3 Analysis of tool temperature

First, the selected approach to transform tool side temperatures to tool contact temperatures is described. Then, the measured tool temperatures on the tool side are presented. Finally, calculated contact temperatures are discussed at the end of this section.

Methodology to calculate tool contact temperatures

To better understand the physics occurring in the tool-chip or tool-workpiece interface, measured tool side temperatures were extrapolated to the mid-plane of the contact section. The methodology was defined in two steps. The first consisted of calculating the heat flux generated due to shear stresses on the rake and flank faces (q_{tool}). The second step was applied to calculate the increase in temperature resulting from the overhang distance (d), which uses as input data the previously calculated heat flux.

This is schematically described in Figure 3.51.

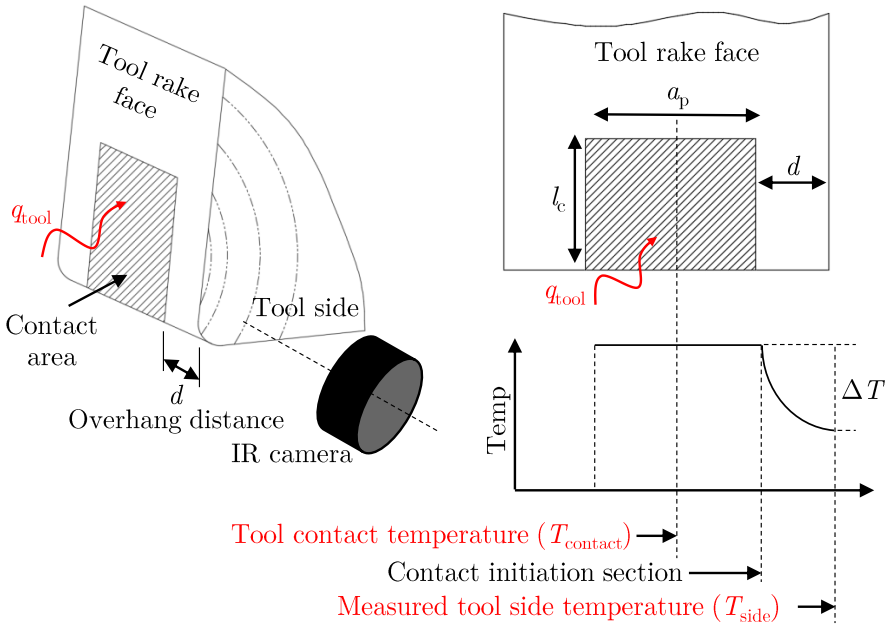

Figure 3.51: Extrapolation method from tool side to mid-plane contact temperature

To address the calculation of the heat flux generated by the shear stresses, some assumptions were made. It was concluded in Section 3.3 that increasing tool wear generated an increase in both cutting and feed forces. Therefore, the forces could be written as an initial force (F_0, the force measured with fresh tools) plus an increase of force due to tool wear (ΔF). For the case of cutting and feed forces these could be described as in Eq. 3.10.

$$\begin{aligned} F_c &= F_{c0} + \Delta F_c \\ F_f &= F_{f0} + \Delta F_f \end{aligned} \tag{3.10}$$

Based on this equation, and supposing that the tool has a perfectly sharp cutting edge, F_{c0} could be attributed to the normal stresses on the rake face, and F_{f0} to the shear stresses on the rake face. It was assumed that with fresh tools no stresses occur on the flank face. If the increase in forces were directly linked to the increase in flank wear, ΔF_c could be attributed to the shear stresses on the flank face, and ΔF_f to the normal stresses on the flank face.

The heat flux on the rake face, which is in turn the heat flux of the secondary shear zone (q_{sh2}), was calculated based on the shear plane model (Merchant 1944). The corresponding friction angle (Eq. 3.11) and the shear plane angle (Eq. 3.12) were calculated based on the static component of the cutting forces (F_{c0} and F_{f0}) and chip thickness (t_2).

$$\lambda = \gamma + \text{arctg}\left(\frac{F_{\text{f0}}}{F_{\text{c0}}}\right) \tag{3.11}$$

$$\phi = \text{actg}\left(\frac{\frac{t_1}{t_2} \cdot \cos\gamma}{1 - \frac{t_1}{t_2} \cdot \sin\gamma}\right) \tag{3.12}$$

The resultant shear forces on the rake (F_{sh2}) were calculated by translating the cutting and feed forces to the tangent and normal directions with respect to the rake face.

$$F_{\text{sh2}} = F_{c0} \cdot \sin\gamma + F_{f0} \cdot \cos\gamma \tag{3.13}$$

The shear stresses on the secondary shear zone (τ_{sh2}) were obtained with Eq. 3.14 on which F_{sh2} was divided by the effective contact area, which was calculated by Eq. 3.15.

$$\tau_{\text{sh2}} = \frac{F_{\text{sh2}}}{A_{\text{sh2}}} \tag{3.14}$$

$$A_{\text{sh2}} = a_{\text{p}} \cdot \frac{t_1 \cdot \sin\left(\phi + \lambda - \gamma\right)}{\sin\phi \cdot \cos\lambda} \tag{3.15}$$

The heat flux on the SSZ was obtained with Eq. 3.16.

$$q_{\text{sh2}} = \tau_{\text{sh2}} \cdot V_{\text{chip}} = \tau_{\text{sh2}} \cdot V_{\text{c}} \cdot \frac{t_1}{t_2} \tag{3.16}$$

The heat flux due to shearing on the flank face, which is also attributed to the heat flux in the tertiary shear zone, was calculated based on the shear stresses. Since shear stresses on the TSZ were linked to ΔF_{c}, based on the assumption that the tool cutting edge was considered perfectly sharp, the stresses with fresh tools in the TSZ were considered to be null. As a result, it was possible to correct flank face temperatures only in the cases at which tool wear occurred. The stresses were calculated with Eq. 3.17, based on the study of Chinchanikar and Choudhury (2015).

$$\tau_{\text{sh3}} = \frac{\Delta F_{\text{c}}}{a_{\text{p}} \cdot V_{\text{B}}} \tag{3.17}$$

The heat flux generated by the shearing effects was determined with Eq. 3.18.

$$q_{\text{sh3}} = \tau_{\text{sh3}} \cdot V_{\text{c}} \tag{3.18}$$

Once the heat fluxes on the SSZ and TSZ were calculated, the amount of friction or shear heat that flows into the tool was determined by the heat partition (Eq. 3.19). It is usually assumed that approximately 3-10% of the friction heat is transferred to the tool (Childs 2000; Soler et al. 2015b).

$$q_{\text{tool}} = \alpha^* \cdot q_{\text{sh}} \tag{3.19}$$

The correction methodology based on the analytical model proposed by Soler et al. (2015b) was employed to correct the influence of the overhang distance. To apply this model some assumptions were also made. First, the analytical model calculates the rise in temperature generated by a unique heat flux on the surface of a semi-infinite solid, not the coupled effect of two heat fluxes acting on two adjacent surfaces of a body (the heat fluxes on the rake and flank faces). For this reason, the rise in temperature is calculated individually for the rake and flank faces, assuming that these heat fluxes do not interfere with each other. In addition, the model was validated to calculate the temperature increase on the rake face of the tool, not on the flank face, although in theory seemed to be applicable. This model has also the implicit assumption that the temperature throughout the contact section is equal, which means that the temperature at the beginning of the contact is considered the same as the one in the mid plane (see the schematic representation in Figure 3.51).

The analytical equation proposed by Soler et al. (2015b) was based on the classical theories of heating, and derived from the calculation of the temperature at the surface of a semi-infinite solid heated over a rectangular area. Eq. 3.20 estimates the temperature rise ΔT at an overhang distance (d) from the tool side. The input parameters required to calculate ΔT are the contact length (l), the heat flux (q) and the conductivity of the tool (K_{tool}). In the case of the rake face, l is substituted by l_{c} or K_{B}, and $q = q_{sh2}$. For the flank face, $l = V_{\text{B}}$ and $q = q_{sh3}$.

$$\begin{aligned}\Delta T = \tfrac{2q_{\text{tool}}}{\pi K_{\text{tool}}} l \Big[1 - \tfrac{d/a_{\text{p}}}{l/a_{\text{p}}} \sinh^{-1}\left(\tfrac{l/a_{\text{p}}}{d/a_{\text{p}}}\right) \\ + \sinh^{-1}\left(\tfrac{d/a_{\text{p}}+1}{d/a_{\text{p}}}\right) - \sinh^{-1}\left(\tfrac{d/a_{\text{p}}}{l/a_{\text{p}}}\right) \Big]\end{aligned} \tag{3.20}$$

Tool side temperature

Before the analysis of results, it should be noted that tool side temperatures when orthogonal cutting the C45 and C60 were recorded with an overhang distance of 0.3 mm, while in the tests of the 16MnCr5 and 27MnCr5 this had to be increased to 0.5 mm. This modification in the overhang was necessary to avoid the obstruction that the severe workpiece lateral side flow was generating between the camera and the tool side in the latter two steels. As a consequence, the direct comparison of T_{side} between the steels was affected, as the overhang distance is known to affect the results (Soler et al. 2015b). However, T_{side} results are still briefly presented, to later on be compared to the corrected T_{contact} in the next section.

- Overview of tool side temperatures

Temperatures measured on the tool side showed an increasing trend during the orthogonal cutting process up to a certain value above which the temperature became stable. Once the temperature stabilizes the process is commonly considered under steady state, and thus temperatures are considered to be constant throughout the rest of the process. Tool temperatures were measured in the flank and rake faces, with the aim of better understanding the individual phenomena occurring when analyzing the flank and the crater wear. Figure 3.52-a shows a captured thermal field of the tool, in which the measured regions are identified. In Figure 3.52-b the evolution of rake and flank face temperatures over time are plotted. For both selected regions it was observed that the steady state was reached before the cutting process ended.

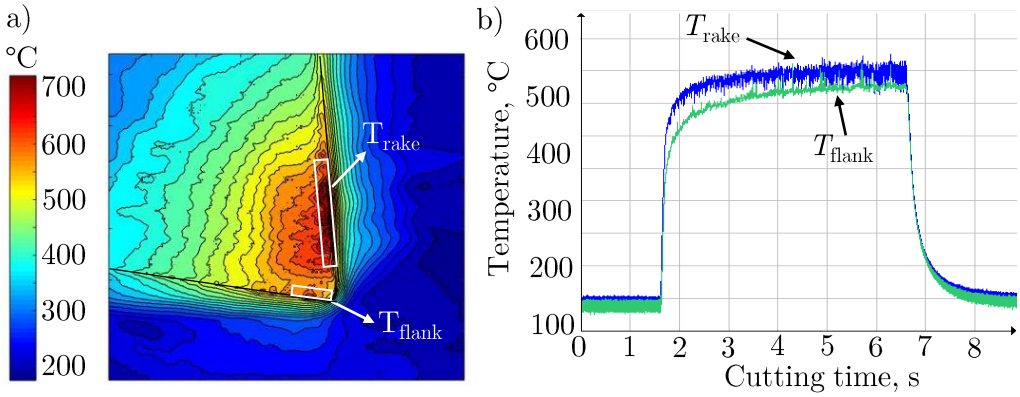

Figure 3.52: a) Thermal field of tool side and b) evolution of temperature on the rake and flank faces for a C45 steel machined at V_c=200 m·min^{-1} f=0.2 mm with fresh tool

Figures 3.53 and 3.54 show the evolution of T_{side} depending on the MR for the rake and flank faces respectively. In general, the maximum temperatures were measured on the rake face, with a maximum value of 710°C. However, taking into account the average temperature of all the tests, those of the rake face were only 10% higher than those of the flank face. In both regions, an increase in tool side temperature occurred with the increase in tool wear. In the same manner as the abovementioned fundamental vari-

ables, the increase ratio of tool side temperature was higher at those conditions in which a greater amount of wear was measured (marked with red arrows in Figure 3.53 and 3.54). The greatest increase appeared when cutting at V_c=200 m·min^{-1} and f=0.1 mm. For the rake face, this reached a maximum when cutting the C45 and C60 steels, whose rise in temperature was 50%. The other steels also experienced the greatest increase under this condition, with ratios of 31% and 13% for 27MnCr5 and 16MnCr5 steels respectively. In the case of the flank the greatest increase was equal for the C45 and C60, with a ratio of 36%, while those of 27MnCr5 and 16MnCr5 was 30% and 11% respectively.

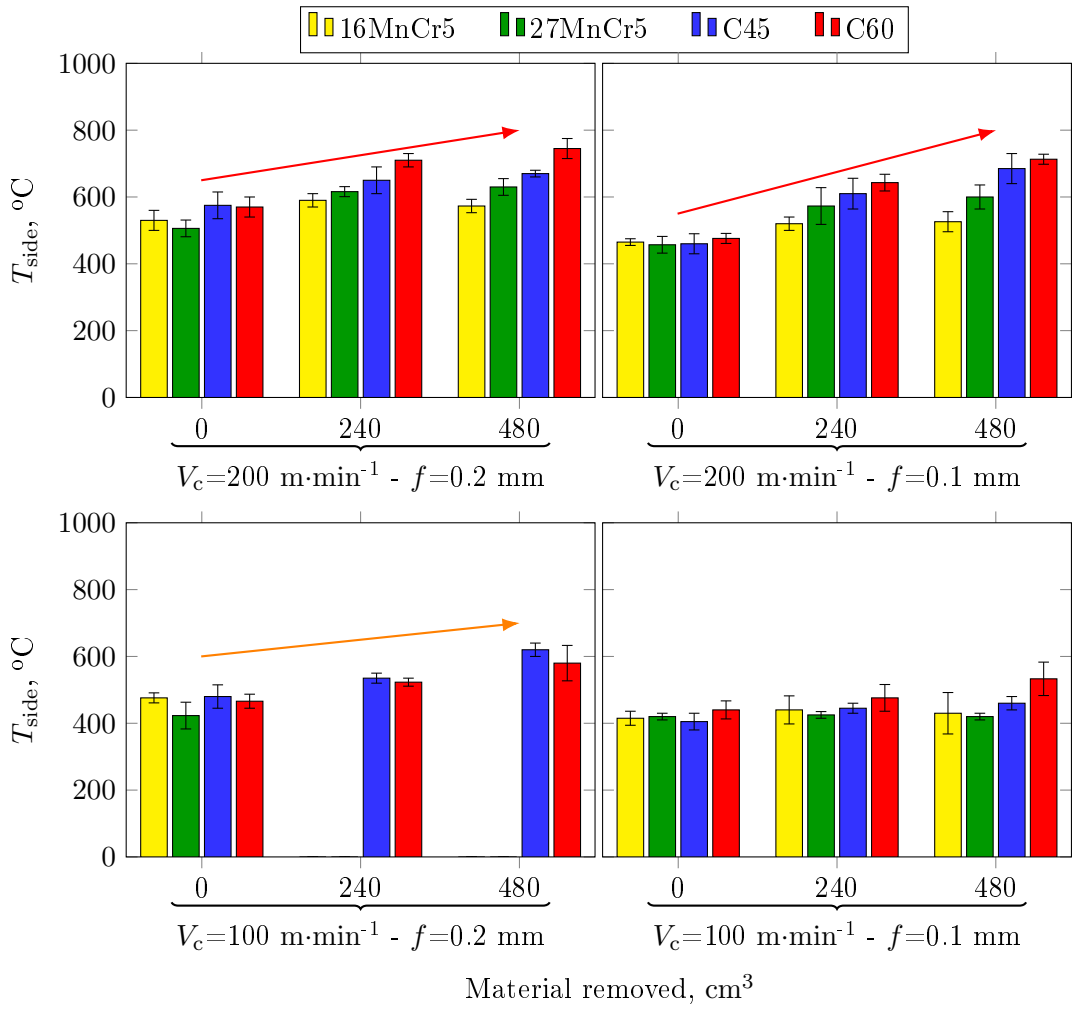

Figure 3.53: Evolution of T_{side} on the rake face for all FP steels at all tested cutting conditions

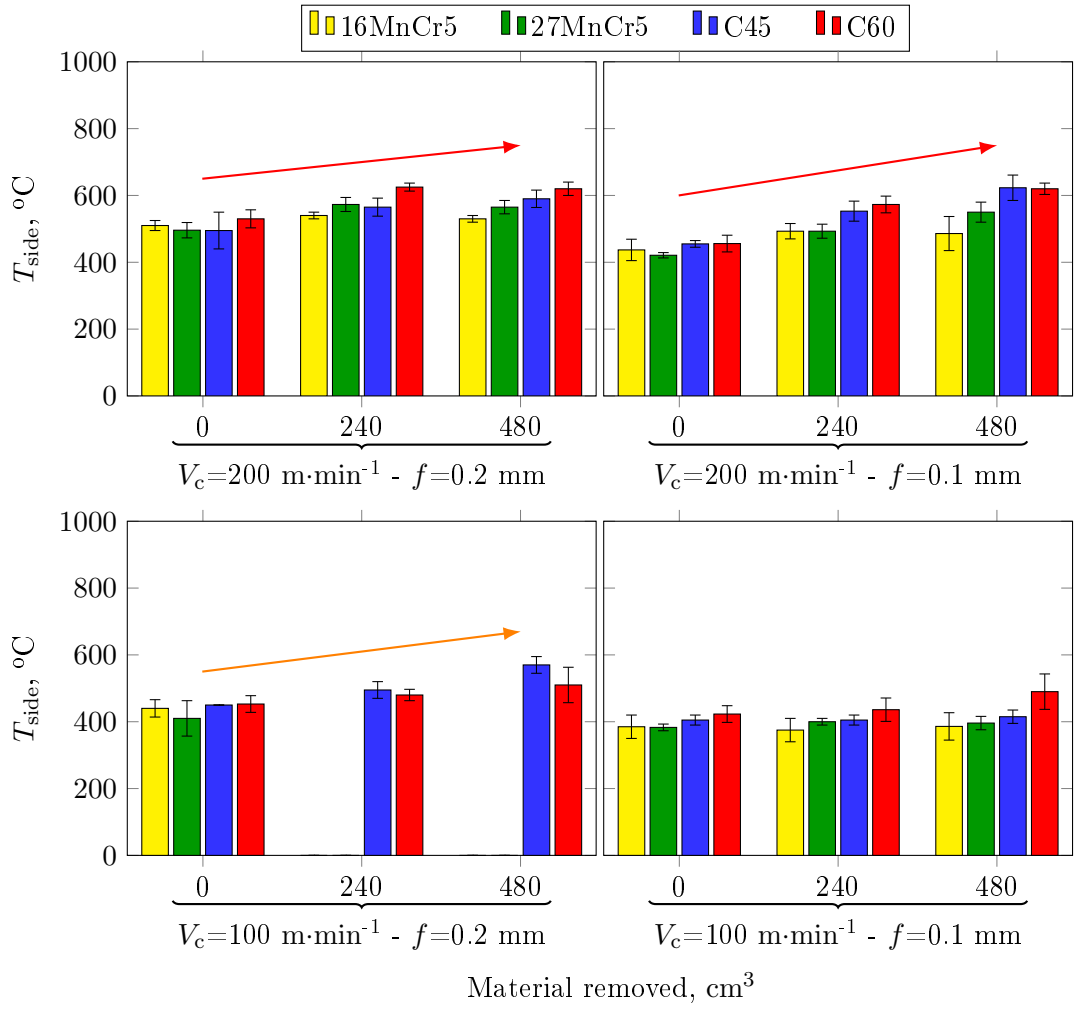

Figure 3.54: Evolution of T_{side} on the flank face for all FP steels at all tested cutting conditions

- Influence that FP steels and cutting conditions had on tool side temperature

Taking into account the differences in overhang, a direct comparison of T_{side} between steels was not possible. However, as presented in Table 3.10, the maximum differences between steels were about 10-11% in both rake and flank faces.

The influence that cutting conditions had on T_{side} was calculated, as this could be assumed to not be affected by the different overhangs that were employed. The average values of T_{side} for the rake and flank faces are summarized in the colored cells in Table 3.10. Regarding the temperature in the rake face, increasing the cutting speed from 100 to 200 m·min^{-1} generated an average increase of 18% in T_{side}. Increasing the feed from 0.1 to 0.2 mm also caused an increase in T_{side}, with an average ratio of 14%. Analyzing the temperature results on the flank face, an average increase of 17% and 12% was found when varying the cutting speed and the feed respectively. In general, the results suggest that increasing the cutting speed resulted in a slightly higher temperature rise, although the difference in the ratio was slight, in the range of 4-5%.

Table 3.10: Average T_{side} results (°C) and comparison with C45 reference steel (%) for rake and flank faces. In colored cells: average T_{side} (°C) for each tested cutting condition

		16MnCr5	27MnCr5	C45	C60	Average
Tool side temperature (rake face)	V_c=100 m·min^{-1} f=0.1 mm	430±40 -1%	420±10 -3%	435±20 *Ref.*	485±40 11%	440±30
	V_c=100 m·min^{-1} f=0.2 mm	—	—	545±25 *Ref.*	525±30 -4%	535±30
	V_c=200 m·min^{-1} f=0.1 mm	505±20 -13%	545±40 -7%	585±40 *Ref.*	610±20 4%	560±30
	V_c=200 m·min^{-1} f=0.2 mm	565±25 -10%	585±20 -7%	630±30 *Ref.*	675±30 7%	615±25
	Average	-8%	-6%	*Ref.*	9%	540±30
Tool side temperature (flank face)	V_c=100 m·min^{-1} f=0.1 mm	380±40 -7%	395±15 -3%	410±20 *Ref.*	450±40 10%	410±30
	V_c=100 m·min^{-1} f=0.2 mm	—	—	505±20 *Ref.*	480±30 -5%	490±25
	V_c=200 m·min^{-1} f=0.1 mm	470±35 -13%	490±20 -10%	545±30 *Ref.*	550±20 1%	515±25
	V_c=200 m·min^{-1} f=0.2 mm	525±15 -5%	545±20 -1%	550±40 *Ref.*	590±20 7%	550±25
	Average	-8%	-5%	*Ref.*	3%	490±25

Tool contact temperature

Contact temperatures were calculated based on the approach presented at the beginning of Section 3.4.3. As explained previously, these were calculated as the sum of $T_{contact} = T_{side} + \Delta T$. In the calculations, the heat partition was set to $\alpha^* = 4\%$.

- Analysis of calculated temperature rise from T_{side} to $T_{contact}$

A comparison between T_{side} and calculated $T_{contact}$ for the rake and flank regions is shown in Figure 3.55 when machining at V_c=200 m·min^{-1} and f=0.2 mm. Note that temperatures in the flank are only given for the MR states at which flank wear occurred.

Substantial temperature increases were calculated once the analytical equations were applied. These were more significant in the case of the rake face, in which the temperature corrections were in the range of ΔT=130-395°C. This ΔT, compared to that T_{side}, means an increase of 30-64%. On the flank face, the calculated temperature corrections were ΔT=10-395°C (3-67% of increase compared to T_{side}).

In both regions, the greatest values of ΔT were obtained at high cutting speeds, and

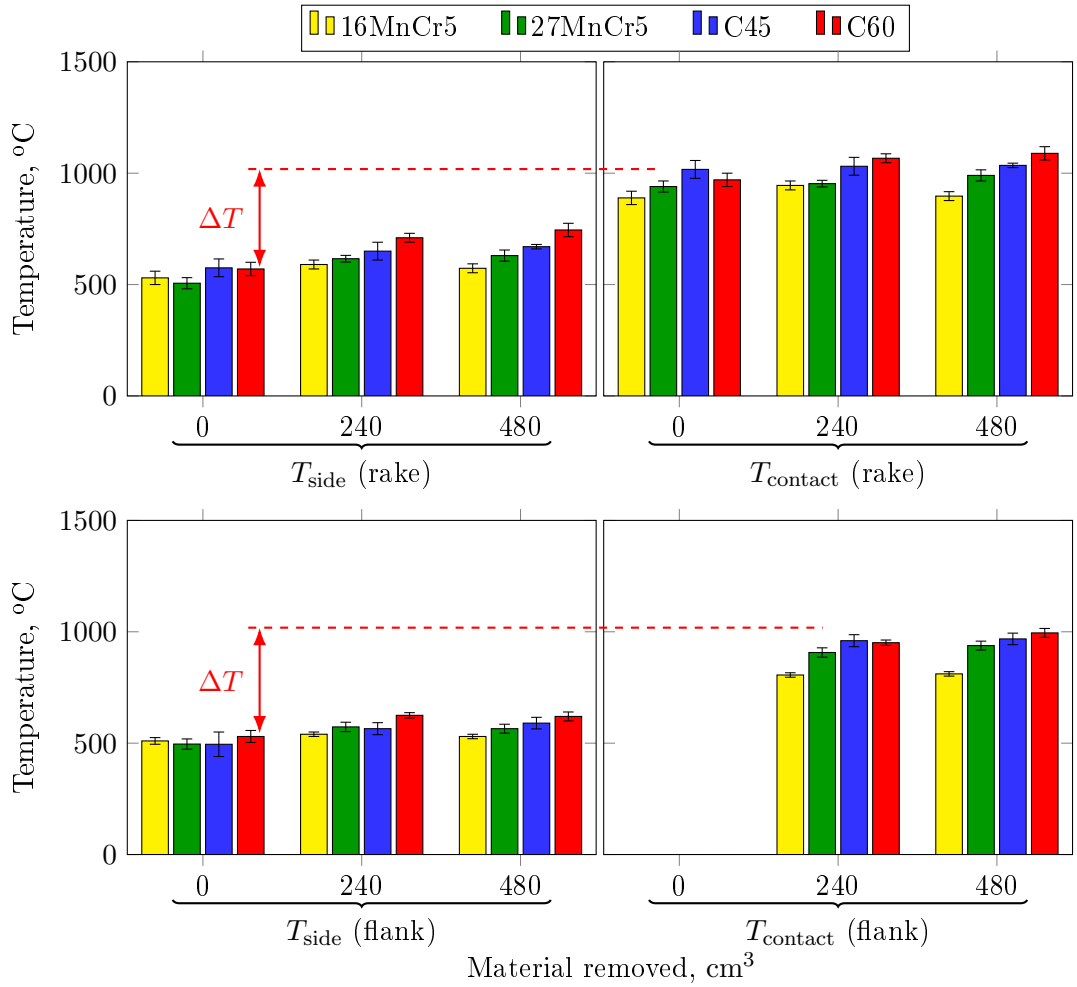

Figure 3.55: Evolution of tool side and tool mid plane temperatures of rake and flank faces when cutting at V_c=200 m·min^{-1} and f=0.2 mm

these were maximum when cutting at 0.2 mm feed. The greatest ΔT was achieved in the case of C45, followed in decreasing order by the C60, 27MnCr5 and 16MnCr5. Unexpectedly, the ΔT for the case of C45 was greater than that of C60. However, the overall differences between steels were of less than 10%. The fact that ΔT of C45 and C60 were close to that of 27MnCr5 and 16MnCr5 was linked to the corrections applied to compensate the different overhang distances (Soler et al. 2015b).

- Overview of contact temperatures

In Figures 3.56 and 3.57 the evolution $T_{contact}$ depending on the MR for the rake and flank faces are shown respectively.

Focusing on the trends in both the rake and flank face temperatures, increasing tool wear caused a slight increase in tool temperature. When cutting with fresh tools (MR=0 cm^3), the differences between steels were not significant (marked with orange arrows in Figures 3.56 and 3.57). However, the differences between steels grew in the

conditions of increased tool wear (marked with red arrows). The maximum temperature increase on the rake face was 110°C, which was 12% higher compared to T_{contact} with a fresh tool. In the case of the flank face the maximum increase was 80°C (an 8% increase compared to T_{contact} with a fresh tool). The values of T_{contact} were in the range of 550-1090°C on the rake face and 400-995°C in the flank face.

- Influence of FP steels on contact temperatures

In general, the C60 steel achieved the highest contact temperatures, followed in decreasing order by the C45, 27MnCr5 and 16MnCr5. However, this trend was not always followed.

Concerning the results on the rake face (Figure 3.56), it is noteworthy that the calculated temperatures when machining the C45 were greater than those of the C60 when cutting at V_c=200 m·min^{-1} and f=0.2 mm with a fresh tool, and at V_c=100 m·min^{-1} and f=0.2 mm across all the amount of MR. There was a similar occurrence when

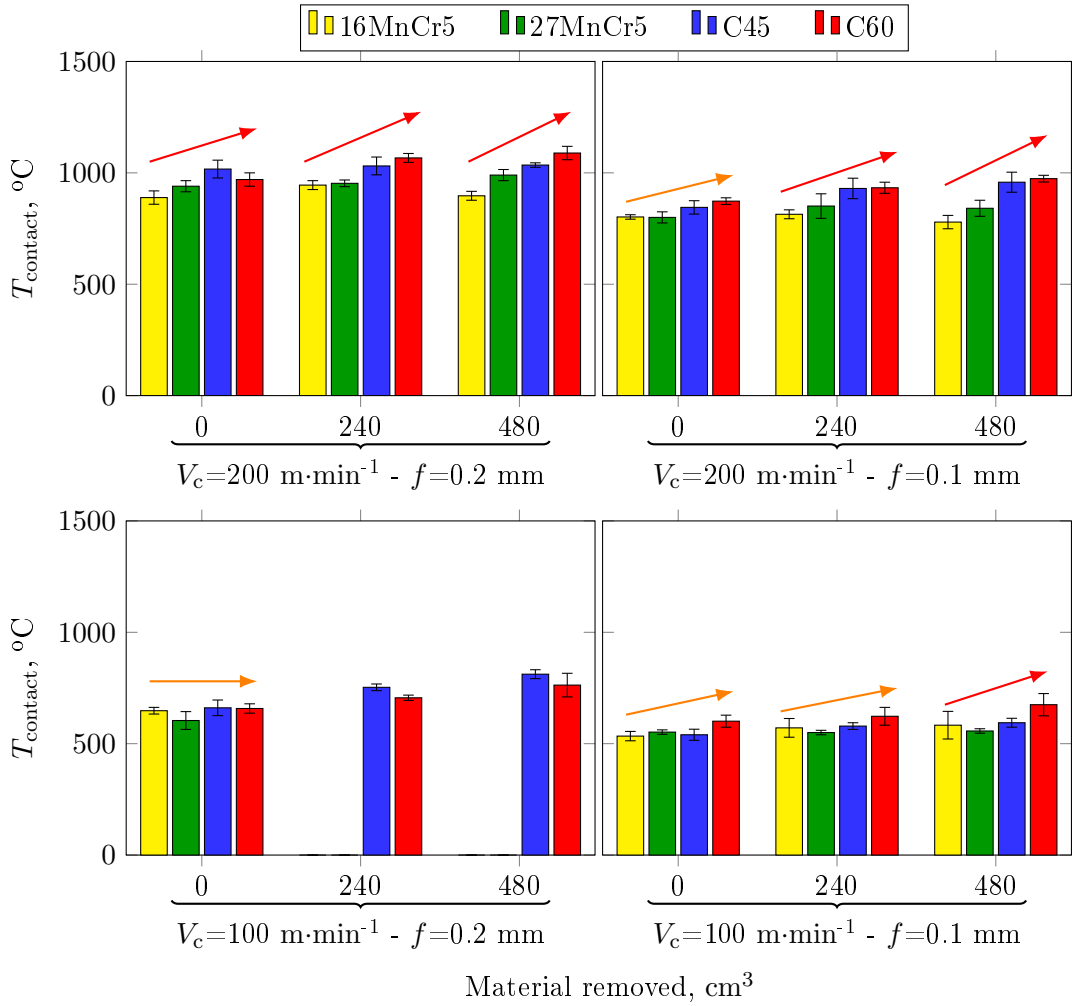

Figure 3.56: Evolution of T_{contact} on the rake face for all FP steels at all tested cutting conditions

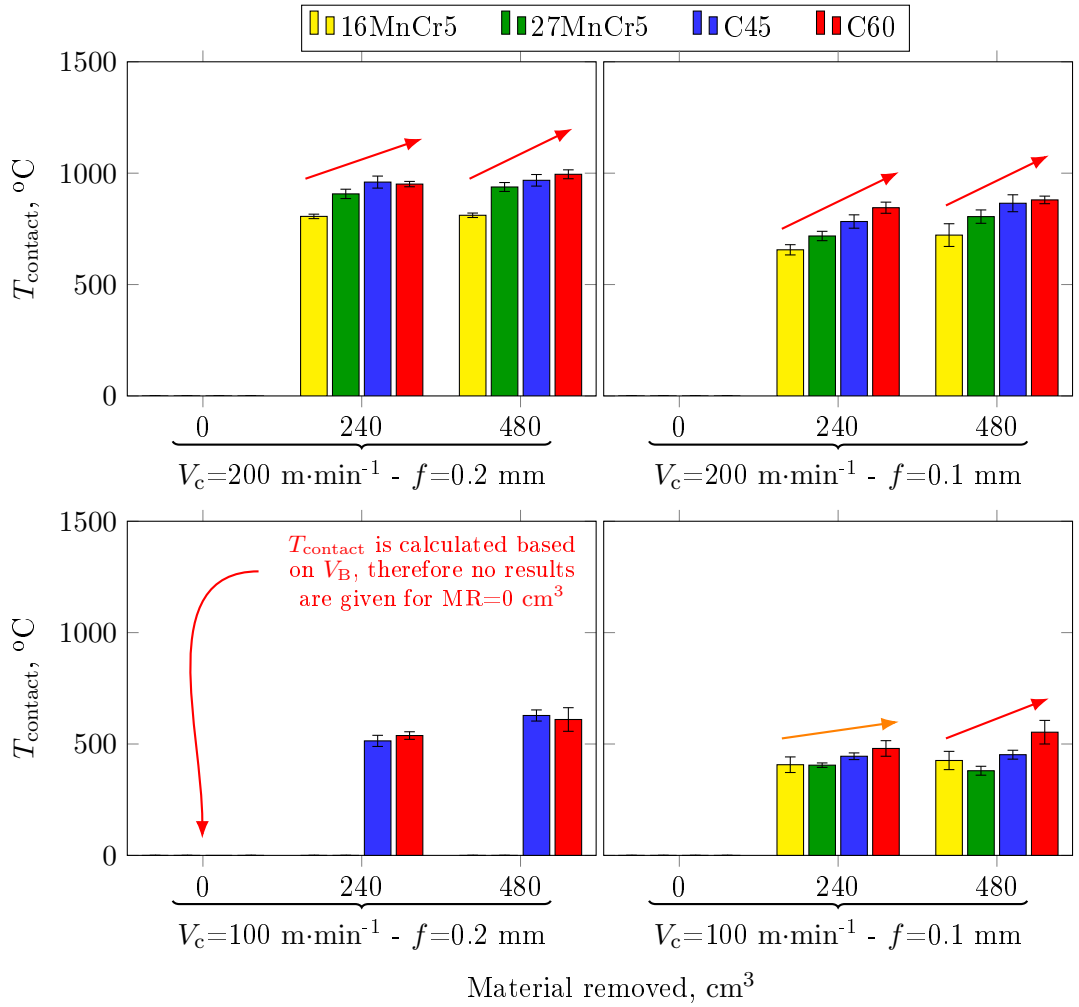

Figure 3.57: Evolution of tool flank face temperature in the mid plane of the contact section for all FP steels at all tested cutting conditions

comparing the 16MnCr5 and 27MnCr5 when cutting at V_c=100 m·min^{-1}. The $T_{contact}$ of the former was greater than that of the latter. The maximum $T_{contact}$ of 1090°C was achieved when cutting the C60 at V_c=200 m·min^{-1} and f=0.2 mm. At that specific condition, the maximum $T_{contact}$ of C45, 27MnCr5 and 16MnCr5 were 1035°C, 990°C and 900°C respectively. By the end of the tests, the minimum temperature of 550°C was obtained at V_c=100 m·min^{-1} and f=0.1 mm in the case of 27MnCr5. At this latter condition the differences between the steels were less than 120°C. The maximum difference in $T_{contact}$ between the steels was observed at V_c=200 m·min^{-1}, and was 190°C.

With regards to the flank face (Figure 3.57), in all analyzed conditions $T_{contact}$ was highest in the C60, followed by C45, 27MnCr5 and 16MnCr5. The maximum of 995°C was achieved when cutting at V_c=200 m·min^{-1} and f=0.2 mm, while the minimum of 380°C was calculated for the condition of V_c=100 m·min^{-1} and f=0.1 mm. The maximum differences between grades were in the range of 160-180°C.

In order to analyze in-depth the influence that FP steels had on T_{contact}, for each tested condition and FP steel, the average temperature throughout the measured MR states was calculated (see Table 3.11). In general, 16MnCr5 and 27MnCr presented an 8% and 6% lower temperature in the contact region of the rake face, and a 13% and 8% in the flank face, respectively. When comparing the C60 and C45, the average temperature was found to be 3% higher on the rake face, while on the flank face was 6%.

- Influence of cutting conditions on contact temperatures

To analyze the influence that cutting conditions had on T_{contact}, for each cutting condition the average temperature was calculated. The data set is summarized in the colored cells in Table 3.11. Focusing on the rake face results, increasing the cutting speed provoked an increase of 38% in T_{contact}. Increasing the feed generated an increase of 14%. In the case of the flank face, the effect of varying the cutting speed from 100 to 200 m·min^{-1} caused an average temperature rise of 50%, while the the effect of modifying the feed from 0.1 to 0.2 mm caused an increase of 19%. The results suggest that duplicating the cutting speed was more sensitive to T_{contact} increase, compared to the effect of duplicating the feed. Increasing the cutting speed influenced the temperatures on the flank face to a higher degree than the rake face, while the effect of feed was

Table 3.11: Average T_{contact} results (°C) and comparison with C45 reference steel (%) of for rake and flank faces. In colored cells: average T_{contact} result (°C) for each tested cutting condition

		16MnCr5	27MnCr5	C45	C60	Average
Tool contact temperature (rake face)	V_c=100 m·min^{-1} f=0.1 mm	560±40 -2%	555±10 -3%	570±20 *Ref.*	635±40 11%	580±30
	V_c=100 m·min^{-1} f=0.2 mm	650±30	605±25	740±25 *Ref.*	710±30 -5%	675±30
	V_c=200 m·min^{-1} f=0.1 mm	800±20 -12%	830±40 -9%	910±40 *Ref.*	930±20 2%	865±30
	V_c=200 m·min^{-1} f=0.2 mm	910±25 -11%	960±20 -6%	1030±30 *Ref.*	1040±30 2%	985±30
	Average	-8%	-6%	*Ref.*	3%	775±30
Tool contact temperature (flank face)	V_c=100 m·min^{-1} f=0.1 mm	415±40 -7%	390±15 -12%	450±20 *Ref.*	515±40 15%	445±30
	V_c=100 m·min^{-1} f=0.2 mm	—	—	565±25 *Ref.*	575±30 2%	570±30
	V_c=200 m·min^{-1} f=0.1 mm	690±40 -16%	760±25 -7%	825±35 *Ref.*	860±20 5%	785±30
	V_c=200 m·min^{-1} f=0.2 mm	810±10 -16%	920±20 -4%	965±30 *Ref.*	975±20 1%	915±20
	Average	-13%	-8%	*Ref.*	6%	680±30

sightly more appreciable in the case of the rake face.

- Discussion of contact temperature

With reference to the calculated ΔT, the close values obtained when comparing the calculated temperature rises of the 16MnCr5 and 27MnCr5 to the C45 and C60 are worth noting. However, this was to be expected as the analytical equations developed by Soler et al. (2015b) predicted greater temperature rise as the overhang distance (d) increases, which is the case of 16MnCr5 and 27MnCr5.

It is also important to note the lower ΔT achieved in the C60 compared to C45 when focusing on the rake face, in spite of being studied with the same overhang. The C60 achieved a unexpected short K_{B} or l_{c}, fact possibly linked to the extremely high degree of K_{T} which occurred when cutting this steel. Taking into account that the applied analytical equations are also dependent on the contact length, the lower predicted temperature rise in the case of C60 was reasonable. In general, the calculated temperature rises were greater than those estimated by Soler et al. (2015b), who stated that temperatures on the tool side could be underestimated by 30%. In the case of this research, up to 64% of ΔT was calculated.

The variations which occurred in the effect of cutting conditions on tool temperature when switching from T_{side} to T_{contact} were significant. In the case of the former, the influence of cutting speed and feed do not differ much, with a maximum rate difference of 5%. In the latter case, the influence of both cutting speed and feed was more significant, with cutting speed showing a difference in rates up to 33%. Comparing these results with those found in the literature, the cutting speed is commonly identified as the cutting parameter that most affects tool temperature. For example, Trent and Wright (2000) observed that varying the feed from 0.1 to 0.2 mm when machining a low alloyed steel may generate a increase of approximately 10%, while increasing the cutting speed from 100 to 200 m·min^{-1} had an influence of 20%. These findings suggest that the analysis carried out in this study with regards to T_{contact} better described the thermal behavior during cutting. However, it must be taken into account that the results in the contact section were obtained based on analytical equations, and the heat partition coefficient (α^* in Eq. 3.19) was adjusted to best fit the numerical modeling results that are shown in Chapter 4.

3.4.4 Summary of fundamental variable results

Table 3.12 summarizes the main results achieved in the analysis of fundamental variables.

Table 3.12: Summary of fundamental variable results

	General trends and link with FP steels	Influence of cutting conditions	Influence of tool wear
Chip morphology	• l_c related to K_B and increased with ferrite content • t_2 increased with ferrite content and tool wear • t_2 varied a 25% between FP steels	• $\uparrow V_c \Rightarrow \downarrow 11\%$ t_{eq} $\uparrow f \Rightarrow \downarrow 24\%$ t_{eq}	• Up to $\uparrow 43\%$ in t_{eq}
Cutting forces	• K_{sc} and K_{sf} increased with tool wear • K_{sc} differed between steels only with wear K_{sc} varied only 7% between FP steels • K_{sf} increased with ferrite content but increasing wear reduced differences K_{sf} varied 15% between steels	• $\uparrow V_c \Rightarrow \simeq K_{sc}$ $\uparrow f \Rightarrow \downarrow 23\%$ K_{sc} • $\uparrow V_c \Rightarrow \simeq K_{sf}$ $\uparrow f \Rightarrow \downarrow 41\%$ K_{sc}	• Up to $\uparrow 33\%$ in K_{sc} • Up to $\uparrow 54\%$ in K_{sf}
Tool temperature	• T_{side} and $T_{contact}$ increased with tool wear • T_{side} varied 17% between steels on rake face T_{side} varied 11% between steels on flank face • Calculated ΔT from T_{side} to $T_{contact}$: 140-370°C on rake face 35-340°C on flank face • $T_{contact}$ varied 11% on rake face and 19% in flank face between steels • $T_{contact}$ more sensitive to cutting conditions	• $\uparrow V_c \Rightarrow \uparrow$38-50% $T_{contact}$ $\uparrow f \Rightarrow \uparrow$14-19% $T_{contact}$	• Up to $\uparrow$36-50% on T_{side} (170-240°C) • Up to $\uparrow$8-12% in $T_{contact}$ (80-110°C)

3.5 An approach to understanding wear mechanisms and development of the wear rate law

In the tool wear analysis for both K_T and V_B it was observed that inserts wear more rapidly at the cutting speed of 200 m·min^{-1}. It was also concluded from the analysis of wear rate over the length of cut, $\frac{dW}{dL}$, that the wear did not only depend on mechanical causes, but also on thermal phenomena.

Before analyzing this, it should be clarified that V_B was transformed into the height of the flank face (V_H). This was done so as to have a fully comparable situation between the wear on the rake and the wear on the flank. If the wear phenomena is idealized, this occurs in a perpendicular direction to the contact surface (Xie et al. 2005; Klocke and Frank 2006). This is the case of K_T, but not the case of V_B, which corresponds to a measurement parallel to the contact surface. As depicted in Figure 3.58, transforming V_B into the direction of wear, gives the real value of the amount of material being removed. Ideally, V_H can be expressed as $V_H = V_B \cdot \tan(\alpha)$.

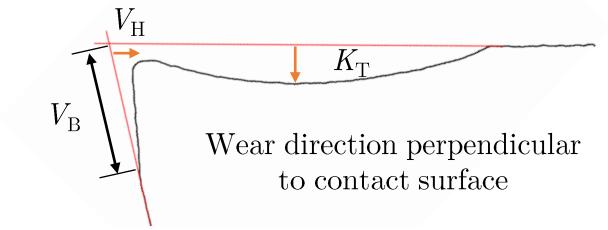

Figure 3.58: Direction of wear for flank and rake faces. Transformation from V_B to V_H

If the abovementioned statement that wear was also caused by thermally activated mechanisms, increasing $T_{contact}$ would give an increase of $\frac{dW}{dL}$. In Figure 3.59 the wear rates of $\frac{dV_H}{dL}$ and $\frac{dK_T}{dL}$ are plotted in function of $T_{contact}$.

In both crater and flank wear rates the same trend was observed. Below a certain temperature, $\frac{dW}{dL}$ was almost constant. This region could be attributed to a mechanical type wear (Takeyama and Murata 1963; Usui et al. 1984). Once a specific temperature was reached, $\frac{dW}{dL}$ increased exponentially. Above this point, the wear phenomenon could be linked to a combination of thermal and mechanical wear mechanisms (Takeyama and Murata 1963; Usui et al. 1984). This specific temperature is also called the activation temperature for thermal wearing mechanisms. It is worth noting the greater increase in $\frac{dK_T}{dL}$ than that in $\frac{dV_H}{dL}$. For an in-depth analysis, in Figure 3.60, $\frac{dK_T}{dL}$ and $\frac{dV_H}{dL}$ depending on $T_{contact}$ are plotted together.

As mentioned previously, the trends of both $\frac{dK_T}{dL}$ and $\frac{dV_H}{dL}$ were almost equal. The results of both overlapped each other. In both regions it was possible to observe that the activation temperature was nearly the same, and was estimated to be 850°C. In the detailed plot in Figure 3.60 the region that could be attributed ideally to mechan-

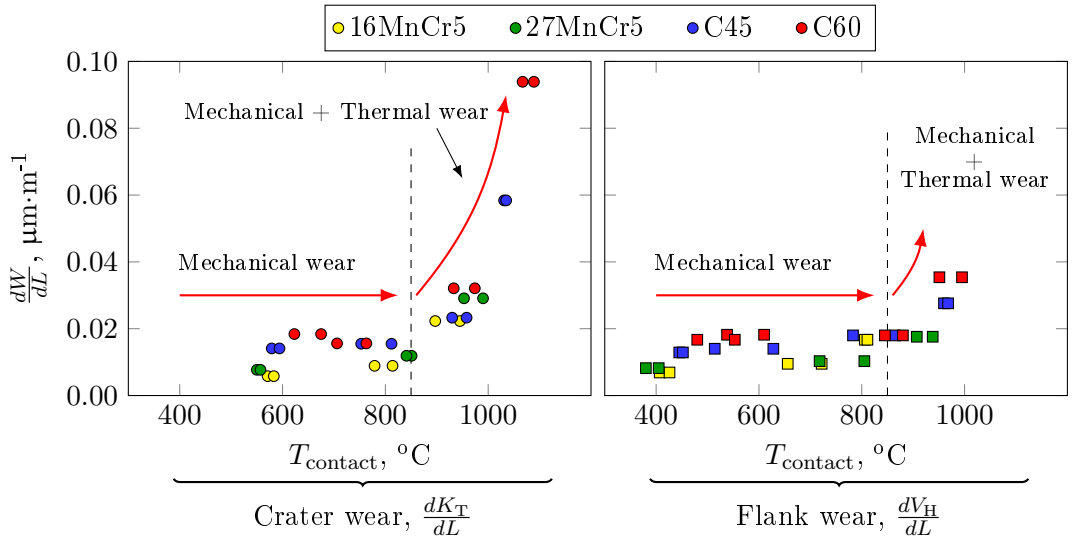

Figure 3.59: $\frac{dK_T}{dL}$ (left) and $\frac{dV_H}{dL}$ (right) plotted against T_{contact} to analyze the wear mechanisms which occurred

ical effects is shown. One of the conclusions that were extracted from this, was that $\frac{dK_{T,\text{mechanical}}}{dL}$ and $\frac{dV_{H,\text{mechanical}}}{dL}$ were in the same range, as the square and round marks for each steel lie almost in the same line. In addition, it is significant the clear differences that were found in $\frac{dW_{\text{mechanical}}}{dL}$ between the steels. This was greater when cutting the C60, followed in decreasing order by the C45, 27MnCr5 and 16MnCr5.

From the analysis of those results, it appears to be almost certain that tool wear was affected by mechanical and thermal mechanisms. Thus, the wear rate may be written as the sum of mechanically and thermally activated terms, commonly as in Eq. 3.21.

$$\frac{dW}{dt} = \frac{dW_{\text{mechanical}}}{dL} \cdot \frac{dL}{dt} + \frac{dW_{\text{thermal}}}{dt} = \frac{dW_{\text{mechanical}}}{dL} \cdot V_c + A_w \cdot \exp\left[-\frac{E_a}{R \cdot T}\right] \quad (3.21)$$

The mechanical term was represented ideally as a function of the length of cut (L). As the thermal term has some activation energy (E_a), it was represented by an Arrhenius type equation (Takeyama and Murata 1963; Usui et al. 1984). If running-in wear is ignored, Eq. 3.21 may be integrated and re-arranged to give Eq. 3.22. If numbers are given to $\frac{dW_{\text{mechanical}}}{dL}$ and to T, a plot of the natural logarithm of the left-hand side against $1/T$ would give a straight line, if the wear behaved as assumed in Eq. 3.22. The activation energy (E_a) could be obtained from the slope of the line.

$$W - \frac{dW_{\text{mechanical}}}{dL} \cdot (V_c \cdot \Delta t) = A_w \cdot \Delta t \cdot \exp\left[-\frac{E_a}{R \cdot T}\right] \quad (3.22)$$

In order to give numbers to $\frac{dW_{\text{mechanical}}}{dL}$, the first assumption that was made is that

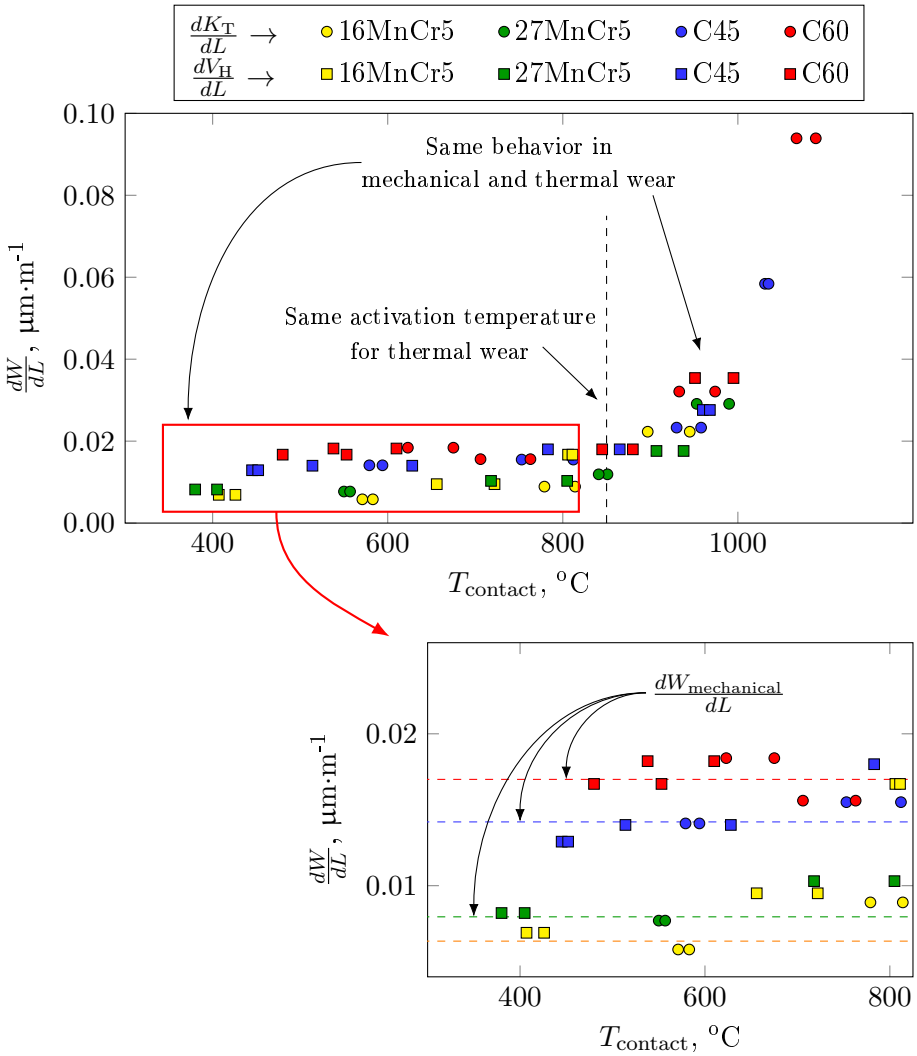

Figure 3.60: $\frac{dK_T}{dL}$ and $\frac{dV_H}{dL}$ plotted together against $T_{contact}$ (top figure). Detailed view of the wear attributed to mechanical mechanisms (bottom figure)

$\frac{dK_{T,mechanical}}{dL} = \frac{dV_{H,mechanical}}{dL}$. As explained previously, this was nearly certain in all the cases. $\frac{dW_{mechanical}}{dL}$ was calculated as the mean value of $\frac{dK_{T,mechanical}}{dL}$ and $\frac{dV_{H,mechanical}}{dL}$ in the region attributed only to mechanical wear. This is graphically explained in Figure 3.60, and the results are summarized in Table 3.13.

Table 3.13: Estimation for mechanical wear rate values

$\frac{dW_{mechanical}}{dL}$, µm·m^{-1}	
16MnCr5	0.00635
27MnCr5	0.00795
C45	0.0142
C60	0.017

Figure 3.61 plots the natural logarithm of the left-hand side of Eq. 3.22 against $1/T_{\text{contact}}$. The values of $\frac{dW_{\text{mechanical}}}{dL}$ are taken from Table 3.13, Δt varies depending on the tested condition as explained in the methodology and summarized in Table 3.1 and T_{contact} was obtained experimentally for the rake and flank faces.

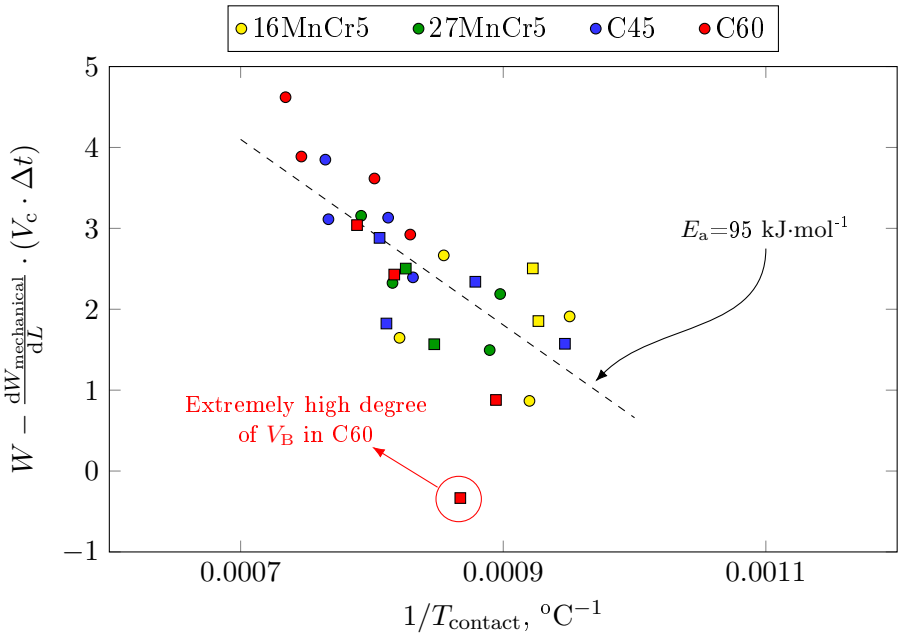

Figure 3.61: Logarithm of thermal wear plotted against $1/T_{\text{contact}}$ so as to obtain activation energies of FP steels with a P25 grade tool

In general, the results lie on the plotted straight line with little scatter. However, the high temperature range showed greater accuracy than the lower. It is also noticeable a specific test marked on the plot that belongs to the V_H of C60. This latter corresponds to a test in which an extremely high degree of V_B (and therefore V_H) of 560 µm was obtained. The results of the rake face (circle marks) and flank face (square marks) were mixed, which suggests that the thermal mechanisms could be the same for both regions. In addition, there was no marked deviation between steels, which also suggests that the thermal mechanisms which occurred when cutting any of the steels could be almost the same. By looking at the slope of the fitted line in Figure 3.61, the activation energy was estimated to be $E_a \simeq 95$ kJ·mol^{-1}.

Above all, the wear model describing the behavior of K_T and V_H , could be written as in Eq. 3.23, in which E_a=95 kJ·mol^{-1} and the universal gas constant R=8.314 J·mol^{-1}·K^{-1}. The mechanical wear rate value is obtained from Table 3.13.

$$W = \frac{dW_{\text{mechanical}}}{dL} \cdot (V_c \cdot \Delta t) + 185164 \cdot \exp\left[-\frac{E_a}{R \cdot (T_{\text{contact}} + 273)}\right] \tag{3.23}$$

Discussion of results

The trends achieved were in line with those found in the literature concerning the comparison $\frac{dW}{dL}$ -T_{contact}. A mechanical mechanism is followed by a coupled mechanical and thermally activated mechanism (Takeyama and Murata 1963). Commonly, the mechanical one could be attributed to abrasion (Ozcatalbas and Ercan 2003; Takeyama and Murata 1963), while the thermal activated one to adhesion and/or diffusion (Ozcatalbas and Ercan 2003). During the tests material adhered to the surfaces of the inserts was observed, which was removed prior to the measurements in the profilometer. Therefore, it seems that adhesion occurred. It was possible that diffusion also occurred, however no SEM analysis was carried out on the inserts.

In addition to the wear mechanisms, the results suggest that both flank and crater wear were affected by the same mechanisms, although the former was less influenced by thermal wear. Indeed, the results in Figure 3.60 almost concluded that mechanical wear $\frac{dW_{\text{mechanical}}}{dL}$ was the same in both regions. The presented results regarding thermal activation (Figure 3.61) also demonstrated that the activation energy E_{a} could be the same for both regions, which is also in line with having a similar activation temperature at around 850$^{\text{o}}$C. This did not agree with the results of Usui et al. (1984), who gave different equations for crater and flank faces. However, these were also dependent on analytically calculated normal stresses. In contradiction to this, Lorentzon and Järvstråt (2008) accurately predicted tool wear when machining nickel-based alloy 718 with a unique equation for both crater and flank faces, which suggests that wear phenomena were almost the same in the two regions, in the same manner that occurred in this research.

The results also contributed to the understanding of tool wear from the point of view of selected FP steel. With regards to the mechanical wear, $\frac{dW_{\text{mechanical}}}{dL}$ was clearly differentiated between steels, as shown in Figure 3.60. A first approach was carried out to correlate $\frac{dW_{\text{mechanical}}}{dL}$ with the analytically calculated normal stresses, in the same way that was suggested by Usui et al. (1984). However, no clear correlation was found. Increasing wear rate was probably caused by the higher abrasive behavior of the material. This could be linked to several properties such as strength, pearlite content and interlamellar spacing. However, when dividing the $\frac{dW_{\text{mechanical}}}{dL}$ by the carbon content %C, the results of FP steels became closer. This is shown in Table 3.14. Nevertheless, the close relationship found does not directly attribute mechanical wear to %C, it is only a suggestion that can be taken into account. If the mechanical wear is written in terms of %C, $\frac{dW_{\text{mechanical}}}{dL}$ leads to Eq. 3.24.

$$\frac{dW_{\text{mechanical}}}{dL} = 0.031 \cdot \%\text{C} \cdot (V_c \cdot \Delta t) \tag{3.24}$$

Of further interest are the results regarding thermal wear mechanisms. In spite of the low degree of scatter observed in Figure 3.61, the results suggest that the activation

Table 3.14: Estimation for mechanical wear rate values depending on %C

$\frac{dW_{\text{mechanical}}}{dL}$/%C, $\mu m \cdot m^{-1}$	
16MnCr5	0.028
27MnCr5	0.031
C45	0.0318
C60	0.033

energy E_a of the tool was almost the same when cutting any of the FP steels. This was about 95 kJ·mol^{-1}. Activation energy numbers differ considerably in the literature. For example, Filice et al. (2007) and Ceretti et al. (2009) applied in their studies an activation energy of E_a=75.35 kJ·mol^{-1} to successfully model tool wear when cutting a mild-steel with a P25 grade insert. In contrast, Takeyama and Murata (1963) stated that activation energy was E_a=290 kJ·mol^{-1} when cutting a heat resistant G18B alloy with a P10 grade tool. Although in this latter both tool and workpiece materials differ from those of this study, results of E_a are six times greater. Usui et al. (1984) concluded that E_a was in the range of 45-180 kJ·mol^{-1} depending if the rake or the flank face is analyzed, and also seemed to be independent of the carbon content of the material. Other researchers as Sacristan et al. (2016) studied the wear behavior of alloy Ti-6Al-4V, and obtained that E_a was in the range of 195-215 kJ·mol^{-1}. Above all, the results of E_a in this research seemed to be in the lower range compared to those found in the literature, but globally are in line with them. However, it is important to note that thermal activated mechanisms such as diffusion or adhesion are dependent on the affinity of tool-workpiece material pair. As in this study the employed P25 grade carbide was uncoated, it seems reasonable that the E_a required to promote thermal wear is reduced.

3.6 Conclusions of the chapter

In this chapter the machinability of the steels 16MnCr5, 27MnCr5, C45 and C60 was assessed. A complete orthogonal cutting study was carried out in which tool wear was characterized at different cutting conditions. During the wear process, the fundamental variables such as cutting and feed forces, tool temperatures, chip thickness and contact length were recorded. In addition, a specific setup to obtain real tool temperatures without the need to characterize the emissivity of the tool was successfully developed. The main conclusions derived from this chapter are listed below:

- In general, K_T and V_B were found to be higher in the steels with higher pearlite content or higher strength. The same occurred with tool temperature, T_{side} and $T_{contact}$, and with specific cutting forces, K_{sc}. In contrast, machining the steels with higher ferrite content achieved longer initial contact length, l_c, and also

longer K_B depending on the cutting condition and amount of MR. Chip thickness, t_2 was also greater in steels with a higher amount of ferrite. Finally, calculating $T_{contact}$ enabled the observation of differences in temperature that were not observable when analyzing only T_{side}. The increase in the fundamental variables with increased tool wear was only relevant at those conditions in which a large degree of wear occurred. These were mostly at cutting speed of 200 m·min^{-1}. The K_{sf} was the variable most affected by tool wear (up to 54% increase), followed by the t_{eq} (43% increase), K_{sc} (33% increase) and finally $T_{contact}$ (8-12% increase).

- From the analysis of $\frac{dW}{dL}$ - $T_{contact}$, two main regions of tool wear were differentiated. At lower temperatures the wear mechanism was mostly mechanical, while above an activation temperature thermal wear became significant. The wear behavior which occurred on the flank and rake faces was found to be the same, and could be modeled with the same wear rate equation. Concerning the wear behavior of the steels, these seemed only to differ in the wear attributed to mechanical effects ($\frac{dW_{mechanical}}{dL}$). The wear linked to thermal activated mechanisms was almost the same for all the steels. If modeled with an Arrhenius-type equation, the calculated activation energy was E_a=95 kJ·mol^{-1} when cutting with an uncoated carbide P25 grade. Above all, it was possible to characterize a wear rate law, in which the mechanical wear was roughly written in function of the %C of the steels. However, it was not possible to directly link the mechanical type wear with any of the analyzed fundamental variables such as stresses.

Some more in-depth conclusions were achieved from the results of this chapter. These are the following:

- The designed orthogonal cutting procedure to record simultaneously the tool wear and fundamental variables successfully gave the required data sets to validate the numerical models and to develop a wear rate model to be implemented in the FE codes. The setup to establish a direct relationship between the radiation of tool surface (interpreted in digital levels by the camera) and the real surface temperature seemed to give realistic temperature values. Although it has not been presented in this chapter, tool inserts were verified to be not oxidized, which was necessary to be confident of achieved temperature values. This setup had the benefit that the relationship of (DL, T) was characterized at the same focusing field and integration time as the one employed in the orthogonal procedure.

- Globally, machining the C60 steel obtained the highest degree of V_B by the end of the tests, followed in decreasing order as the amount of pearlite content in the material decreased. However, at the beginning of the tests, the amount of flank wear was almost equal when cutting any of the steels, or even higher in the case of the 16MnCr5 and 27MnCr5, in spite of their lower pearlite content. A hypothesis of these unexpected results is that the Al_2O_3 inclusions that appeared in the latter two steels, combined with the shorter interlamellar spacing, generated this first

higher wear increase. In general, cutting the C60 steel experienced a 39% of higher V_B than cutting the C45 steel, and a 22% and 23% lower for the case of 27MnCr5 and 16MnCr5 respectively. With regards to the cutting conditions, increasing both cutting speed and feed involved increasing flank wear. The influence of the former was greater than that of the latter.

- Crater wear presented the same trend in all cutting conditions. Increasing pearlite content in the machined FP steel generated a higher degree of K_T from the beginning to the end of the trials. Increasing cutting speed and feed also generated an increase in K_T, but the effect of the former was six times greater than that of the latter. Increasing the cutting speed increased rake face temperature to a higher degree than the feed did, therefore generating a higher amount of wear. This conclusion was in line with the results of the rate $\frac{dK_T}{dL}$, which suggested that K_T was highly affected by a thermally activated wear mechanism, apart from abrasive mechanisms. In general, cutting the C60 caused a 60% of higher degree of K_T compared to that of C45, while cutting the 27MnCr5 and 16MnCr5 the K_T was reduced a 40% and 50% respectively.

- The crater length presented diverse trends, which seemed to be linked to the amount of K_T. When K_T was not significant, K_B was higher in the steels with higher amount of ferrite. In contrast, increasing K_T caused a change to the trends, obtaining almost longer K_B when cutting the steels with a higher amount of pearlite. However, this only occurred in all the cases except in the C60. It was believed that the extremely high degree of K_T found in this steel, which generated a significant concave on the rake face, was not allowing the length of the crater to increase in the same manner as in the other steels.

- In the qualitative analysis carried out from the collected chips, chip serration and chip side flow was observed in some cases. These were more severe as the amount of pearlite was greater in the steels. In addition, cutting at the feed of 0.2 mm also promoted the apparition of these types of chip formations. The chip thickness ratio, t_{eq}, was greater in the steels with a higher amount of ferrite. Increasing both cutting speed and feed caused a decrease in t_{eq}, but the effect of the feed was two times greater than that of the cutting speed. The measured contact lengths with a fresh tool (beginning of the tests) were greater in the steels with a higher amount of ferrite.

- The specific cutting forces differed between the steels only when the tool started to wear. Before this point, the K_{sc} of all steels converged in the same value, while above a certain degree of wear, the steels that presented a higher K_{sc} were those with higher amount of pearlite. In contrast, the specific feed forces, K_{sf}, were always higher in the steels with a higher ferrite ratio.

- An approach was established to calculate tool contact temperatures based on measured tool side temperatures and fundamental variables of cutting and feed

forces, chip thickness and contact length. Temperature corrections in the range of 140-370°C on the rake face and 35-340°C on the flank face were calculated to overcome the effect of the overhang. The contact temperatures between the steels differ in the same manner than those of the tool side. The change was greater when analyzing the influence that cutting conditions had on contact temperatures. In this case, increasing the cutting speed caused an increase of 38-50% in temperature, while increasing the feed provoked an increase of 14-19% for the rake-flank faces. For this reason calculated contact temperatures were more sensitive to the variation of cutting conditions than the tool side temperatures.

Chapter 4

Machinability prediction based on finite element modeling

The finite element based modeling has become one of the most widely employed tools, not only for the prediction of industrial relevant outcomes, but also to help in the understanding of the manufacturing processes. Data sets of scientific or fundamental variables that can not be measured experimentally can be obtained by FE models, making them interesting tools for both researchers and industrial engineers. This research work has developed a numerical FE-based model focused on machinability prediction in terms of tool wear.

This chapter is divided in two main sections. First a literature review sets out the fundamentals of FE models, and focuses on the main inputs, outputs and developed models in the field of machining. Secondly, the developed work and main conclusions are described.

As set out in Figure 4.1, the developed machining model consists of an Arbitrary Eulerian Lagrangian model (ALE), in which the cutting procedure is realized in 2D. The most significant input parameters were characterized during this research and are

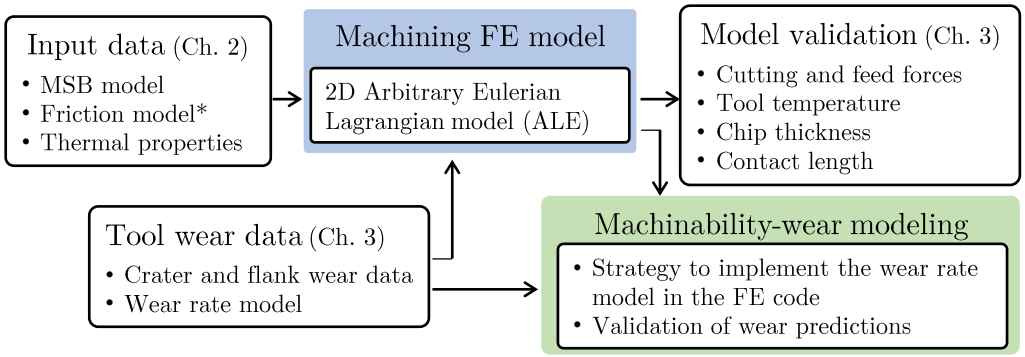

Figure 4.1: Flowchart of the chapter (*Friction model is not characterized in Chapter 2)

discussed in Chapter 2. Additionally, the modeled friction behavior, which plays an important role in machining together with the flow stress model, is presented in this chapter. The friction was not characterized directly in this Ph.D., but a representative model was extracted from the research projects in which this thesis was involved. First, the validity of the model was set by comparing the predicted results with those achieved in Chapter 3. Cutting and feed forces, tool contact temperature, chip thickness and tool chip contact length were the fundamental variables compared. The second step was to predict industrial relevant outcomes, that in this case referred to machinability or tool wear. A strategy was established to integrate the wear rate model in the FE code, enabling the automatic generation of wear in the tool. The reliability of wear predictions is discussed at the end of this chapter.

4.1 Literature review

In recent decades, analytical, numerical and even empirical models have been developed in the field of machining modeling. This research focuses only in the FE-type numerical models, as they can connect with industrial aspects (surface integrity or tool life) and obtain fundamental process parameters, which is in line with the objectives proposed in this research.

First, the most significant FE models developed to represent cutting operation are analyzed. Following this analysis, the inputs required and the relevance of these is presented. An in-depth description is carried out only on those inputs that have not been previously presented in this document. The applicability of the predictive models is divided into (*Stage 1*) fundamental or scientific variables and (*Stage 2*) industrial relevant outcomes (Figure 1.3). A short description of the performance of FE machining models in terms of fundamental variables is presented. After that, the necessary procedure to move from *Stage 1* to *Stage 2* to predict tool wear is analyzed. This is carried out by wear rate laws, previously developed in Chapter 3. The methodology for integration of a wear rate law into the FE codes is discussed, to finally evaluate the performance of the most relevant *Stage 2* machining models.

4.1.1 Machining FE-based models

In the next lines the most commonly employed machining FE models are described, which are namely the Lagrangian models (based on element deletion or remeshing techniques), the ALE model and the CEL model. In the review of Arrazola et al. (2013) other modeling techniques were introduced, such as meshless techniques, Smooth Particle Hydrodynamics (SPH), Constrained Natural Element Method (CNEM) and Volume of Solid (VOS). Although some of those were also analyzed during this Ph.D., it was decided to focus only on the most relevant models employed for machining processes.

Lagrangian formulation and element deletion

These simulation models follow the Lagrangian formulation, which means that deformation of solid (workpiece material) drives deformation of mesh. In order to avoid element distortion in the cutting edge vicinities as a consequence of material separation, elements are deleted prior to being excessively distorted. In all cases, once the element is deleted, volume loss and discontinuities in tool-workpiece contact occur. This directly causes discontinuities in the thermo-mechanical state of the contact surfaces.

The criteria to delete the elements are material state dependent, which can be set as a function of effective strain (also named shear failure models) (Guo and Wen 2005), effective stress (or tensile failure models), energetic models based on the energy produced for plastic deformation, or even the combination or modification of the aforementioned (Ceretti et al. 1999; Obikawa et al. 1997).

Two types of methodologies can be found in the literature that apply element deletion techniques. The first one consists of applying the same criteria to the whole workpiece, which lets the material state itself delete the critical elements (Ducobu et al. 2011; Umbrello 2008). In the second approach the deletion criteria is only applied to a line or a few lines of elements at the height of the cutting edge (Guo and Liu 2002; Lin and Lo 2001; Obikawa et al. 1997). Thus, only these elements can be deleted, preventing the deletion in non desirable regions.

The element deletion technique is also employed to predict chip segmentation and discontinuous chip formation (Ceretti et al. 1999; Guo and Wen 2005; Umbrello 2008; Bäker et al. 2002; Ducobu et al. 2011). However, the formation of segmented chips is not only caused by the deletion technique, it also requires an appropriate flow stress model that predicts strain softening (Ducobu et al. 2015). An example of predicted saw-toothed chip formation compared to that of an experimental chip when cutting a Ti-6Al-4V is illustrated in Figure 4.2.

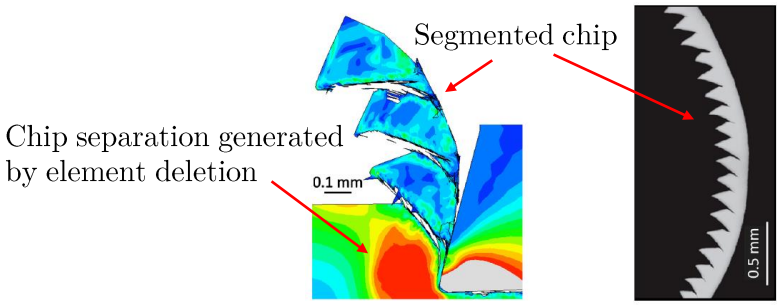

Figure 4.2: Predicted saw-toothed chip formation compared to an experimentally obtained chip when cutting a Ti-6Al-4V alloy, adapted from Ducobu et al. (2011)

Lagrangian formulation and element remeshing

Instead of deleting the highly deformed elements, in these type of models the elements are continuously remeshed (generation of new mesh) to enable chip separation and to prevent mesh distortion. In this field two types of models are distinguished: full remeshing models, which means that the entire workpiece is remeshed, and local remeshing models, in which the remeshing is only performed in the highly deformed areas. The remeshing methodology is applied prior to reaching the distortion of the elements. At certain defined time intervals, the contour of the workpiece or contour of the highly deformed region is extracted, and a new mesh is then generated. This new mesh is commonly created based on Delaunay triangulation, and for this reason most common remeshing models are limited to triangular or tetrahedral elements. Once the new mesh is created, results from the deformed mesh are mapped to the new undeformed mesh.

This technique is one of the major advantages that commercial software such as TWS-Advantedge (Childs and Rahmad 2009; Childs 2009) and SFTC-Deform (Özel 2006; Umbrello et al. 2004) have implemented in their FE codes. However, it can also be developed with general purpose software such as Abaqus. In this field, the studies of Prof. Schulze and his co-workers was found to be relevant. In their prior models the remeshing technique was applied to the full workpiece (Schulze and Zanger 2011; Schulze et al. 2011; Schulze et al. 2012), however in their last published research the developed algorithm was optimized to only remesh the local elements that were highly deformed (Zanger et al. 2015).

The remeshing technique has some drawbacks however. The first is the complicated algorithms that have to be programmed. The second problem, which can not be avoided, is the diffusion or slight variation of results while interpolating state variables from mesh to mesh.

An example of local remeshing developed by Zanger et al. (2015) is shown in Figure 4.3. The remeshing is set in four stages. First the deformed element, the one that does not assess the sufficient mesh quality (element shape criteria), is detected (Figure 4.3-a). To achieve the new mesh with non-distorted elements, the mesh around the detected element is deleted (Figure 4.3-b). Then, a new part is generated with the geometrical properties of the deleted mesh. This is meshed with non-distorted elements (Figure 4.3-c) and integrated into the old mesh (Figure 4.3-d).

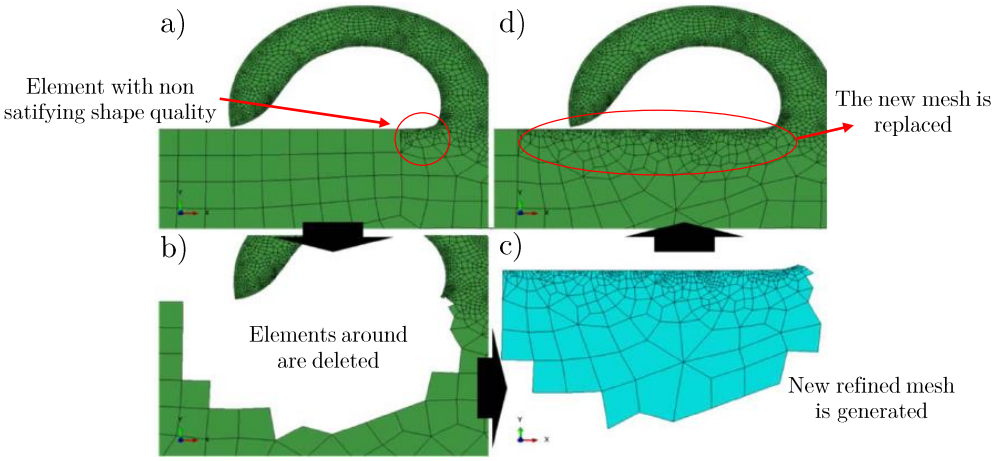

Figure 4.3: Remeshing steps: a) detection of non satisfying shape element, b) deletion of elements around, c) create a new mesh and d) mesh replacement, adapted from Zanger et al. (2015)

Arbitrary Eulerian Lagrangian formulation - ALE

This technique combines the unique features of Lagrangian and Eulerian formulations. Two main approaches are found in the literature: ALE model with Eulerian and Lagrangian boundaries (Figure 4.4-a) and ALE model with only Lagrangian boundary conditions (Figure 4.4-b). The former requires a predefined chip assumption, and chip flow is modeled as an inlet of material flowing against the tool (in flow). Two outlets of material are defined in the Eulerian surfaces, the chip flow and out flow of the workpiece. Both tool and workpiece are fixed in space. The geometry of the model and the mesh is adapted by means of adaptive meshing, which leads the nodes to displace in such a manner that they are adjusted to the material deformation (Arrazola and Ozel 2008; Courbon et al. 2013; Courbon et al. 2011). In contrast, the model with Lagrangian boundaries is free of any geometrical assumption, and the chip is generated by means of only mesh adaptivity (Arrazola et al. 2010; Ducobu et al. 2011). One of the parts, the tool or the workpiece, is fixed in space while the other moves at a velocity equal to V_c.

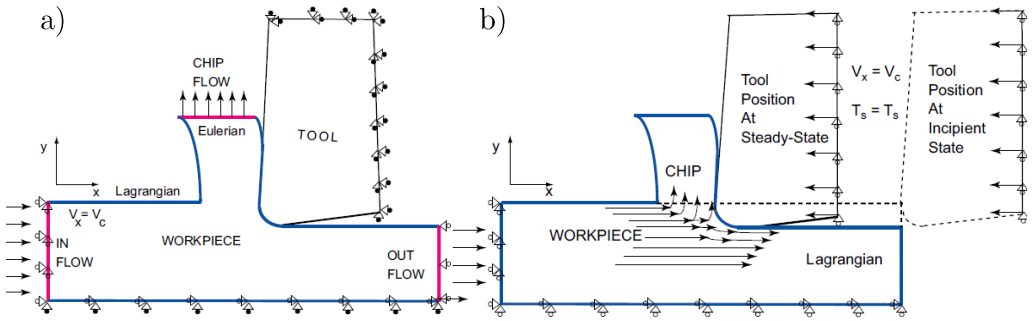

Figure 4.4: FEM models for ALE formulation with (a) Eulerian and Lagrangian boundary conditions, and (b) pure Lagrangian boundary conditions, adapted from Arrazola et al. (2010)

Coupled Eulerian Lagrangian formulation - CEL

The coupled Eulerian Lagrangian (CEL) formulation also attempts to capture the strengths of the Lagrangian and Eulerian formulations. The cutting tool is modeled under a Lagrangian frame, in the same manner that is done in the ALE formulation. In contrast, the workpiece is modeled in a fully Eulerian domain (Zhang et al. 2015). In the latter, the mesh is static and the material flows through the elements while is being deformed. The Eulerian region is divided into two sections. One of them is composed of "filled" elements, modeling the workpiece, and the other is set with "void" elements. While the chip is being generated, the material flows filling the void elements based on a Eulerian Volume Fraction (EVF). This EVF represents the ratio of material fraction that the element has, with values in the range of 0-1 for totally void or filled elements respectively (Ducobu et al. 2016). The boundary of the tool is taken as a kinematic constraint in the Eulerian calculation and the stresses from the Eulerian cell are used to calculate the resulting surface stress (Mav 2013). In the earliest developed CEL models (Raczy et al. 2004), the thermal transfer between domains was still not possible in commercial FE softwares. However, as was demonstrated by Ducobu et al. (2017a), in current FE software such as Abaqus, thermal transfer between Lagrangian tool and Eulerian workpiece has become possible.

Two different strategies were found in the literature to model the cutting process. The first option consists of a fixed tool and a fixed workpiece mesh, in which an inlet of material flows against the tool (Raczy et al. 2004; Zhang et al. 2015), as shown in Figure 4.5-a. The main advantage of this strategy is the lower number of elements required, as is not necessary to model the whole workpiece length, only an inlet of material. The second option consists of a moving tool, which interacts with a static workpiece inside the Eulerian domain (Ducobu et al. 2016) (Figure 4.5-b).

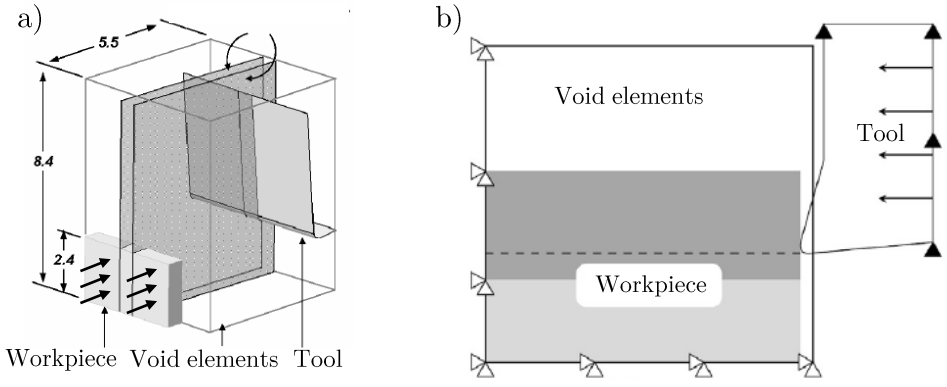

Figure 4.5: CEL model with workpiece inlet flowing against the tool, adapted from Raczy et al. (2004). (b) CEL model with tool moving against the workpiece, adapted from Ducobu et al. (2016)

4.1.2 Necessary inputs to develop a FE-based cutting model

From the scientific framework analyzed in Section 1.1, it is worth noting that input parameters in numerical modeling are of considerable influence when obtaining representative results (Childs 2010; Sartkulvanich et al. 2005).

In the latests reviews that deal with the modeling of the cutting process (Arrazola et al. 2013; Leopold 2014; Melkote et al. 2017), it is possible to find a section only dedicated to input parameters, specifically that published by Melkote et al. (2017). Since the sensitivity analysis carried out by Arrazola et al. (2004) or even the works regarding friction modeling of Özel (2006) and Childs (2006), it is almost certain that most influencing parameters are the constitutive or flow stress model, friction model and the thermo-physical properties of tool and workpiece. These are analyzed below.

Constitutive or flow stress model

The constitutive models are analyzed in-depth in Section 2.1.3. Arrazola et al. (2013) and Melkote et al. (2017) made a distinction in two main groups: phenomenological models and physically-based models. However, in this study an intermediate group named physical-phenomenological models is also distinguished. The main advantages and disadvantages of these models is set out in the critical analysis of Section 2.1.4. One of the main contributions of this thesis is the development of a physical-phenomenological model, named MSB model, presented in Section 2.6.

Friction model

Friction between contacting bodies is important in machining process applications, as the plastic deformations of workpiece occurring under high pressure states are dependent on this phenomena (Melkote et al. 2017). The coefficient of friction (μ) is defined as the ratio of the forces acting parallel (F) and perpendicular (N) to the interface between the two bodies in relative motion ($\mu = F/N$). The mechanisms responsible for friction are mostly adhesion, plastic deformation of asperities and ploughing action occurring in the vicinities of rounded edges (Holmberg et al. 1998).

A large number of studies have been published to date with the objective of representing the most realistic contact behavior between chip and tool. In the current practice, in most studies friction has been modeled with a constant coefficient based on the Coulomb model ($\mu = F/N$). It is in the work of Zorev (1963) that two regions of contact, sticking and sliding regions, were first distinguished. As shown in Figure 4.6, the zone of sticking is situated near the cutting edge. In this region the shear stress exhibits a plateau, which can be determined by the shear friction factor ($\tau_f = mk$, where k is the shear flow strength of the material). Above the sticking region, the stress distribution satisfies the Coulomb friction law ($\tau_c = \mu\sigma_c$). In the regions of

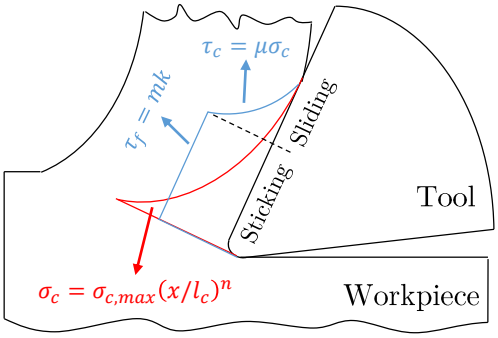

Figure 4.6: Contact stress distribution model of Zorev (1963)

constant shear friction, m typically ranges from 0.1 to 0.9. When $m = 1$ the contact behavior is fully plastic (Melkote et al. 2017).

Shirakashi and Usui (1973) proposed Eq. 4.1 to model the shear stresses in the interface (τ_f). Basically, the shear strength of material (k) is related to the normal stresses on the face (σ_n) by an inverse exponential function. This equation leads the modeling of a behavior similar to that sticking-sliding proposed by Zorev (1963).

$$\tau_f = k\left(1 - e^{-\mu\sigma_n/k}\right) \tag{4.1}$$

A modification of the abovementioned expression was developed by Childs et al. (1989) which was studied experimentally by orthogonal cutting tests with split tools (Eq. 4.2). They included in the equation the principle of a maximum saturation shear stress in the form of $\tau_f = mk$. The values of m were in the range of 0-1. A further refinement, which affects τ_f in the transition between $\tau_f = \mu\sigma_n$ and mk, is Eq. 4.3 (Childs 2000).

$$\tau_f = mk\left(1 - e^{-\mu\sigma_n/mk}\right) \tag{4.2}$$

$$\tau_f = mk\left(1 - e^{(-\mu\sigma_n/mk)^n}\right)^{(1/n)} \tag{4.3}$$

This latter formulation was tested on a FE cutting model over a wide range of μ, m and n values in the study of Dirikolu et al. (2001). Both simulation and experimental results were in a good agreement as far as cutting forces were concerned. In contrast, the model had a tendency to underestimate the measured average rake face temperatures.

The determination of the friction coefficient in machining has also been assessed experimentally. At least two main methodologies are distinguished to identify this coefficient: cutting force measurements and tribometers. The first approach has been commonly employed in turning operations (Özel and Zeren 2004; Arrazola 2003), but it has the drawback that is unable to differentiate between sticking and sliding regions caused by

variations in local sliding velocity, contact pressure and temperature (Melkote et al. 2017).

Concerning the approach of characterizing friction based on tribometers, conventional and specially designed tribometers are found in the literature. In general, conventional tribometers such as pin-on-disc, do not simulate the relevant tribological conditions that occur when machining, as there is no surface refreshment and characterizations are independent from the cutting forces (Melkote et al. 2017). For this reason the specially designed open tribometers have became widely employed. The main features of these techniques are (i) continuous surface refreshment, (ii) high contact pressures and (iii) high sliding velocities in the range of those occurred during cutting. Several devices have been developed to accomplish these abovementioned objectives, which are summarized in the review of Melkote et al. (2017).

The improved open tribometer developed by Zemzemi et al. (2008) was found relevant. The setup consists of a cylindrical pin rubbing on a fresh surface during rotation of the workpiece (Figure 4.7). A large feed of the pin enables a helical movement in order to avoid superposition of the scratches produced on the cylinder. This is installed on a lathe, which permits reaching high sliding velocities. In addition, it also provides high contact pressures between pin and bar, and permits the calculation of the heat partition coefficient at the interface (Claudin et al. 2010). The unique drawback attributed to this setup is that the measured friction coefficient is in reality an apparent friction coefficient, which is affected by the intense contact pressures and plastic deformations. Therefore, the measured values have to be corrected by an analytical model based on the observation of the scratches occurring on the bar (Claudin et al. 2010).

Concerning their main works focused on ferrite-pearlite steels, Abdelali et al. (2012) characterized the friction coefficient during dry cutting of an AISI 1045 steel. Three main sliding regions were identified (Figure 4.8). For low sliding velocities (1), the pins had an important adhesive layer of steel inside the contact area, which hampered the movement of the pin. Therefore a high value of apparent friction coefficient was

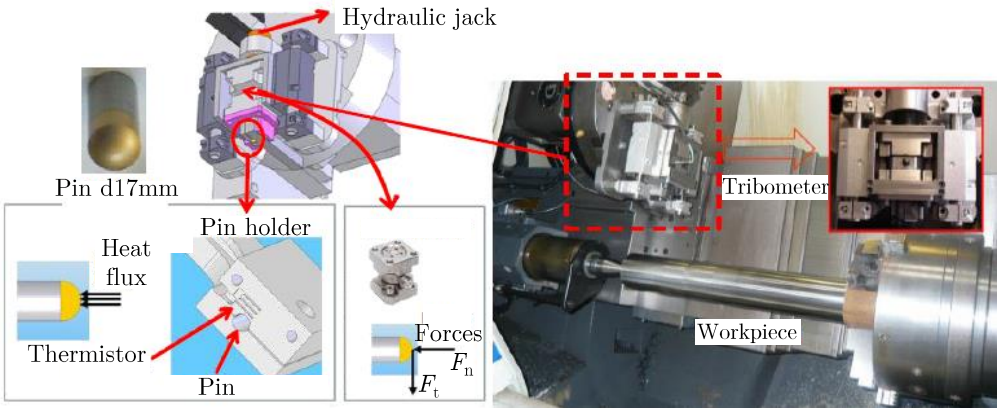

Figure 4.7: Open tribometer developed by Zemzemi et al. (2008), adapted from Arrieta et al. (2017)

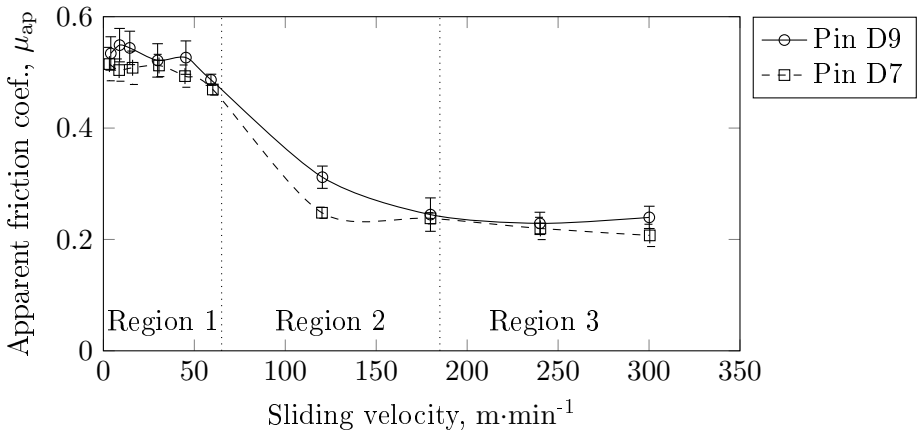

Figure 4.8: Evolution of apparent friction coefficient versus sliding velocity, adapted from Abdelali et al. (2012)

obtained. For intermediate sliding velocities (2), the material flowing through the side of the pins was responsible for the adhesion observed on the pins, in which the effective contact pressure was very low and thus the apparent friction was reduced. Finally, for large sliding velocities (3), a lack of adhesion phenomenon facilitated the movement of the pins, which was coherent with a low apparent friction coefficient.

Arrieta et al. (2017) employed the same open tribometer to characterize the effect of ferrite-pearlite microstructures on friction. Tribological tests of different FP steel grades with a wide range of carbon content and microstructure morphologies were developed. A high degree of correlation was found with the ferrite content and with the macroscopic hardness of the steels. Increasing ferrite content (from 10% to 30%), caused the friction coefficient to increase steadily, until reaching a threshold when the ferrite content was greater than 35% (Figure 4.9-a). Concerning the comparison with

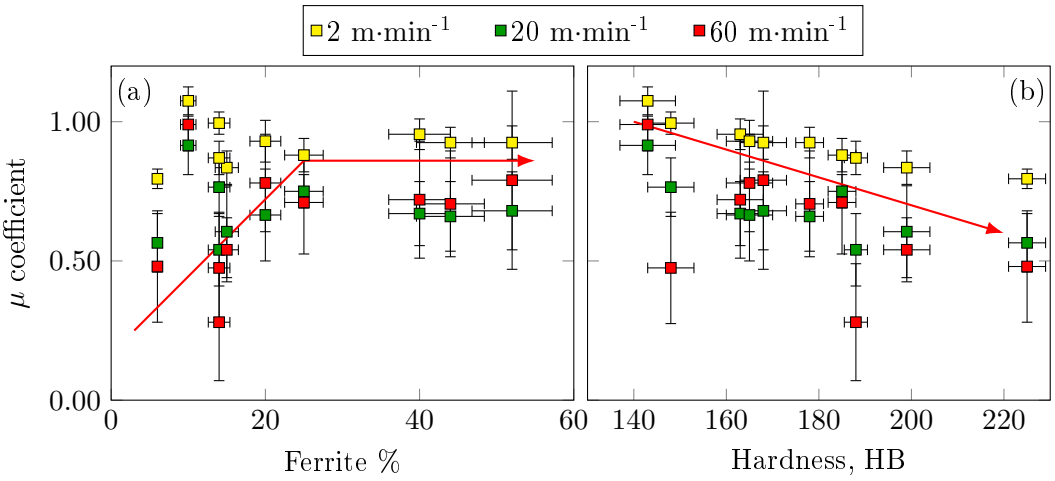

Figure 4.9: (a) Influence of ferrite content and (b) influence of macro-hardness on apparent friction coefficient, adapted from Arrieta et al. (2017)

the hardness of the material, a decreasing pattern was observed with increased hardness (Figure 4.9-b).

Thermal data and models

The accuracy of cutting process simulation is dependent on the accuracy of the heat transfer model, including the temperature-dependent physical and mechanical properties of the model.

- Thermal and physical properties of materials

The commonly required data for modeling machining are thermal diffusivity κ, the specific heat C_{p}, the coefficient of thermal expansion β and the density ρ (Melkote et al. 2017). By means of these properties it is possible to calculate the thermal conductivity $K = \kappa\rho C_p$. These have been characterized in the course of this research, and have already been presented and discussed in Section 2.4. However, it is important to note the special significance that thermal diffusivity and thermal effusivity ($b = \sqrt{kC_p\rho}$) have in heat conduction. The former means the ability of the material to conduct energy relative to its ability to store it, whereas the latter is a measure of the rate at which the material can absorb heat. Materials with low b value are commonly linked to high temperatures.

- Thermal conductance

In the majority of works that were analyzed from the literature, the thermal conductance k_{i} was assumed to be infinity (perfect contact) with values in the range of $10^4 - 10^6\,\mathrm{Wm^{-2}K^{-1}}$ or higher (Arrazola et al. 2013; Melkote et al. 2017). These values seemed reasonable for uncoated tools. However, coated tools are commonly employed to improve tool life and reduce friction. Although the present research is constrained to uncoated tools, it is worth highlighting the existence of studies that identify the k_{i} depending on the size and type of the coatings, which are summarized in the work of Melkote et al. (2017).

- Heat partition

The size of friction stress τ between chip and tool, or between tool and workpiece, gives rise to a friction heating rate. Some fraction of the heat (α^*) flows into the chip and the remaining fraction (1-α^*) flows into the workpiece. This coefficient α^* is the heat partition coefficient. Childs (2000) derived an analytical equation to calculate α^* in the tool-chip interface (Eq. 4.4), which depends on a shape factor S_f (common values in the range 1-2), the thermal number $[U_{\mathrm{work}} f \tan\theta/\kappa_{\mathrm{work}}]$, the Péclet number β, the relative conductivity of tool and workpiece materials $[K = K_{\mathrm{tool}}/K_{\mathrm{work}}]$, the relative sliding velocity of workpiece U_{work}, and geometrical parameters of shear angle θ and feed f.

$$\begin{aligned} &\alpha^* \left[1 + \frac{(0.45\pm0.15)}{S_f} \left(\frac{K_{\text{tool}}}{K_{\text{work}}}\right) \left(\frac{\kappa_{\text{work}}}{U_{\text{work}} f \tan\theta}\right)^{\frac{1}{2}}\right] \\ &\approx 1 - \frac{(1.35\pm0.5)}{S_f} \frac{(1-\beta)}{U_{\text{work}} f \tan\theta / \kappa_{\text{work}}} \left(\frac{K_{\text{tool}}}{K_{\text{work}}}\right) \end{aligned} \tag{4.4}$$

However, the presented assumption starts to fail for $[U_{\text{work}} f \tan\theta / \kappa_{\text{work}}] < 5$, and for this reason some corrections were carried out by Childs (2000) to allow the calculations in the lower speed range.

In addition to the analytical procedures to calculate the heat partition, Zemzemi et al. (2009) calculated empirically the heat flux flowing into the pin during tribological tests in the open tribometer. During friction tests, the heat flux transmitted to the pin was estimated from the evolution of the temperature measured by a thermistor located in the pin holder. To a further extent, Abdelali et al. (2012) employed this setup to establish the heat partition when cutting steel AISI 1045. The evolution of the heat flux partition versus sliding velocity is plotted in Figure 4.10. This figure shows that the heat partition coefficient is strongly influenced by the sliding velocity. Two regimes can be distinguished: Below 60 m·min^{-1} (1), α^* decreased with sliding velocity from 50% to 20%. This meant that a larger percentage of heat was transmitted to the workpiece. Above 60 m·min^{-1} (2), α^* decreased very slowly from 20% to 10% even if sliding velocity increased from 60 to 300 m·min^{-1}.

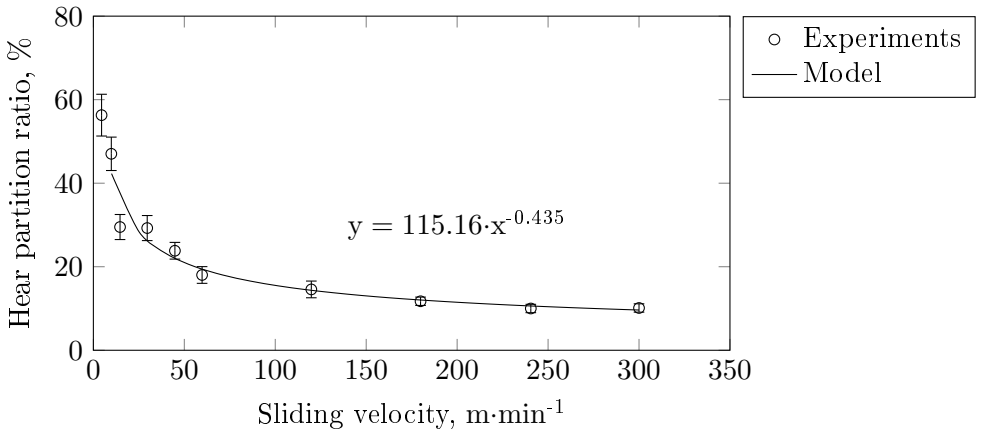

Figure 4.10: Evolution of heat partition (α^*) versus sliding velocity, adapted from Abdelali et al. (2012)

4.1.3 Outputs from FE models

In the scientific framework (Section 1.1) two types of outputs were distinguished: fundamental variables (*Stage 1*) and industrial relevant outcomes (*Stage 2*). The prediction of industry-relevant parameters requires the prediction of fundamental process variables as a prerequisite (Arrazola et al. 2013). For instance, FE models directly provide the data set regarding the fundamental variables. The same does not occur with *Stage 2* results. For the specific case of tool wear, additional wear rate models are required to correlate certain variables from *Stage 1* to obtain representative results in *Stage 2*.

Tool wear prediction with FE models

One of the main applications of wear models is to predict tool wear in combination with FE models. The required physical inputs for the wear equations (see Section 3.1.5) are extracted from the numerical model, thus enabling the prediction of wear patterns in the different contact regions of the tools. For example, in the work of Lorentzon and Järvstråt (2008) different friction and wear models were analyzed, as well as their impact on the predicted wear profile. The tested equations referred to Usui's and Takeyama and Murata's models. They found excellent experimental agreement in crater and flank wear simulation of cemented carbide tools when machining Ni-based alloy 718. A comparison of the predicted and measured 2D profiles for crater and flank faces are depicted in Figure 4.11. They concluded that a lower friction coefficient in the area around the tool tip together with Usui's empirical wear equation achieved the best experimental agreement.

Recently, other authors such as Hosseinkhani and Ng (2015) and Bencheikh et al. (2017) have also combined FE methods with empirically characterized wear models to predict tool wear in 2D. However, these are mainly focused on the prediction of flank wear.

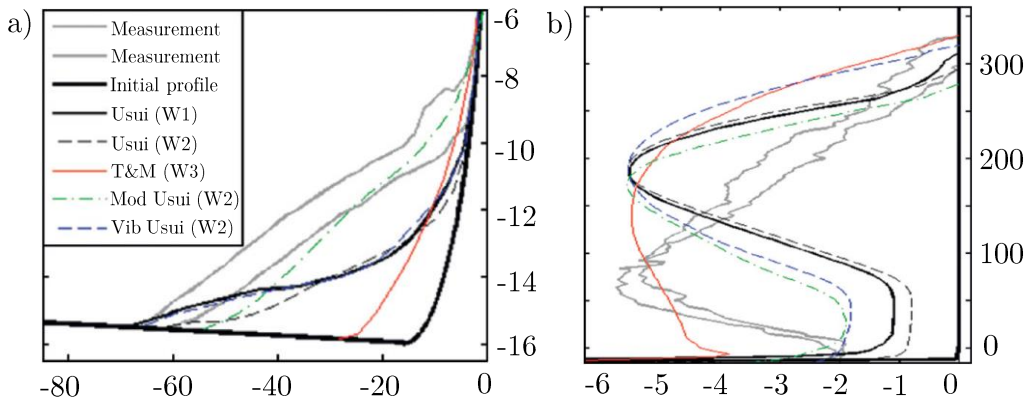

Figure 4.11: Predicted and measured wear profiles of flank face (a) and rake face (b) (Lorentzon and Järvstråt 2008)

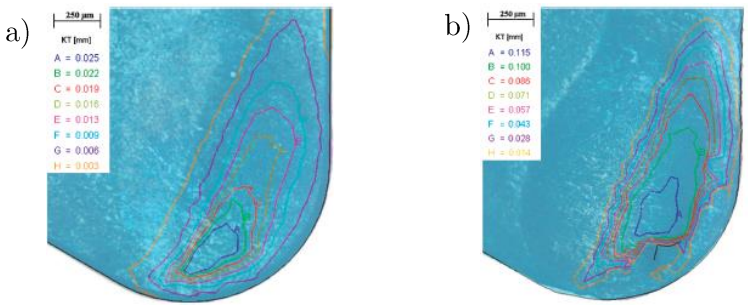

Figure 4.12: Experimental (a) and simulated (b) crater wear (Attanasio et al. 2008)

Wear patterns in 3D geometries have also been predicted by Attanasio et al. (2008) and Binder et al. (2015). The former applied Takeyama and Murata's model to predict diffusive wear on uncoated WC tools when machining AISI 1045. The flank wear trends and the crater wear patterns were in line with experimental tests. An example of crater wear pattern is shown in Figure 4.12. The latter extended tool wear studies to machining with coated tools. In this case the tests were focused on machining AISI 1045 with PVD-TiAlN-coated carbide. For the predictions Usui's wear rate model was employed. They concluded that tool wear simulations that do not consider initial wear tend to underestimate flank wear. However, the predictions of wear rate, crater depth and its geometrical location were in good agreement with the experiments. Recently, Attanasio et al. (2017) improved the abovementioned modeling strategy to predict tool wear in the drilling process, but without updating the geometry of the tool.

In a certain number of studies tool wear is modeled explicitly (Yen et al. 2004; Klocke and Frank 2006; Xie et al. 2005; Filice et al. 2007; Attanasio et al. 2008). In these, the boundary nodes from the tool are moved by the amount of calculated wear in a direction normal to the contact surface. To represent K_T or V_B, the nodes are moved perpendicular to the rake and flank faces respectively (Klocke and Frank 2006). For the case of the cutting edge, the displacement of each node depends upon the location on the curved surface (Xie et al. 2005; Yen et al. 2004). Figure 4.13-a shows a diagram representing the displacement of nodes on the rake and flank faces, and in Figure 4.13-b the methodology most widely employed for the cutting edge.

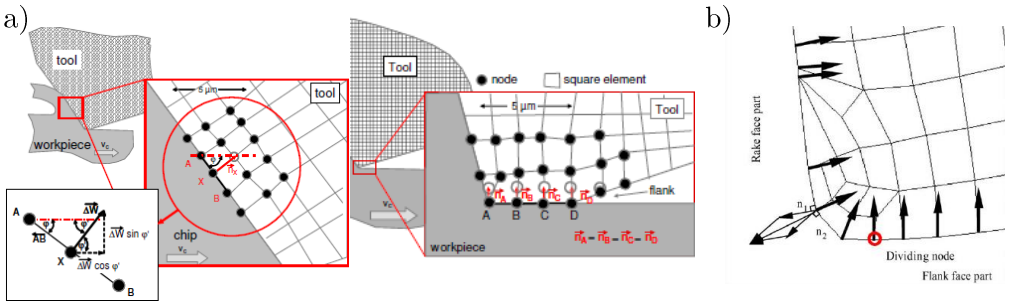

Figure 4.13: a)Nodal movement on the rake and flank faces, adapted from Klocke and Frank (2006) and b) nodal movement on the cutting edge, adapted from Xie et al. (2005)

4.1.4 Critical analysis

Numerical FEM-based models have been successfully employed for the prediction of a certain number of fundamental issues and industrial outcomes during recent decades (Arrazola et al. 2013). In spite of the large number of studies carried out, currently there are still many attempting to accurately identify the mandatory input parameters, developing more reliable FE cutting models and trying to identify the best link between scientific and industrial issues.

Focusing on the FE methodology to model the cutting operation, those developed under the Lagrangian formulation are the most extended for research purposes. These models require specific criteria such as element deletion or remeshing to enable chip formation. In general, the need of chip separation criteria makes the Lagrangian methods more accurate when the remeshing technique is applied. However, these are mostly constrained to commercial FE-software due to the difficulties in the development of remeshing algorithms. Although employing commercial software gives the user facilities to model the cutting process, the accuracy of results might not be as good as expected (Ducobu et al. 2017a).

During the last decade, ALE and CEL models have become of great interest due to the lack of necessity of a specific criteria for chip formation. Their main differences are the initial predefined conditions and the contact modeling. In the case of the ALE model with Eulerian boundaries, a predefined geometry of chip is required to simulate the cutting process (Arrazola and Ozel 2008; Arrazola et al. 2010). However, this issue can be solved if employing the ALE with only Lagrangian boundaries, although its development is less extended (Özel and Zeren 2005). In contrast, in the CEL method there is no need for a pre-shape of the chip. In spite of this advantage, the CEL model is limited to penalty type contact in FE software such as Abaqus (Ducobu et al. 2016), while in the case of the ALE model other types of contacts such as kinematic or specially designed subroutines are also possible (Courbon et al. 2011). In addition, CEL models are very sensitive to mesh size and orientation (Ducobu et al. 2017b). In Table 4.1 the main advantages and disadvantages of the models are listed.

In matters of input characterization, the flow stress and friction play the most important role for precise simulation. However, the thermal contact between solids, heat partition coefficient and thermal conductance are issues that can affect results more than expected (Arrazola and Özel 2009). In the majority of research a perfect contact is assumed in which thermal conductance is fixed to $10^8\,\mathrm{W{\cdot}m^{-2}{\cdot}K^{-1}}$, and the heat partition between tool and workpiece is set to 0.5. However, researchers such as Abdelali et al. (2012) have found that heat partition varies together with the relative tool-work motion, affecting simulation results (Courbon et al. 2011). Additionally, as summarized in the review of Melkote et al. (2017), assuming a perfect contact between tool and workpiece might not be accurate, specifically in the cases in which coated tools are employed.

Table 4.1: Advantages and disadvantages of the most representative FE models of the machining process

Langrangian - Remeshing criteria	
Adv.	• No material volume loss • Continuous thermo-mechanical contact between solids • Possible in implicit and explicit • Accurate tool-workpiece interface contact modeling
Disadv.	• Complex coding in general purpose FE software • Convergence of model depends on the refinement of remeshing code • Diffusion of results in mapping operation
Langrangian - Element deletion criteria	
Adv.	• Simple coding and implementation in general purpose FE software • Precise chip morphology
Disadv.	• Volume loss and thermo-mechanical contact discontinuities • Results depend on the selected deletion criteria • Difficult to accurately characterize deletion criteria
Arbitrary Eulerian Lagrangian - ALE (Eulerian boundaries)	
Adv.	• Accurate tool-workpiece interface contact modeling • No chip separation criteria • Simple coding in 2D and 3D
Disadv.	• Results depend on adaptive meshing criteria • Initial predefined geometry required • Limited to explicit calculations
Coupled Eulerian Lagrangian - CEL	
Adv.	• No chip separation criteria • Simple coding in 3D
Disadv.	• Limited to explicit calculations • Only penalty type contact • Not highly accurate contact between Lagrangian and Eulerian domains

Friction is still investigated in-depth by researchers (Melkote et al. 2017). Most of them agree that shear stresses in the rake face present a plateau in which the chip almost sticks to the tool. Above this plateau the chip starts sliding over the rake face and the shear stresses diminish. One of the most reliable studies comparing friction models is that of Özel (2006), however, it is still not at all clear which of the models is more accurate to simulate the cutting physics. Concerning the characterization of the friction coefficient, the use of laboratory tribo tests has given rise to relating the friction coefficient with the sliding velocity (Abdelali et al. 2012), and to correlate friction values with microstructural and mechanical properties of FP steels (Arrieta et al. 2017). Although their accuracy seems to be in agreement with experimental data

sets, there is still a gap in which components of the measured friction are linked to adhesion, ploughing or sliding mechanisms, which might be determinant to develop a friction model.

In the majority of studies, tool wear is modeled updating the coordinates of the nodes that belong to the external surfaces of the tool. However, it is also possible to model explicitly tool wear with the use of techniques such as XFEM (Bencheikh et al. 2017), although the difficulty to integrate the algorithms in the FE codes becomes more complicated.

4.2 Orthogonal cutting model in 2D: Development and validation

This section deals with the development of an orthogonal cutting FE model that has the implicit objective of (1) testing the validity of the MSB constitutive model and (2) integrating the input parameters characterized in this research. The validation of the whole input-FE model set is achieved by comparing the simulation results with those achieved experimentally in Chapter 3.

- Selection of the FE modeling technique

The objective of this research was not focused on the development of a new technique to simulate the cutting process. For this reason, the most appropriate model from those analyzed in the literature was selected. In the selection process, the following considerations were taken:

- *General purpose software.* Although software such as SFTC-Deform and TWS-Advantedge are highly regarded in the research community, due to their license cost and the limited possibilities of expansion they offer, a general purpose FE software was employed. From the general purpose software available, Abaqus was assessed as the most appropriate, being widely employed in machining modeling.

- *Simplicity and reliability of results.* Due to the lack of a predefined remeshing code in Abaqus, the modeling was almost constrained to Lagrangian formulation with element deletion technique, and combined Eulerian-Lagrangian formulations (ALE and CEL techniques). The element deletion technique was disregarded as thermo-mechanical information is lost each time an element is deleted. This drives a non accurate contact behavior prediction, which is mandatory for machinability prediction. Both ALE and CEL techniques share the feature that they do not require any chip separation criteria, however, the ALE needs a pre-shape of the chip. The ALE has been widely validated in metal cutting simulations, not as much the CEL model. In addition, the contact behavior can be better controlled in the ALE than in the CEL, as the contact is directly defined between two

Lagrangian surfaces, rather than between a Lagrangian surface and a Eulerian frame.

- *2D or 3D model.* Assuming that the orthogonal cutting procedure undertaken in Chapter 3 was developed to be comparable to an idealized plane strain criteria, there is no real need to model the cutting process in 3D.

Based on the abovementioned considerations, the ALE approach was selected as the most suitable tool to implement the microstructure based inputs, establish a wear prediction strategy, and finally predict tool wear.

4.2.1 Developed Arbitrary Lagrangian Eulerian model

In this section the main attributes of the developed ALE model are specified in the following manner: (1) general description, (2) boundary conditions and predefined fields, (3) tool-workpiece interface contact definition, (4) mesh discretization and (5) tool and workpiece material properties.

General description of the model

Conceptually, the idea of the model is to visualize the workpiece as a fluid flowing through a deformable "pipe" that interacts with a solid part (tool). The entry of material is associated with the deformable workpiece, and the exits correspond to the flow of the chip and the finished workpiece. The quantity of material that is evacuated from each of the exits is not predefined.

The corresponding part of the tool was modeled as a rigid body fixed in space, assuming that deformations in the tool are negligible compared to those of the workpiece. Geometrically, the rake face, the flank face and the rounded cutting edge can be differentiated (Figure 4.14). The rake angle (6^o), the clearance angle (6^o) and the cutting edge radius (40 μm) were identical to those of the orthogonal cutting experiments.

Concerning the initial pre-shape of the part that corresponds to the workpiece, two main sections were differentiated: the workpiece itself and the chip. The geometry was delimited by a certain number of surfaces which are illustrated in Figure 4.14:

- *Free surface (AB).* Lagrangian free surface of the outer part of the workpiece (not machined surface).
- *Exit chip (BC).* Eulerian surface to simulate the material flowing through the chip.
- *Workpiece contact (CD).* Lagrangian surface that makes contact with the surfaces of the tool.

- *Exit material (DE)*. Eulerian surface to simulate the exiting material flow.
- *Bottom part (EF)*. Lagrangian surface on the bottom of the workpiece which is fixed in space and constrains the movement of the workpiece.
- *Entry material (FA)*. Eulerian surface to recreate the material flowing against the tool at a velocity equal to the cutting speed.

The dimensions of the model were fixed so that the limits of the boundaries did not affect the different areas of analysis. The length and height of the model were large enough so as to not have stress and thermal concentrations in the limits, and the tool was sufficiently wide that the boundaries did not interfere with the heat flow.

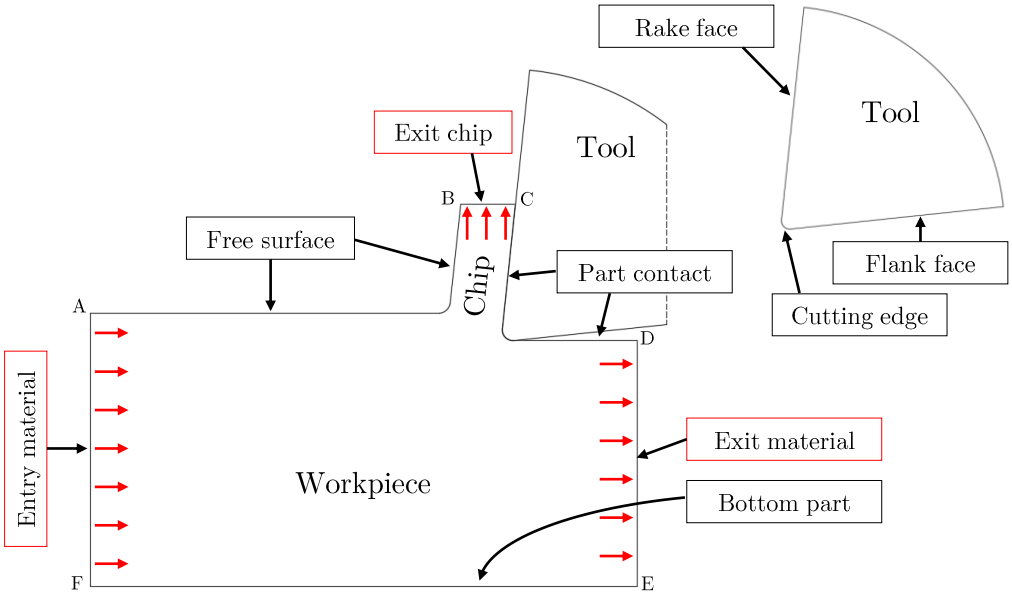

Figure 4.14: Schematic representation of the ALE model

Boundary conditions and predefined fields

Boundary conditions are classified in mechanical and thermal boundaries, which are specified in Figure 4.15. Thermal conduction, convection and radiation in the outer surfaces of the model were disregarded. Only conduction was enabled in the contact between tool and workpiece once the gap between the two bodies was less than 10^{-4} mm. The workpiece was fixed at the bottom, where displacements were constrained in both directions. Concerning the Eulerian boundaries, in the entry and exit material surfaces the displacement was constrained in U_1 direction, while the surface assigned for the chip outflow was $U_2 = 0$. The degrees of freedom of the tool were constrained $U_1, U_2, R_3 = 0$. The boundary conditions are summarized in Table 4.2.

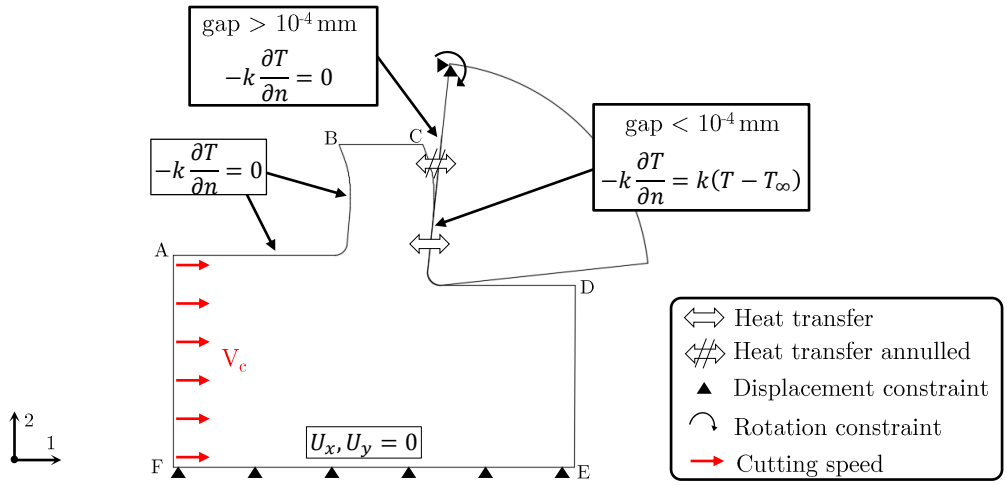

Figure 4.15: Mechanical and thermal boundary conditions of the ALE model

With regards to the predefined fields, both tool and workpiece were set at 20°C, and from the beginning of the simulations in the Entry surface (surface F-A) a material flow of $\frac{dU_1}{dt} = V_c$ was defined.

Table 4.2: Mechanical and thermal boundary conditions of the ALE model

Surface	Thermal boundary conditions	Mechanical boundary conditions
A-B	Convection and radiation negligible $-K\frac{\partial T}{\partial n} = 0$	No restrictions
B-C	Heat flux due to chip out-flow $-K\frac{\partial T}{\partial n} = 0$	Free material flow $U_2 = 0$
C-D	Heat flux between tool-workpiece gap $< 10^{-4} \Rightarrow -K\frac{\partial T}{\partial n} = K(T - T_\infty)$ gap $> 10^{-4} \Rightarrow -K\frac{\partial T}{\partial n} = 0$	No restrictions
D-E	Heat flux due to material out-flow $-K\frac{\partial T}{\partial n} = 0$	Free material flow $U_1 = 0$
E-F	Conduction negligible $-K\frac{\partial T}{\partial n} = 0$	$U_1 = 0, U_2 = 0$
F-A	Material in-flow at T_{ambient} $-K\frac{\partial T}{\partial n} = 0$	Material flow at $\frac{dU_1}{dt} = V_c$ $U_2 = 0$
Tool	Heat flux between tool-workpiece gap $< 10^{-4} \Rightarrow -K\frac{\partial T}{\partial n} = K(T - T_\infty)$ gap $> 10^{-4} \Rightarrow -K\frac{\partial T}{\partial n} = 0$	$U_1 = 0, U_2 = 0, R_3 = 0$

Contact model in the tool-workpiece interface

The mechanical contact was modeled by the Coulomb law with a sliding velocity dependent friction coefficient μ. This model is certified in the literature to accurately represent the contact behavior in the interface between tool and workpiece.

The characterization of the friction coefficient was conducted inside the frame of the European project IMMAC, and with the collaboration of the École nationale d'ingénieurs de Saint-Étienne ENISE. Tribological tests were carried out in the open tribometer presented previously in the literature review (Zemzemi et al. 2008; Abdelali et al. 2012; Arrieta et al. 2017). The setup mounted on a lathe consists of a cylindrical pin rubbing against a fresh surface during rotation of the workpiece (Figure 4.7). During motion, the components of the forces are measured to then establish the friction coefficient.

The tribological tests were carried out at the sliding velocities of 10, 100 and 300 m·min^{-1} for the whole set of FP steels. It is worth noting that the tests in the core of the European project were made with TiN coated carbide pins in dry cutting conditions. In contrast, uncoated carbide inserts were employed in the orthogonal cutting tests undertaken in this research. For this reason, the measured friction coefficient and that of the orthogonal tests of this research were not equivalent. In order to have friction data similar to that of cutting with uncoated tools, unpublished data of tribological tests for a C45-uncoated carbide pair was supplied by ENISE. Based on the differences in friction between coated and uncoated tests for the case of C45, it was possible to estimate those of the C60, 27MnCr5 and 16MnCr5. In Figure 4.16 the results of the TiN coated tests and the extrapolated results of uncoated pins are shown.

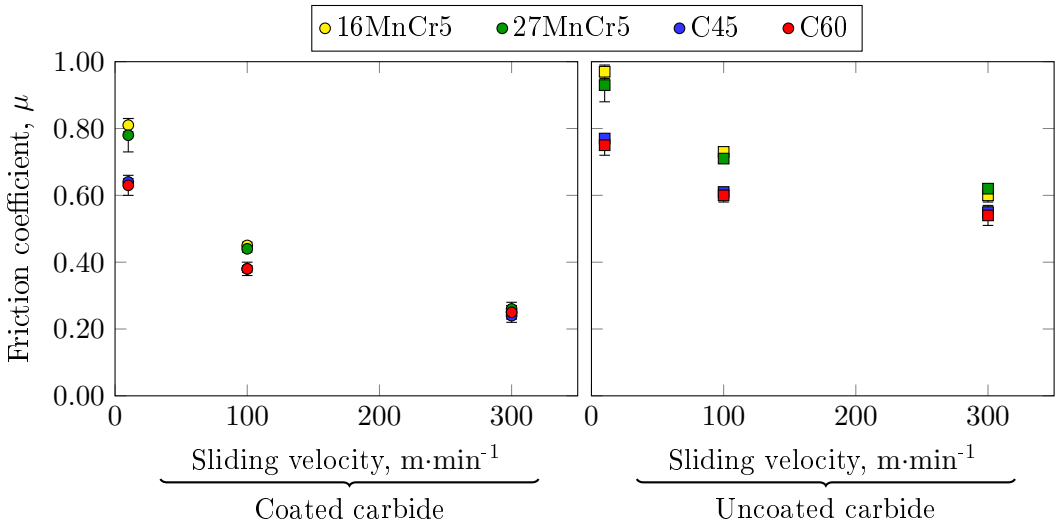

Figure 4.16: Measured friction coefficient of WC-Co + TiN coated carbide inserts (D'Eramo et al. 2017) and estimated friction coefficient of uncoated carbide inserts based on Rech and Courbon (2017)

As shown in the figure, the friction coefficient is strongly dependent on the sliding velocity. Differences between the coated and the estimated friction coefficient also varied depending on the sliding velocity in a range of μ=0.1-0.3. From the microstructure point of view, the steels with greater ferrite content were those that presented higher friction value, which in turn was linked to the adhesive effect of ferrite. Globally the frictional behavior could be represented by the following Eq. 4.5.

$$\mu(V_{\mathrm{sl}}) = \mu_{\mathrm{k}} + (\mu_{\mathrm{k}} - \mu_{\mathrm{s}}) \cdot \exp(-d_{\mu}||V_{\mathrm{sl}}||) \tag{4.5}$$

The friction values μ_{k}, μ_{s} and the exponential term d_{μ} were fitted to specific equations in function of the ferrite content (f_{α}) of the steels (Eq. 4.6, 4.7 and 4.8).

$$\mu_{\mathrm{k}} = 0.5035 \cdot f_{\alpha}^{-0.1249} \tag{4.6}$$

$$\mu_{\mathrm{s}} = 0.1525 \cdot f_{\alpha}^{-0.5244} \tag{4.7}$$

$$d_{\mu} = 0.06029 \cdot f_{\alpha} - 0.003425 \tag{4.8}$$

Figure 4.17 compares the empirically estimated friction values, and the curves predicted by the abovementioned model. The highest deviations between the proposed model and the calculated friction coefficients were found at the lowest sliding velocities. However, the maximum deviations were less than 10%.

The penalty contact algorithm was set as contact constraint enforcement method. This method searches for slave node penetrations in the current configuration. Forces that

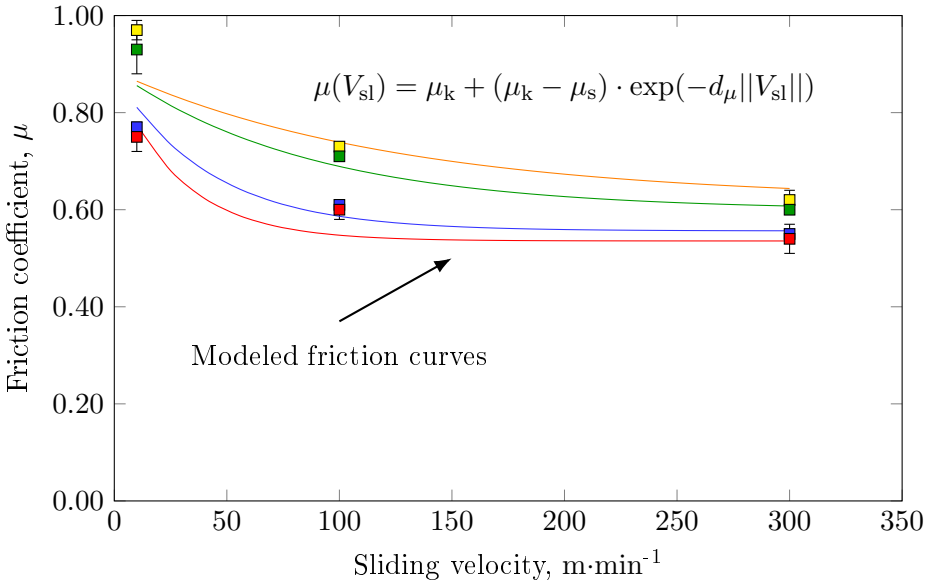

Figure 4.17: Estimated friction coefficient of uncoated carbide inserts and comparison with proposed model

are a function of the penetration distance are applied to the slave nodes to oppose the penetration, while equal and opposite forces act on the master surface at the penetration point. The master surface contact forces are distributed to the nodes of the two contacting edges (Hibbitt et al. 2014).

Besides mechanical contact, is also of great importance the thermal transfer between tool and workpiece. The transfer of heat between two solids is determined by Eq.4.9.

$$\frac{q}{A} = -k_i \frac{\partial T}{\partial n} = k_{\mathrm{i}}(T_{\mathrm{hot}} - T_{\mathrm{cold}}) \tag{4.9}$$

Melkote et al. (2017) summarized that most of authors of research concerning machining modeling assume that the contact between tool and workpiece is infinity (perfect contact). In contrast, there is also a certain number of studies that consider it as a variable parameter dependent on aspects such as the size of the asperities between surfaces or the contact pressures (Attia and Kops 2004). However, with the aim of simplifying the model and reducing the amount of independent variables, in this developed ALE model the general assumption of perfect contact was applied ($k_{\mathrm{i}} = 10^8\,\mathrm{W{\cdot}m^{-2}{\cdot}K^{-1}}$). A similar consideration was taken when assuming a heat partition between tool and workpiece of 50% (Γ=0.5), and the amount of friction energy transformed to heat was 100%. Table 4.3 summarizes the input parameters employed to model the contact behavior in the ALE model.

Table 4.3: Input parameters of contact behavior employed in the ALE model

Contact properties		Value
Thermal contact	Thermal conductance, k_{i} ($\mathrm{W{\cdot}m^{-2}{\cdot}K^{-1}}$)	$1{\cdot}10^8$
	Partition coefficient, Γ	0.5
Mechanical contact	Friction coefficient, μ	Eq. 4.5
	Friction energy converted into heat, η	1

Mesh discretization

The mesh of the numerical model was formed by coupled temperature-displacement elements of the type CPE4RT. These are of reduced integration quadrilateral elements under plane strain condition.

The topology of the workpiece was divided into diverse sections to enable meshing with refined elements in the regions of interest (Figure 4.18). These are mostly the three shear zones (PSZ, SSZ, and TSZ), including the vicinities of the cutting edge. The tool was also refined up to a radii longer than the contact with the workpiece. The dimensions of the elements oscillate between 4 µm and 100 µm. The elements with the smallest size were near the cutting edge. The workpiece was modeled with 15600 elements and the tool with 9300 elements.

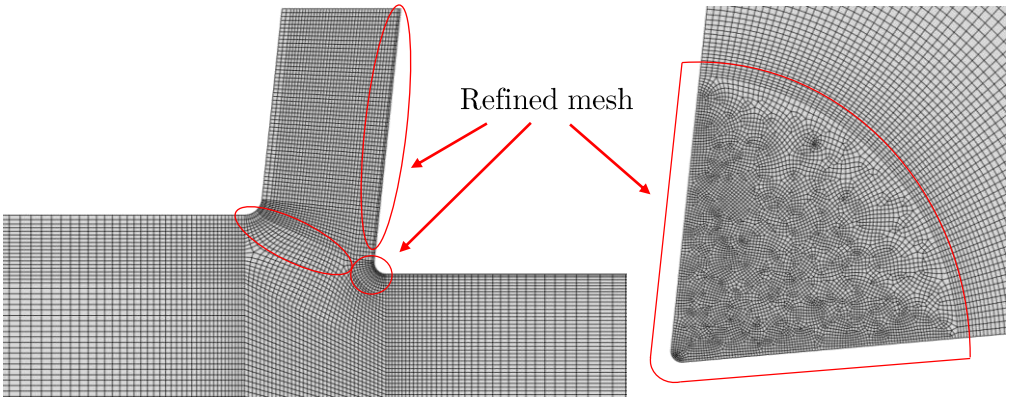

Figure 4.18: Discretized mesh of the ALE model

The whole workpiece was defined under the *Adaptive Meshing* domain based on the Arbitrary Lagrangian Eulerian formulation. The main feature of this formulation is that the material can behave under Lagrangian or Eulerian formulation depending on the absence or presence of the domain and type of the outer surfaces of the model.

In the region under Eulerian domain the mesh is allowed to move independently of the material, but without altering the topology of the mesh. The limits of the model can be set with adaptive Lagrangian or Eulerian contours. When a Lagrangian surface is selected, this deforms together with the material. In contrast, if the surface selected is that of Eulerian type, it permits the material flow through the borders. As shown in Figure 4.14, the Entry material, Exit material and Exit chip surface were modeled as Eulerian, allowing the material flow through them. The surfaces named Free surface and Part contact were modeled with adaptive Lagrangian surfaces. No constraints were fixed in these surfaces so as to permit adaptation while the chip is forming.

During each adaptive meshing increment, the new mesh is created by performing one or more mesh sweeps (mesh adaptivity) and then advecting (or mapping) the solution variables to the new mesh (Hibbitt et al. 2014). These are controlled by the parameters *Mesh Sweeps* (number of mesh adaptations carried out at a time) and *Frequency* (controls the number of time increments to then perform the adaptive meshing). The employed input parameters of the adaptive mesh domain are summarized in Table 4.4.

Table 4.4: Input parameters of adaptive mesh employed in the ALE model

Input parameters of adaptive mesh			Value
Adaptive meshing	Adaptive mesh parameters	Initial mesh sweeps	5
		Mesh sweeps	1
		Frequency	1
	Method for adaptive meshing		Volume
	Geometric enhancement		Yes
	Curvature refinement		1
Advection	Momentum advection		H.I.S.
	Order advection		2

Material properties

In coupled thermo-mechanical analyses the thermal and mechanical properties of the workpiece are mandatory. These were defined in function of the temperature, as the simulation was considered as adiabatic, and the variation that temperature causes in material properties were known to be significant. Four different workpiece materials were defined in the scope of this research, which have already been presented in this document: 16MnCr5, 27MnCr5, C45 and C60. Their mechanical behavior was modeled as thermo-elastic-viscoplastic. The elastic behavior was defined by Hooke's law, and was identical for all the steels (Table 4.5). In contrast, the thermo-plastic behavior differed between the steels, and was represented with the MSB constitutive model developed in this research and presented in Chapter 2.

The plastic deformations that occur in the different regions of the workpiece provoke flow stresses that depend on temperature, plastic strain and plastic strain rate. From the generated deformation energy ($\int \sigma d\epsilon$) a specific quantity is transformed into heat (the ratio is defined by the Taylor-Quiney coefficient, β), which drives a global rise in temperature. This temperature rise is a function of the density (ρ), specific heat (C_{p}) and thermal conductivity (K). In addition, this incresae in temperature also causes the material to dilate, the degree of which depends on the thermal expansion coefficient (α_{L}). All these properties were characterized for all the FP steels and selected tool material in this Ph.D. The characterization procedure is described in Chapter 2 and a summary of results is presented in Table 4.5.

Table 4.5: Input parameters related to workpiece and tool material

		16MnCr5	27MnCr5	C45	C60	Carbide
Young modulus, E (MPa)			$210 \cdot 10^3$			
Poisson coefficient, υ			0.3			
Plasticity (MPa)			MSB model			
Inelastic heat fraction, β			0.9			
Density, ρ ($kg \cdot m^{-3}$)	20°C	7800	7795	7765	7830	14970
	300°C	7720	7715	7685	7745	14910
	700°C	7570	7565	7535	7600	14800
Conductivity, K ($W \cdot m^{-1} \cdot K^{-1}$)	20°C	52.6	36.5	32.2	30.8	112.7
	300°C	0.4	38.3	34.3	28.8	72.1
	700°C	30.7	24.1	20.7	14.4	28.8
Specific heat, C_p ($J \cdot Kg^{-1} \cdot K^{-1}$)	20°C	365	375	395	430	200
	300°C	515	500	545	530	210
	700°C	825	745	800	590	105
Thermal expansion, α_L ($10^{-6} \cdot {}^{o}C^{-1}$)	20°C	5.5	6.5	5.5	4.75	
	300°C	12.9	12.5	12.9	12.6	
	700°C	14.9	14.9	14.8	14.6	

4.2.2 Experimental validation of the numerical model

To assess the validity of the developed ALE model, including the developed MSB constitutive model and the implemented sliding velocity based friction model, numerical results were compared to those of the experiments. Only the results with fresh tools were taken into account for validation purposes, and the experimentally measured variables that were selected are listed below:

- Chip thickness.
- Tool-chip contact length.
- Cutting and feed forces.
- Tool temperature (in the contact section).

Overview of simulations

Figure 4.19 shows the deformed geometry of the chip-workpiece after reaching the steady state. Compared to the initial pre-shape of the model, the chip was curved and swelled by the material flow, which in part was enabled by the adaptive meshing

and the configured outer Lagrangian boundaries. In the upper part of the chip the separation between chip and tool is observed. The length of the pre-shape of the chip was sufficient to not interfere in the tool-chip contact. In the figure, an example of l_c and t_2 are identified. The obtained deformed mesh was uniformly distributed throughout the workpiece. The simulation time was in the range of 20-70 hours depending on the cutting condition for a cutting time of 8 milliseconds, with a single 2.30 GHz Intel Xeon core processor.

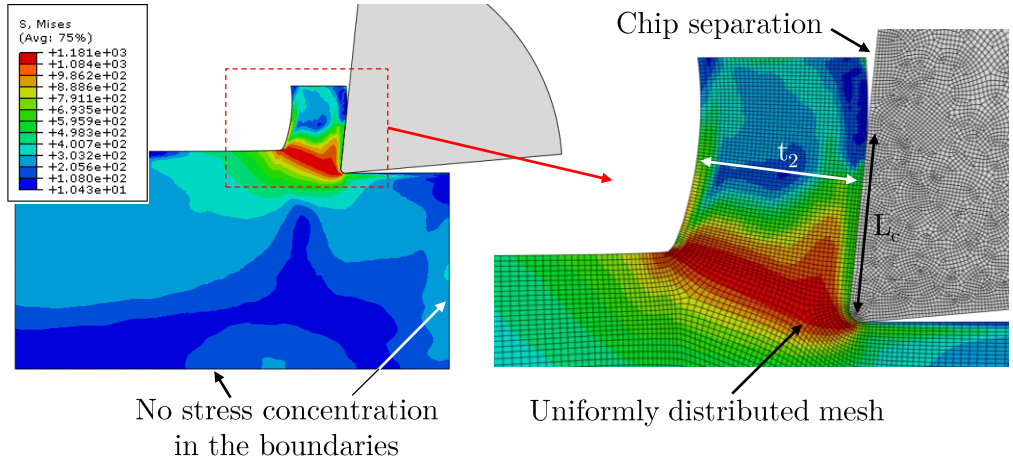

Figure 4.19: Example of the deformed configuration of the ALE model after reaching the steady state when cutting the C45 at V_c=200 m·min^{-1} and f=0.2 mm. The output is Mises stress

Chip thickness and contact length

An example of the formed chips for all the FP steels when simulated at V_c=200 m·min^{-1} and f=0.2 mm is illustrated in Figure 4.20. The differences in t_2 and l_c are evident.

Both experimental and simulated chip thickness results are compared in Figure 4.21. The correlation of the simulations was highly accurate from the point of view of trends and values. In most of the analyzed cases differences between both frameworks were nearly not appreciable, and the decreasing t_2 with the pearlite increase was always

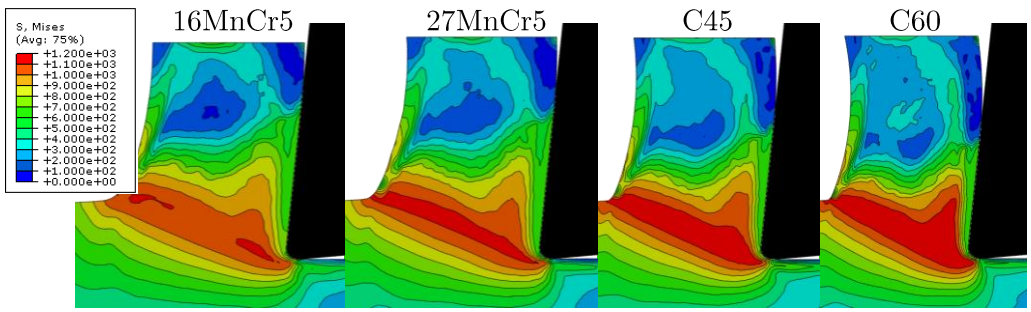

Figure 4.20: Comparison of formed chips for all FP steels when simulated at V_c=200 m·min^{-1} and f=0.2 mm

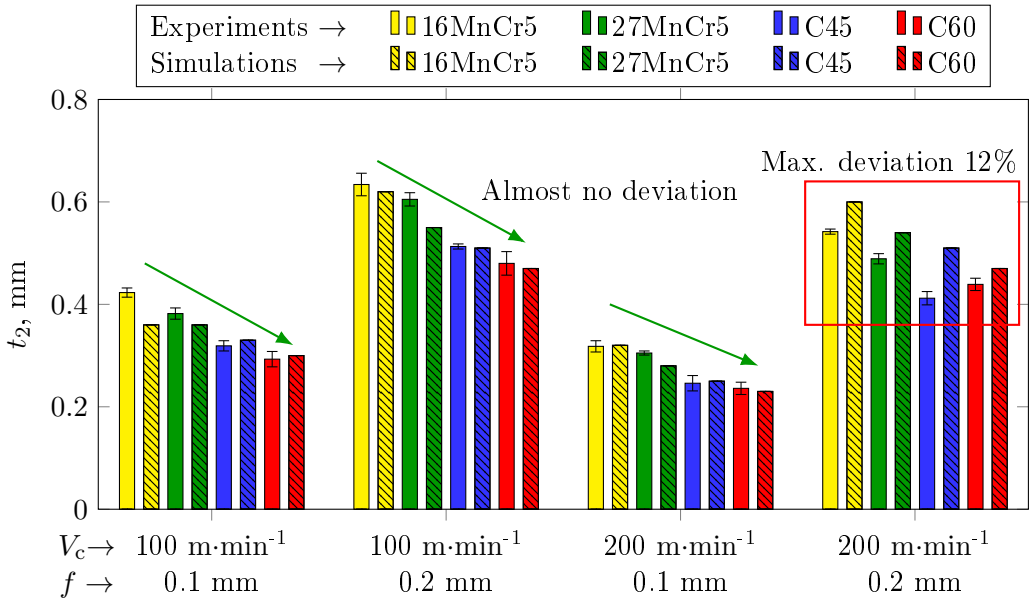

Figure 4.21: Experimental and simulation results of t_2 for all the FP steels and cutting conditions machined with fresh tools

predicted. The greatest differences were observed at the condition of V_c=200 m·min^{-1} and f=0.2 mm, in which the average deviation was 12%.

Predictions of l_c were not as accurate as expected, although the main trends were satisfied. All the simulations showed a remarkably shorter contact than that obtained experimentally, and the achieved deviations were in the range of 25-60%. These were more significant in the case of lower feed (Figure 4.22).

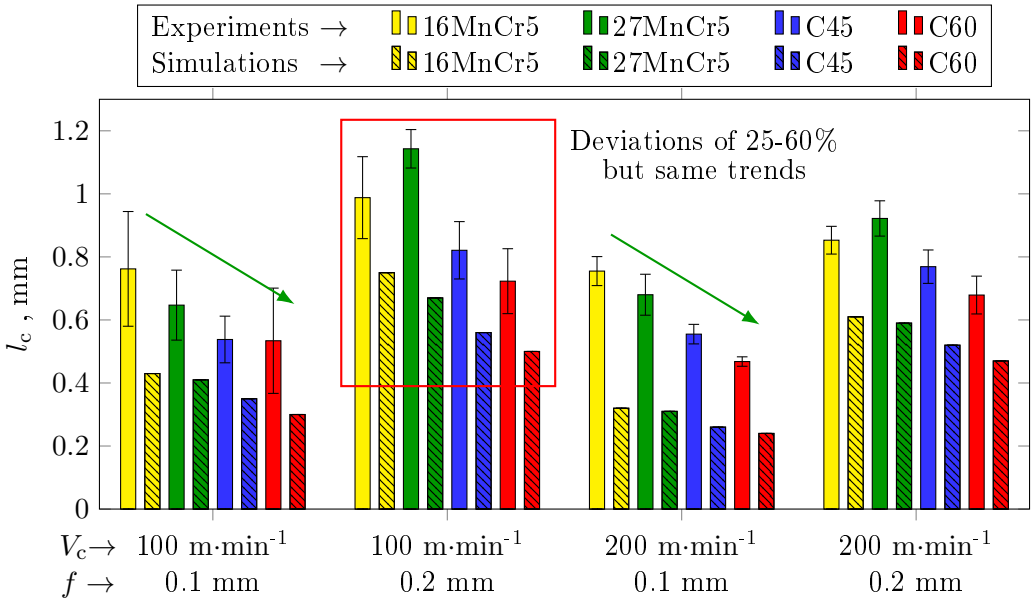

Figure 4.22: Experimental and simulation results of l_c for all the FP steels and cutting conditions machined with fresh tools

Cutting and feed forces

Simulated results of F_c and F_f were established as the average force of the last 20% of the simulation. The comparison of F_c between the simulations and experimental results is plotted in Figure 4.23. In general, the predicted F_c were in line with the results of the experiments, but simulated F_c were always slightly higher than the experimental values. Simulation results were more accurate in the cases of 0.1 mm feed, in which the highest deviation was less than 15%. The trends were also accurate when cutting at f=0.1 mm. For example, at V_c=100 m·min^{-1} and f=0.1 mm in both experiments and simulations a slight lowering of F_c was observed with increasing pearlite content (marked with green arrows). The comparisons when cutting at f=0.2 mm presented higher discrepancies and were more significant at the cutting condition of V_c=100 m·min^{-1} and f=0.2 mm (marked with a red rectangle). Almost negligible differences were found between the steels in the experimentally measured F_c when cutting at f=0.2 mm. In contrast, simulations predicted a clear lowering of F_c when moving from the 16MnCr5 to the C60 steel. Simulated F_c obtained in some cases a 20% higher value than that measured experimentally.

Concerning the influence of the cutting conditions, the simulations predicted the same trend as the experiments. The lowering in F_c with the increase of cutting speed was accurately predicted, while the obvious increase in F_c with the increase in the feed was also observed. In the numerical model, increasing the cutting speed caused F_c to lower by 14%, compared to the 10% obtained experimentally. The predicted increase for the case of the feed was 53% while experimentally was 47%.

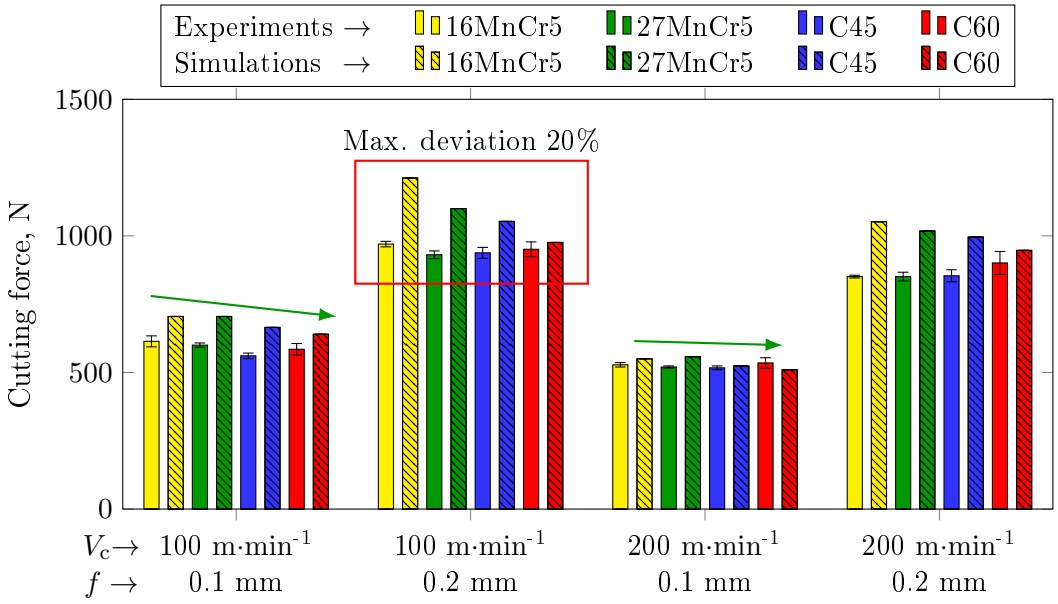

Figure 4.23: Experimental and simulation results of F_c for all the FP steels and cutting conditions machined with fresh tools

With regards to the F_f, the comparison between simulated and experimental results is depicted in Figure 4.24. In general, the predictions showed a significantly lower F_f in all the analyzed cases. Differences of up to 45% occurred when cutting at V_c=200 m·min^{-1} and f=0.1 mm. At the other conditions the maximum error was in the range of 25-30%, which was always maximum in the case of the 16MnCr5 steel. In spite of these differences, however, the model was able to represent the experimental trends. In all the tested conditions, the decrease in F_f when moving from the 16MnCr5 to the C60 (or increasing the pearlite content) was accurately described. Furthermore, in those conditions in which a higher difference in F_f was found between the steels, higher differences were also predicted (marked with green arrows). For example, cutting at V_c=100 m·min^{-1} and f=0.2 mm, the difference in F_f between 16MnCr5 and C60 steels was 42-43% in both the experimental and numerical results. The effect of varying the cutting conditions was greater in the results from the simulations. The predictions of increasing the cutting speed made the F_f to decrease by 31%, while increasing the feed caused an increase of 32%. In contrast, experimentally a decrease of 23% and an increase of 24% were achieved respectively. The model was approximately 10% more sensitive to the cutting condition change.

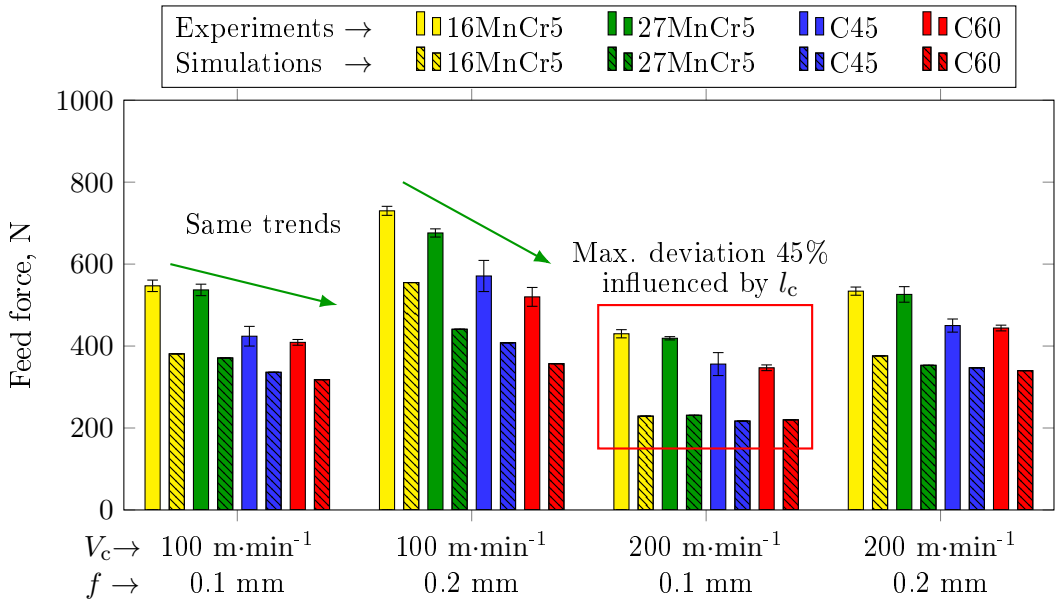

Figure 4.24: Experimental and simulation results of F_f for all the FP steels and cutting conditions machined with fresh tools

Tool temperature

Figure 4.25-a shows the comparison of tool temperature fields between the FP steels when simulated at the condition of V_c=200 m·min^{-1} and f=0.2 mm. The maximum temperature was located in the rake face, and the highest values were obtained in the simulations of the C60 steel. The maximum temperature of the tool lowered when

moving from the C60 to the 16MnCr5 steel. Concerning the thermal field resulted from the variation of the cutting conditions, an example for the case of the C45 is shown in Figure 4.25-b. The maximum temperature in all the simulations was still found in the rake face. However, this was more evident when simulating at V_c=200 m·min^{-1}. At the lowest cutting speed of 100 m·min^{-1}, the differences in temperature between the rake face and the cutting edge were diminished.

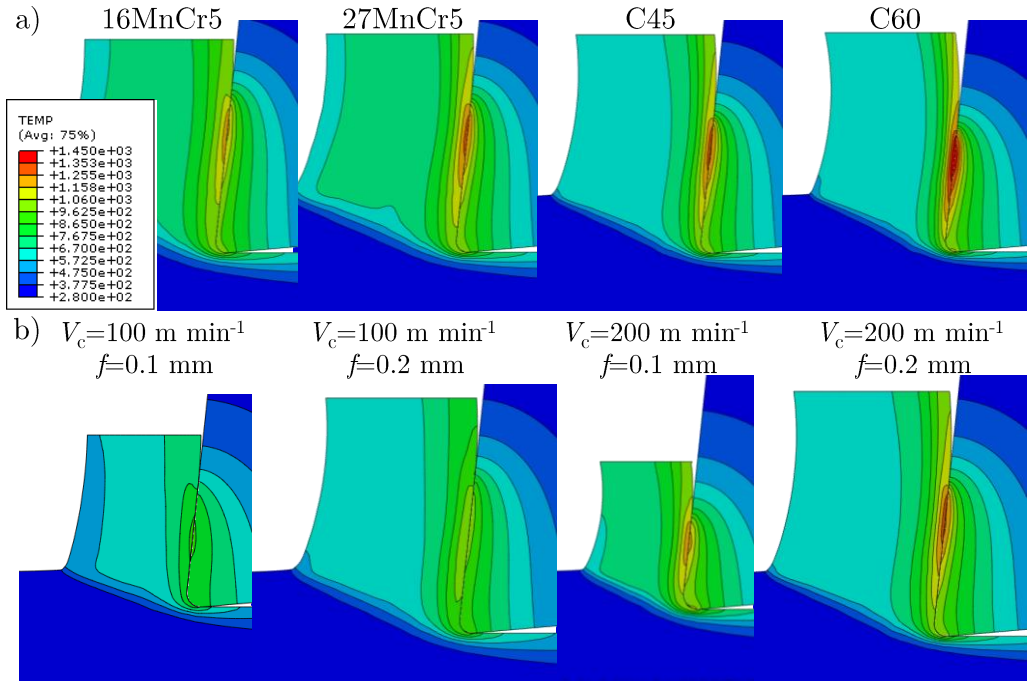

Figure 4.25: (a) Temperature comparison between all FP steels when simulated at V_c=200 m·min^{-1} and f=0.2 mm. (b) Tool temperature for all selected cutting conditions for the case of C45 steel

The comparison of the maximum temperatures between the simulation and the experiments is shown in detail in Figure 4.26. These correspond to those experimental and analytically calculated $T_{contact}$ in the rake face which are already described in Section 3.4.3.

In general terms, simulated temperature results were highly accurate when compared to those calculated from the experiments. The main trends were almost identical in both frameworks. While in the experiments the effect of increasing feed and cutting speed caused an average temperature rise of 38% and 14% respectively, in the case of the simulations the corresponding effect was 35% and 15%. With regards to the specific temperature values, the maximum deviations found in the complete set of simulations was less than 18%, while the average error was less than 10%. This was maximum when simulating the C60 steel, in which the average error was 16%. The average deviation in the C45, 27MnCr5 and 16MnCr5 was 9%, 4% and 4% respectively. From the abovementioned results, it was possible to conclude that the model was able to represent the temperatures in the tool with a high degree of accuracy.

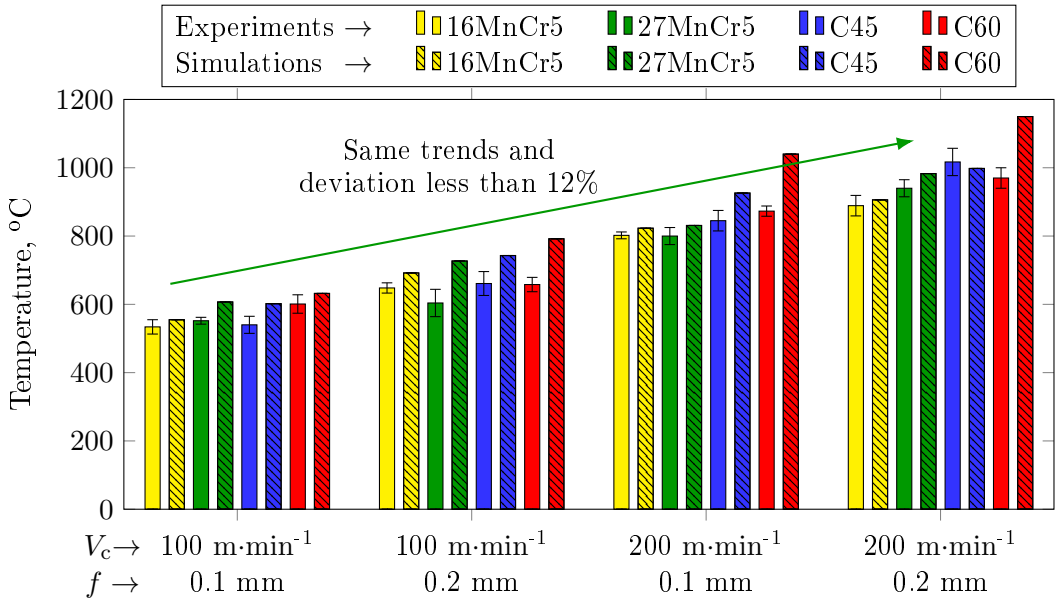

Figure 4.26: Experimental and simulation results of T_{contact} on the rake face for all the FP steels and cutting conditions machined with fresh tools

Discussion of simulation results

The overall simulation results showed that all trends concerning the variation of both workpiece material and cutting conditions was accurately predicted. Concerning the measured values of the analyzed variables, the simulations precisely predicted the chip thickness, cutting forces and tool temperature. High deviations were observed in the predictions of feed force and contact length. These latter are two variables that are linked with each other. The feed forces are directly derived from the normal stresses in the cutting edge and the shear stresses on the rake face in the cases when cutting with fresh tools, otherwise the effect of the flank wear should also be taken into account (Merchant 1944). For this reason, the simulated shorter l_c directly drove to the prediction of these lower values of F_f. However, it is worth noting that an increase in l_c also may cause an increase in F_c, which may then generate larger differences between experiments and simulations. Nevertheless, it must be taken into account that the experimentally obtained l_c was significantly longer than those reported in the literature.

In spite of the dependence of F_f in l_c, the shear stresses acting on the secondary shear zone are also significant for an accurate F_f prediction. Figure 4.27 shows an example of the material state in the SSZ, for the case of the C45 steel when machined at V_c=200 m·min^{-1} and f=0.2 mm.

The simulated results gave plastic strain values in the range of 10-30, strain rates up to $10^5\,s^{-1}$ and temperatures from 700°C to 1000°C. Concerning the constitutive model, this was fitted to experimental compression tests on which the specimens were subjected to plastic strains of less than 1, strain rates up to $10^4\,s^{-1}$ and maximum temperatures

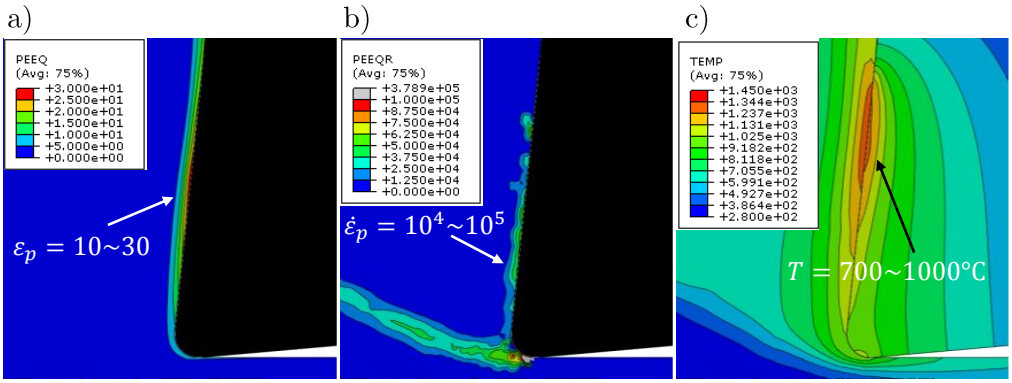

Figure 4.27: (a) Equivalent plastic strain, (b) equivalent plastic strain rate and (c) temperature for the case of C45 simulated at V_c=200 m·min^{-1} and f=0.2 mm

of 680°C. Therefore, the material behavior in the SSZ was extrapolated by the MSB constitutive model from those conditions at which compression tests were carried out, which as observed were far from those which occurred during the process. For this reason, depending on the extrapolation method or selected extrapolation function, the stress prediction at those extreme thermo-mechanical conditions could vary, and thus also the shear stresses. Equally important is the selected friction model, and the characterization of the friction coefficient. The employed friction coefficient function of the sliding velocity predicted the stress state shown in Figure 4.28 for the same prior case (C45, V_c=200 m·min^{-1} and f=0.2 mm).

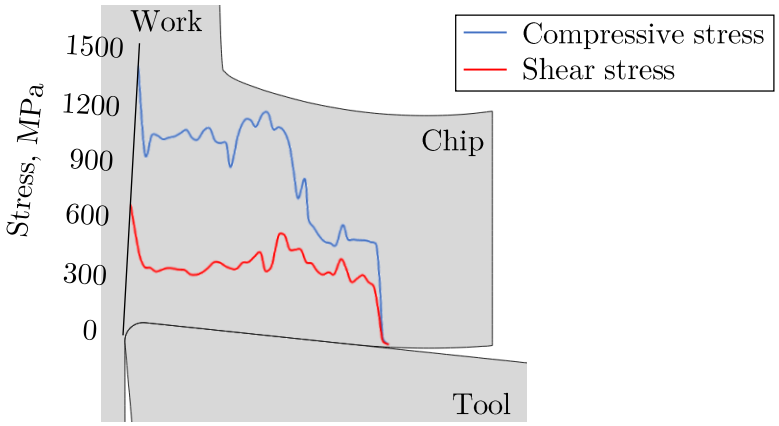

Figure 4.28: Compressive and shear stresses acting on the rake face for the case of C45 steel at V_c=200 m·min^{-1} and f=0.2 mm

In the first $\frac{2}{3}$ of l_c the compressive stresses were almost constant followed by a decrease to 600 MPa, to finally turn null when the chip looses contact. In contrast, the shear stresses were almost constant along the whole l_c, which finally also became zero. The average shear stress was 380 MPa. In the literature two types of contact were distinguished, sticking and sliding. In the sticking region, the shear stresses are constant and commonly depend on the shear flow strength of the material ($\tau_f = mk$). When the

contact is of sliding type, the stress distribution normally satisfies the Coulomb friction law ($\tau_c = \mu\sigma_c$). In the present model, the selected friction model was programmed to satisfy Coulombs law in all the regions of contact. However, as graphed in Figure 4.28, the output of stress when applying the sliding velocity based friction coefficient was of the type sticking-sliding (constant shear stress followed by a decrease). This behavior seems to be in accordance with other models proposed in the literature (Malakizadi et al. 2017). However, the degree of contact stress is still defined by the shear flow strength of the material, which in turn is function of the constitutive model, and the friction coefficient. It is noteworthy that the friction coefficients of all steels were extrapolated from characterizations carried out with coated tools. It is the opinion of the author that, based on the extremely long l_c measured in orthogonal tests, the modeled friction coefficient of the uncoated tools could be underestimated. An increase in μ might lead to first increase the shear stresses, the sticking effect, and as a consequence probably also the l_c.

4.3 Tool wear prediction with FEM

For the estimation of machinability, a tool wear prediction strategy was defined and implemented in the ALE model. This strategy was employed to predict tool wear at previously specified cutting times or material removal states. The developed approach and the validation of the model is presented in this section.

4.3.1 Tool wear prediction strategy

The objective of the strategy was to update the geometry of the modeled tool based on tool wear calculations. The wear calculations take into account the previously proposed wear rate law, which depends on the temperature and the sliding distance (Section 3.5).

A program based on Python and Matlab scripting was designed to perform tool wear calculation and tool geometry updates automatically, until an specified cutting time was reached. In general terms, a Python subroutine is executed that first launches an initial ALE cutting simulation with an unworn tool. The inputs are automatically selected based on specified cutting conditions and workpiece material. Once the simulation finishes, after reaching the steady state of forces and temperature, the required process variables to calculate the amount of wear are extracted from the nodes in the rake, flank and cutting edge. The amount of wear is calculated only for the nodes that are in contact between tool and workpiece, to later update their coordinates. Once the coordinates of these nodes are updated, a new mesh is generated in the tool, and a new simulation is launched. This cyclic process is repeated until a specified cutting time is reached. A flow chart of the wear calculation program is shown in Figure 4.29.

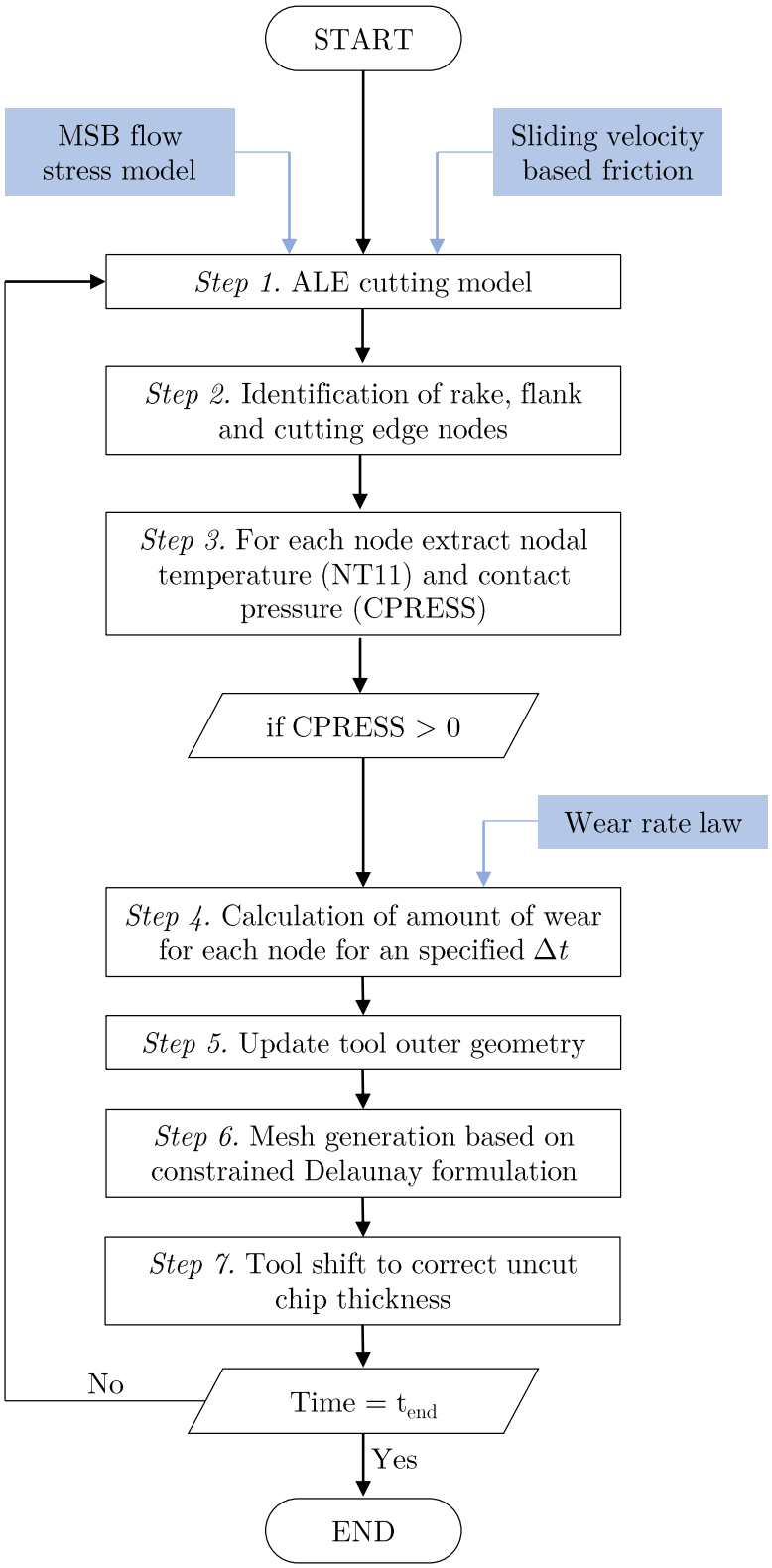

Figure 4.29: Flow chart of the wear calculation program

- *Step 1.* ALE cutting model

The ALE cutting model employed to predict tool wear is already described in Section 4.2.1. The input of the model is created by a Python script, in which the selection of the cutting conditions and workpiece materials are automatically integrated into the input code. In addition, the geometry of the model is updated depending on the selected feed. Once all these process parameters and material properties are selected, a first model in which the geometry of the tool is unworn is automatically launched. In the following cycles, the launched model corresponds to that in which the tool presents a worn geometry.

- *Step 2.* Identification of rake, flank and cutting edge nodes

Based on a predefined set of nodes specified in the input, the nodes that belong to the rake face, flank face and cutting edge are identified and their x-y coordinates are extracted. In the first cycle of the simulation, these coordinates correspond to those of the unworn tool. In the further cycles, the coordinates of the nodes are those of the worn geometry of the tool.

- *Step 3.* Extract process or fundamental variables in the nodes

The unique variable required by the wear rate law (Eq. 4.10) is the nodal temperature (NT11). However, tool wear is only applied to those nodes of the tool that are in contact with the workpiece. For this reason, to establish if a node is in contact or not, the mechanical variable of contact pressure (CPRESS) is also required. These two variables are extracted from the last computed increment of the simulation by the Python script.

- *Step 4.* Nodal wear calculation

The characterized wear rate law presented in Eq. 4.10 is employed in the calculation of nodal wear. The model sets out a wear rate behavior modeled as uncoupled mechanical and thermally activated wear phenomena. The experimental procedure undertaken in this research to establish the wear characteristic constants is discussed in Section 3.5.

$$W = \frac{dW_{\text{mechanical}}}{dL} \cdot (V_{\text{c}} \cdot \Delta t) + A_{\text{w}} \cdot \exp\left[-\frac{E_{\text{a}}}{R \cdot (T_{\text{contact}} + 273)}\right] \tag{4.10}$$

The thermally activated wear mechanisms were found to be the same for all the steels, which led to the definition of the same value of the constant A_{w}=185164 μm and activation energy E_{a}=95 kJ·mol^{-1}. In contrast, $\frac{dW_{\text{mechanical}}}{dL}$ had a unique value for each of the steels, which are summarized in Table 3.13. However, as discussed in Section 3.5, the mechanical wear rate of all the steels had a stretch correlation with the amount of %C. For this reason, the mechanical term of Eq. 4.10 was written as in Eq 4.11.

$$\frac{dW_{\text{mechanical}}}{dL} = 0.031 \cdot \%C \cdot (V_{\text{c}} \cdot \Delta t) \tag{4.11}$$

In the given Eq. 4.10 the unique process variable required is the nodal temperature of the nodes in the interface (NT11 in Abaqus) and the calculation of the sliding distance ($V_c \cdot \Delta t$). To calculate this latter, it is necessary to define a time increment Δt. If short increments of Δt are defined, the precision of the wear predictions might be more accurate, however, the number of simulations required to reach a specific cutting time (t_{end}) are increased.

As tool wear only occurs in those nodes of the tool that are in contact with the workpiece, from the whole node set extracted in *Step 2*, the amount of wear is calculated for those nodes that have a non-zero value of contact pressure (CPRESS $>$ 0 in Abaqus).

- *Step 5.* Nodal displacement

Up to this point, the amount of wear, W, of each node is already defined. However, the nodal move direction differs between the nodes in the rake face from those of the flank face and cutting edge, and vice versa. In the same manner as Klocke and Frank (2006) and Xie et al. (2005), the nodes are moved perpendicular to the relative direction of motion.

In Figure 4.30 the performed nodal displacement is schematically described. The nodal movement in the rake face is performed in a direction perpendicular to the surface of the rake. For this reason, the nodes are moved in both x and y coordinates depending on the rake angle. The nodes of the flank are moved perpendicular to the machined surface, only in the y direction. For the case of the cutting edge, the displacement of each node depends upon the location on the curved surface.

When large time increments Δt are specified to calculate the nodal wear, the y-coordinate of a certain number of nodes in the lower region of the cutting edge or on the flank face can be greater than that of the nodes in the flank face that were

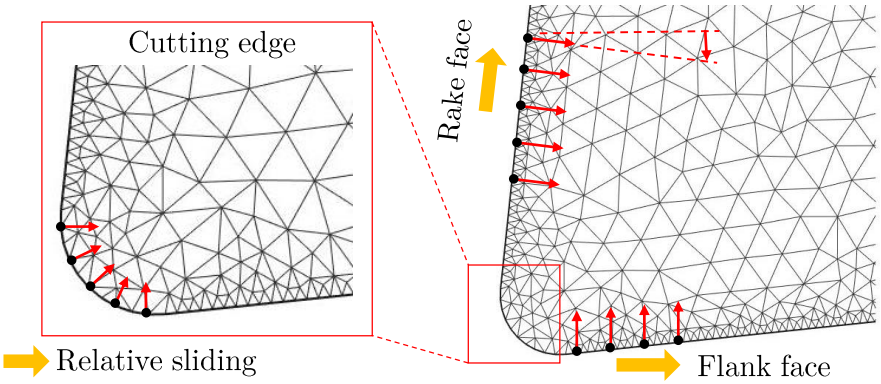

Figure 4.30: Nodal movement strategy

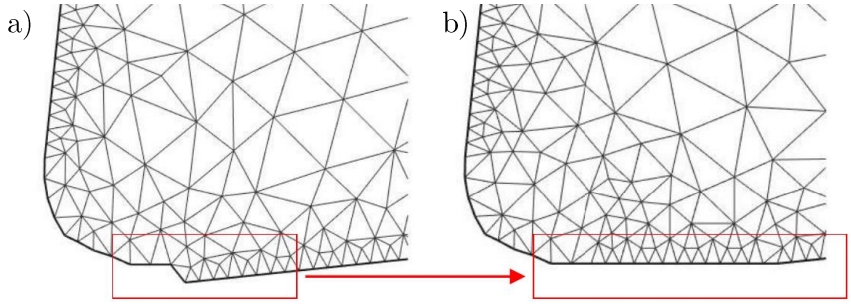

Figure 4.31: Nodal movement strategy in the flank face

not in contact (CPRESS = 0) and no wear was applied. If this happens, the worn geometry of the tool would look like that observed in Figure 4.31-a. To prevent this type of non-realistic flank wear, the Python wear subroutine specifies moving all the y-coordinates of the non contacting nodes on the flank face to a y-coordinate equal to that of the lowest node that already was in contact. This permits the correction of the aforementioned geometry to that observed in Figure 4.31-b.

The wear generated on the rake face is also affected when large Δt are employed. Due to the high degree of crater wear calculated in the last node of the tool-chip contact, the transition from the nodes in the worn region to those on the unworn rake face might be significantly severe, as shown in Figure 4.32-a. To prevent this type of transition between worn and unworn surfaces, a smoothed transition was set by adding a certain degree of wear to the first nodes above contact. This leads to an improved transition at the end of the crater wear (Figure 4.32-b).

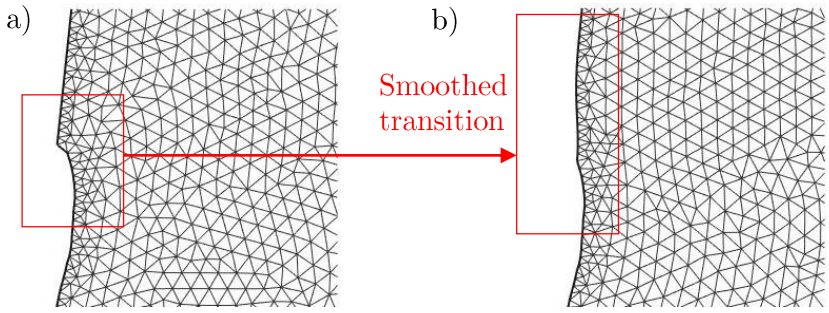

Figure 4.32: Nodal movement strategy on the rake face

- *Step 6.* Mesh generation based on constrained Delaunay technique

Once the outer geometry of the tool was defined after the nodal wear calculations and nodal movements, the next step consisted of creating a new FE mesh in the inner region of the tool. Based on the work of Engwirda (2014), a new mesh was defined with a constrained Delaunay algorithm implemented in Matlab, which was executed in background mode by the main Python script. This unstructured mesh is constrained by the outer boundary of the tool. In the contact surfaces the "classical" Delaunay

refinement technique was applied for an improved process variable calculation.

- *Step 7.* Tool shifting to correct the uncut chip thickness

When the geometry of the tool is modified due to flank wear, the lowest y-coordinate of the tool is modified, and thus the relative distance between tool and workpiece no longer matches the uncut chip thickness (Figure 4.33-a). Therefore, the last step of the strategy consists of shifting the tool in the direction of the y-coordinate in order to ensure that the simulated uncut chip thickness in the next cycle is that of the selected cutting condition. In general, the tool is shifted in the negative y-coordinate until the lower node makes contact with the machined surface of the workpiece (Figure 4.33-b).

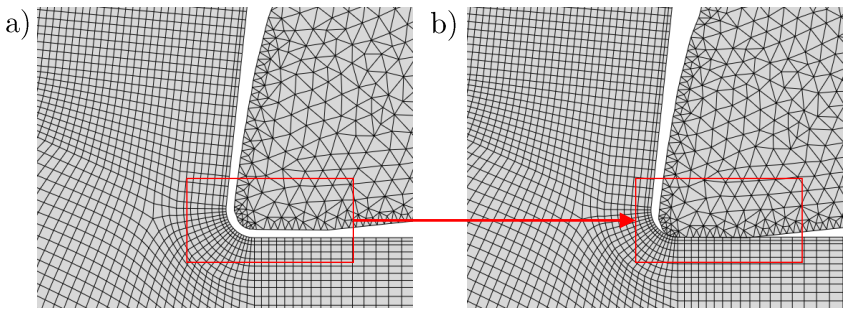

Figure 4.33: Tool shifting strategy to correct the variation of the uncut chip thickness generated by the predicted flank wear

4.3.2 Simulation of tool wear

In order to test the developed strategy, tool wear simulations were carried out for all the FP steels in all the selected conditions. For each workpiece material-cutting condition case, tool wear was predicted first at the MR of 240 cm^3 based on the simulations with fresh tools already presented in Section 4.2.2. In a second step, from the results of the simulations with the predicted worn geometry after MR=240 cm^3, tool wear was predicted at the MR=480 cm^3. The time increment Δt required in the wear prediction strategy was defined according to Table 3.1 for each tested cutting condition. This was directly set as the corresponding time for an MR=240 cm^3. The matrix of simulations is summarized in Table 4.6. A total of 32 simulations were carried out for wear prediction, apart from the initial 16 simulations in which the geometry of the tool was unworn.

Table 4.6: Matrix of simulations developed to test the wear prediction strategy

General data for tool wear simulations	
Workpiece materials	16MnCr5, 27MnCr5, C45, C60
Cutting conditions	100-200 $m \cdot min^{-1}$, 0.1-0.2 mm
Wear analysis states	MR=240-480 cm^3
Time increment employed in wear strategy	Equivalent time for MR=240 cm^3

4.3.3 Tool wear prediction: Results and validation

First, a general overview of the wear predictions is set out, where aspects related to flank and crater wear morphology, the influence of cutting conditions on wear patterns and a brief comparison between predictions and experimental results are set out. Then, an in-depth analysis of K_T and V_B predictions is carried out in comparison with experimental wear results.

Overview of tool wear predictions

Prediction of tool wear up to the MR=480 cm^3 was directly set in two steps in order to reduce the amount of simulations. Although the time increment Δt was considered somewhat large, it was possible to simulate the evolution of tool wear in an accurate manner for all the studied cases. An example of the prediction of wear for the case of C45 is shown in Figure 4.34. In the figure the variation of the tool profiles with increasing MR for the cutting conditions of V_c=100 and 200 m·min^{-1} and f=0.2 mm are depicted. At both cutting conditions the increase in tool wear is clearly observed

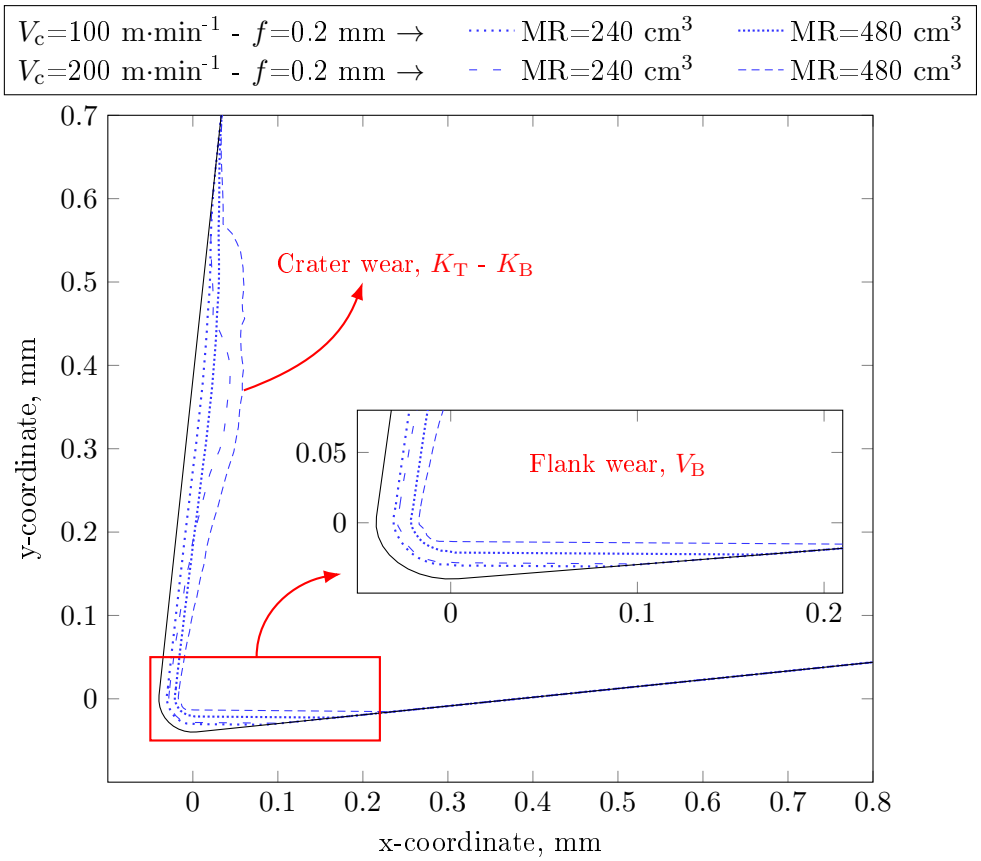

Figure 4.34: Predicted worn profiles of C45 steel when simulated at V_c=100 and 200 m·min^{-1} and f=0.2 mm after MR of 240 and 480 cm^3

when comparing the profiles at 240 and 480 cm^3. It is noticeable the change on the length and depth of the crater which occurred at V_c=200 $m \cdot min^{-1}$ and f=0.2 mm. The flank wear V_B also increased with increasing MR.

In Figure 4.35 a comparison of the predicted worn profiles for all the steels when machined at V_c=200 $m \cdot min^{-1}$ and f=0.2 mm is shown. The predicted land of the flank wear was in all the cases a flat surface parallel to the machined surface of the workpiece. These results were in line with the programmed nodal movement in the Python code. In the detail of the figure the differences in V_B between the steels are noticeable, with the C60 steel achieving the longest V_B in the case of the example. The cutting edge also presented a certain degree of wear, which caused a reduction of the edge radius.

The crater was presented as the expected concavity in the rake face. Differences in K_T between the steels were more significant than those of V_B, in which the C60 presented a severe K_T prediction compared to the other steels (Figure 4.35). The contact length K_B also varied between the steels, with the 16MnCr5 achieving the longest contact in the example. The differences in contact length also caused variations in the location of the maximum K_T. In the case of shorter K_B, the maximum depth was located nearer the cutting edge.

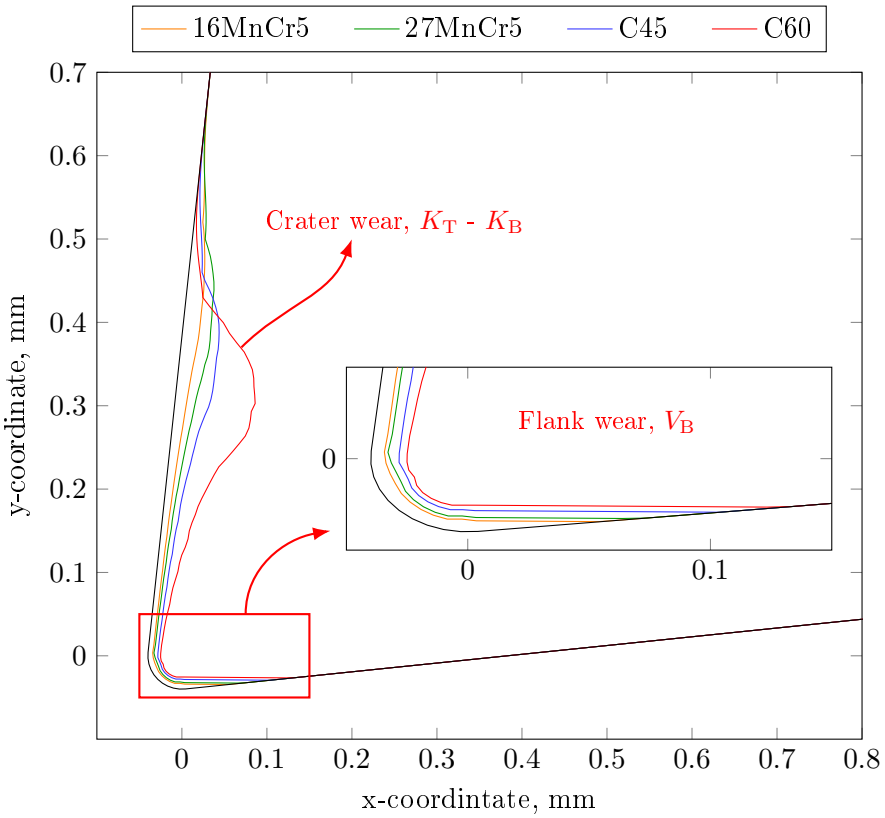

Figure 4.35: Predicted worn profiles of all steels when simulated at V_c=200 $m \cdot min^{-1}$ and f=0.2 mm (MR=240 cm^3)

In general, the modeled wear evolutions were in line with the experimental trials. In all the cases both K_T and V_B were the greatest when machining the C60 steel, followed by the C45, 27MnCr5 and 16MnCr5 steels. A more in-depth analysis is set out in the following subsection.

The influence that cutting conditions had in tool wear was also modeled. An example of this study is presented in Figure 4.36 for the case of C45 steel. The predicted worn profiles of the tool are compared for all the cutting conditions after a MR of 240 cm^3. The morphology of the profiles concerning V_B did not differ between the cutting conditions. The predicted flank wear land was in all cases a flat surface parallel to the machined surface of the workpiece. Only variations in the length of V_B were obtained. In contrast, the morphology of the crater presented significant differences depending on the cutting condition. An almost flat surface with a constant K_T was predicted when machining at V_c=100 m·min^{-1}, while a dip concave was predicted at high cutting speed conditions. As expected, the higher temperatures obtained at these latter cutting conditions caused the thermal wear mechanisms to activate, which caused in a higher degree of K_T in the regions of higher temperature. This trend showed a good agreement with the measured worn profiles of the orthogonal cutting tests.

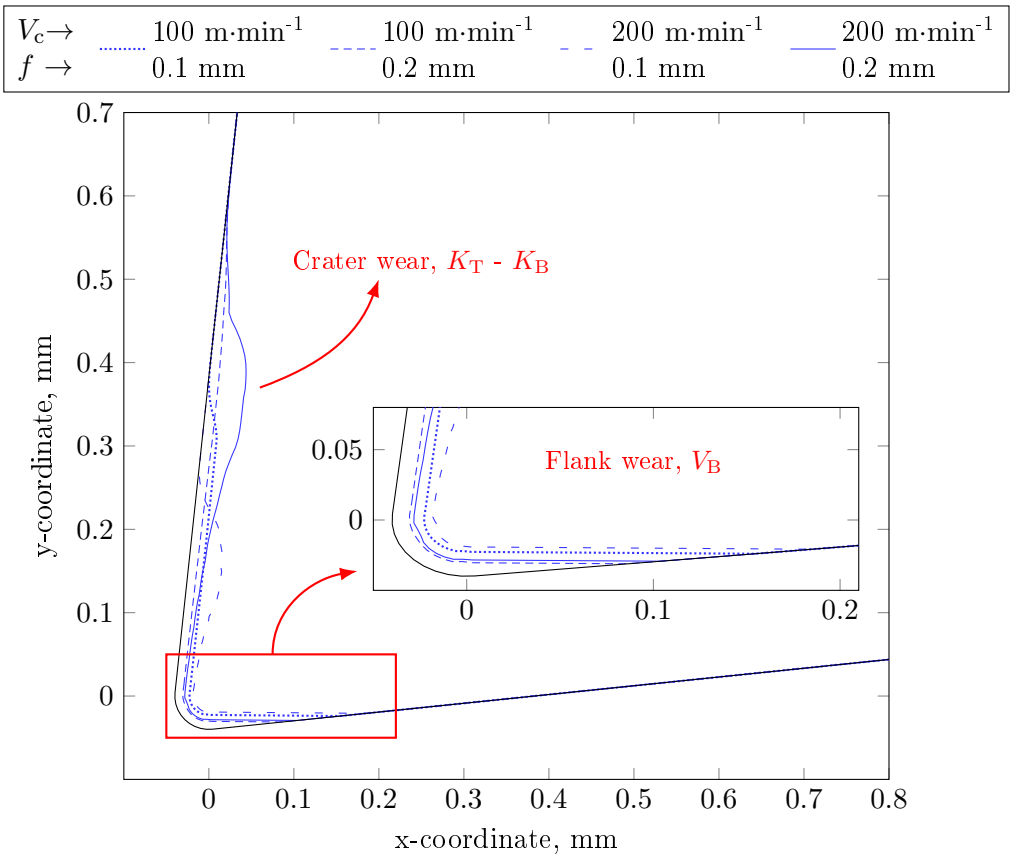

Figure 4.36: Predicted worn profiles of C45 steel for all cutting conditions (MR=240 cm^3)

Validation of tool wear predictions

For validation purposes, a comparison between wear predictions and experimental wear measurements is set out in terms of K_T and V_B. Since the predicted contact length K_B was always shorter than that measured experimentally, this was not employed as a validation criteria. Nevertheless, improving K_B was defined as a future task for the next releases of the numerical model. A comparison between predicted and measured worn profiles is graphed in Figure 4.37 for the case of the C45 steel. As mentioned, K_B in the experiments was clearly larger than that of the predictions. However, the prediction of K_T was in the same range of values as those observed in machining experiments. A higher degree of accuracy was observed in the predictions of V_B. Observing the detailed graph of the figure, the length of the flank wear land and the orientation were almost equal. Only slight differences could be observed in the amount of wear in the cutting edge.

In Figure 4.38 the results of K_T for all the analyzed cutting conditions, materials and wear states are compared. In general, an overprediction of K_T was observed in all the analyzed cases. This was more significant when comparing the results at

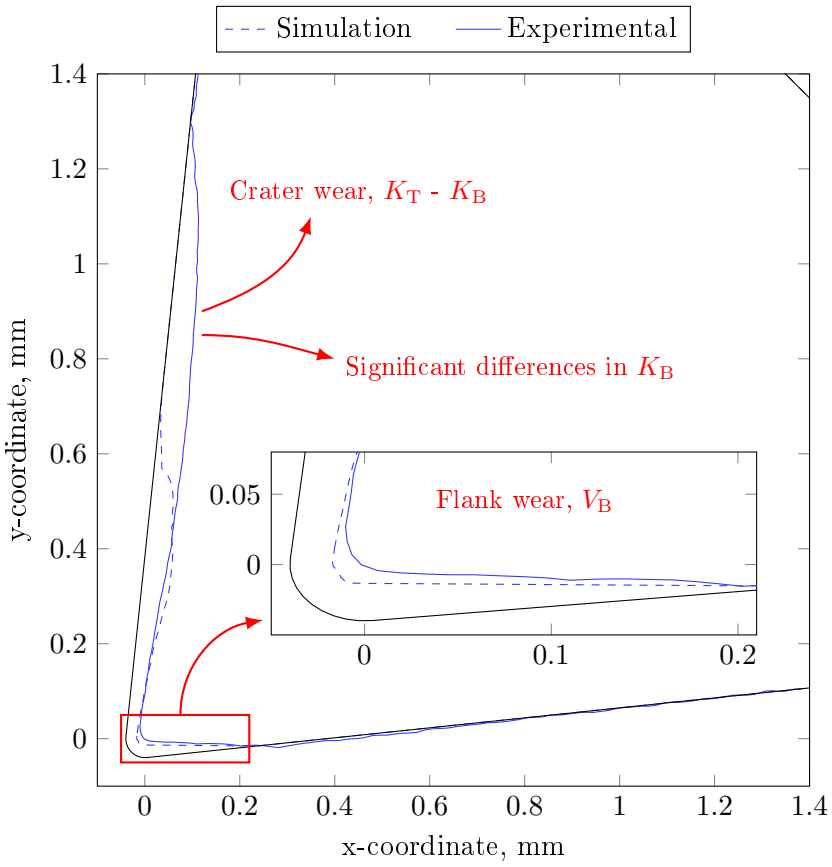

Figure 4.37: Predicted and experimentally measured worn profiles for the case of C45 at V_c=200 m·min^{-1} and f=0.2 mm (MR=480 cm^3)

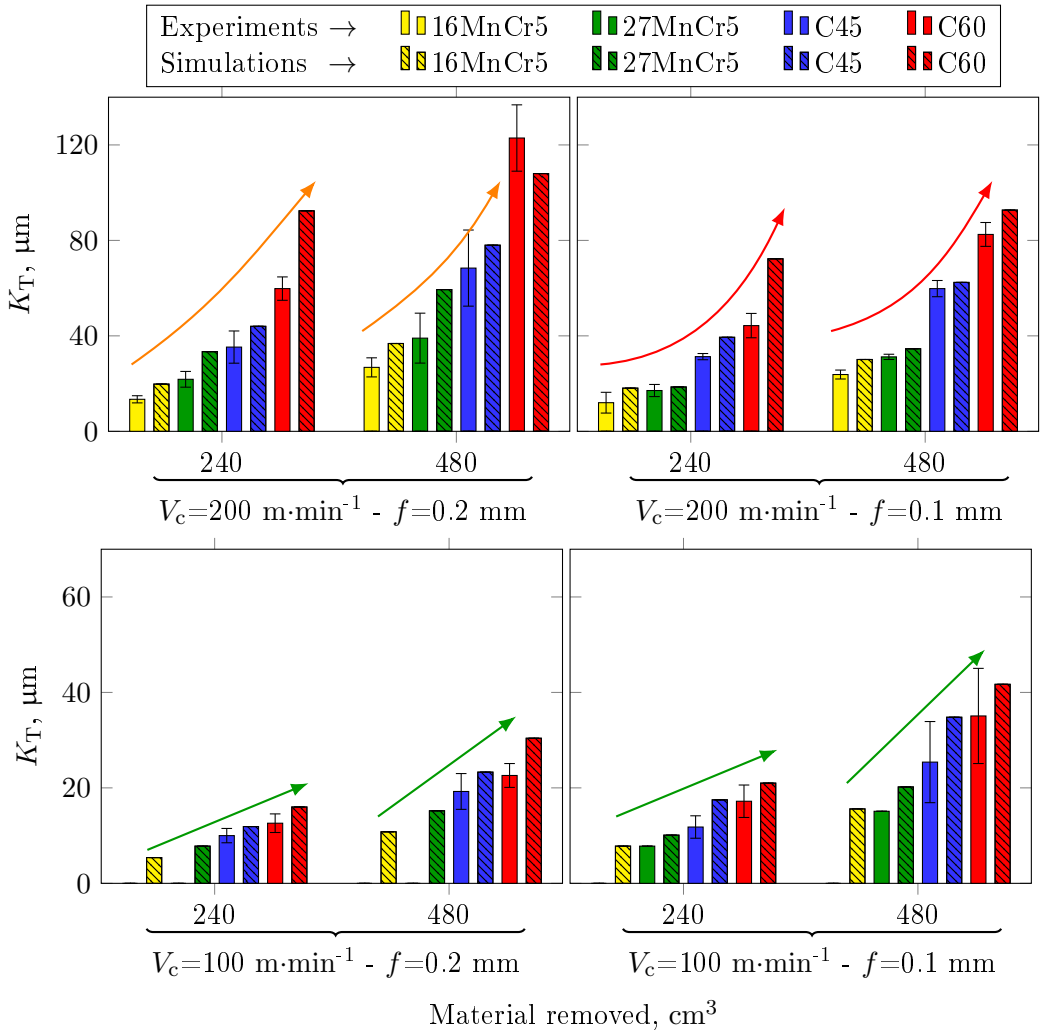

Figure 4.38: Experimental and simulation results of K_T for all the FP steels and cutting conditions

200 m·min^{-1}, in which deviations reached ratios of up to 35%. The average deviation was 22%. However, the predictions concerning the main trends were highly accurate. For example, at V_c=200 m·min^{-1} and f=0.1 mm large differences in K_T were measured between 16MnCr5 and 27MnCr5 compared to the C45 and C60. This trend was also predicted by the numerical model (marked with red arrows). The differences between the steels when cutting at V_c=200 m·min^{-1} and f=0.2 mm were more linear, in the same manner that was predicted (marked with orange arrows). At the cutting conditions of V_c=100 m·min^{-1}, the slight variations in K_T were also accurately simulated (marked with green arrows, note that the y-scale in the plots is varied).

In general, predicted results of V_B were close to the experimental measurements, and inside the range of the measured deviations (Figure 4.39). Only the results at the cutting condition of V_c=200 m·min^{-1} and f=0.2 mm were underpredicted, in which a maximum error of 45% and an average of 35% was obtained. The overall deviation in the prediction of V_B was less than 20%. With regards to the main trends, the

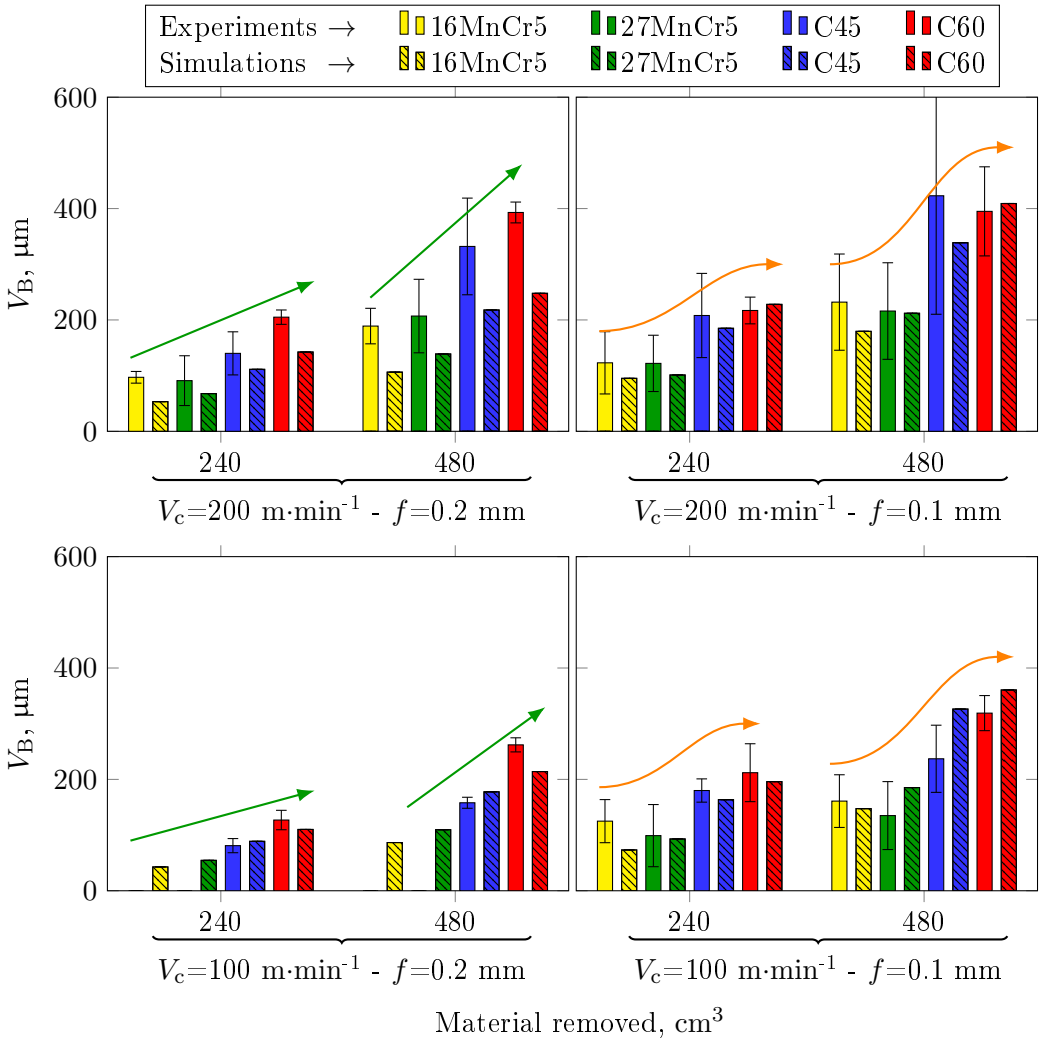

Figure 4.39: Experimental and simulation results of V_B for all the FP steels and cutting conditions

predictions were considered accurate. In the results of the orthogonal tests at a feed of 0.1 mm, the V_B of 16MnCr5 and 27MnCr5 differ in a greater manner than that of C45 and C60. In the predictions the same trend was captured (marked with orange arrows). In contrast, at f=0.2 mm in both experimental and numerical frameworks, the increase in V_B was smoother (marked with green arrows).

Discussion of wear prediction results

The most significant deviation in the wear predictions concern K_B. In some cases the experimentally measured contact length was double than that of the predictions. Since simulations with fresh tools already obtained significantly lower l_c (see Section 4.2.2), the implementation of tool wear into the FE code did not affect the improvement of those predictions. In the same manner that was concluded previously, the contact

length might be improved in further releases of the model by characterizing the real friction behavior between the workpiece materials and the uncoated carbide, and analyzing in more depth the material behavior at temperatures above 1000°C.

Regarding the predictions of K_T, in both frameworks the profile of the crater was presented as a severe concavity or as a type of flat surface depending on the cutting condition, which in turn was a direct cause of the temperature achieved on the rake face. In the cutting conditions of lower temperature range, V_c=100 m·min^{-1} and f=0.1 and 0.2 mm, the crater was mostly affected by an abrasive mechanism, and predictions were highly accurate. In contrast, at V_c=200 m·min^{-1} and f=0.2 mm the temperatures in the tool were much higher, and the crater was dominated by both mechanical and thermally activated mechanisms. At this cutting condition the deviations were found to increase. However, this makes sense if it is taken into account that the wear rate law was fitted to the temperature results calculated from the experiments, and these were slightly lower than those predicted at V_c=200 m·min^{-1} and f=0.2 mm (See Figure 4.26). Nevertheless, a slight recalculation of the activation energy, taking into account for example the numerical temperatures rather than the experimental ones, might improve the predictions.

In general the predictions of V_B were accurate. Considering that the flank wear is mostly affected by abrasion, the results seemed to confirm the reliability of the abrasive term of the wear rate equation. However, at V_c=200 m·min^{-1} and f=0.2 mm wider deviations compared to the other cutting conditions were found again. If it is supposed that at this cutting condition the wear in the flank face begins to be affected by a thermally activated mechanism, and lower simulated temperatures could be the reason for the shorter predicted V_B.

4.4 Conclusions of the chapter

The ALE model and wear simulation strategy provides the prediction of machinability related outputs based on input parameters that can be written as a function of microstructure and composition properties. The major finding is the prediction of industrial relevant outcomes such as crater depth K_T and flank wear land V_B with an average error of 20%, and similar trends as those found in the orthogonal wear tests. It is worth highlighting that all these results were assessed for steels with a wide range of ferritic-pearlitic microstructures for commonly employed cutting conditions in turning operations.

Of equal importance is the validation of the model from the point of view of fundamental or scientific variables. The model accurately predicted the cutting forces, tool temperatures and chip thickness results when compared to those achieved in the orthogonal cutting tests. The maximum error of these variables was less than 10%, 18% and 12% respectively. The major limitation of the developed model was found in the

prediction of contact length, which was underestimated in a range of 25-60%. These results directly caused a prediction of 25-45% lower feed forces, and crater lengths K_B sometimes half of those found in the experimental tests. In spite of these limitations, the main empirical trends of all the measured variables were accurately predicted.

The results suggest that further experimental investigations are needed to characterize the friction behavior in the interface between the range of workpiece materials and the uncoated carbide tool. It is possible that the implemented friction data interpolated from characterizations carried out with coated tools was underestimating the real friction taking place in the interface. This might be a reason for the underestimations of contact length. In addition, in a further extension of material behavior modeling, the flow stress data at temperatures above 1000°C should also be characterized, and the MSB flow stress model should be experimentally readjusted. Improving the material behavior at the temperatures which occurred in the secondary shear zone could also help to correct the contact length and shear stresses, and therefore the feed forces.

Chapter 5

Conclusions

The principal scope of this Ph.D. work is the development of a procedure based on finite element modeling to predict machinability and tool wear evolution considering the effect of the microstructure, and additionally contribute in the understanding of the machinability of lamellar ferrite-pearlite steels. The conclusion yielded throughout this research that gives response to the main objective is listed below:

> The developed Arbitrary Eulerian Lagrangian orthogonal cutting model and the wear simulation strategy enables the qualitative prediction of machinability based on input parameters that can be written as a function of microstructure and composition properties. In addition, the empirical procedure undertaken in this research permits the characterization of the wear rate law, and contributes to the data sets required for validation. In general, the trends observed in the simulations were in good agreement to the orthogonal cutting tests concerning both scientific and industrial relevant outputs. The values of crater depth (K_{T}) and flank wear land (V_{B}), and the scientific variables of cutting forces (F_{c}), chip thickness (t_2) and tool temperature were predicted with an error in the range of 5-20%. The major limitation of the developed model was found in the prediction of contact length (l_{c}) or crater length (K_{B}) and feed forces (F_{f}), which were underestimated by 25-60%.

In the course of reaching the main objective, a certain number of operational objectives were identified. The main conclusions from these are described in the following lines:

- Based on rheological characterization tests, a new material constitutive model was proposed to represent the behavior of ferrite-pearlite steels. This was named the MicroStructure Based model (MSB model). The strain hardening behavior was modeled as function of chemical composition, and the microstructure parameters of pearlite fraction, interlamellar spacing and ferritic mean grain size. Thermal softening as well as the coupling between temperature and strain rate were also introduced, and were found to be almost equal for all the studied ferrite-pearlite

steels. The proposed material constitutive model showed significant improvement in terms of flow stress prediction compared to the widely employed conventional model of Johnson and Cook (1983) and Abouridouane et al. (2012). The achieved maximum deviation was less than 10% compared to empirical σ-ε data.

- The identified thermal properties did not represent significant variations between the ferrite-pearlite steels. Only the calculated conductivity of 16MnCr5 was found to be 50-60% higher, a direct effect of the greater diffusivity that this steel showed. However, for modeling purposes thermal properties of commonly employed ferrite-pearlite steels might be considered equal, independent of the composition or even microstructure morphology.
- The orthogonal cutting strategy to empirically characterize the wear behavior of steels successfully gave a reliable tool wear rate model that reproduced the wear evolution of all the analyzed steels with a unique equation. This sets out a wear rate behavior as uncoupled mechanical and thermally activated wear phenomena that represent the wear for both crater and flank. The thermally activated wear mechanisms were found to be the same for all the steels, which led to the definition of the same value of activation energy E_{a}=95 kJ·mol^{-1} in an Arrhenius type equation. In contrast, $\frac{dW_{\mathrm{mechanical}}}{dL}$ differed for each of the steels. However, it was found that this mechanical wear rate had a stretch correlation with the amount of %C when comparing all the steels. For this reason, this was written as a unique equation in function of %C.

It is worth highlighting other contributions concerning the methodologies of the characterization of process variables and the machinability of ferrite-pearlite steels. The main findings are reported below:

- The developed setup to establish a direct relationship between the radiation of tool surface and the real surface temperature seemed to give realistic temperature values without the need of characterizing the emissivity of the tool. In addition, the developed setup had the benefit of relating (DL, T) at the same focusing field and integration time as those employed in the orthogonal procedure.
- Based on measured tool side temperatures, an approach was established to calculate tool contact temperatures and correct the effect of the overhang (distance between the tool-chip contact section and the surface on which temperatures were recorded). The required inputs in this approach are the cutting and feed forces, chip thickness and tool-chip contact length. It was calculated that temperature increases by 55-67% when shifting from tool side to tool contact temperature. With this approach it was assessed that contact temperatures were more sensitive to the variation of cutting conditions than recorded tool side temperatures. The sensitivity increased by 5-32% depending on the tested condition, which suggested that the temperature analysis carried out in the contact section better described the thermal behavior during cutting.

- Flank wear (V_B) was linked to the pearlite content or the strength of the material. Globally, machining the C60 steel obtained the highest degree of wear by the end of the tests, followed in decreasing order as the amount of pearlite content in the material decreased. However, at the beginning of the tests, the amount of flank wear was almost equal when cutting any of the steels, or even higher in the case of the 16MnCr5 and 27MnCr5, in spite of their lower pearlite content. A hypothesis of these unexpected results is that the Al_2O_3 inclusions that appeared in these steels, combined with the shorter interlamellar spacing, was generating this first higher wear increase than in the C45 and C60 steels. Crater wear (K_T) presented the same trend in all cutting conditions. Increasing pearlite content in the machined ferrite-pearlite steel generated a higher degree of K_T from the beginning up to the end of the trials. Both V_B and K_T were more sensitive to the cutting speed than to the feed, although increasing both process parameters caused the wear to increase.

- The crater length (K_B) presented diverse trends, which seemed to be linked to the amount of K_T. When K_T was not significant, K_B was higher in the steels containing a higher amount of ferrite. In contrast, increasing K_T caused a change in the trends, obtaining almost longer K_B when cutting the steels with higher amount of pearlite. However, this was followed in all the cases except in the C60. It was believed that the extremely high degree of K_T found in this steel, which generated a large concave on the rake face, was not permitting the length of the crater to increase in the same manner as in the other steels.

- Tool temperature, T_{side} and $T_{contact}$, and specific cutting forces, K_{sc}, were found to be higher in the steels with higher pearlite content or higher strength. In contrast, the steels with higher ferrite content achieved longer initial contact length, l_c, and also longer K_B depending on the cutting condition and amount of material removed. Chip thickness, t_2, and specific feed force, K_{sf}, were also greater in the steels with greater amount of ferrite. An increase in fundamental variables was observed when tool wear was relevant, mostly at V_c=200 m·min^{-1}. The variable most affected was the K_{sf} (↑54%) followed by t_2 (↑43%), K_{sc} (↑33%) and finally $T_{contact}$ (↑8-12%). Concerning the influence of ferrite-pearlite steels in fundamental variables, the greatest difference was found in t_2 (up to 25% of difference between steels), followed by $T_{contact}$ (11-19%), K_{sf} (15%) and K_{sc} (7%).

Chapter 6

Future outlook

In addition to the newly generated knowledge, the research undertaken in this Ph.D. has given rise new research paths. The future lines related to improving the results of this research are listed below:

- In a further extension of material behavior modeling, the flow stress data at temperatures above 1000°C should be characterized, and then the MSB flow stress model should be empirically readjusted. This would lead to improving the material behavior at the temperatures occurring in the secondary shear zone, which might help predict with a higher degree of accuracy the shear stresses taking place in the rake face, and therefore the feed forces. In addition, improving the material behavior model at these temperatures might also affect the predictions of contact length.

- Experimental investigations are required to characterize the friction behavior in the tool-work interface for the range of studied ferrite-pearlite steels and the employed uncoated carbide tool. It is expected that new characterizations could lead to the identification of a more realistic friction coefficient, which might improve aspects such as tool-chip contact length, shear stresses and feed forces, which are the major drawbacks of the developed FE model.

From an global point of view, the following future lines are interesting in order to expand the research:

- Concerning the rheological characterization of materials, determining the most adequate mechanical testing procedure to represent the state of the materials during machining processes is of high interest. For example, shear tests in which strains of up to 400% are reached might be an option to improve the accuracy of the models. In addition, the effect that heating rate has on flow stress was

not studied in this thesis, which could have an impact on the mechanical and microstructural properties of the steels.

- The development of advanced empirical techniques in order to measure variables such as the stresses and pressures acting in the contact regions, the sliding velocities and the temperature fields in the tool-chip interface are interesting for increasing the understanding of the cutting process.
- The developed orthogonal cutting strategy could be extended to characterize the wear behavior of steels with other type of microstructures such as globulized pearlite or coarsened ferrite-pearlite grains. This analysis would identify if the differences in wear are due to mechanical or thermally activated mechanisms, which might help in the development of specially designed microstructures to improve machinability.
- The developed Arbitrary Eulerian Lagrangian approach could be compared with other modeling techniques such as fully Lagrangian or Coupled Eulerian Lagrangian models. Furthermore, the microstructurally determined inputs and wear prediction strategy in these types of models could be implemented to try to improve the accuracy of predictions. Developing a 3D cutting model would also enable the prediction of surface integrity and tool wear in operations such as nose turning or drilling.

Chapter 7

Scientific contribution

Publications in international journals:

Soler, D., Aristimuño, P.X., Sáez-de-Buruaga, M., Garay, A., Arrazola P.J. (2018). New calibration method to measure rake face temperature of the tool during dry orthogonal cutting using thermography. *Applied Thermal Engineering*, 137, 74-82.

Medina-Clavijo, B., Sáez-de-Buruaga, M., Motz, C., Soler, D., Chuvilin, A., Arrazola, P.J. (2018). Microstructural aspects of the transition between two regimes in orthogonal cutting of {AISI} 1045 steel. *Journal of Materials Processing Technology*, 260, 87-96.

Publications in conferences:

Sáez-de-Buruaga, M., Poveda, I., Arrazola, P.J. (2015). Tool Wear Prediction in Machining Process Using a Microstructure-Based Finite Element Model. *Key Engineering Materials*, 651-653, 1229-1234.

Sáez-de-Buruaga, M., Esnaola, J.A., Aristimuño, P.X., Soler, D., Björk, T. and Arrazola, P.J. (2017). A Coupled Eulerian Lagrangian Model to Predict Fundamental Process Variables and Wear Rate on Ferrite-pearlite Steels. *Procedia CIRP*, 58, 251-256.

Appendix A

Extended results of material characterization

In this Appendix, the following is presented:

- Schematic representation of the employed MTS 810 and the specially designed compression die to perform the uniaxial compression tests.
- Experimental flow stress curves of the 16MnCr5, 27MnCr5, C45 and C60 for the temperatures of 20, 500 and 680°C and strain rates of 0.5, 5, 50, 2000 and 4000 s^{-1}.

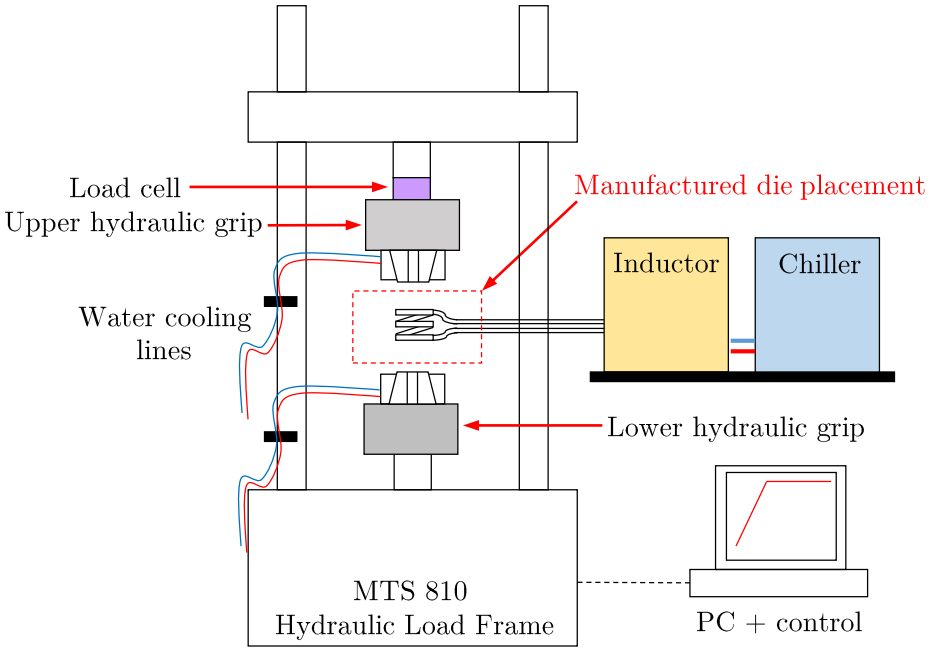

Figure A.1: Schematic of MTS compression setup

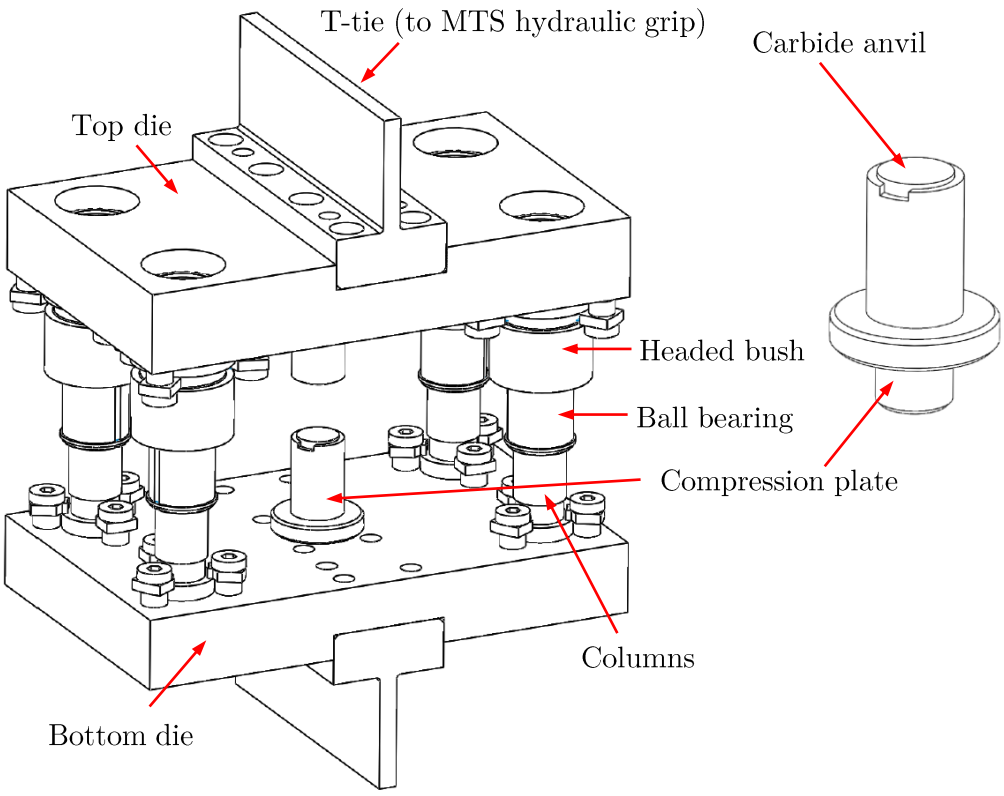

Figure A.2: Manufactured die for compression tests

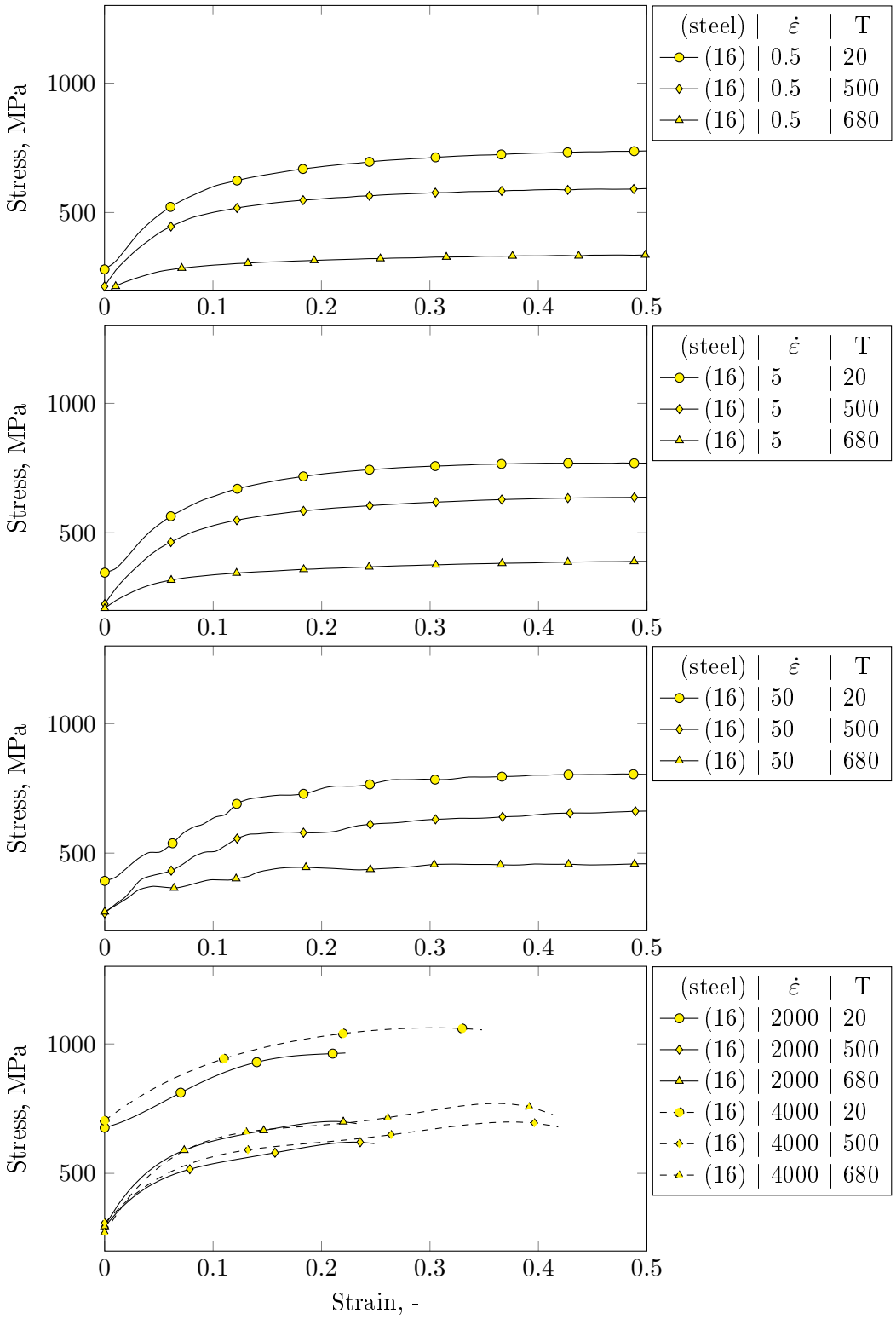

Figure A.3: Flow stress curves of 16MnCr5 steel

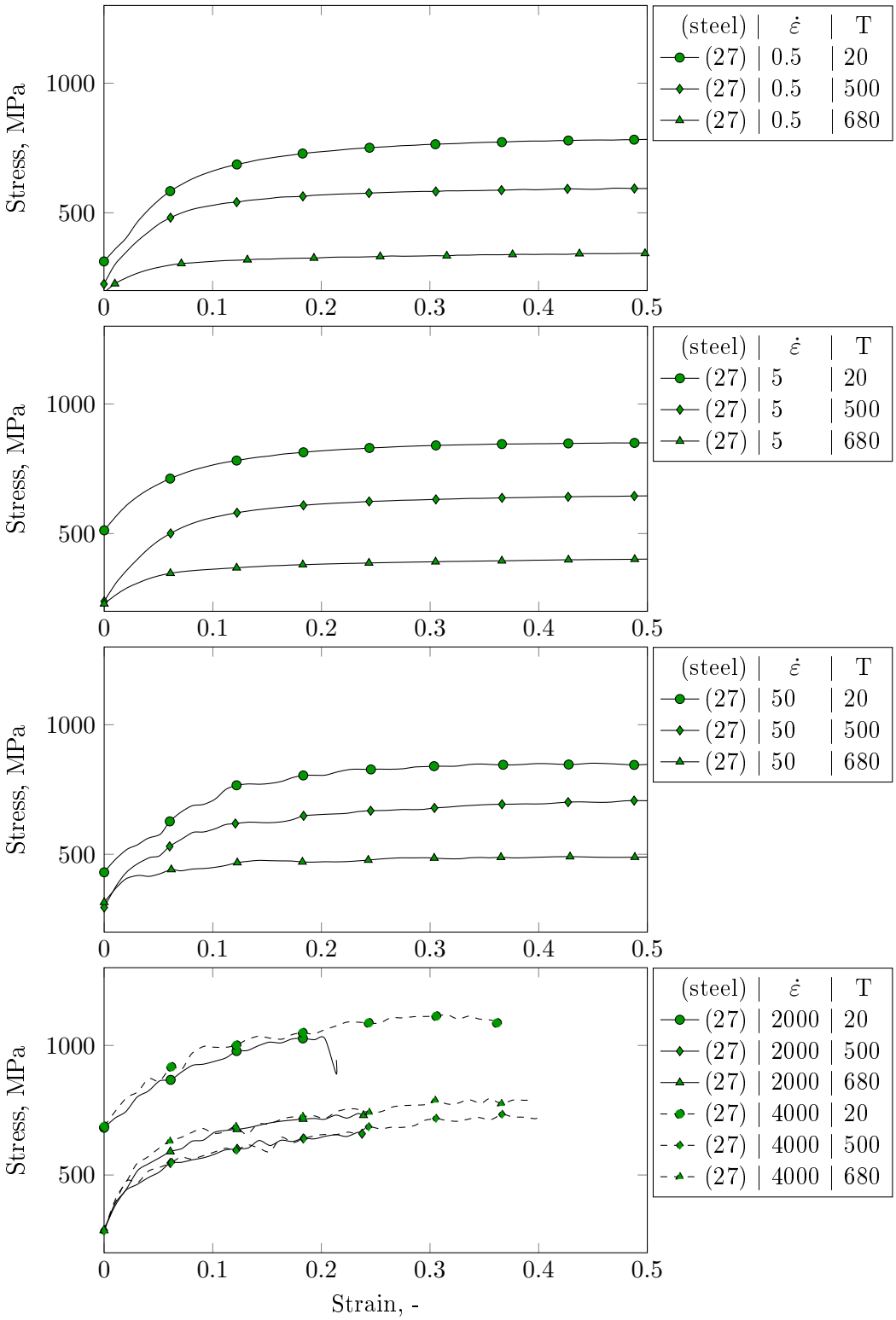

Figure A.4: Flow stress curves of 27MnCr5 steel

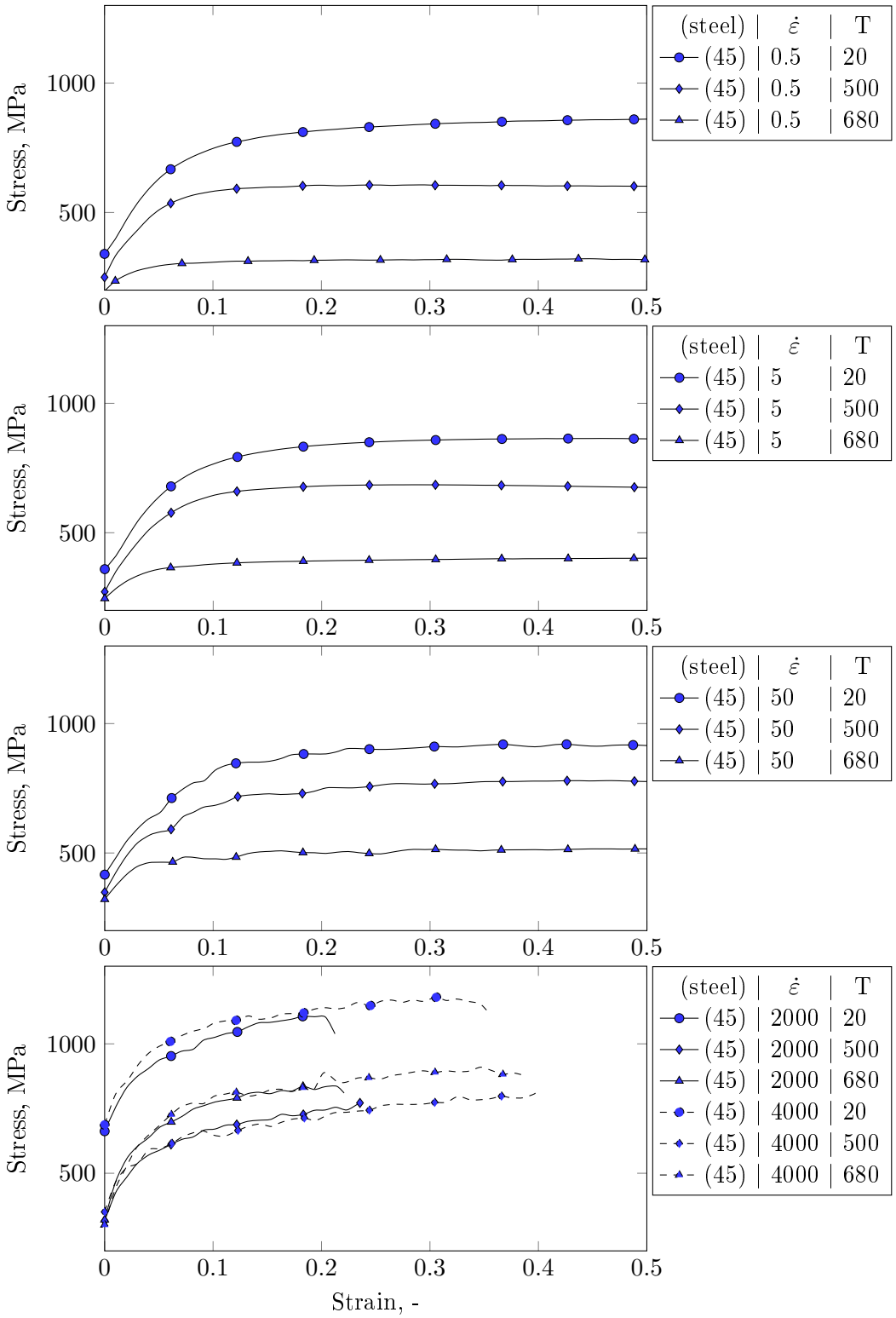

Figure A.5: Flow stress curves of C45 steel

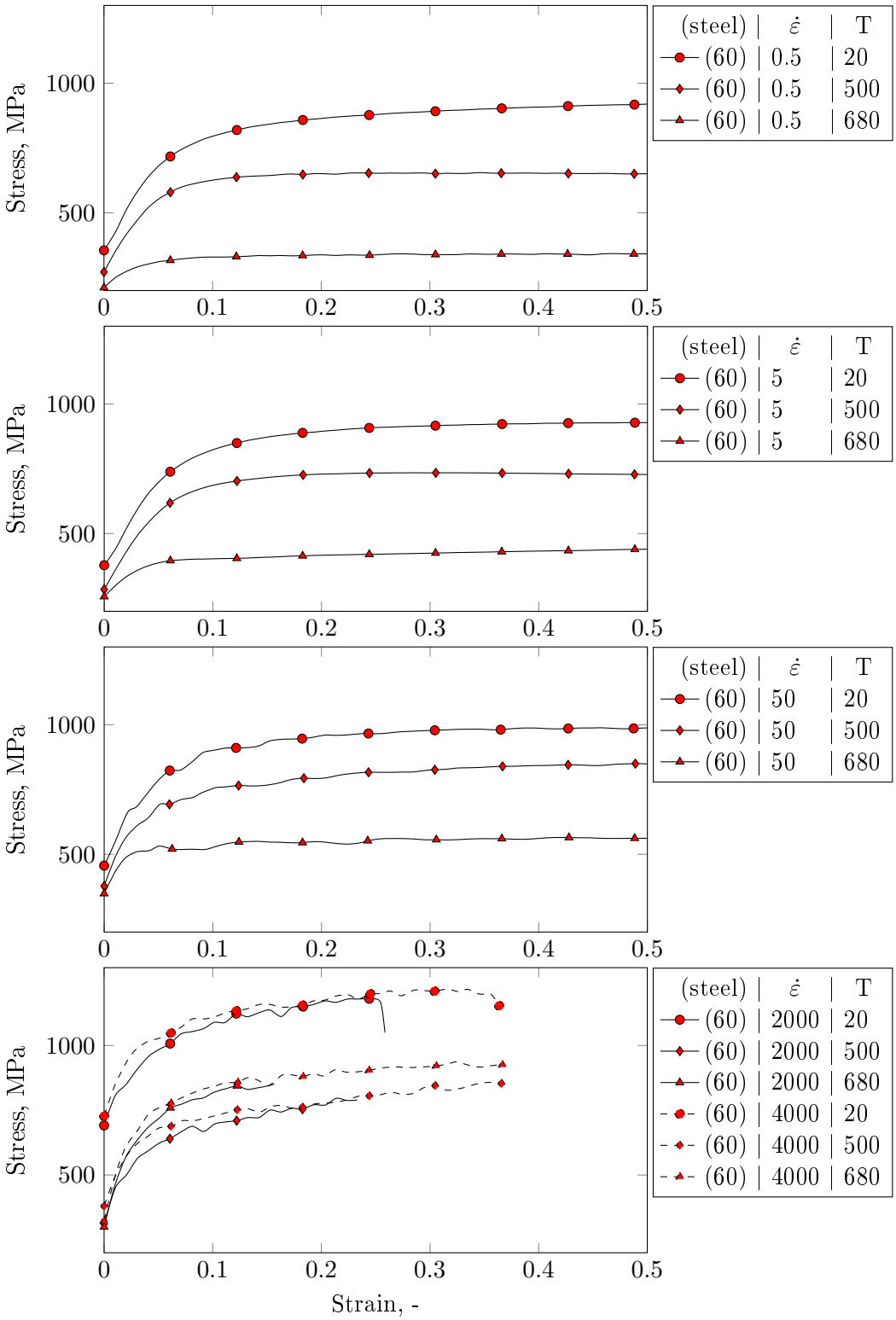

Figure A.6: Flow stress curves of C60 steel

Appendix B

Extended results of orthogonal cutting tests

In this Appendix the following extended analysis is reported:

- 2D geometry of worn flank and rake faces of the tool, and worn profile of the mid plane contact section of all steels.
- Macroscope images of chip morphology showing the free and contact surfaces of the chip.
- Micrographs of etched and polished chips.

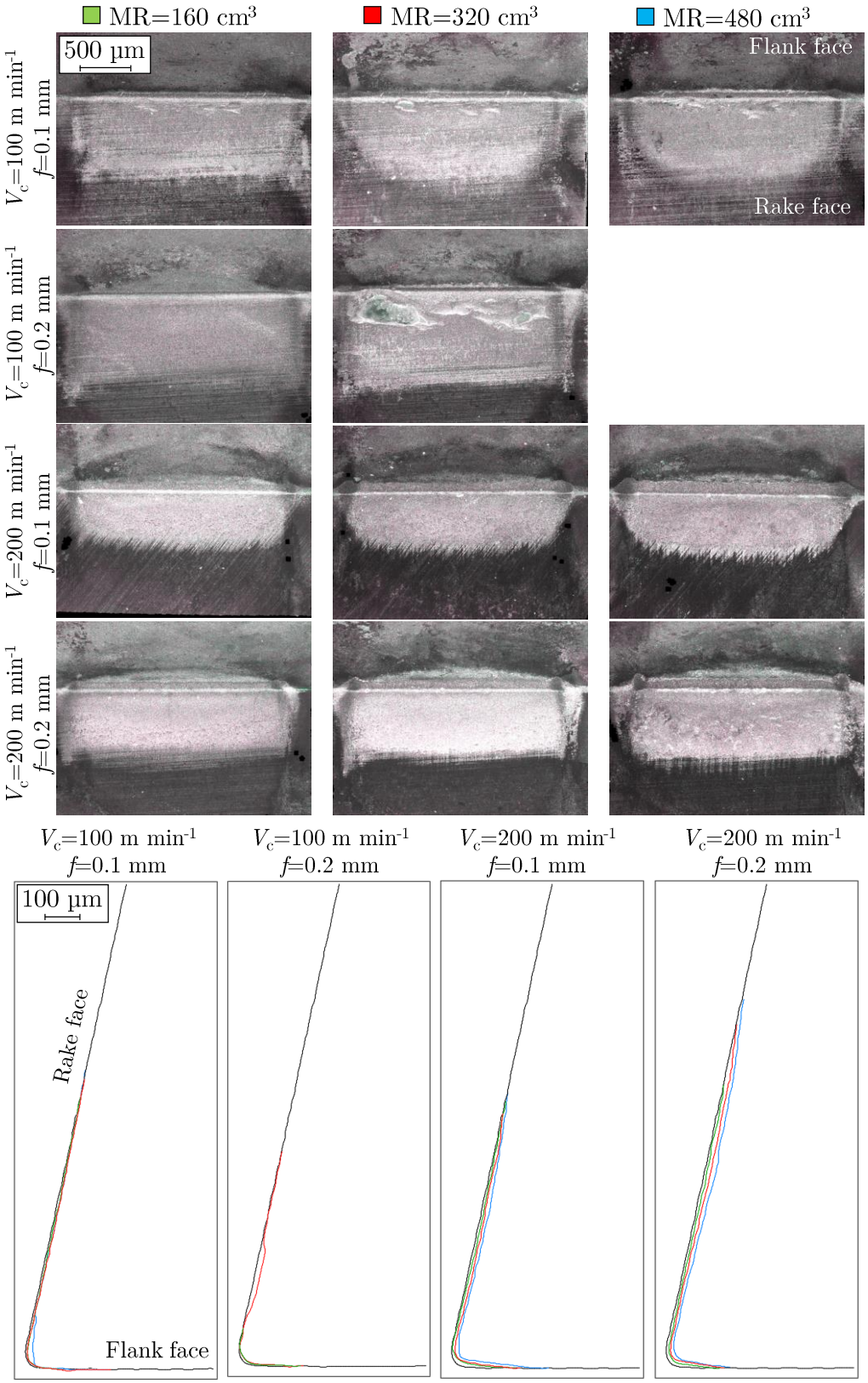

Figure B.1: 2D geometry of worn flank and rake faces of the tool, and worn profile of the mid plane contact section. Captures extracted at the MR of 160, 320 and 480 cm^3 for 16MnCr5 steel

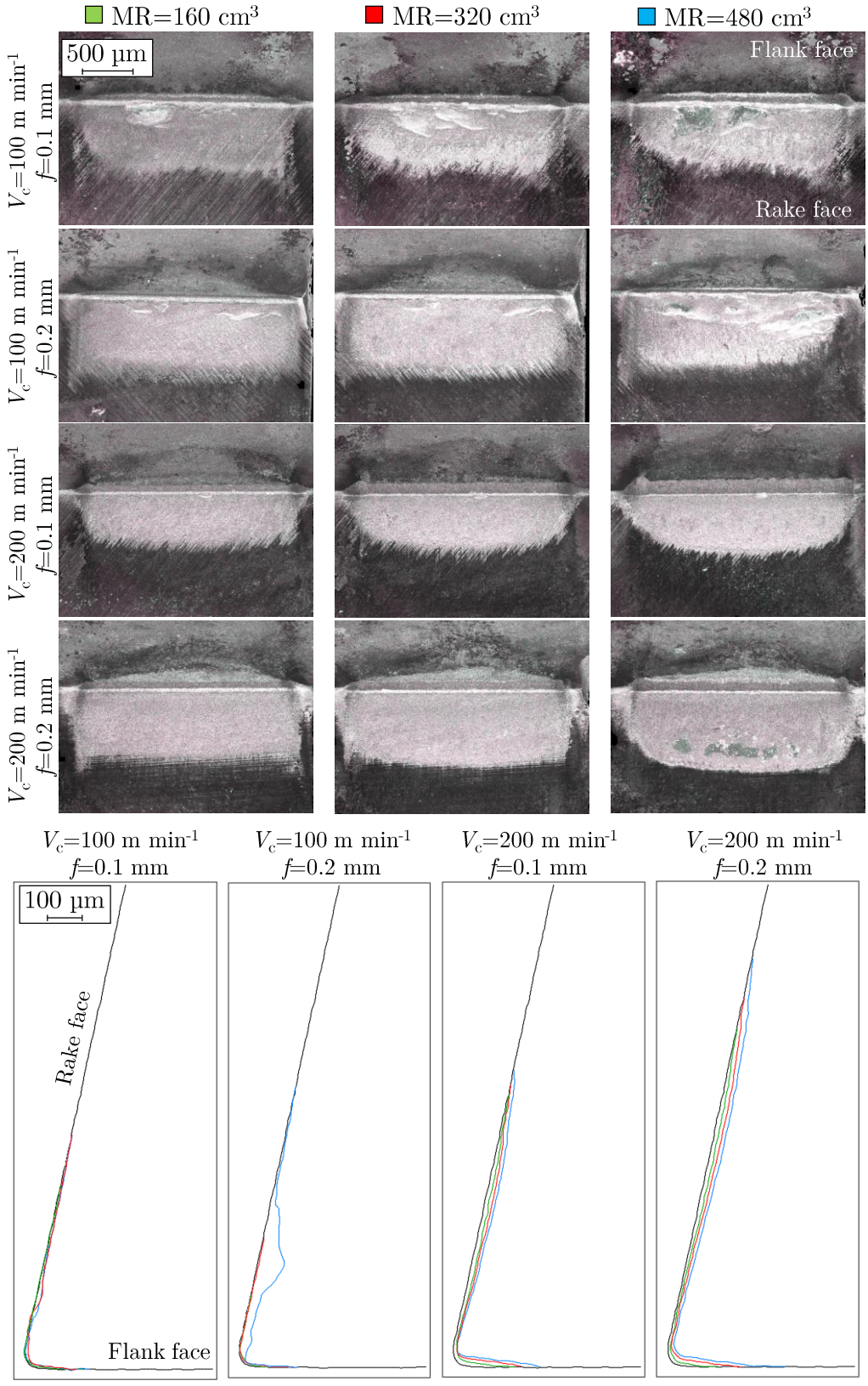

Figure B.2: 2D geometry of worn flank and rake faces of the tool, and worn profile of the mid plane contact section. Captures extracted at the MR of 160, 320 and 480 cm^3 for 27MnCr5 steel

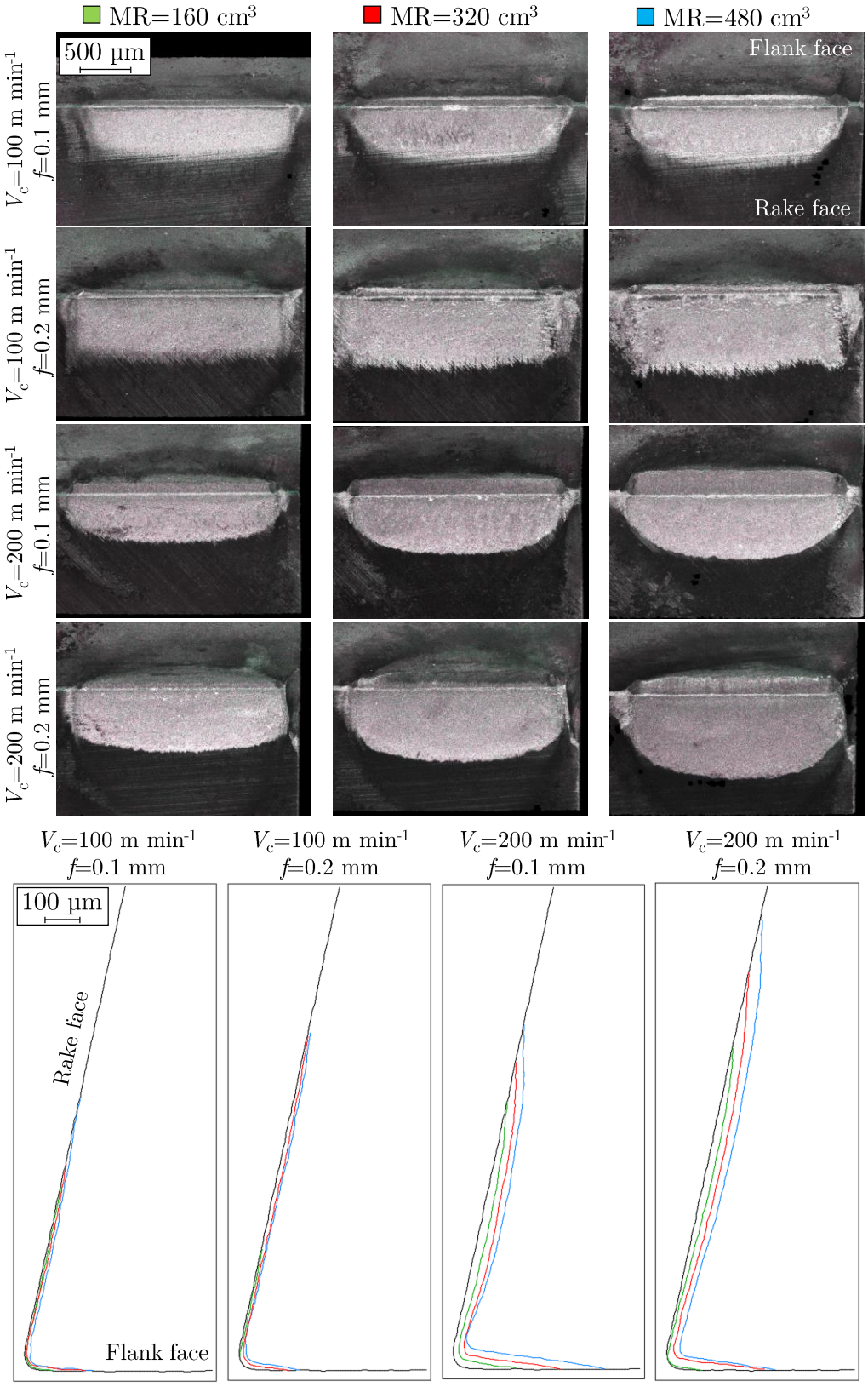

Figure B.3: 2D geometry of worn flank and rake faces of the tool, and worn profile of the mid plane contact section. Captures extracted at the MR of 160, 320 and 480 cm^3 for C45 steel

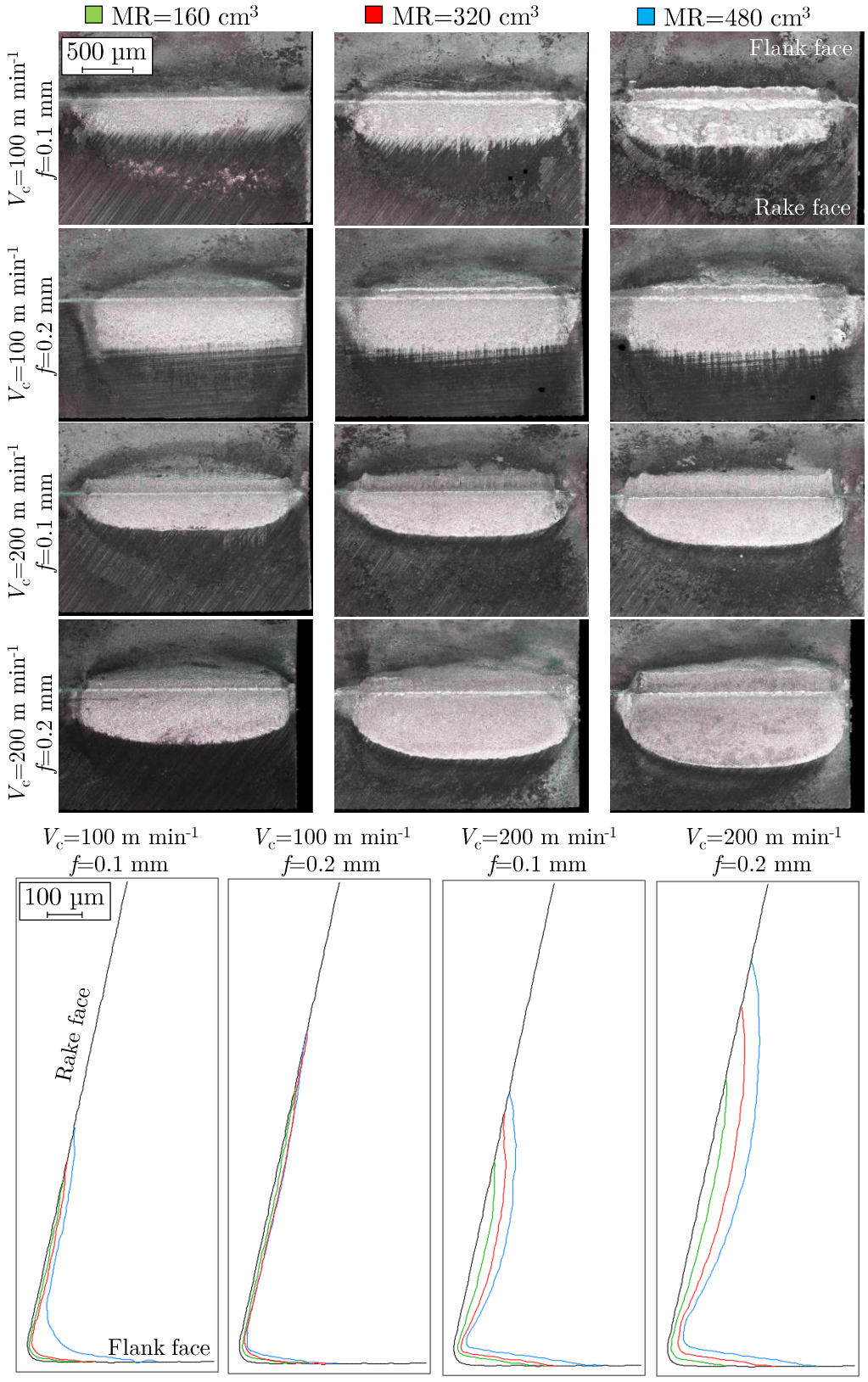

Figure B.4: 2D geometry of worn flank and rake faces of the tool, and worn profile of the mid plane contact section. Captures extracted at the MR of 160, 320 and 480 cm^3 for C60 steel

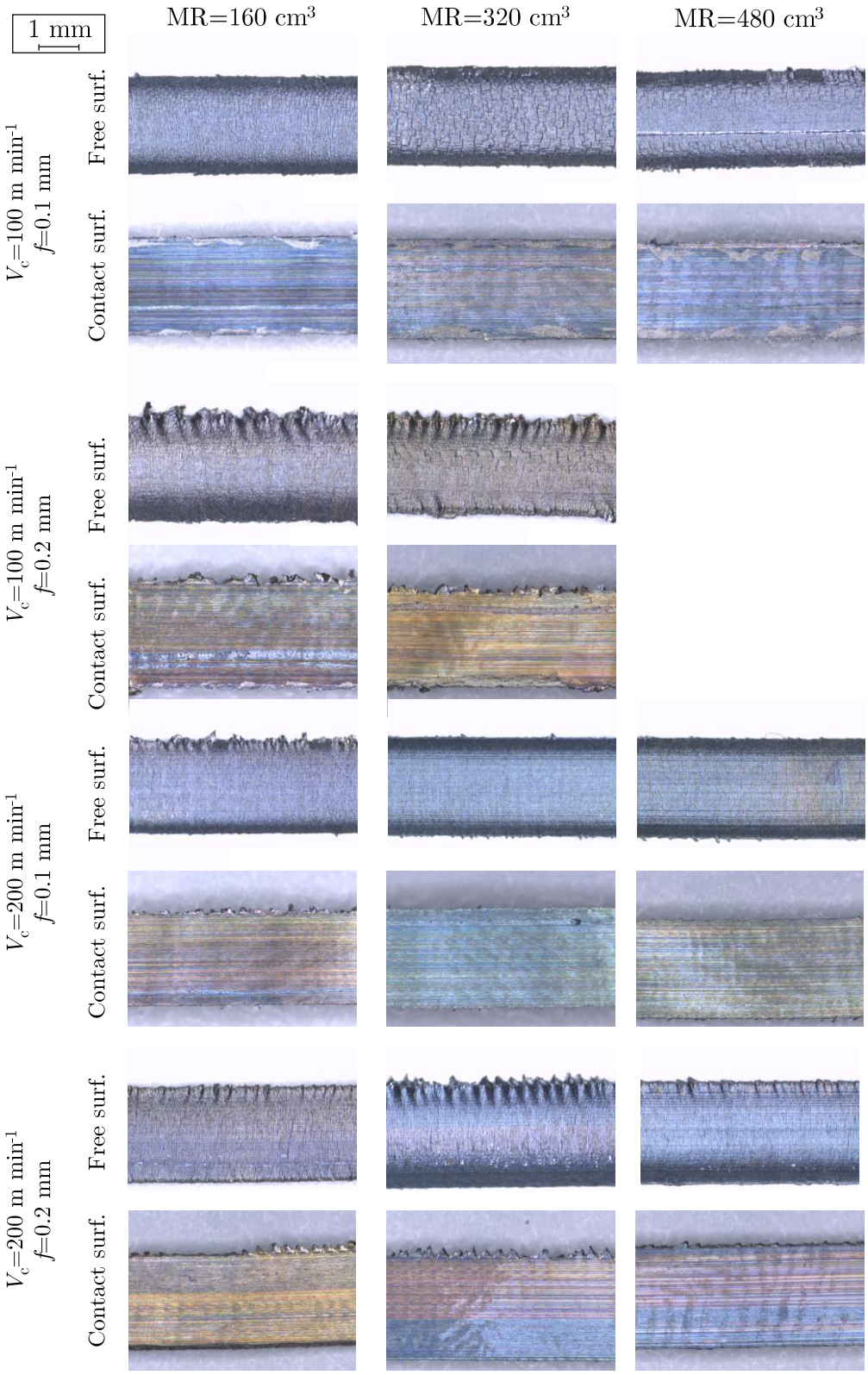

Figure B.5: Macroscope images of chip morphology showing the free and contact surfaces of the chip. Captures extracted at the MR of 160, 320 and 480 cm^3 for 16MnCr5 steel

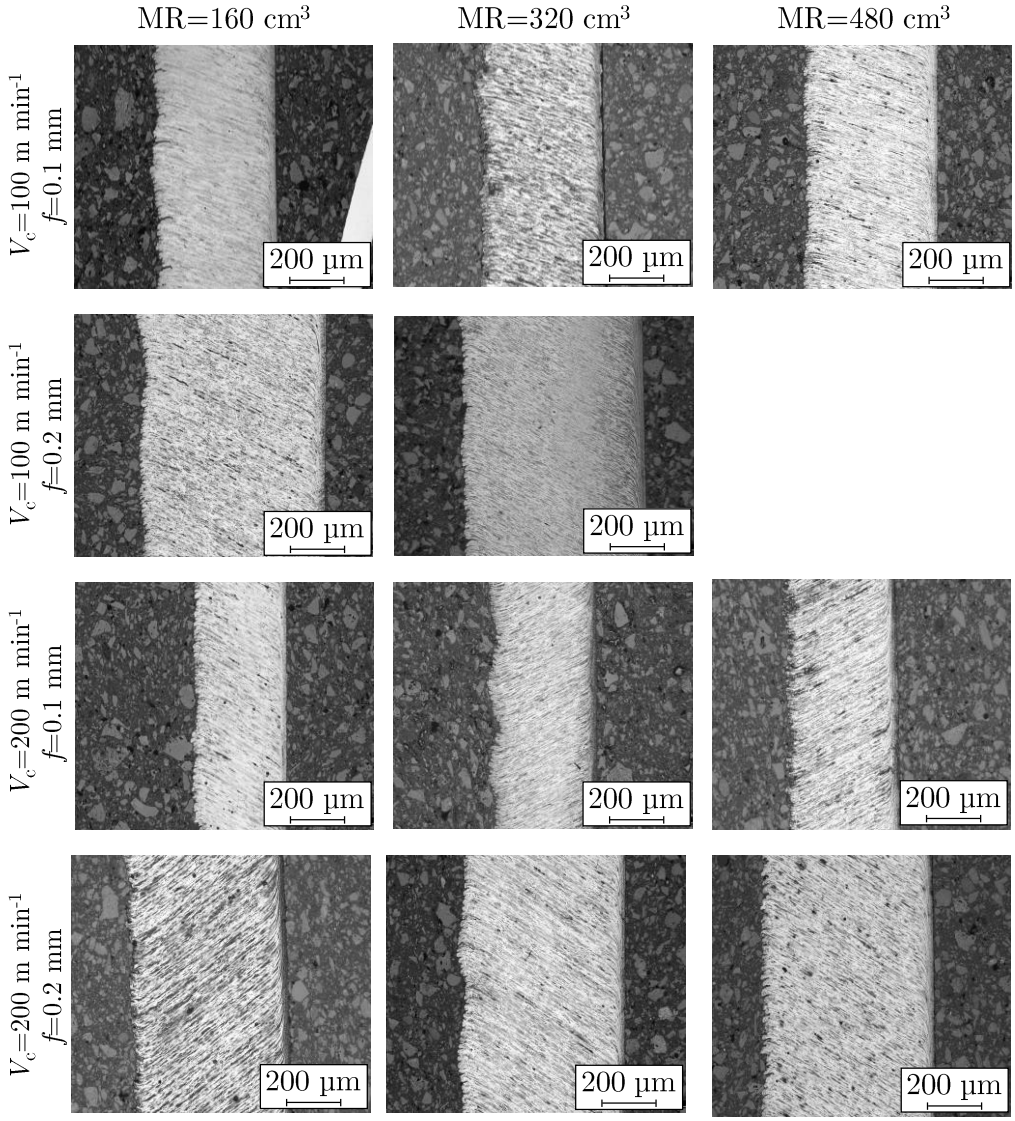

Figure B.6: Micrographs of etched and polished chips. Captures extracted at the MR of 160, 320 and 480 cm^3 for 16MnCr5 steel

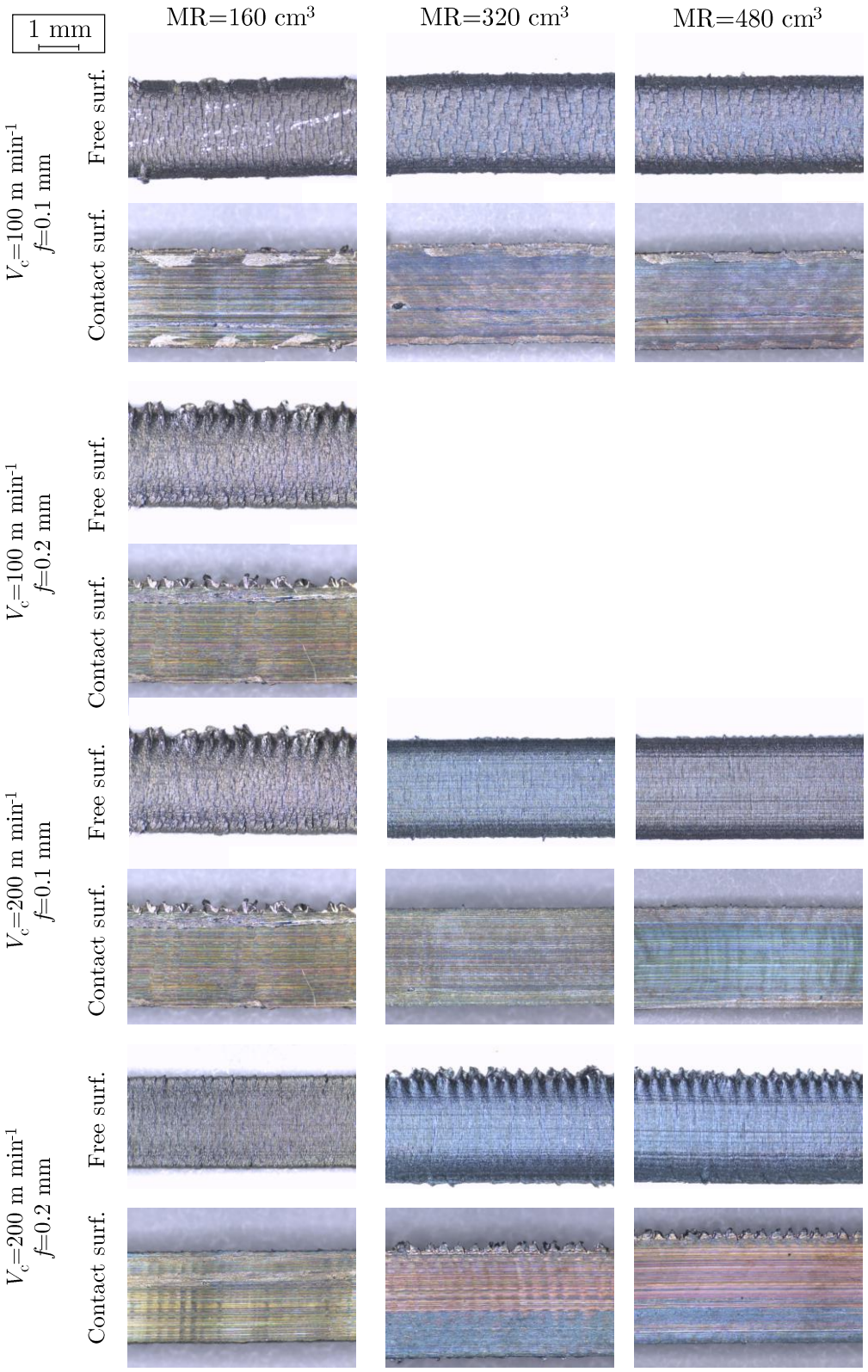

Figure B.7: Macroscope images of chip morphology showing the free and contact surfaces of the chip. Captures extracted at the MR of 160, 320 and 480 cm^3 for 27MnCr5 steel

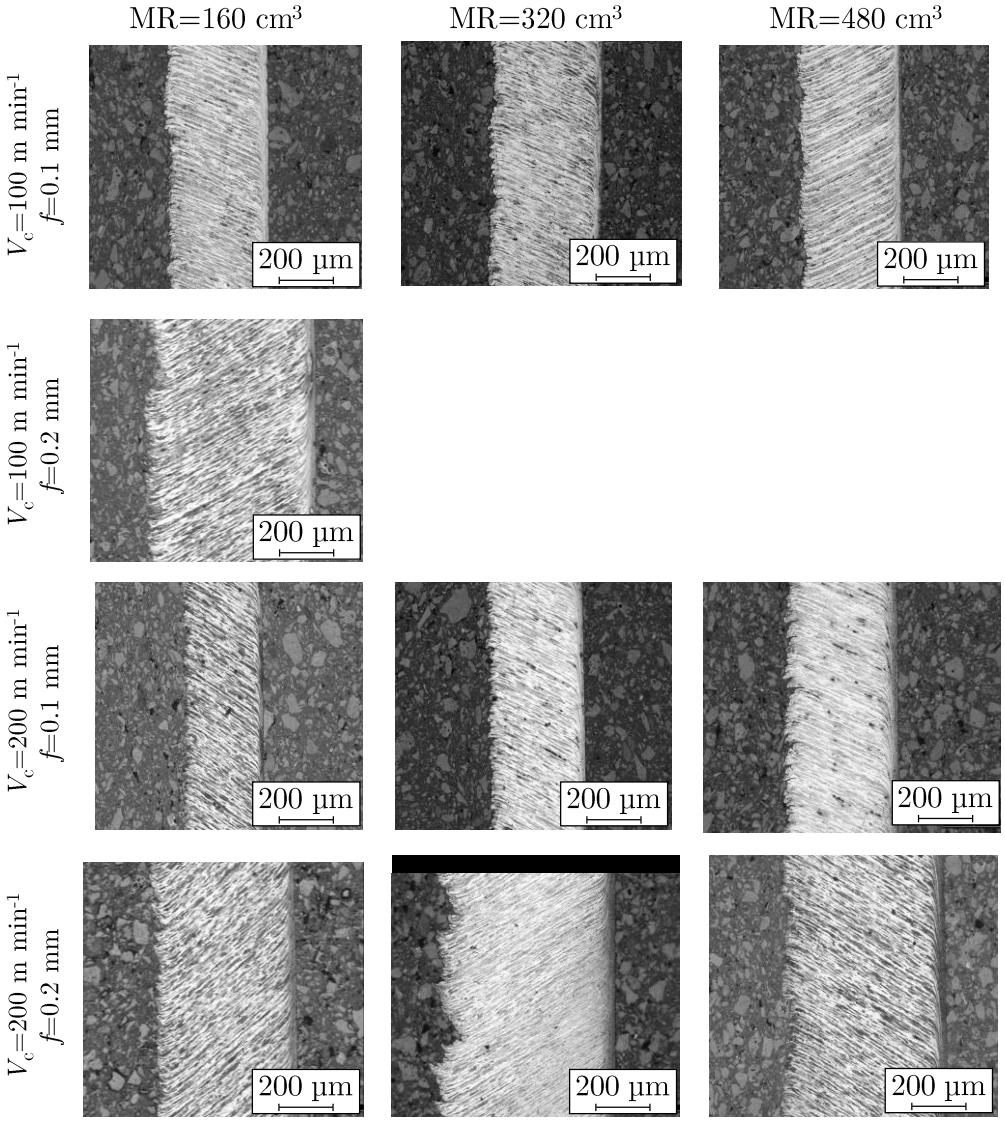

Figure B.8: Micrographs of etched and polished chips. Captures extracted at the MR of 160, 320 and 480 cm^3 for 27MnCr5 steel

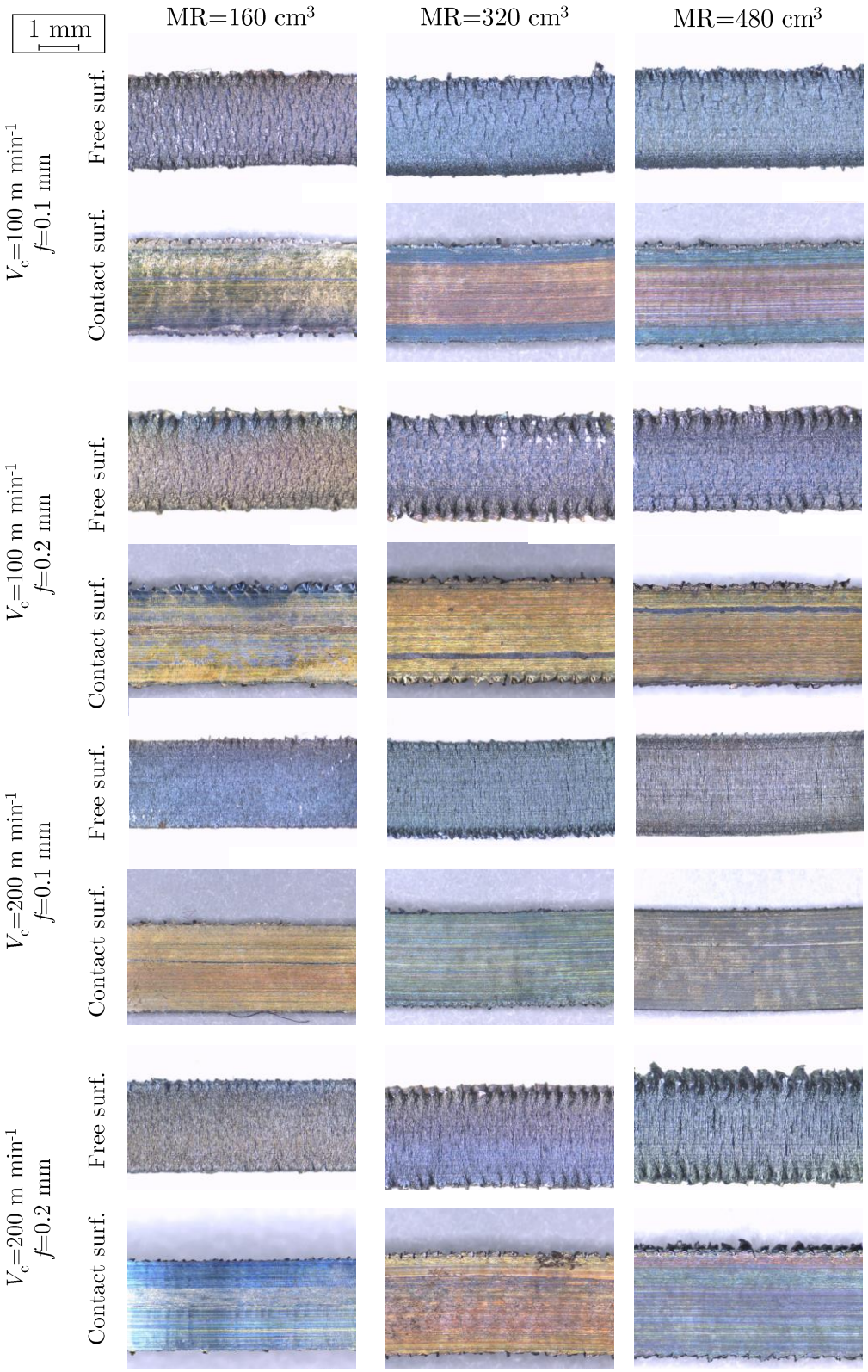

Figure B.9: Macroscope images of chip morphology showing the free and contact surfaces of the chip. Captures extracted at the MR of 160, 320 and 480 cm^3 for C45 steel

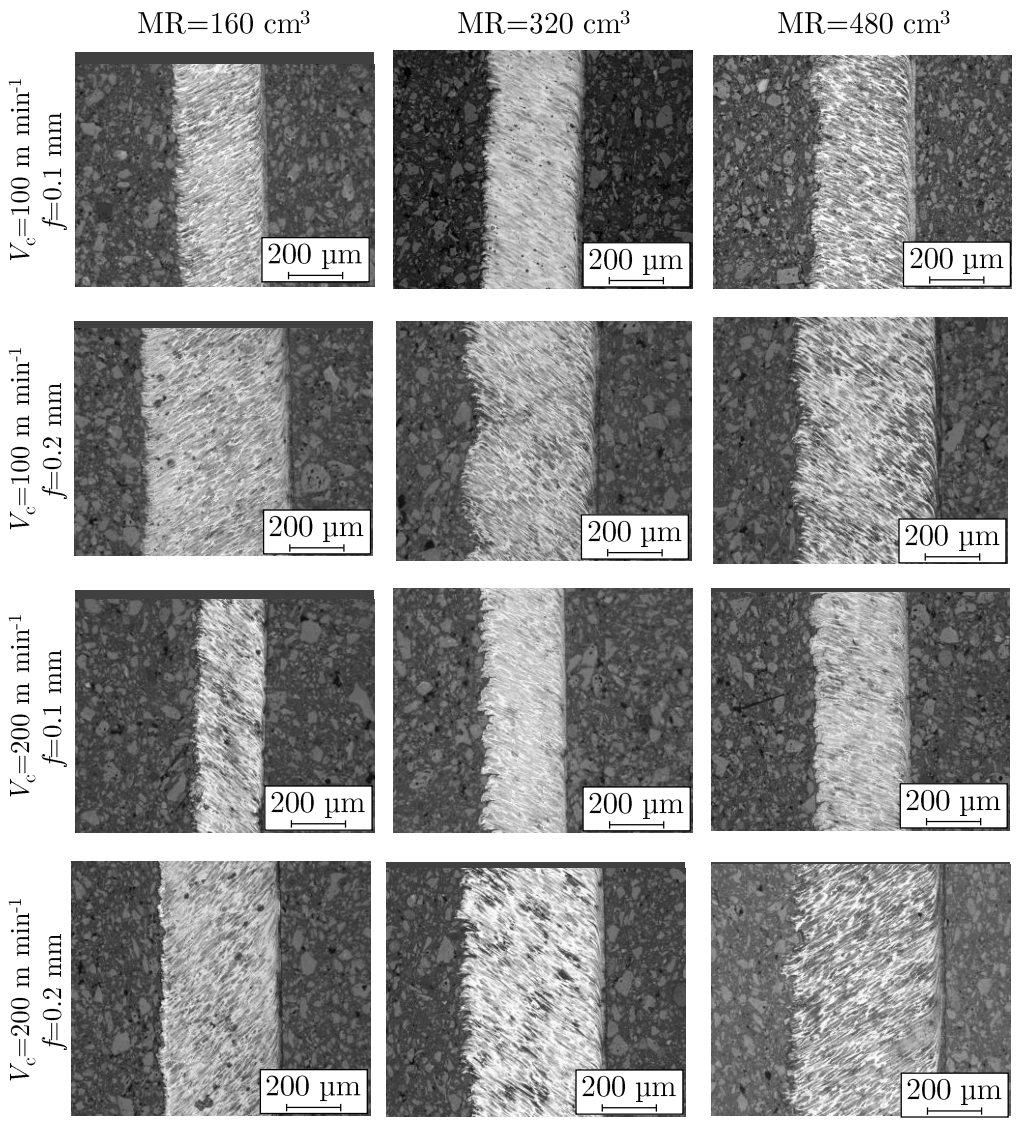

Figure B.10: Micrographs of etched and polished chips. Captures extracted at the MR of 160, 320 and 480 cm^3 for C45 steel

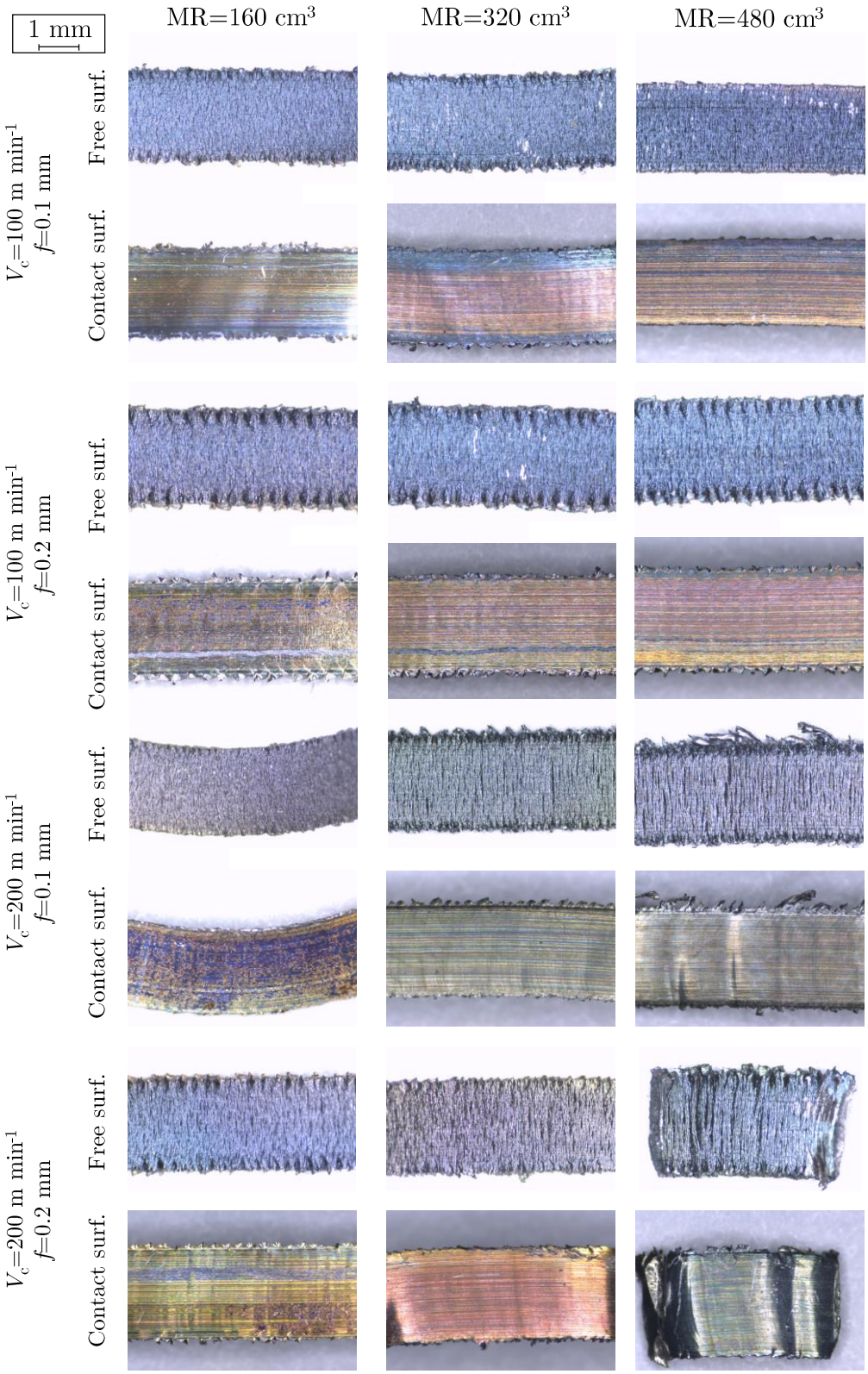

Figure B.11: Macroscope images of chip morphology showing the free and contact surfaces of the chip. Captures extracted at the MR of 160, 320 and 480 cm^3 for C60 steel

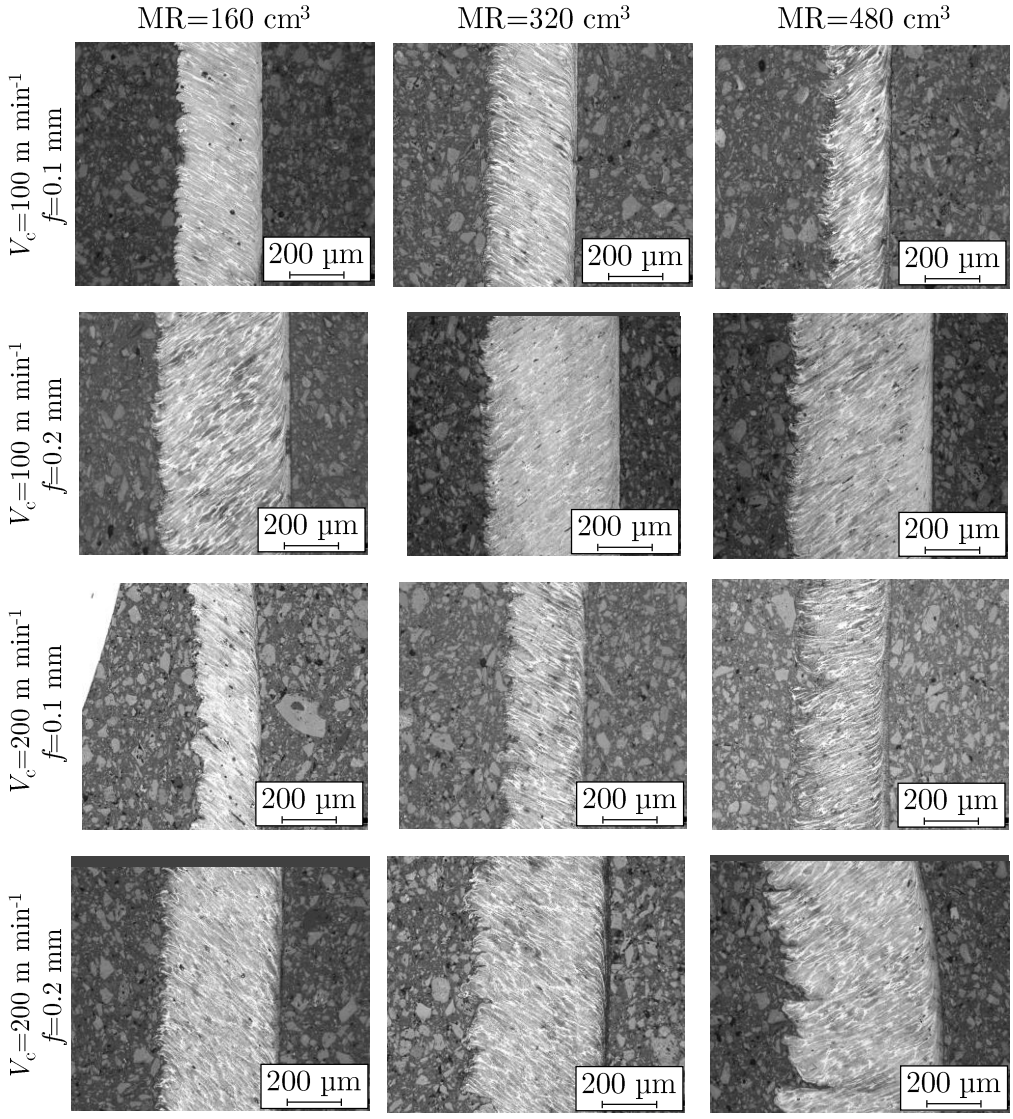

Figure B.12: Micrographs of etched and polished chips. Captures extracted at the MR of 160, 320 and 480 cm^3 for C60 steel

Bibliography

Abdelali HB, Claudin C, Rech J, Salem WB, Kapsa P, and Dogui A (2012). Experimental characterization of friction coefficient at the tool–chip–workpiece interface during dry cutting of AISI 1045. *Wear* 286:108–115.

Abouridouane M, Klocke F, Lung D, and Adams O (2012). Size Effects in Micro Drilling Ferritic-Pearlitic Carbon Steels. *Procedia CIRP* 3:91–96.

Abouridouane M, Klocke F, and Döbbeler B (2016). Analytical temperature prediction for cutting steel. *CIRP Annals-Manufacturing Technology* 65 (1):77–80.

Albrecht P (1960). New developments in the theory of the metal-cutting process: part I. The ploughing process in metal cutting. *Journal of engineering for industry* 82 (4):348–357.

Allain S and Bouaziz O (2008). Microstructure based modeling for the mechanical behavior of ferrite–pearlite steels suitable to capture isotropic and kinematic hardening. *Materials Science and Engineering: A* 496 (1):329–336.

Allain S, Bouaziz O, and Lemoine X (2009). A viscoplastic behavior law for ferritic steels at low homologous temperature. *Revue de Métallurgie–International Journal of Metallurgy* 106 (2):80–89.

Araki T and Yamamoto S (1978). An Evaluation of Machinability of Low-Alloy Steel Materials With or Without Heat Treatment. *Machinability Testing and Utilization of Machining Data*:117–131.

Armendia M, Garay A, Villar A, Davies M, and Arrazola P (2010). High bandwidth temperature measurement in interrupted cutting of difficult to machine materials. *CIRP Annals-Manufacturing Technology* 59 (1):97–100.

Arrazola PJ et al. (2010). Investigations on the effects of friction modeling in finite element simulation of machining. *International Journal of Mechanical Sciences* 52 (1):31–42.

Arrazola PJ, Aristimuno P, Soler D, and Childs T (2015). Metal cutting experiments and modelling for improved determination of chip/tool contact temperature by infrared thermography. *CIRP Annals-Manufacturing Technology* 64 (1):57–60.

Arrazola P (2003). Modélisation numérique de la coupe: étude de sensibilité des paramètres d'entrée et identification du frottement entre outil-copeau. PhD thesis.

Arrazola P, Arriola I, and Davies M (2009). Analysis of the influence of tool type, coatings, and machinability on the thermal fields in orthogonal machining of AISI 4140 steels. *CIRP Annals-Manufacturing Technology* 58 (1):85–88.

Arrazola P, Arriola I, Davies M, Cooke A, and Dutterer B (2008). The effect of machinability on thermal fields in orthogonal cutting of AISI 4140 steel. *CIRP Annals-Manufacturing Technology* 57 (1):65–68.

Arrazola P, Garay A, Fernandez E, and Ostolaza K (2014). Correlation between tool flank wear, force signals and surface integrity when turning bars of Inconel 718 in finishing conditions. *International Journal of Machining and Machinability of Materials* 7 15 (1-2):84–100.

Arrazola P, Meslin F, Maître FL, and Marya S (2004). Sensitivity study in numerical cutting modelling. *7th CIRP*.

Arrazola P and Özel T (2009). Finite element modelling of machining processes. *Intelligent machining: modeling and optimization of the machining processes and systems. ISTE, London*:125–163.

Arrazola P and Ozel T (2008). Numerical modelling of 3D hard turning using arbitrary Lagrangian Eulerian finite element method. *International Journal of Machining and Machinability of Materials* 4 (1):14–25.

Arrazola P, Özel T, Umbrello D, Davies M, and Jawahir I (2013). Recent advances in modelling of metal machining processes. *CIRP Annals-Manufacturing Technology* 62 (2):695–718.

Arrieta I, Courbon C, Cabanettes F, Arrazola PJ, and Rech J (2017). Influence of the ferritic-pearlitic steel microstructure on surface roughness in broaching of automotive steels. *AIP Conference Proceedings*. Vol. 1896. (1). AIP Publishing, p. 090011.

Arriola I, Whitenton E, Heigel J, and Arrazola P (2011). Relationship between machinability index and in-process parameters during orthogonal cutting of steels. *CIRP Annals-Manufacturing Technology* 60 (1):93–96.

ASTM E112-13 (2013). *Standard test methods for determining average grain size*. ASTM International, West Conshohocken, PA.

ASTM E209-00 (2010). *Standard Practice for Compression Tests of Metallic Materials at Elevated Temperatures with Conventional or Rapid Heating Rates and Strain Rates*. ASTM International, West Conshohocken, PA.

ASTM E21-09 (2009). *Standard Test Methods for Elevated Temperature Tension Tests of Metallic Materials*. ASTM International, West Conshohocken, PA.

ASTM E8 / E8M-16a (2016). *Standard Test Methods for Tension Testing of Metallic Materials*. ASTM International, West Conshohocken, PA.

ASTM E9-09 (2009). *Standard Test Methods of Compression Testing of Metallic Materials at Room Temperature*. ASTM International, West Conshohocken, PA.

Attanasio A, Ceretti E, Rizzuti S, Umbrello D, and Micari F (2008). 3D finite element analysis of tool wear in machining. *CIRP Annals-Manufacturing Technology* 57 (1):61–64.

Attanasio A, Faini F, and Outeiro J (2017). FEM Simulation of Tool Wear in Drilling. *Procedia CIRP* 58:440–444.

Attia M and Kops L (2004). A new approach to cutting temperature prediction considering the thermal constriction phenomenon in multi-layer coated tools. *CIRP Annals-Manufacturing Technology* 53 (1):47–52.

Ay H and Yang WJ (1998). Heat transfer and life of metal cutting tools in turning. *International Journal of Heat and Mass Transfer* 41 (3):613–623.

Bäker M, Rösler J, and Siemers C (2002). Finite element simulation of segmented chip formation of Ti6A14V. *Journal of manufacturing science and engineering* 124 (2):485–488.

Bartarya G and Choudhury S (2012). State of the art in hard turning. *International Journal of Machine Tools and Manufacture* 53 (1):1–14.

Bencheikh I, Bilteryst F, Nouari M, and Makich H (2017). Wear Estimation of Coated Tools Using XFEM/Level Set Function. *Procedia CIRP* 58:428–433.

Bergström Y (1970). A dislocation model for the stress-strain behaviour of polycrystalline α-Fe with special emphasis on the variation of the densities of mobile and immobile dislocations. *Materials Science and Engineering* 5 (4):193–200.

Bhattacharya D (1987). Machinability of steel. *JOM Journal of the Minerals, Metals and Materials Society* 39 (3):32–35.

Binder M, Klocke F, and Lung D (2015). Tool wear simulation of complex shaped coated cutting tools. *Wear* 330:600–607.

Björkeborn K, Klement U, and Oskarson HB (2008). Ranking of materials by their machinability applying a short-term test. *Proceedings of the 2nd International Conference on Innovative Cutting Processes Smart Machining, France.*

Björkeborn K, Klement U, and Oskarson HB (2010). Study of microstructural influences on machinability of case hardening steel. *The International Journal of Advanced Manufacturing Technology* 49 (5-8):441–446.

Boothroyd G (1988). *Fundamentals of metal machining and machine tools.* Vol. 28. Crc Press.

Bouaziz O and Le Corre C (2003). Flow stress and microstructure modelling of ferrite-pearlite steels during cold rolling. *Materials Science Forum.* Vol. 426. Trans Tech Publ, p. 1399–1404.

Brooks CR (1996). *Principles of the heat treatment of plain carbon and low alloy steels.* ASM international.

Brunzel YM and Fomin I (1997). Effect of the pearlite structure of structural steel on its machinability. *Metal science and heat treatment* 39 (1):33–35.

Buchkremer S, Klocke F, and Döbbeler B (2016). Impact of the Heat Treatment Condition of Steel AISI 4140 on Its Frictional Contact Behavior in Dry Metal Cutting. *Journal of Manufacturing Science and Engineering* 138 (12):121006.

Bui-Van A, Allain S, Lemoine X, and Bouaziz O (2009). An improved physically based behaviour law for ferritic steels and its application to crash modelling. *International Journal of Material Forming* 2:527–530.

Bünger L, Anhalt K, Taubert R, Krüger U, and Schmidt F (2015). Traceability of a CCD-camera system for high-temperature measurements. *International Journal of Thermophysics* 36 (8):1784–1802.

Calamaz M, Coupard D, and Girot F (2008). A new material model for 2D numerical simulation of serrated chip formation when machining titanium alloy Ti–6Al–4V. *International Journal of Machine Tools and Manufacture* 48 (3):275–288.

Calistes R, Swaminathan S, Murthy T, Huang C, Saldana C, Shankar M, and Chandrasekar S (2009). Controlling gradation of surface strains and nanostructuring by large-strain machining. *Scripta Materialia* 60 (1):17–20.

Ceretti E, Lucchi M, and Altan T (1999). FEM simulation of orthogonal cutting: serrated chip formation. *Journal of Materials Processing Technology* 95 (1):17–26.

Ceretti E, Giardini C, Attanasio A, Filice L, Rizzuti S, and Umbrello D (2009). Diffusion wear modelling in 3D cutting process. *International Journal of Machining and Machinability of Materials* 6 (1-2):95–105.

Céspedes HV (2011). Measuring cutting forces in machining processes. *Journal of Tropical Engineering* 11 (1-2).

Charpentier P, Stone B, Ernst S, and Thomas J (1986). Characterization and Modeling of the High Temperature Flow Behavior of Al 2024. *Metall. Trans* 17:22–27.

Chen G, Ren C, Qin X, and Li J (2015). Temperature dependent work hardening in Ti–6Al–4V alloy over large temperature and strain rate ranges: Experiments and constitutive modeling. *Materials & Design* 83:598–610.

Chen Z, Trent E, and Wise M (1985). The influence of carbide morphology of the machinability of BS970:708M40 steel. Vol. Proceedings of microstructure and mechanical behavior of materials, p. 967–974.

Childs T (2006). Friction modelling in metal cutting. *Wear* 260 (3):310–318.

Childs T (2009). Modelling orthogonal machining of carbon steels. Part I: strain hardening and yield delay effects. *International Journal of Mechanical Sciences* 51 (5):402–411.

Childs T (2010). Surface energy, cutting edge radius and material flow stress size effects in continuous chip formation of metals. *CIRP Journal of Manufacturing Science and Technology* 3 (1):27–39.

Childs T, Mahdi M, and Barrow G (1989). On the stress distribution between the chip and tool during metal turning. *CIRP Annals-Manufacturing Technology* 38 (1):55–58.

Childs T and Rahmad R (2009). The effect of a yield drop on chip formation of soft carbon steels. *Machining Science and Technology* 13 (4):471–487.

Childs T (2000). *Metal machining: theory and applications*. Butterworth-Heinemann.

Chinchanikar S and Choudhury S (2015). Predictive modeling for flank wear progression of coated carbide tool in turning hardened steel under practical machining conditions. *The International Journal of Advanced Manufacturing Technology* 76 (5-8):1185–1201.

Chinchanikar S and Choudhury S (2016). Cutting force modeling considering tool wear effect during turning of hardened AISI 4340 alloy steel using multi-layer TiCN / Al2O3 / TiN-coated carbide tools. *The International Journal of Advanced Manufacturing Technology* 83 (9-12):1749–1762.

Claudin C, Mondelin A, Rech J, and Fromentin G (2010). Effects of a straight oil on friction at the tool–workmaterial interface in machining. *International Journal of Machine Tools and Manufacture* 50 (8):681–688.

Cohen P and Voigt R (2003). Influence of Section Size on the Machinability of Ductile Irons (Observations on the Machinability of Ductile Irons).

Colding BN (1961). Machinability of metals and machining costs. *International Journal of Machine Tool Design and Research* 1 (3):220–248.

Coromant S (1994). El mecanizado moderno. *Manual Práctico. AB Sandvik Coromant. S-811* 81.

Courbon C, Mabrouki T, Rech J, Mazuyer D, Perrard F, and D'Eramo E (2013). Towards a physical FE modelling of a Dry cutting operation: influence of dynamic recrystallization when machining AISI 1045. *Procedia CIRP* 8:516–521.

Courbon C, Mabrouki T, Rech J, Mazuyer D, and D'Eramo E (2011). New thermal issues on the modelling of tool-workpiece interaction: application to dry cutting of AISI 1045 steel. *Advanced Materials Research*. Vol. 223. Trans Tech Publ, p. 286–295.

Courbon C, Mabrouki T, Rech J, Mazuyer D, Perrard F, and D'Eramo E (2014). Further insight into the chip formation of ferritic-pearlitic steels: Microstructural evolutions and associated thermo-mechanical loadings. *International Journal of Machine Tools and Manufacture* 77:34–46.

Cuesta M, Aristimuño P, Garay A, and Arrazola P (2016). Heat transferred to the workpiece based on temperature measurements by IR technique in dry and lubricated drilling of Inconel 718. *Applied Thermal Engineering* 104:309–318.

D'Eramo E et al. (2017). *Innovative Method dedicated to the development of a ferrite-pearlite grade regarding its MAChinability - IMMAC - Annual Report*. Tech. rep.

Davies MA, Yoon H, Schmitz T, Burns T, and Kennedy M (2003). Calibrated thermal microscopy of the tool–chip interface in machining. *Machining science and technology* 7 (2):167–190.

Davim JP (2013). *Machining and Machine-tools: Research and Development*. Elsevier.

Dearnley P and Trent E (1982). Wear mechanisms of coated carbide tools. *Metals Technology* 9 (1):60–75.

Demir H (2008). The effects of microalloyed steel pre-heat treatment on microstructure and machinability. *The International Journal of Advanced Manufacturing Technology* 35 (9-10):1041–1046.

Devillez A, Lesko S, and Mozer W (2004). Cutting tool crater wear measurement with white light interferometry. *Wear* 256 (1):56–65.

Dirikolu M, Childs T, and Maekawa K (2001). Finite element simulation of chip flow in metal machining. *International Journal of Mechanical Sciences* 43 (11):2699–2713.

Dlouhy J, Hauserova D, and Novy Z (2016). Influence of the carbide-particle spheroidisation process on the microstructure after the quenching and annealing of 100CrMnSi6-4 bearing steel. *Materiali in tehnologije* 50 (1):159–162.

Doane DV (1988). Softening high hardenability steels for machining and cold forming. *Journal of Heat Treating* 6 (2):97–109.

Dollar M, Bernstein I, and Thompson A (1988). Influence of deformation substructure on flow and fracture of fully pearlitic steel. *Acta Metallurgica* 36 (2):311–320.

Dorogoy A and Rittel D (2009). Determination of the Johnson–Cook material parameters using the SCS specimen. *Experimental mechanics* 49 (6):881.

Ducobu F, Arrazola PJ, Rivière-Lorphèvre E, de Zarate GO, Madariaga A, and Filippi E (2017a). The CEL method as an alternative to the current modelling approaches for Ti6Al4V orthogonal cutting simulation. *Procedia CIRP* 58:245–250.

Ducobu F, Rivière-Lorphèvre E, and Filippi E (2016). Application of the Coupled Eulerian-Lagrangian (CEL) method to the modeling of orthogonal cutting. *European Journal of Mechanics-A/Solids* 59:58–66.

Ducobu F, Rivière-Lorphèvre E, and Filippi E (2017b). Mesh influence in orthogonal cutting modelling with the Coupled Eulerian-Lagrangian (CEL) method. *European Journal of Mechanics-A/Solids*.

Ducobu F, Arrazola PJ, Rivière-Lorphèvre E, and Filippi E (2015). Comparison of several behaviour laws intended to produce a realistic Ti6Al4V chip by finite elements modelling. *Key Engineering Materials*. Vol. 651. Trans Tech Publ, p. 1197–1203.

Ducobu F, Rivière-Lorphèvre E, and Filippi E (2011). A Lagrangian FEM model to produce saw-toothed macro-chip and to study the depth of cut influence on its formation in orthogonal cutting of Ti6Al4V. *Advanced Materials Research*. Vol. 223. Trans Tech Publ, p. 3–11.

Ebrahimi A and Moshksar M (2009). Evaluation of machinability in turning of microalloyed and quenched-tempered steels: Tool wear, statistical analysis, chip morphology. *Journal of materials processing technology* 209 (2):910–921.

Ee K, Dillon O, and Jawahir I (2005). Finite element modeling of residual stresses in machining induced by cutting using a tool with finite edge radius. *International Journal of Mechanical Sciences* 47 (10):1611–1628.

Engwirda D (2014). Locally optimal Delaunay-refinement and optimisation-based mesh generation. PhD thesis. University of Sydney.

Estrin Y (1996). Dislocation-density-related constitutive modeling. *Unified constitutive laws of plastic deformation* 1:69–106.

Eurostat NACE (2017). *Manufacturing statistics - NACE Rev. 2 - statistical classification of economic activities in the european community*. Office for Official Publications of the European Communities, Luxemburg.

Fais A (2016). *How do I know what material my car is made of*. URL: `https://www.quora.com/How-do-I-know-what-material-my-car-is-made-of` (visited on 01/11/2018).

Filice L, Micari F, Settineri L, and Umbrello D (2007). Wear modelling in mild steel orthogonal cutting when using uncoated carbide tools. *Wear* 262 (5):545–554.

Gåård A (2008). Wear mechanisms in sheet metal forming: Effects of tool microstructure, adhesion and temperature. PhD thesis. Karlstad University.

Goetz R and Semiatin S (2001). The adiabatic correction factor for deformation heating during the uniaxial compression test. *Journal of materials engineering and performance* 10 (6):710–717.

Gol'dshtein YE and Morozov A (1980). Steels with selenium and calcium. *Metal Science and Heat Treatment* 22 (11):787–793.

González B, Matos J, and Toribio J (2009). Relación microestructura-propiedades mecánicas en acero perlítico progresivamente trefilado. *Anales de Mecánica de la Fractura*. Vol. 26, p. 142–147.

Gray GT, Vecchio K, and Livescu V (2016). Compact forced simple-shear sample for studying shear localization in materials. *Acta Materialia* 103:12–22.

Guo Y and Liu C (2002). FEM analysis of mechanical state on sequentially machined surfaces.

Guo Y and Wen Q (2005). *A hybrid modeling approach to investigate chip morphology transition with the stagnation effect by cutting edge geometry*. Society of Manufacturing Engineers.

Gutiérrez I and Altuna M (2008). Work-hardening of ferrite and microstructure-based modelling of its mechanical behaviour under tension. *Acta Materialia* 56 (17):4682–4690.

Haddag B and Nouari M (2013). Tool wear and heat transfer analyses in dry machining based on multi-steps numerical modelling and experimental validation. *Wear* 302 (1):1158–1170.

Hamann J, Grolleau V, and Le Maître F (1996). Machinability improvement of steels at high cutting speeds–study of tool/work material interaction. *CIRP Annals-Manufacturing Technology* 45 (1):87–92.

Hamann J, Le Maître F, and Guillot D (1994). Selective transfer built-up layer displacement in high-speed machining–consequences on tool wear and cutting forces. *CIRP Annals-Manufacturing Technology* 43 (1):69–72.

Handbook M (1990). Vol. 1. *ASM international*:981–994.

Hastings W, Mathew P, Oxley P, and Taylor J (1980). Estimated cutting temperatures and their use as a predictor of tool performance when machining plain carbon steels. *Proceedings of the Twentieth International Machine Tool Design and Research Conference*. Springer, p. 313–320.

Herve P, Cedelle J, and Negreanu I (2012). Infrared technique for simultaneous determination of temperature and emissivity. *Infrared Physics & Technology* 55 (1):1–10.

Hibbitt H, Karlsson B, and Sorensen P (2014). Abaqus analysis user's manual version 6.14. *Dassault Systèmes Simulia Corp.: Providence, RI, USA*.

Holmberg K, Matthews A, and Ronkainen H (1998). Coatings tribology - contact mechanisms and surface design. *Tribology International* 31 (1):107–120.

Hopkinson B (1914). A method of measuring the pressure produced in the detonation of high explosives or by the impact of bullets. *Philosophical Transactions of the Royal Society of London. Series A, Containing Papers of a Mathematical or Physical Character* 213:437–456.

Hor A, Morel F, Lebrun JL, and Germain G (2013). An experimental investigation of the behaviour of steels over large temperature and strain rate ranges. *International Journal of Mechanical Sciences* 67:108–122.

Hosford WF (2010). *Mechanical behavior of materials*. Cambridge University Press.

Hosseinkhani K and Ng E (2015). A combined empirical and numerical approach for tool wear prediction in machining. *Procedia CIRP* 31:304–309.

Huang Y and Liang SY (2004). Modeling of CBN tool flank wear progression in finish hard turning. *Transactions-American Society of Mechanical Engineers Journal of Manufacturing Science and Engineering* 126 (1):98–106.

Huang Y and Liang SY (2005). Modeling of cutting forces under hard turning conditions considering tool wear effect. *Transactions of the ASME-B-Journal of Manufacturing Science and Engineering* 127 (2):262–270.

Humphry-Baker S, Marshall J, Smith G, and Lee W (2017). Thermophysical properties of Co-free WC-FeCr hardmetals.

ISO 3685 (1999). *Tool-life testing with single-point turning tools*. International Organization for Standardization.

Iturbe A, Giraud E, Hormaetxe E, Garay A, Germain G, Ostolaza K, and Arrazola P (2017). Mechanical characterization and modelling of Inconel 718 material behavior for machining process assessment. *Materials Science and Engineering: A* 682:441–453.

Jaspers S and Dautzenberg J (2002). Material behaviour in conditions similar to metal cutting: flow stress in the primary shear zone. *Journal of Materials Processing Technology* 122 (2):322–330.

Johnson GR and Cook WH (1983). A constitutive model and data for metals subjected to large strains, high strain rates and high temperatures. *Proceedings of the 7th International Symposium on Ballistics*. Vol. 21. The Hague, Netherlands: International Ballistics Committee, p. 541–547.

Karlsson B and Linden G (1975). Plastic deformation of ferrite-pearlite structures in steel. *Materials Science and Engineering* 17 (2):209–219.

Kim S, Lee Y, and Byon S (2003). Study on constitutive relation of AISI 4140 steel subject to large strain at elevated temperatures. *Journal of Materials Processing Technology* 140 (1):84–89.

Klocke F and Frank P (2006). Simulation of tool wear in hard turning. *9th CIRP International Workshop on Modelling of Machining Operations*, p. 11–12.

Klocke F and Kuchie A (2011). Cutting. *Manufacturing Processes 1*. Springer.

Klocke F, Raedt HW, and Hoppe S (2001). 2D-FEM simulation of the orthogonal high speed cutting process.

Kop T, Sietsma J, and Van Der Zwaag S (2001). Dilatometric analysis of phase transformations in hypo-eutectoid steels. *Journal of Materials Science* 36 (2):519–526.

Korkut I and Donertas M (2007). The influence of feed rate and cutting speed on the cutting forces, surface roughness and tool–chip contact length during face milling. *Materials & design* 28 (1):308–312.

Krauss G (2015). *Steels: processing, structure, and performance*. Asm International.

Kronenberg M (1966). *Machining science and application: theory and practice for operation and development of machining processes*. Pergamon Press.

Kurimoto T, Barrow G, and Davies B (1982). The influence of aqueous fluids on the wear characteristics and life of carbide cutting tools. *CIRP Annals-Manufacturing Technology* 31 (1):19–23.

Kwon P (2000). Predictive models for flank wear on coated inserts. *ASME J. Tribol* 122 (1):340–347.

Laasraoui A and Jonas J (1991). Prediction of steel flow stresses at high temperatures and strain rates. *Metallurgical transactions A* 22 (7):1545–1558.

Lane J, Stam J, and Wolfe K (1967). General introductory review of the relationship between metallurgy and machinability.

Leopold J (2014). Approaches for modelling and simulation of metal machining - a critical review. *Manufacturing Review* 1:7.

Li B (2012). A review of tool wear estimation using theoretical analysis and numerical simulation technologies. *International Journal of Refractory Metals and Hard Materials* 35:143–151.

Lin ZC and Lo SP (2001). 2-D discontinuous chip cutting model by using strain energy density theory and elastic-plastic finite element method. *International journal of mechanical sciences* 43 (2):381–398.

Lorentzon J and Järvstråt N (2008). Modelling tool wear in cemented-carbide machining alloy 718. *International Journal of Machine Tools and Manufacture* 48 (10):1072–1080.

Luo X, Cheng K, Holt R, and Liu X (2005). Modeling flank wear of carbide tool insert in metal cutting. *Wear* 259 (7):1235–1240.

Lurdos O, Montheillet F, and Damamme G (2008). Empirical and physically based flow rules relevant to high speed processing of 304L steel. *International Journal of Material Forming* 1:1431–1434.

Maekawa K, Shirakashi T, and Usui E (1983). Flow stress of low carbon steel at high temperature and strain rate. II: Flow stress under variable temperature and variable strain rate. *Bulletin of the Japan Society of Precision Engineering* 17 (3):167–172.

Malakizadi A, Gruber H, Sadik I, and Nyborg L (2016). An FEM-based approach for tool wear estimation in machining. *Wear* 368:10–24.

Malakizadi A, Hosseinkhani K, Mariano E, Ng E, Del Prete A, and Nyborg L (2017). Influence of friction models on FE simulation results of orthogonal cutting process. *The International Journal of Advanced Manufacturing Technology* 88 (9-12):3217–3232.

Mathew P (1989). Use of predicted cutting temperatures in determining tool performance. *International Journal of Machine Tools and Manufacture* 29 (4):481–497.

Mav RK (2013). Numerical analysis of bird strike damage on composite sandwich structure using Abaqus/Explicit. *San José State University.*

Mecking H and Kocks U (1981). Kinetics of flow and strain-hardening. *Acta Metallurgica* 29 (11):1865–1875.

Medvedeva A, Bergström J, Gunnarsson S, Krakhmalev P, and Nordh LG (2011). Influence of nickel content on machinability of a hot-work tool steel in prehardened condition. *Materials & design* 32 (2):706–715.

Melkote SN, Grzesik W, Outeiro J, Rech J, Schulze V, Attia H, Arrazola PJ, M'Saoubi R, and Saldana C (2017). Advances in material and friction data for modelling of metal machining. *CIRP Annals* 66 (2):731–754.

Merchant ME (1944). Basic mechanics of the metal cutting process. *Journal of Applied Mechanics* 11 (A):168–175.

Mian AJ, Driver N, and Mativenga PT (2010). A comparative study of material phase effects on micro-machinability of multiphase materials. *The International Journal of Advanced Manufacturing Technology* 50 (1):163–174.

Milovic R and Wallbank J (1983). The machining of low carbon free cutting steels with high speed steel tools. *Journal of Applied Metalworking* 2 (4):249–257.

Modi O, Deshmukh N, Mondal D, Jha A, Yegneswaran A, and Khaira H (2001). Effect of interlamellar spacing on the mechanical properties of 0.65% C steel. *Materials Characterization* 46 (5):347–352.

Nemat-Nasser S and Guo WG (2003). Thermomechanical response of DH-36 structural steel over a wide range of strain rates and temperatures. *Mechanics of Materials* 35 (11):1023–1047.

Nordgren A and Melander A (1989). Deformation behaviour of different types of inclusion during chip formation in turning of quenched and tempered steels. *Materials science and technology* 5 (9):940–951.

Nordgren A and Melander A (1990). Tool wear and inclusion behaviour during turning of a calcium-treated quenched and tempered steel using coated cemented carbide tools. *Wear* 139 (2):209–223.

Obikawa T, Takemura Y, Akiyama Y, Shinozuka J, and Sasahara H (2009). Microscopic phase-dependent residual stresses in the machined surface layer of two-phase alloy. *Journal of Materials Processing Technology* 209 (9):4496–4501.

Obikawa T, Sasahara H, Shirakashi T, and Usui E (1997). Application of computational machining method to discontinuous chip formation. *Journal of Manufacturing Science and Engineering* 119 (4B):667–674.

Oh S, Semiatin S, and Jonas J (1992). An analysis of the isothermal hot compression test. *Metallurgical and Materials Transactions A* 23 (3):963–975.

Okusa K, Kitagawa R, and Akasawa T (1978). Method of Testing Steel Machinability by Face-Milling End of Cylindrical Workpiece. *Machinability Testing and Utilization of Machining Data*:36–50.

Opitz H and Gappisch M (1962). Some recent research on the wear behaviour of carbide cutting tools. *International Journal of Machine Tool Design and Research* 2 (1):43–73.

Outeiro J, Pina J, M'saoubi R, Pusavec F, and Jawahir I (2008). Analysis of residual stresses induced by dry turning of difficult-to-machine materials. *CIRP Annals-Manufacturing Technology* 57 (1):77–80.

Oxley PLB and Young H (1989). The mechanics of machining: an analytical approach to assessing machinability.

Oxley P (1966). Introducing strain-rate dependent work material properties into the analysis of orthogonal cutting. *CIRP* 13 (2):127–138.

Ozcatalbas Y and Ercan F (2003). The effects of heat treatment on the machinability of mild steels. *Journal of Materials Processing Technology* 136 (1):227–238.

Özel T, Sima M, Srivastava A, and Kaftanoglu B (2010). Investigations on the effects of multi-layered coated inserts in machining Ti–6Al–4V alloy with experiments and finite element simulations. *CIRP Annals-Manufacturing Technology* 59 (1):77–82.

Özel T and Ulutan D (2012). Prediction of machining induced residual stresses in turning of titanium and nickel based alloys with experiments and finite element simulations. *CIRP Annals-Manufacturing Technology* 61 (1):547–550.

Özel T (2006). The influence of friction models on finite element simulations of machining. *International Journal of Machine Tools and Manufacture* 46 (5):518–530.

Özel T (2009). Computational modelling of 3D turning: Influence of edge micro-geometry on forces, stresses, friction and tool wear in PcBN tooling. *Journal of Materials Processing Technology* 209 (11):5167–5177.

Özel T and Zeren E (2004). Determination of work material flow stress and friction for FEA of machining using orthogonal cutting tests. *Journal of Materials Processing Technology* 153:1019–1025.

Özel T and Zeren E (2005). Finite element method simulation of machining of AISI 1045 steel with a round edge cutting tool. *Proceedings of the 8th CIRP International Workshop on Modeling of Machining Operations*, p. 533–542.

Padilla Montes D (2011). Validación de un fluido de corte para máquinas-herramienta.

Pálmai Z (2013). Proposal for a new theoretical model of the cutting tool's flank wear. *Wear* 303 (1):437–445.

Pawade R, Joshi SS, and Brahmankar P (2008). Effect of machining parameters and cutting edge geometry on surface integrity of high-speed turned Inconel 718. *International Journal of Machine Tools and Manufacture* 48 (1):15–28.

Pickering F and Gladman T (1963). Metallurgical developments in carbon steels. *ISI Special Report* 81 (10).

Pujana J, Del Campo L, Pérez-Sáez R, Tello M, Gallego I, and Arrazola P (2007). Radiation thermometry applied to temperature measurement in the cutting process. *Measurement Science and Technology* 18 (11):3409.

Q'Donnelly B, Reuben R, and Baker T (1984). Quantitative assessment of strengthening parameters in ferrite-pearlite steels from microstructural measurements. *Metals Technology* 11 (1):45–51.

Raabe D (2006). Steels for Automotive Applications. *steel research international* 77 (9-10):619–619.

Raczy A, Elmadagli M, Altenhof W, and Alpas A (2004). An Eulerian finite-element model for determination of deformation state of a copper subjected to orthogonal cutting. *Metallurgical and materials transactions a* 35 (8):2393–2400.

Rao K and Hawbolt E (1992). Development of constitutive relationships using compression testing of a medium carbon steel. *Journal of Engineering Materials and Technology* 114 (1):116–123.

Ray K and Mondal D (1991). The effect of interlamellar spacing on strength of pearlite in annealed eutectoid and hypoeutectoid plain carbon steels. *Acta metallurgica et materialia* 39 (10):2201–2208.

Rech J and Courbon C (2017). *Internal report - Friction coefficient of AISI-1045 steel-uncoated carbide workpiece-tool material pair*. Tech. rep. École nationale d'ingénieurs de Saint-Étienne ENISE.

Rech J and Moisan A (2003). Surface integrity in finish hard turning of case-hardened steels. *International Journal of Machine Tools and Manufacture* 43 (5):543–550.

Renault 1193 (1969). *Normalisation Renault Automobiles Service 60201, Section Normes et Cahiers des Charges, Structures de globulisation aciers mi-durs recuits*. Normalisation Renault Automobiles, Service 60201, Section Normes et Cahiers des Charges.

Renault 1194 (1969). *Normalisation Renault Automobiles Service 60201, Section Normes et Cahiers des Charges, Structures ferrite-perlite lamellaire aciers doux recuits*. Normalisation Renault Automobiles, Service 60201, Section Normes et Cahiers des Charges.

Rossetto S and Koch U (1970). An investigation of temperature distribution on tool flank surface.

Sacristan I, Garay A, Hormaetxe E, Aperribay J, and Arrazola PJ (2016). Influence of oxygen content on the machinability of Ti-6Al-4V alloy. *The International Journal of Advanced Manufacturing Technology* 86 (9-12):2989–3005.

Sacristan I (2016). Rough turning of Ti-6Al-4V and Ti-10V-2Fe-Â·AL: Understanding machinability by looking at the link between machining parameters and material properties. PhD thesis. Mondragon University.

Samanta SK (1968). Resistance to dynamic compression of low-carbon steel and alloy steels at elevated temperatures and at high strain-rates. *International Journal of Mechanical Sciences* 10 (8):613IN1619–618IN2636.

Sartkulvanich P, Altan T, and Göcmen A (2005). Effects of flow stress and friction models in finite element simulation of orthogonal cutting-a sensitivity analysis. *Machine Science and Technology* 9 (1):1–26.

Saunders P (2007). *Radiation Thermometry: Fundamentals and Applications in the Petrochemical Industry*. Vol. 78. SPIE press.

Schulze V, Zanger F, Michna J, Ambrosy F, and Pabst R (2011). Investigation of the Machining Behavior of Metal Matrix Composites (MMC) using Chip Formation Simulation. *13th CIRP Conference on Modelling of Machining Operations, Sintra, Portugal*, p. 20–29.

Schulze V, Boev N, and Zanger F (2012). Simulation of metal cutting process with variable cutting thickness during broaching. *Procedia CIRP* 1:437–442.

Schulze V and Zanger F (2011). Development of a simulation model to investigate tool wear in Ti-6Al-4V alloy machining. *Advanced Materials Research*. Vol. 223. Trans Tech Publ, p. 535–544.

Semiatin S and Jonas J (2003). Torsion testing to assess bulk workability. *Materials Park, OH: ASM International, 2003*.86–121.

Seo S, Min O, and Yang H (2005). Constitutive equation for Ti–6Al–4V at high temperatures measured using the SHPB technique. *International journal of impact engineering* 31 (6):735–754.

Shaw M and Dirke S (1956). On the wear of cutting tools. *Microtechnic* 10 (4):187–193.

Shaw MC and Cookson J (2005). *Metal cutting principles*. Vol. 2. Oxford university press New York.

Shi G, Deng X, and Shet C (2002). A finite element study of the effect of friction in orthogonal metal cutting. *Finite Elements in Analysis and Design* 38 (9):863–883.

Shirakashi T and Usui E (1973). Friction characteristics on tool face in metal machining. *JSPE* 39:966–972.

Siddhpura M and Paurobally R (2012). A review of chatter vibration research in turning. *International Journal of Machine tools and manufacture* 61:27–47.

Sima M and Özel T (2010). Modified material constitutive models for serrated chip formation simulations and experimental validation in machining of titanium alloy Ti–6Al–4V. *International Journal of Machine Tools and Manufacture* 50 (11):943–960.

Simoneau A, Ng E, and Elbestawi M (2007). Grain size and orientation effects when microcutting AISI 1045 steel. *CIRP Annals-Manufacturing Technology* 56 (1):57–60.

Soler D, Aristimuño P, Garay A, and Arrazola PJ (2015a). Uncertainty of temperature measurements in dry orthogonal cutting of titanium alloys. *Infrared Physics & Technology* 71:208–216.

Soler D, Childs TH, and Arrazola PJ (2015b). A note on interpreting tool temperature measurements from thermography. *Machining Science and Technology* 19 (1):174–181.

Soltani A (2013). Effect of Adiabatic Heating on Strain Induced Phase Transformations in Stainless Steels.

Stephenson D (1993). Tool-work thermocouple temperature measurements-theory and implementation issues. *Transactions-American Society of Mechanical Engineers Journal of Engineergin for Industry* 115:432–432.

Takeyama H and Murata R (1963). Basic investigation of tool wear. *Journal of engineering for industry* 85:33.

Tata H and Sampsell R (1973). *Effect of Additives on the Machinability and Properties of Alloy-Steel Bars*. Tech. rep. SAE Technical Paper.

Taylor F (1907). *On the art of metal cutting*. Trans. ASME 28.

Tisza M (2001). *Physical metallurgy for engineers*. Asm International.

Trent EM and Wright PK (2000). *Metal cutting*. Butterworth-Heinemann.

Trigger K and Chao B (1956). The mechanism of crater wear of cemented carbide tools. *Trans. ASME* 78 (5):1119.

Ulutan D and Ozel T (2011). Machining induced surface integrity in titanium and nickel alloys: a review. *International Journal of Machine Tools and Manufacture* 51 (3):250–280.

Umbrello D (2008). Finite element simulation of conventional and high speed machining of Ti6Al4V alloy. *Journal of materials processing technology* 196 (1):79–87.

Umbrello D, Hua J, and Shivpuri R (2004). Hardness-based flow stress and fracture models for numerical simulation of hard machining AISI 52100 bearing steel. *Materials Science and Engineering: A* 374 (1):90–100.

Usui E, Shirakashi T, and Kitagawa T (1984). Analytical prediction of cutting tool wear. *Wear* 100 (1):129–151.

Verdeja LF, Verdeja JI, and González R (2009). Machinability improvement through heat treatment in 8620 low-carbon alloyed steel. *Machining Science and Technology* 13 (4):529–542.

Wagner V, Baili M, Dessein G, and Lallement D (2010). Experimental characterization of behavior laws for titanium alloys: application to Ti5553. *Key Engineering Materials*. Vol. 446. Trans Tech Publ, p. 147–155.

Wang J, Guo WG, Gao X, and Su J (2015). The third-type of strain aging and the constitutive modeling of a Q235B steel over a wide range of temperatures and strain rates. *International Journal of Plasticity* 65:85–107.

Warnecke G and Oh JD (2002). A new thermo-viscoplastic material model for finite-element-analysis of the chip formation process. *CIRP Annals-Manufacturing Technology* 51 (1):79–82.

Wassdahl J (2008). Modeling of wear mechanisms in mechanical cutting. PhD thesis.

Wu X and Gorham D (1997). Stress equilibrium in the split Hopkinson pressure bar test. *Le Journal de Physique IV* 7 (C3):C3–91.

Xie LJ, Schmidt J, Schmidt C, and Biesinger F (2005). 2D FEM estimate of tool wear in turning operation. *Wear* 258 (10):1479–1490.

Xiong W, Lohmar J, Bambach M, and Hirt G (2015). A new method to determine isothermal flow curves for integrated process and microstructural simulation in metal forming. *International Journal of Material Forming* 8 (1):59–66.

Xu J, Liu Z, Guo G, and Chen M (2013). An investigation on wear mechanism of high-speed turning of free-cutting steel AISI 1215 using uncoated and multi-layer coated tools. *The International Journal of Advanced Manufacturing Technology*:1–17.

Yen YC (2004). Modeling of metal cutting and ball burnishing-Prediction of tool wear and surface properties. PhD thesis. The Ohio State University.

Yen YC, Söhner J, Lilly B, and Altan T (2004). Estimation of tool wear in orthogonal cutting using the finite element analysis. *Journal of Materials Processing Technology* 146 (1):82–91.

Zanger F, Boev N, and Schulze V (2015). Novel approach for 3D simulation of a cutting process with adaptive remeshing technique. *Procedia CIRP* 31:88–93.

Zaslavsky A, Gorokh A, Goldshtein YE, and Shenk R (1969). Interaction of selenium and tellurium with iron and carbon steel. *Fiz-Khim Mekhan Mat* 5 (2):243–245.

Zemzemi F, Bensalem W, Rech J, Dogui A, and Kapsa P (2008). New tribometer designed for the characterisation of the friction properties at the tool/chip/workpiece interfaces in machining. *Lubrication Science* 14 (1):11–25.

Zemzemi F, Rech J, Salem WB, Dogui A, and Kapsa P (2009). Identification of a friction model at tool/chip/workpiece interfaces in dry machining of AISI4142 treated steels. *Journal of Materials Processing Technology* 209 (8):3978–3990.

Zerilli FJ and Armstrong RW (1987). Dislocation-mechanics-based constitutive relations for material dynamics calculations. *Journal of Applied Physics* 61 (5):1816–1825.

Zhang Y, Outeiro J, and Mabrouki T (2015). On the selection of Johnson-Cook constitutive model parameters for Ti-6Al-4V using three types of numerical models of orthogonal cutting. *Procedia CIRP* 31:112–117.

Zhao D (2000). Testing for Deformation Modeling. *Materials Park, OH: ASM International, 2000.*798–810.

Zhao H, Barber G, and Zou Q (2002). A study of flank wear in orthogonal cutting with internal cooling. *Wear* 253 (9):957–962.

Zhu D, Zhang X, and Ding H (2013). Tool wear characteristics in machining of nickel-based superalloys. *International Journal of Machine Tools and Manufacture* 64:60–77.

Zorev N (1963). Inter-relationship between shear processes occurring along tool face and shear plane in metal cutting. *International research in production engineering* 49:42–49.